ABSTRACT

Title of dissertation: EFFECTS OF OPTICAL ILLUMINATION ON SUPERCONDUCTING QUANTUM DEVICES

Rangga P. Budoyo, Doctor of Philosophy, 2015

Dissertation directed by: Professor Frederick Wellstood
Department of Physics

I report measurements of two different types of superconducting devices illuminated by 780 nm light, one of the wavelengths needed in a proposed atom-superconductor hybrid quantum system.

I illuminated a thin-film Al lumped-element resonator and observed the resonator quality factor and resonance frequency as a function of illumination intensity, microwave power, and temperature. The resonator was mounted in a 3d aluminum cavity. The variation in optically-induced loss due to microwave power was similar to the behavior expected for loss from a distribution of two-level systems. Although this behavior may suggest the presence of optically activated two-level systems, I found that the loss is better explained by the presence of nonequilibrium quasiparticles generated by the illumination and excited by the microwave drive. I described a model of the system where optical absorption creates an effective source of phonons and solved the coupled quasiparticle-phonon rate equations. I found good agreement between the simulation and the measured resonator quality factor and frequency shift as a function of temperature, microwave power, and optical illumination.

I fabricated a transmon qubit and studied the qubit transition frequency and relaxation time as a function of illumination intensity and temperature. The qubit was mounted in a 3d aluminum cavity and coupled to the cavity forming a Jaynes-Cummings system. Qubit relaxation showed non-exponential behavior that I fit to a quasiparticle fluctuation model with two characteristic times. The transition frequency and both characteristic times decreased with increasing illumination intensity. For comparison, I described a nonequilibrium quasiparticle model for the expected frequency shift and relaxation time due to quasiparticle tunneling through the Josephson junction. While the quasiparticle simulation predicted the general qualitative behavior of the frequency shift and relaxation time, there were some significant discrepancies with the data. This suggests the model needs to be extended, for example by including a different gap in the two superconductor layers forming the junction, and by taking into account other possible sources of loss and decoherence.

EFFECTS OF OPTICAL ILLUMINATION ON SUPERCONDUCTING QUANTUM DEVICES

by

Rangga Perdana Budoyo

Dissertation submitted to the Faculty of the Graduate School of the
University of Maryland, College Park in partial fulfillment
of the requirements for the degree of
Doctor of Philosophy
2015

Advisory Committee:
Professor Frederick Wellstood, Chair/Advisor
Professor Christopher Lobb, Co-Advisor
Professor Luis Orozco
Professor Steven Anlage
Professor John Cumings

In the memory of my grandparents

Acknowledgments

I don't know how people can write such long acknowledgments in their dissertations, but I'm going to try. This is going to be either short and rambling, or most likely long and rambling. So here goes...

I would like to thank Prof. Fred Wellstood for serving as my main research advisor. I learned a lot from him with his wealth of knowledge, and ultimately enjoyed the various discussions I had with him, even though they often got quite long or loud. A special shout out to the 'Fred Red', which improved the manuscripts I have written, including this dissertation of course (although not this sentence). Prof. Chris Lobb has deep insight on many things, and always lightens up the mood in the labs or at meetings. Most importantly, I thank these two for keeping me employed for the past seven years.

Prof. Luis Orozco has such dedicated passion for physics that was noticeable from my few interactions with him. I would also like to acknowledge other professors in the Atoms on SQUIDs project, Prof. Steve Rolston and Prof. Bob Anderson. I would like to confess and apologize to Bob that I rarely read the articles the he dutifully print and bring down to the lab everyday. I also thank Prof. Steve Anlage and Prof. John Cumings for agreeing to be in my dissertation committee.

In addition to the professors, I also learned a lot by working with the students and postdocs in the lab over the years. I started working with the group on phase qubits in the Sub-Basement, and learned a lot from my predecessor grad students Tony Przybysz, Hyeokshin Kwon, and Ben Cooper. Cody Ballard helped me a lot

over the years with his skills in machining and magic. After a while I moved up the elevator shaft to the Atoms on SQUIDs lab, and I thank Kristen Voigt for being fine with me basically taking over part of her project. I thank the postdocs, Zaeill Kim who basically set up the superconducting side of the project at the beginning, Jared Hertzberg for his dedication and plastic cockroaches, and Sudeep Dutta for taking over the transmon measurements and possible exorcism duty that may come with it. I also thank Roberto Ramos for his visit, and for his dancing that helped me pinpoint the source of the mystery fluctuations. I must not forget the various contributions made by the undergrads working at the lab: Erik Crowe, Ben Cheng, Adnan Choudhary, Liam Fowl, and Zhongzheng Tian.

I enjoyed the constant interactions with the atomic side of the Atoms on SQUIDs: grad students Jon Hoffman, Jeff Grover, Sylvain Ravets, and Pablo Solano, postdoc Jongmin Lee, and many undergrads and summer students. I can't list all of them here because there are a lot of them and I don't remember many of their names. Sorry! There is another inhabitant of the sub-basement that I must not forget. I enjoyed various discussions I had with Alex Jeffers, especially at the many lunches we had.

I also thank the people at the superconducting qubit groups at LPS. Ben Palmer lets me use their SEM for my fabrications, and I thank him and his group members: Vitaley Zaretskey, Bala Suri, Sergey Novikov, Shavi Premaratne, and Jenhao Yeh for stopping what they are doing to let me in to use the SEM, in addition to many helps and discussions. I also have many discussions with Kevin Osborn and the members of his group over the years.

I thank you, dedicated reader, for being so dedicated that you read a random paragraph in the middle of the acknowledgments. Or you might just be really lucky and accidentally stumble into reading this paragraph. I will treat the first person who told me the magic phrase ("Traktir makan") to lunch. The people mentioned here are not eligible though.

I need to acknowledge the many help by the many staff members. These include Al Godinez, Jesse Anderson, Linda O'Hara, Jane Hessing, Paulina Alejandro, and Pauline Rirksopa in Physics, Mary Sutton, Brian Straughn, and Doug Bensen in CNAM, and Tom Loughran, John Abrahams, and Jon Hummel at FabLab. I also thank Oxford Instruments engineers Nick Denton, Dave Marsh, and Paul Brodie for making sure the dilution fridges are running properly. This last category also include the tiny elves called 'Helium mix' running around inside the fridge lines 24/7 when it's cold.

I thank my undergrad advisor, Prof. Tsampikos Kottos, for many things including for convincing me to go to grad school and for suggesting University of Maryland as one of the school choices.

I also thank the funding agencies that kept me paid and kept the experiments running. These include NSF (through PFC), LPS, JQI, and CNAM.

I made many friends in the area that I can't list them all, but I want to acknowledge the members of the house that was at one point (not really) known as BEARD including Nameless Cat #1 and Nameless Cat #2 (RIP), the members of the house that was at one point called MAJAR13 especially Rufus Reed, and the members of the Wrhatnala gamelan group.

No thanks to From Software (especially Hidetaka Miyazaki and the Smelter Demon), Arkane Studios, Bethesda, Ubisoft, CD Projekt Red, Eidos, Bioware, Namco Bandai, Square Enix, Konami, and Hideo Kojima (for ZOE, not MGS).

Finally, I thank my parents, Liliek Eko Budoyo and Siswari Kunsaparti, and my sister, Saras Kenia Budoyo, for their constant support and being patient with me while I was finishing grad school.

It was long and rambling.

Table of Contents

List of Tables

List of Figures

Chapter 1: Introduction

1.1 Quantum Computers

Feynman was the first to propose using quantum states for computation [1]. Specifically, he proposed using a quantum computer to simulate other quantum mechanical systems because classical computers are very inefficient for simulating large quantum systems. Several years later, Deutsch and Josza found that, due to the nature of quantum entanglement, there are classes of problems that could be solved much faster using a quantum computer than classical computers [2, 3].

Since then, several distinct quantum algorithms have been proposed that are theoretically capable of solving certain problems significantly faster than classical computers. Two of the most famous quantum algorithms are Grover's algorithm and Shor's algorithm. Grover's algorithm is used to search elements of a large unstructured database [4]. Shor's algorithm can be used to find the prime factor of very large numbers [5]. This is of particular importance because the current standard for cryptography, RSA encryption, uses the fact that it takes a classical computer a time that grows exponentially as the number of digits to factorize large numbers [6]. Since Shor's algorithm factors prime numbers in a time that is polynomial in the number of digits [5], a quantum computer could break RSA encryption.

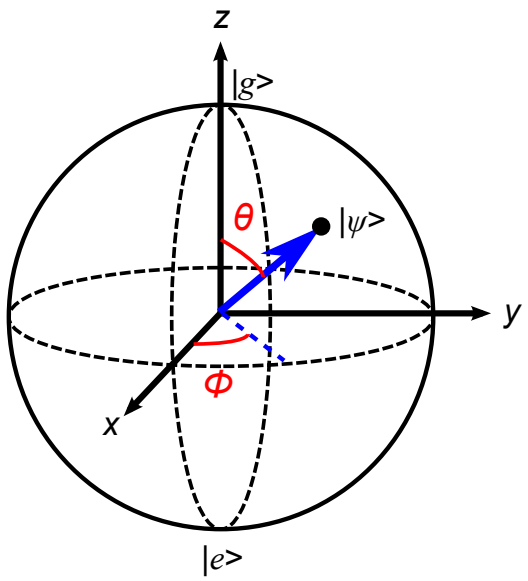

Figure 1.1: Bloch sphere representation of a pure quantum state of a qubit. A qubit state $|\psi\rangle$ can be any point in the surface of the sphere (black dot) given by the angles θ and ϕ

Information in a classical computer is stored in bits, each of which can have values 0 or 1. Information in a quantum computer will be stored in many quantum bits (qubits). A qubit has two quantum eigenstates. The lower energy state is called the ground state and typically represented by $|0\rangle$ or $|g\rangle$ in ket notation. The higher energy state is the excited state and represented by $|1\rangle$ or $|e\rangle$. A pure quantum state of a qubit can be represented as a point in the Bloch sphere (see Fig. 1.1). The Bloch sphere has a radius of 1 and $|g\rangle$ is located on the north pole of the sphere and $|e\rangle$ is on the south pole.

Any pure quantum state $|\psi\rangle$ of a qubit can be written as a superposition of $|g\rangle$ and $|e\rangle$ of the form

$$|\psi\rangle \;=\; \cos(\theta/2)|g\rangle \;+\; e^{i\phi}\sin(\theta/2)|e\rangle, \tag{1.1}$$

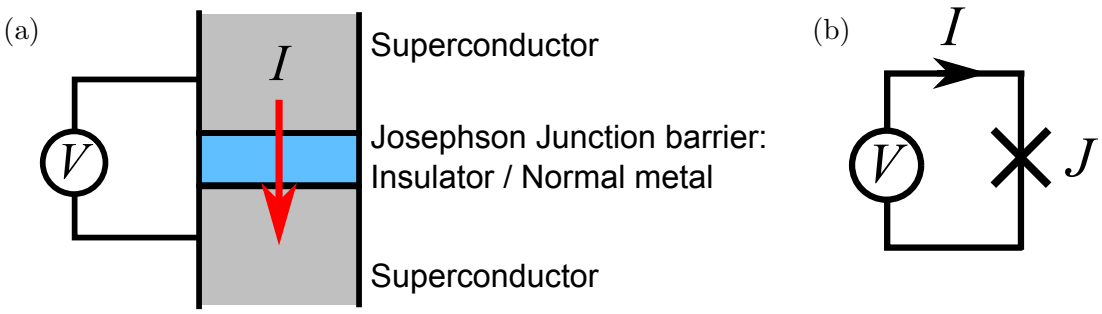

Figure 1.2: (a) Simple picture of a Josephson junction, in which two superconductors are separated by a thin insulator or normal metal. (b) Circuit symbol of a Josephson junction. In both images, V is the voltage across the junction and I is the current passing through the junction.

where θ is the polar angle and ϕ is the azimuthal angle on the Bloch sphere. The probability P_g to find the qubit in the ground state and the probability P_e to find the qubit in the excited state are given by

$$P_g = |\langle\psi|g\rangle|^2 = \cos^2(\theta/2) \tag{1.2}$$

$$P_e = |\langle\psi|e\rangle|^2 = \sin^2(\theta/2). \tag{1.3}$$

Experimentally, many different quantum systems have been proposed for use as a qubit. These include photons [7], trapped ions [8, 9], trapped atoms [10], quantum dots [11], nuclear spins [12], impurities in solids [13], and a wide range of electrical devices Some of the most promising candidates for a qubit are made from superconducting devices [14], as discussed below in Section 1.3.

1.2 Josephson Effect

All superconducting qubits use one or more Josephson junctions to provide anharmonicity or nonlinearity in a quantum system. Anharmonicity is essential

because it allows isolation of two of the states which can then be used as a qubit. As shown in Fig. 1.2(a), a Josephson junction consists of two superconductors separated by a weak link, which can be an insulator, a normal metal, or a constriction in a superconducting connection [15]. The current I through the junction and voltage drop V across the junction obey the Josephson relations [16]

$$I = I_0 \sin\gamma, \tag{1.4}$$

$$V = \frac{\Phi_0}{2\pi}\frac{d\gamma}{dt}. \tag{1.5}$$

where I_0 is the critical current of the junction, $\Phi_0 = h/2e$ is the flux quantum, and γ is the gauge-invariant phase difference across the junction. For currents I larger than I_0, the junction switches to a state where the phase evolves with time. For fixed current $I < I_0$, the phase can be constant in time, and one finds $V = 0$ from Eq. 1.5. Thus current can flow with no voltage drop, up to a maximum value given by I_0. Josephson was awarded the Nobel Prize in physics in 1973 for his prediction of the Josephson effect.

Equations 1.4 and 1.5 can be used to show that

$$V = \frac{\Phi_0}{2\pi\, I_0 \cos\gamma}\frac{dI}{dt} \equiv L_J\frac{dI}{dt}, \tag{1.6}$$

where $L_J = \Phi_0/2\pi I_0 \cos\gamma$ is caled the Josephson inductance. Equation 1.6 implies that a Josephson junction can be represented as an inductor with inductance L_J that depends on γ and hence depends on current I. This current dependent inductance shows that Josephson junctions are nonlinear inductors, and from Eq. 1.6 it can be readily shown that the inductance can be positive, negative or infinite.

1.3 Superconducting Qubits

Nakamura *et al.* reported the first coherent operation of a superconducting qubit in 1999 [17]. Since then, many other groups have researched different aspects of many types of superconducting qubits.

One of the main benchmarks for performance of any superconducting qubit is the coherence time T_2, which is the timescale on which the qubit loses quantum coherence. The definition of the coherence time T_2 in qubits follows the definition used in nuclear magnetic resonance (NMR) [18]. The coherence time T_2 arises from two different time scales: the relaxation time T_1, which is the characteristic time for a qubit to decay from the excited state to the ground state, and the dephasing time T_ϕ, which is the characteristic time for a qubit to lose its phase coherence. The time scales are related by [18]

$$\frac{1}{T_2} = \frac{1}{2T_1} + \frac{1}{T_\phi}. \tag{1.7}$$

The sources of decoherence may be from coupling to other systems, for example two-level systems (TLS) [19] or quasiparticles [20, 21], or from noise coming from external lines or the environment.

For quantum computation, one needs T_2 to be much larger than the typical time τ_g required to do a gate operation on the qubit. For superconducting qubits, this gate operation time can be as short as about 10 ns and is typically in the range of 10-100 ns. While the first superconducting qubit T_1 and T_2 values were of order nanoseconds [17], the characteristic times increased rapidly over the years. Currently the highest T_2 values for superconducting qubits exceed $\sim$ 150 microseconds [22] and

the highest T_1 values are of a few milliseconds [23].

In addition to the characteristic times T_1, T_ϕ, T_2 and τ_g, superconducting qubits also have characteristic energies that determine much of the behavior of the qubit. These characteristic energies are the Josephson energy E_J and the charging energy E_C where

$$E_J = \frac{\Phi_0 I_0}{2\pi}, \tag{1.8}$$

$$E_C = \frac{e^2}{2C_\Sigma}. \tag{1.9}$$

Here C_Σ is the total capacitance of the qubit, which includes the capacitance of the junction and the effective capacitance of all other capacitors shunting the junction. E_C is the electrostatic energy in the capacitor when a single electron is stored in the capacitor.

Over the years, many different superconducting qubit designs have been developed [14]. Each type of superconducting qubit is distinguished by the quantum states used and the ratio E_J/E_C. Charge qubits or Cooper-pair boxes (CPBs) have $E_J/E_C \lesssim 1$ and use the number of Cooper pairs stored in the junction capacitor as their qubit states, which is sharply defined except at certain biases that are used for the actual qubit states [17, 24]. Flux qubits or persistent-current qubits have $E_J/E_C > 1$ and the supercurrent flowing around a superconducting loop is sharply defined for most bias conditions[25, 26]. Phase qubits have $E_J/E_C \gg 1$ and use the fact that the effective potential energy of the system has local minima as a function of phase γ, and use the lowest states within a well as the qubit states [27–29].

The first work on phase qubits began in 1999 at Maryland. The group later

focused on a variant of phase qubits called the dc SQUID phase qubit, and attempted to understand and recuce sources of decoherence in this design [30, 31]. Typically for charge qubits, charge noise limits the decoherence, for flux and qubits, flux noise limits the decoherence, and for phase qubits the relaxation (T_1) limits the decoherence.

More recent qubit designs aim to reduce decoherence by a combination of techniques including adding additional low-loss circuit elements, isolating the device from the environment, using better materials, removing non-essential materials, and removing bias lines. Transmon qubits attempted to reduce charge noise in charge qubit by adding a shunt capacitance. To maintain anharmonicity the capacitance needed to be chosen such that $50 \lesssim E_J/E_C \lesssim 200$ [32], resulting in a device that was very similar to phase qubits except with no bias. Similar methods were implemented for flux qubits [33] and phase qubits [19]. On the other hand, fluxonium qubits attempted to reduce both charge and flux noise by adding a large effective shunt inductance to a charge qubit. The effective inductance was made from an array of dozens of Josephson junctions [34]. More recently, UCSB started using Xmon qubits which can be though of as variants of tunable transmon qubits [35].

I note here that superconducting resonators, which are not qubits, have turned out to be important components in some superconducting quantum computer architectures. In particular, resonators are used in circuit quantum-electrodynamics (CQED) based qubit state readout [36] or for coupling and state transfer between multiple qubits [37]. Studies of resonators by themselves have also proven to be useful in understanding sources of internal loss and have led to improvements in the

materials, fabrication, and design of qubits and resonators [38, 39].

Extensive research has revealed that two-level systems (TLS) in dielectric regions [19, 40, 41] and quasiparticles in the superconductor [42–48] can be major sources of internal loss in superconducting resonators and qubits. Recent approaches to reducing TLS loss include better cleaning of the substrate and improved film deposition techniques, for example by using molecular beam epitaxy (MBE) [39]. Stray light was identified as a major source of quasiparticles, and improvements in shielding the device from stray light have resulted in reduced quasiparticle loss [45, 46]. Embedding qubits inside a superconducting or normal metal 3D resonant microwave cavity resulted in major improvements in the coherence time [49]. The use of a cavity allowed a reduction in dielectric volume, introduced an additional radiation shield, and led to better isolation of the qubit from the microwave environment. In fact, the longest qubit coherence times I mentioned above were achieved by transmon qubits [22] and fluxonium qubits [23] embedded inside 3D cavities. In these "3D qubits", the cavity was also used for qubit readout.

1.4 Hybrid Quantum Systems

The coherence times of superconducting qubits have improved by several orders of magnitude in the last 15 years, but they are still relatively short compared to some other types of qubits. Examples of other solid-state qubits include nitrogen-vacancy (NV) centers in diamond, which have coherence times of order 1 s [50], and phosphorus donors in silicon, which have been shown recently to have coherence

times of about 3 minutes [51]. Examples of atomic qubits include trapped neutral Rb, where the longest coherence time that has been reported is about 3 s [52], and trapped ions, with the longest coherence times of order 10 minutes [9].

Superconducting qubits also have several advantages over many other types of qubits. First, the coherence time is not really a good figure of merit for a quantum computer. What is important is that the gate operation time τ_g is much smaller than the coherence time T_2. This is critical because only for $\tau_g \ll T_2$ can many quantum operations be performed before the quantum computer loses coherence. The gate operation time of superconducting qubits can be as short as $\sim$ 10 ns, faster than many other qubits, and much less than T_2 in the best devices. Furthermore, short τ_g also results in faster computation times and this is a significant advantage. For example, trapped atoms appear to have gate operation time of order 1 μs [53] or 100 times slower. The fast gate time of superonducting qubits is due to the strong coupling between the qubit and the qubit drive line. Finally, superconducting qubits can be typically fabricated using standard micro- and nano-fabrication techniques, and this offers the potential for a technology that can be scaled up to very large numbers of qubits.

The relation between coherence time and gate operation time in superconducting qubits suggests one of the motivations for building a hybrid quantum system in which a superconducting qubit is coupled to another type of quantum system. In a hybrid quantum system, one hopes to harness the advantages of both systems: use the fast gate operation times in superconducting qubits for fast computation and use the long coherence times in another type of qubit for the storage of quantum

infomation. Compared to classical computers, the superconducting qubits act as quantum processor while the other qubits act as a quantum memory.

The coupling between a superconducting qubit and another type of qubit can be achieved directly, using electric (capacitive) coupling or magnetic (inductive) coupling, or indirectly, for example using a resonator or a tuned coupling element, *i.e* the coupler acts as a quantum bus. There have been several different proposals for hybrid quantum systems where superconducting resonators or qubits are coupled to different quantum systems, including trapped ions [54, 55], neutral atoms [56, 57], Rydberg atoms [58, 59], molecules [60, 61], and quantum dots [62]. Some of these proposals are summarized in the review article by Xiang *et al.* [63] and I describe several examples below where the system have been experimentally realized.

NV centers are promising candidates for building a hybrid quantum system [50, 64]. A single NV center consists of a nitrogen atom replacing a carbon atom in a site in a diamond lattice that is next to a vacancy . NV centers occur naturally in diamond and they can also be artificially implanted. An NV center has a ground-to-excited state transition frequency of 2.87 GHz, which is in the microwave regime. It is somewhat lower than the typical superconducting resonator and qubit frequencies, but appears to be usable. The main advantages are the resonance frequency, long coherence time, and the ability to access the system optically and the relative ease to couple to superconducting circuits. Potential disadvantages include optical sensitivity of the superconducting qubit and weak coupling.

Based on a proposal by Marcos *et al.* [65], Zhu *et al.* managed to directly magnetically couple a flux qubit to NV centers in a diamond substrate that was

glued on top of the qubit [66]. A different approach was taken by the Esteve group in France. They magnetically coupled NV centers to a tunable coplanar waveguide superconducting resonator, which in turn was electrically coupled to a transmon [67–70].

In addition to NV centers, coupling between other spin ensembles in solids and a superconducting resonator have been experimentally realized. Schuster *et al.* have coupled Cr^{3+} defects in ruby and P1 defects in diamond to a coplanar waveguide resonator [71] and Bushev *et al.* have coupled Er^{3+} defects in Y_2SiO_5 crystals to a coplanar waveguide resonator [72, 73].

Soykal and Flatté proposed a hybrid system where a cavity is coupled to ferromagnetic magnon modes [74, 75]. Since then magnetic coupling between magnon modes in a yttrium iron garnet (YIG) crystal and coplanar waveguide resonators [76] or microwave 3D cavities [77–79] have been experimentally realized. More recently, Tabuchi *et al.* have reported indirect coherent coupling between magnon modes in a YIG crystal and a transmon qubit, mediated by a 3D cavity [80].

I note here that most of the experimental realizations of hybrid systems so far were between a superconducting resonator or qubit and another solid state system. While there are significant complications and challenges in building such hybrid systems, additional complications arise in hybrid systems in which a superconducting quantum circuit is coupled to a truly atomic non-solid state system, as I discuss in the following sections.

1.5 Proposed Hybrid System

The hybrid quantum system that our group at the University of Maryland (Wellstood/Lobb/Orozco/Rolston Group) is working on is a superconducting quantum circuit coupled to trapped neutral atoms. Specifically, the hyperfine ground states of ^{87}Rb atoms between $|^5S_{1/2}, F = 1\rangle$ and $|^5S_{1/2}, F = 2\rangle$ has a transition frequency at $f_{\mathrm{Rb}} = 6.835$ GHz when no magnetic field is applied. The initial proposal was to directly magnetically couple the Rb atoms to a flux qubit [81]. For atoms trapped about 5 μm from the qubit, the coupling between a single ^{87}Rb atom an a flux qubit is estimated to be around $g_{\mathrm{Rb}}/2\pi \approx 40$ Hz, and the total effective coupling is $g_{\mathrm{eff}} = g_{\mathrm{Rb}}\sqrt{N_{\mathrm{Rb}}}$ where N_{Rb} is the total number of trapped atoms [81].

As a proof-of-principle experiment, we decided to try to magnetically couple trapped ^{87}Rb atoms to a superconducting resonator [83] (see Fig. 1.3). One advantage resonators have is they are larger than flux qubits (~ 1 mm vs ~ 10 μm), which means it is possible to couple to more atoms, resulting in larger effective coupling g_{eff}. Using a resonator, it may also be possible to indirectly couple a superconducting qubit to trapped atoms. In particular, we plan to capacitively couple a transmon qubit to a resonator which in turn is inductively coupled to trapped atoms (see Fig. 1.4).

Our proposed hybrid system has some serious challenges that will need to be overcome. Many of the techniques used to trap neutral atoms, including several proposed for hybrid systems [57, 84], require a strong magnetic field or relatively large optical power. Having a strong magnetic field near a resonator can introduce

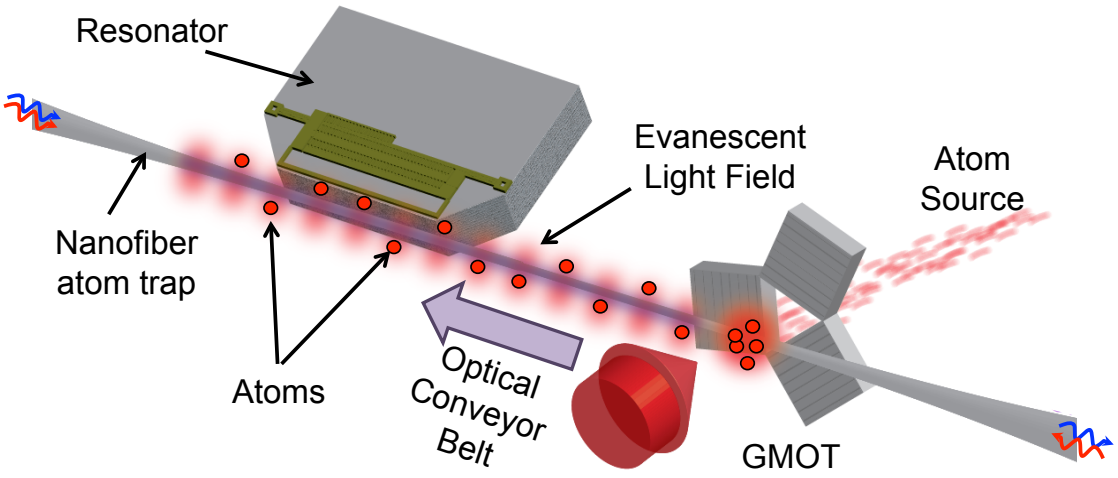

Figure 1.3: Schematic of proposed prototype for a hybrid system where a superconducting resonator is coupled to neutral Rb atoms trapped on a tapered optical nanofiber. The Rb atoms are initially loaded at the nanofiber trap using a grating magneto-optical trap (GMOT) and then transferred using an optical conveyor belt to within 10 μm from the resonator. Figure from Ref. [82].

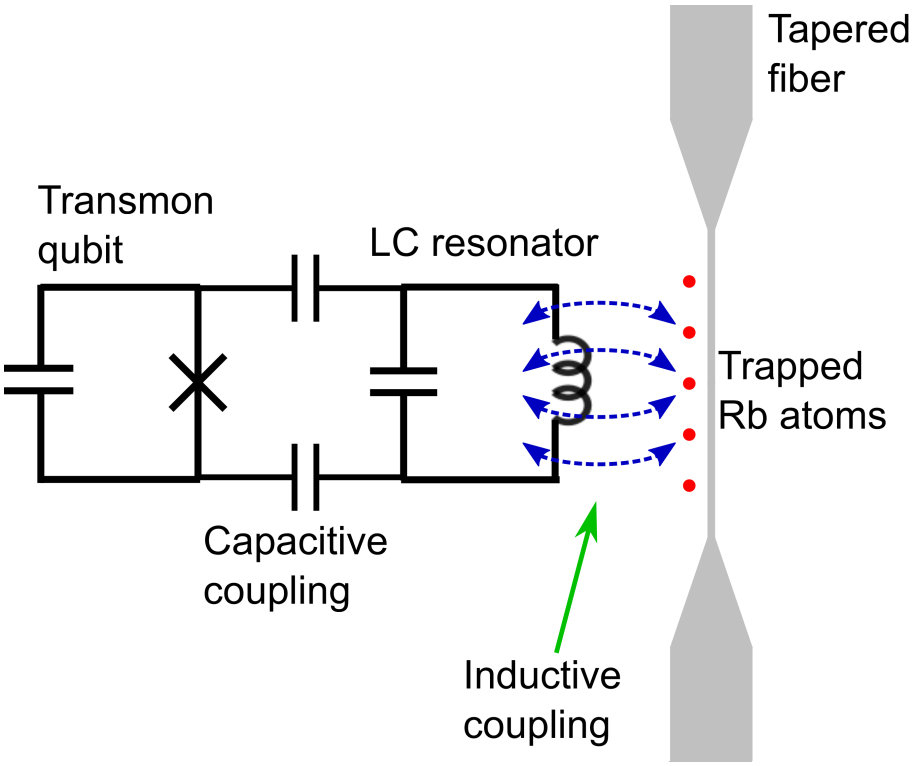

Figure 1.4: Circuit schematic of proposed hybrid system where a transmon is capacitively coupled to a resonator which in turn is inductively coupled to trapped atoms.

magnetic vortices in the film which adds to the loss and can cause dephasing [85]. Similarly, optical illumination of a resonator will create quasiparticles which also increases loss in the resonator [42, 45, 46]. Additionally, the hybrid system will be located at the mixing chamber stage of a dilution refrigerator which has a limited cooling power. For example, the refrigerator that we are currently using is an Oxford Cryofree Triton 200 refrigerator with a cooling power of 200 μW at 100 mK and a base temperature of about 10 mK [86]. Applying high optical power at the mixing chamber ($\sim$ mW) would add too much heat load to the refrigerator, resulting in a refrigerator base temperature that is too high for superconducting qubits. Hence, we will need to minimize the optical illumination of the resonator.

The plan is to use an optical dipole trap around an optical fiber with a diameter smaller than the wavelength of the light passing through the fiber [87–90]. Coupling light through such a "nanofiber" creates an evanescent wave that rides on the outside of the fiber. The square of the electric field is proportional to the potential energy of an atom located outside the fiber. Red detuned light from the D2 transition of Rb (780 nm) creates an attractive potential [87], while blue detuned light creates a repulsive potential. By coupling both red and blue detuned lights of the correct intensity, a potential well can be created around the fiber where the atoms can be trapped [88]. The distance of the trapping well from the surface of the fiber depends on detuning and the optical power. Applying red detuned light from both sides of the fiber creates a standing wave, forming a 1D optical lattice along the fiber.

One possibility is to use a grating magneto-optical trap (GMOT) to initially trap Rb atoms which then need to be loaded onto the fiber trap [91, 92]. To reduce

the heat load to the refrigerator, the GMOT will be anchored to one of the higher temperature stages of the refrigerator, for example to the second pulse tube stage at 3.5 K, which has a much higher cooling power. This means the atoms will be located some distance away, of order 10 cm or more from the resonator. We will need to use an optical conveyor belt scheme [93] to move the atoms along the fiber to within a few μm from the resonator. To initially load the atoms, we are planning to use a 2D magneto-optical trap (MOT) [94] to create a beam of Rb atoms directed at the GMOT. This 2D MOT will be located at room temperature outside the refrigerator, attached to one of the window ports of the refrigerator.

1.6 Challenges in Building the Proposed Hybrid System

There are many constraints and challenges in building our proposed hybrid quantum system. On the atomic side, we want the nanofiber to have as high of a transmission as possible since scattering of light from the fiber will lead to heating and quasiparticle induced loss in exposed superconducting films. One of the sources of light loss is Rayleigh scattering from surface defects, impurities, and inhomogeneities. Jon Hoffman and Sylvain Ravets have developed a procedure to clean and fabricate a nanofiber using a heat-and-pull process [95]. They have found they can produce 500 nm diameter tapered nanofibers with up to 99.95% transmission, which is the highest transmission reported for a tapered optical nanofiber [82, 95–97]. Jeff Grover and Pablo Solano have used one of the fibers to trap in ~ 1 mK deep trap several hundred laser cooled Rb using a room temperature apparatus and

studied the properties of the trapped atoms [98, 99]. The trapping setup would need to be miniaturized to allow us to put it inside the dilution refrigerator. The main problem appears not to be the fiber trap but rather the MOT that is used as a source of cold Rb atoms. The atomic side of the collaboration has built prototypes of 2D MOT for atom source and GMOT for atom loading, but these still need to be tested in the cryogenic environment.

On the superconducting side, ideally we want the linewidth of the resonator resonance to be smaller than the effective coupling g_{eff}. The linewidth of the resonance is given by $\delta\omega_r = \omega/Q$ where ω_r is the resonance frequency and Q the quality factor of the resonance. I note here that if we include N_{rf}, which is the number of rf photons in the resonator, the effective coupling is modified to $g_{\text{eff}} = g_{\text{Rb}}\sqrt{N_{\text{rf}}N_{\text{Rb}}}$. For a proof-of-principle experiment, it should be possible to put the resonator in a Fock state with $N_{\text{rf}} \gg 1$ and hence increase the coupling g_{eff}. For a more conventional qubit coupling experiment we would typically operate the resonator and qubit at low cavity drive powers $N_{\text{rf}} \approx 1$. For $N_{\text{rf}} = 1$, $N_{\text{Rb}} \approx 1000$ Rb atoms, and $g_{\text{Rb}} \approx 40$ Hz, we have $g_{\text{eff}} \approx 2\pi \times 1$ kHz. This suggests we need Q to be in the order of several million. As shown in this dissertation, we have fabricated resonators with Q reliably in the 10^5 range at low rf drive powers, and up to 2×10^6 at high drive powers with $N_{\text{rf}} \approx 10^8$. This means we should be able to observe the coupling between the resonator and the atoms in the proof-of-principle experiment, although we need to improve Q in the long term for the qubit coupling experiment. I note also that Sarabi *et al.* have observed spectroscopic TLS features that are much sharper than the resonator linewidth [100, 101]. This suggests it may not be necessary to

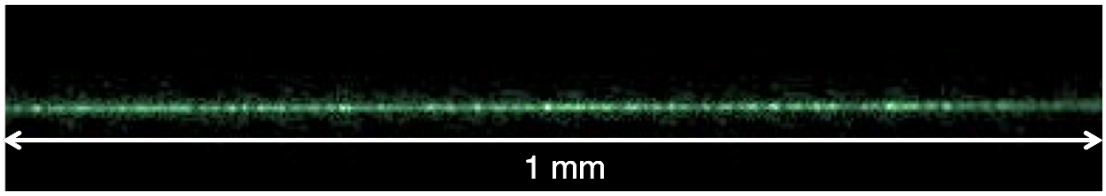

Figure 1.5: False color photograph of Rayleigh scattering of 780 nm light travelling down 500 nm tapered nanofiber. Picture taken by Jon Hoffman [82].

achieve such high Q's in the hybrid system.

Additionally, it will be desirable for the resonator frequency to be tunable to the Rb transition frequency $f_{\mathrm{Rb}} = 6.835$ GHz to allow us to see the splitting in the resonance as direct evidence of the coupling strength. Typical schemes to tune resonators use Josephson junctions [102]. However, as I discussed above, Josephson junctions will introduce nonlinearity into the system. Additionally, the junctions may introduce additional loss [19] which can result in reduced Q. As an alternative approach, Zaeill Kim used a movable superconducting pin to tune a resonator. The pin was mounted on an Attocube piezoelectric stage [103] and changed the effective inductance of the resonator, which in turn changed the resonance frequency. Zaeill showed that he could shift the resonance by about 36 MHz with this tuning scheme [104].

Although the transmission of the best tapered fibers is high, there is still some light scattered from the fiber, as shown in Fig. 1.5. Jon Hoffman measured the Rayleigh scattering from a 500 nm diameter fiber at room temperature to be several nW per mm for a 10 mW transmitted power [82]. For a resonator located 10 μm

away from the fiber, some of this scattered light will be incident on the resonator and cause an increase in loss due to the generation of quasiparticles.

As discussed in the following chapters, my research was focused on understanding the effect of incident light on the loss in resonators and transmons, as well as finding ways to reduce incident light or otherwise limit the increase in loss. As I also discuss, my results have some implications for our hybrid design as well as implications for quasiparticle loss in other superconducting qubits and the design of microwave kinetic-inductance detectors (MKIDs) [105, 106].

1.7 Overview of Dissertation

The structure of the dissertation is as follows. In Chapter 2 I discuss the theory of microwave resonators. I describe the circuit representation of a lumped-element LC resonator and then show how loss affects the resonance frequency and quality factor of the resonator. I describe two sources of loss: the two-level systems (TLSs) and quasiparticles. The distribution of quasiparticles is affected by, among other things, rf drive and optical illumination. I model the optical illumination using a variation of the Parker heating model [107] where the illumination creates hot nonequilibrium phonons that are parameterized by an effective temperature T_{eff}. I discuss how I simulated the nonequilibrium distribution from these effects and find the frequency and quality factor change due to this distribution.

Chapter 3 focuses on the experimental detail of the resonator measurements. Zaeill Kim originally designed and fabricated the resonator, and I discuss how we

modified the resonator to use in our experiment. The resonator was embedded inside a 3d cavity, I discuss the design and fabrication process of the cavity. In this chapter, I also discuss the microwave setup for the resonator transmission measurement, as well as the optical fiber setup that was used to illuminate the resonator.

I separate the results of the resonator measurements into two chapters. In Chapter 4 I discuss the results when no optical power is applied. At base temperature and for low rf powers, the behavior of the quality factor and frequency suggested strong coupling to a single or a few TLSs. At high rf powers, the behavior of the quality factor and frequency as a function of rf power and temperature can be explained by effects from having a nonequilibrium distribution of quasiparticles. At base temperature, I had to include an effective temperature $T_{\text{eff}} \approx 236$ mK, which was most likely due to the presence of a 4 K hot finger near the cavity in the same cooldown.

In Chapter 5 I discuss the results of measurements on the resonator under illumination. The quality factor under illumination appeared to show a TLS-like rf power dependence, suggesting the presence of optically activated TLS. However, this behavior, as well as the frequency, can be explained well by the nonequilibrium quasiparticle behavior. I also discuss several additional measurements I performed. These include a comparison of response between two optical fibers with different orientation, the response to polarized light, and the time-dependent response of the resonance frequency to an optical pulse.

In Chapter 6 I discuss the theory of the transmon. I present the Hamiltonian of the transmon and the Circuit QED system where the transmon is coupled to a

harmonic cavity. I then describe the sources of decoherence and how they affect the relaxation time T_1 and dephasing time T_ϕ of the qubit. Similar to the sources of loss in a resonator, the sources of decoherence in a transmon also include TLSs and quasiparticles. The complete picture of nonequilibrium quasiparticle in a transmon is complicated. I discuss how I simplified this picture and how the nonequilibrium distribution of quasiparticles from this simplified picture affects relaxation time and transition frequency.

Chapter 7 focuses on the experimental detail of the transmon experiments. I will discuss in detail how I designed and fabricated the transmon. This is followed by a lengthy detail on the microwave setup for the qubit drive and readout, including the timing sequences for the different measurements I performed. I also briefly discuss the 3d cavities and the optical illumination setup, but they are largely identical to the setup in the resonator measurements of Chapter 3.

In Chapter 8 I present my results and preliminary analysis of the illuminated transmon measurements. The spectrum of the qubit suggested a significant probability of the qubit being in the excited state, suggesting the qubit was quite hot, either due to background radiation or poor thermalization. Both Rabi oscillations and qubit relaxation did not follow typical qubit behavior. In particular, the relaxation showed a nonexponential decay that may be explained by quasiparticle fluctuations or nonequilibrium quasiparticle effects. I discuss how the transition frequency and relaxation time was affected by increased temperature and optical illumination, and compare my results to the simple nonequilibrium quasiparticle picture of Chapter 6. While the picture captured the general behavior, the agreement with the data is

relatively poor. This suggests the simple picture has left out some essential physics.

Finally, in Chapter 9 I summarize my results and discuss possible extensions to the model and experiments.

Chapter 2: Theory of Loss in Superconducting Microwave Resonators

In this chapter, I discuss the theory of superconducting resonators, with a particular focus on lumped-element LC resonators. I define the two main parameters that we measure in the resonator experiments, the quality factor Q and the resonance frequency f_r of a resonator. I then discuss the sources of loss in resonators, and how they affect the Q and f_r of a resonator, but focus on the two main sources, two level systems (TLS) and quasiparticles. I describe in some detail the nonequilibrium distribution of quasiparticles, how I simulate them, how this distribution affects Q and f_r, and how to incorporate optical illumination into the simulation. Finally, I briefly describe other sources of loss in the resonator, which include trapped vortices and losses to other microwave lines and modes.

2.1 Superconducting LC Resonators

2.1.1 Circuit Representation and Resonance Frequency

The resonator I used in my experiments is discussed in detail in the next three chapters. Here it is sufficient to note that it is a superconducting lumped-element planar LC resonator. This type of resonator consists of a well-defined inductor L

(a)

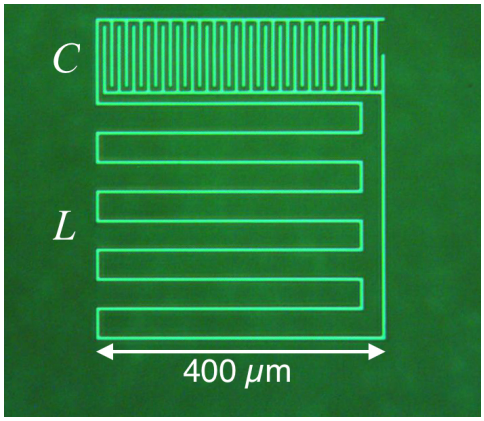

(b)

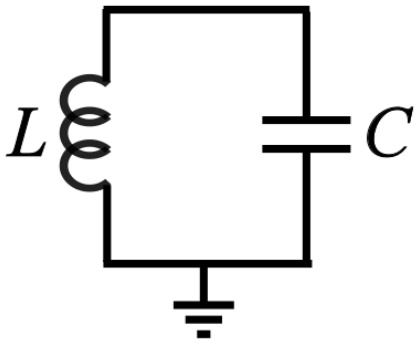

Figure 2.1: (a) Photograph of an LC resonator used in the experiments. (b) Simplified circuit diagram of an LC resonator.

and a separate well-defined capacitor C. Fig. 2.1(a) shows a photograph of the lumped-element resonator I used. I will discuss why we chose the lumped-element design for our experiments in Section 3.1.

Figure 2.1(b) shows a simplified circuit representation of a lumped-element resonator. Let $q = CV$ be the charge stored in the capacitor, where V is the voltage across the capacitor. From Kirchhoff's laws we can write the equations of motion as

$$\begin{aligned} \frac{q}{C} + L\frac{dI}{dt} &= 0 \\ \ddot{q} + \frac{q}{LC} &= 0, \end{aligned} \tag{2.1}$$

where $I = \dot{q}$ is the current flowing through the inductor. Eq. 2.1 is the equation of motion for a simple harmonic oscillator with a resonance frequency

$$f_r = \frac{\omega_r}{2\pi} = \frac{1}{2\pi\sqrt{LC}}. \tag{2.2}$$

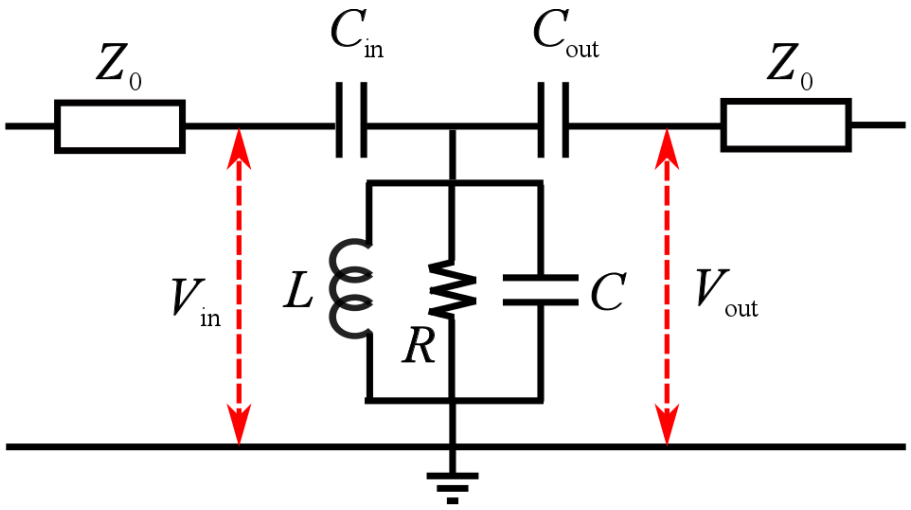

Figure 2.2: Circuit schematic of an S_{21} measurement of an LC resonator.

In the quantum regime, the energy eigenstates of a harmonic oscillator are

$$E_n = \hbar\omega_r \left(n + \frac{1}{2}\right), \tag{2.3}$$

where $n = 0, 1, 2, \ldots$. The energy levels are all separated by $\hbar\omega_r$. One implication is that one can't just isolate two levels to use as a qubit. Hence a superconducting resonator on its own can't be used as a qubit. Nevertheless, superconducting resonators are widely used in superconducting qubit architecture, for coupling microwave pulses to qubits, for coupling multiple qubits together, and for state readout of qubits [36, 37].

2.1.2 Quality Factors and Resonance Shape

The effects of coupling a resonator to external lines and internal losses can be understood by modeling the system. Figure 2.2 shows the circuit schematic of my setup for measuring the resonator. The impedances of the input and output

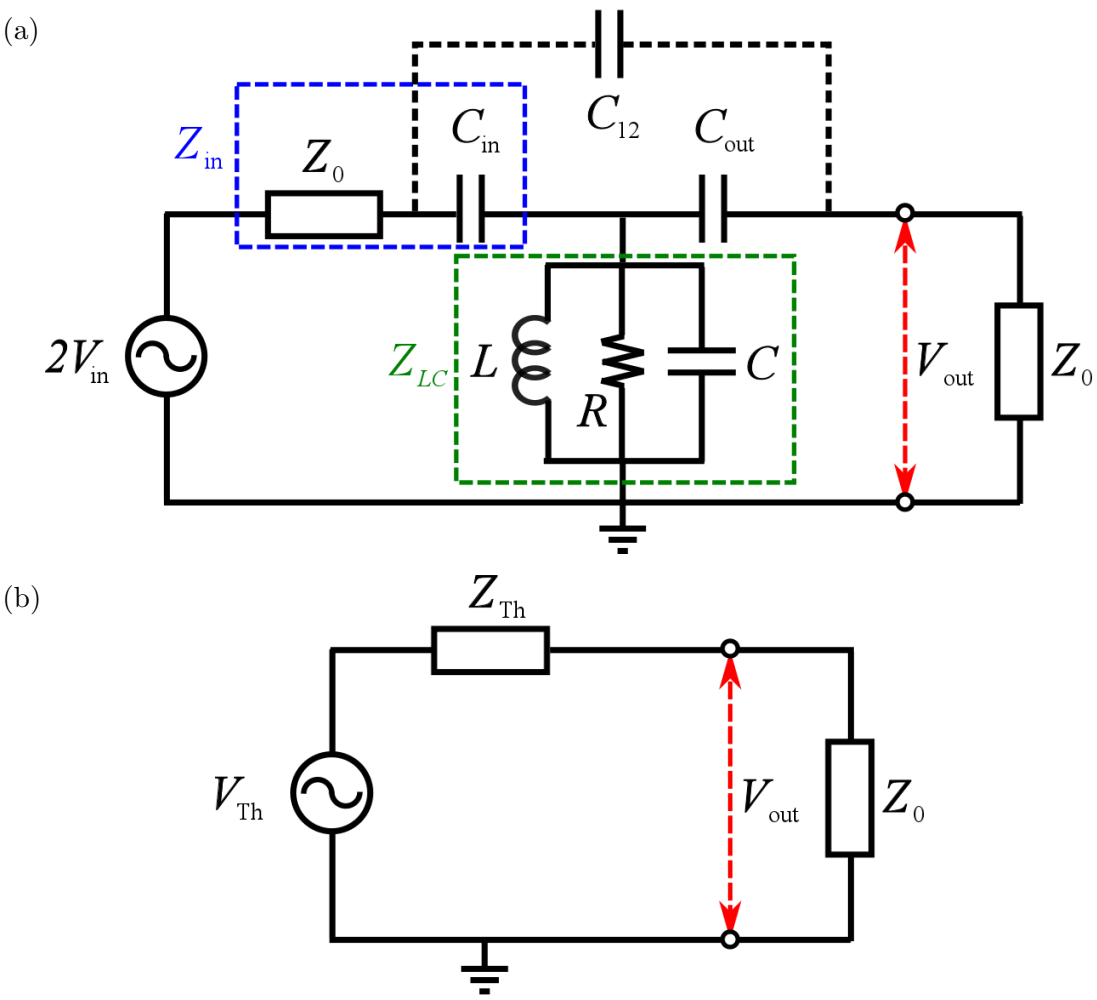

Figure 2.3: (a) Circuit schematic of an S_{21} measurement including the voltage source. (b) Thévenin equivalent circuit of the schematic in (a).

lines are Z_0. The resonator is capacitively coupled to the input line with input capacitance C_{in} and to the output line with output capacitance C_{out}. I assume very weak couplings, such that $\omega C_{\text{in}}, \omega C_{\text{out}} \ll 1/Z_0$. Typically there is also an even weaker direct capacitive coupling between the input and output with capacitance C_{12}, but here I will ignore them. The resistance R represents all of the internal losses in the resonator.

In some of my experiments, I measure the transmission $S_{21} \equiv V_{\text{out}}/V_{\text{in}}$ as a function of rf drive frequency f. To find an expression for S_{21}, I need to include a representative voltage source, as shown in Fig. 2.3(a). Note that the voltage supplied by this source is $2V_{\text{in}}$ [108]. This is because when there is no device to test and the input and output ports are shorted, the circuit can be represented by Fig. 2.3(b) with $Z_{\text{Th}} = Z_0$ and the total impedance is $2Z_0$. Since for such a setup $S_{21} = 1$ or $V_{\text{out}} = V_{\text{in}}$, the voltage source needs to be defined as $2V_{\text{in}}$.

The green dashed square in Fig. 2.3(a) represents the LC resonator. The impedance Z_{LC} and the admittance Y_{LC} inside this square are found from

$$Y_{LC} \;=\; \frac{1}{Z_{LC}} \;=\; i\left(\omega C - \frac{1}{\omega L}\right) + \frac{1}{R}. \tag{2.4}$$

The impedance Z_{in} and admittance Y_{in} inside the blue dashed square in Fig. 2.3(a) is

$$Z_{\text{in}} \;=\; \frac{1}{Y_{\text{in}}} \;=\; Z_0 + \frac{1}{i\omega C_{\text{in}}}. \tag{2.5}$$

Following Schuster [109], I define $x_{\text{in}} \equiv \omega C_{\text{in}} Z_0$. Since $\omega C_{\text{in}} \ll 1/Z_0$, $x_{\text{in}} \ll 1$. I can then rewrite Eq. 2.5 to get

$$Y_{\text{in}} \;=\; \frac{i\omega C_{\text{in}} + x_{\text{in}}^2/Z_0}{1 + x_{\text{in}}^2} \;\approx\; i\omega C_{\text{in}} + x_{\text{in}}^2/Z_0. \tag{2.6}$$

Figure 2.3(b) show the Thévenin equivalent circuit of Fig. 2.3(a) with equivalent voltage V_{Th} and equivalent impedance Z_{Th} [110]. Using Thévenin's theorem I can calculate V_{Th} and Z_{Th}

$$\begin{aligned} V_{\text{Th}} &= \frac{Z_L C}{Z_{\text{in}} + Z_{LC}} 2V_{\text{in}} \\ &= \frac{Y_{\text{in}}}{Y_{\text{in}} + Y_{LC}} 2V_{\text{in}} \end{aligned} \tag{2.7}$$

$$
\begin{aligned}
Z_{\mathrm{Th}} &= \frac{1}{i\omega C_{\mathrm{out}}} + \left(\frac{1}{Z_{\mathrm{in}}} + \frac{1}{Z_{LC}}\right)^{-1} \\
&= \frac{1}{i\omega C_{\mathrm{out}}} + \left(Y_{\mathrm{in}} + Y_{LC}\right)^{-1}. \qquad (2.8)
\end{aligned}
$$

I can then calculate V_{out}

$$
\begin{aligned}
V_{\mathrm{out}} &= \frac{Z_0}{Z_0 + Z_{\mathrm{Th}}} V_{\mathrm{Th}} \\
&= \left(\frac{Z_0}{Z_0 + 1/i\omega C_{\mathrm{out}} + (Y_{\mathrm{in}} + Y_{LC})^{-1}}\right)\left(\frac{Y_{\mathrm{in}}}{Y_{\mathrm{in}} + Y_{LC}}\right) 2V_{\mathrm{in}}. \qquad (2.9)
\end{aligned}
$$

Using a definition similar to Eq. 2.5 I can define Z_{out} and Y_{out}

$$
Z_{\mathrm{out}} = \frac{1}{Y_{\mathrm{out}}} = Z_0 + \frac{1}{i\omega C_{\mathrm{out}}}. \qquad (2.10)
$$

And similarly, by defining $x_{\mathrm{out}} \equiv \omega C_{\mathrm{out}} Z_0 \ll 1$, I can write

$$
Y_{\mathrm{out}} = \frac{i\omega C_{\mathrm{out}} + x_{\mathrm{out}}^2/Z_0}{1 + x_{\mathrm{out}}^2} \approx i\omega C_{\mathrm{out}} + x_{\mathrm{out}}^2/Z_0. \qquad (2.11)
$$

From Eq. 2.9 I can write

$$
\begin{aligned}
S_{21} &= \frac{2Z_0 Y_{\mathrm{in}} Y_{\mathrm{out}}}{Y_{\mathrm{in}} + Y_{\mathrm{out}} + Y_{LC}} \\
&= \frac{2Z_0(i\omega C_{\mathrm{in}} + x_{\mathrm{in}}^2/Z_0)(i\omega C_{\mathrm{out}} + x_{\mathrm{out}}^2/Z_0)}{1/R + x_{\mathrm{in}}^2/Z_0 + x_{\mathrm{out}}^2/Z_0 + i\left[\omega(C + C_{\mathrm{in}} + C_{\mathrm{out}}) - 1/\omega L\right]} \qquad (2.12)
\end{aligned}
$$

The imaginary component of the denominator is zero when

$$
\omega = \omega_0 \equiv \frac{1}{\sqrt{L(C + C_{\mathrm{in}} + C_{\mathrm{out}})}}. \qquad (2.13)
$$

ω_0 is the coupled resonance frequency of the resonator, shifted down from the uncoupled resonance frequency $1/\sqrt{LC}$. Typically we expect this shift to be small since $C_{\mathrm{in}}, C_{\mathrm{out}} \ll C$. Also, I typically just focus on the S_{21} in a region very near the

resonance. I can define $\omega = \omega_0 + \delta\omega$ with $|\delta\omega| \ll \omega_0$, and the imaginary component of the denominator can then be written as

$$\left[\omega(C + C_{\text{in}} + C_{\text{out}}) - \frac{1}{\omega L}\right] \approx \left[(\omega_0 + \delta_\omega)(C + C_{\text{in}} + C_{\text{out}}) - \frac{1}{\omega_0 L}\left(1 - \frac{\delta\omega}{\omega_0}\right)\right] = \frac{2\delta\omega}{\omega_0^2 L}. \tag{2.14}$$

Since $x_{\text{in}}, x_{\text{out}} \ll 1$, I can approximate the numerator on the right hand side of Eq. 2.12 as $-2Z_0\omega_0^2 C_{\text{in}} C_{\text{out}}$.

I define the internal quality factor Q_i, the input coupling quality factor Q_{in}, and the output coupling quality factor Q_{out} by

$$\frac{1}{Q_i} \equiv \frac{\omega_0 L}{R} \tag{2.15}$$

$$\frac{1}{Q_{\text{in}}} \equiv \frac{\omega_0 L x_{\text{in}}^2}{Z_0} \approx \omega_0^3 C_{\text{in}}^2 L Z_0 \tag{2.16}$$

$$\frac{1}{Q_{\text{out}}} \equiv \frac{\omega_0 L x_{\text{out}}^2}{Z_0} \approx \omega_0^3 C_{\text{out}}^2 L Z_0. \tag{2.17}$$

I can then define the total external quality factor Q_e and overall quality factor Q

$$\frac{1}{Q_e} \equiv \frac{1}{Q_{\text{in}}} + \frac{1}{Q_{\text{out}}} \tag{2.18}$$

$$\frac{1}{Q} \equiv \frac{1}{Q_i} + \frac{1}{Q_e} = \frac{1}{Q_i} + \frac{1}{Q_{\text{in}}} + \frac{1}{Q_{\text{out}}}. \tag{2.19}$$

I note here that the internal quality factor Q_i includes all internal loss sources. In particlular, this includes two-level systems and quasiparticles. In general, I can write

$$\frac{1}{Q_i} = \frac{1}{Q_{\text{TLS}}} + \frac{1}{Q_{\text{qp}}} + \frac{1}{Q_0} \tag{2.20}$$

where Q_{TLS} is the quality factor from two-level systems, Q_{qp} is the quality factor from quasiparticles, and Q_0 is the quality factor from all other internal sources of

loss. Using these definitions, S_{21} can then be written as

$$S_{21}(\omega) \;=\; -\frac{2Q/\sqrt{Q_{\rm in}Q_{\rm out}}}{1+2iQ(\omega-\omega_0)/\omega_0}. \tag{2.21}$$

This is the complex expression for S_{21} that I used to fit to measured resonance peaks, as I discuss in Chapter 3.

One way to visualize S_{21} is by plotting $|S_{21}|^2 = |V_{\rm out}/V_{\rm in}|^2 = P_{\rm out}/P_{\rm in}$, the ratio between transmitted power $P_{\rm out}$ and input power $P_{\rm in}$. The powers are defined as

$$P_{\rm out} \;= \frac{|V_{\rm out}|^2}{Z_0} \tag{2.22}$$

$$P_{\rm in} \;= \frac{|V_{\rm in}|^2}{Z_0} \tag{2.23}$$

The expression for $|S_{21}(\omega)|^2$ can be written as

$$|S_{21}|^2(\omega) \;=\; \frac{4Q^2/Q_{\rm in}Q_{\rm out}}{1+[2Q(\omega-\omega_0)/\omega_0]^2}. \tag{2.24}$$

I note that this expression yields a Lorentzian shaped peak with a full width at half maximum of ω_0/Q. The height of the peak at resonance is $4Q^2/Q_{\rm in}Q_{\rm out}$. If $Q_{\rm in} = Q_{\rm out}$, then $Q_e = \frac{1}{2}\sqrt{Q_{\rm in}Q_{\rm out}} = Q_{\rm in}/2 = Q_{\rm out}/2$. If $Q_{\rm in} = Q_{\rm out}$ and $1/Q_i = 0$, the height of the peak at resonance is 1, which means all of the power is transmitted from the input port (1) to the output port (2).

Fig. 2.4(a) shows a simulated $|S_{21}|^2$ as a function of ω with arbitrarily chosen dimensionless parameters: $C = 1$, $L = 1$, $Z_0 = 1$, $C_{\rm in} = 0.001$, $C_{\rm out} = 0.005$, and $R = 0.001$. The resonance frequency is $\omega_0 = 1/\sqrt{L(C + C_{\rm in} + C_{\rm out})} \approx 0.997$. Using Eq. 2.15 to 2.19, the inverse quality factors are $1/Q_i \approx 9.97 \times 10^{-4}$, $1/Q_{\rm in} \approx 9.91 \times 10^{-7}$, $1/Q_{\rm out} \approx 2.48 \times 10^{-5}$, and $1/Q \approx 1.02 \times 10^{-3}$. The width of the peak

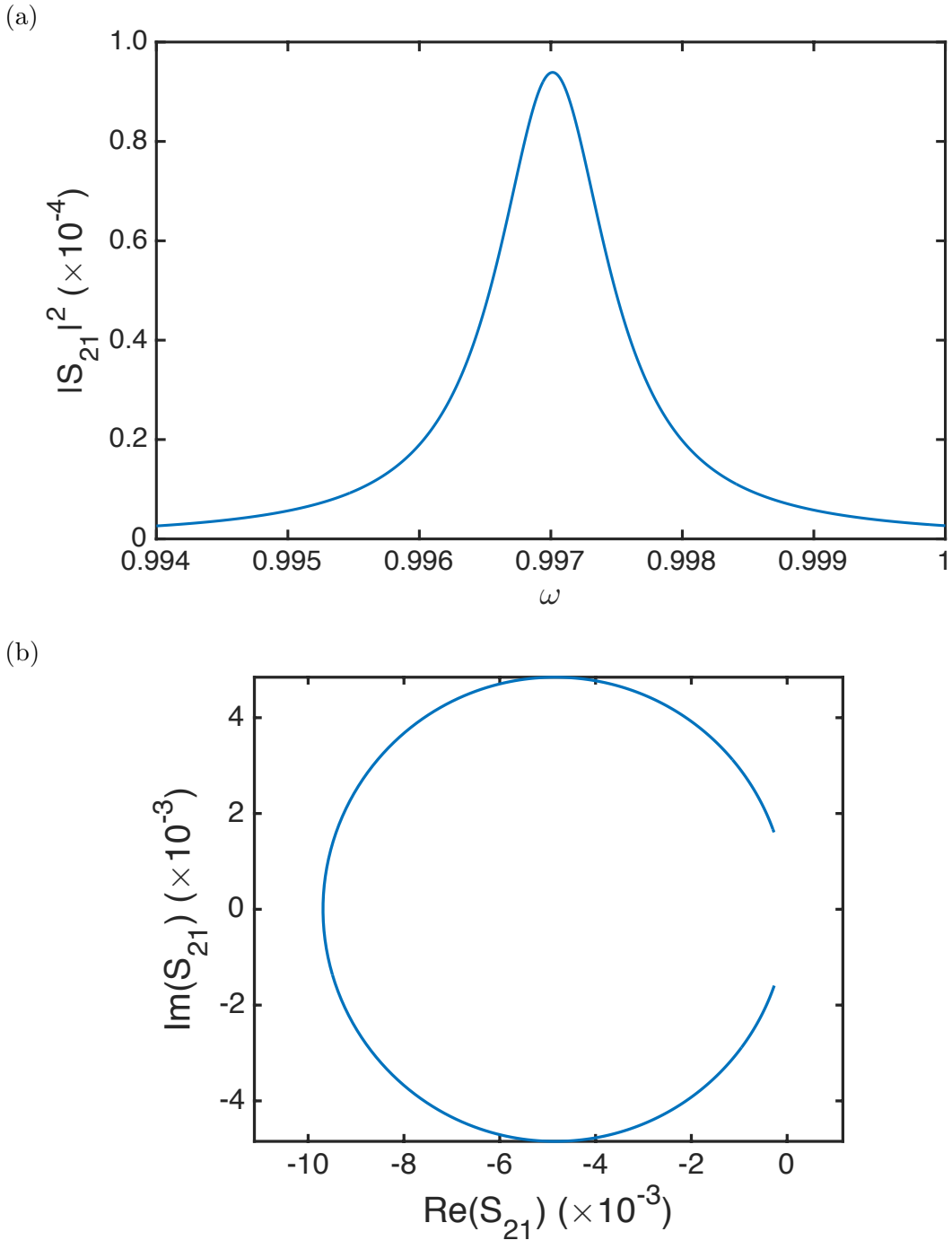

Figure 2.4: Plot of resonance peak in different S_{21} representations. (a) Lorentzian peak in $|S_{21}|^2$ vs ω. (b) Circle in S_{21} complex plane. Parameters used for both plots are in the text.

can be calculated to be $\omega_0/Q \approx 1.02 \times 10^{-3}$ and the height of the peak can be calculated to be $4Q^2/Q_{\rm in}Q_{\rm out} \approx 9.39 \times 10^{-5}$. The calculated values are consistent with Fig. 2.4(a).

Another way to visualize the response of the LCR circuit is by plotting S_{21} in the complex plane, that is, to parametrically plot $\mathrm{Im}(S_{21})$ vs $\mathrm{Re}(S_{21})$. One finds a circle with diameter $2Q/\sqrt{Q_{\rm in}Q_{\rm out}}$ centered at $(-Q/\sqrt{Q_{\rm in}Q_{\rm out}}, 0)$. Fig. 2.4(b) shows a simulated parametric plot of $\mathrm{Im}(S_{21})$ vs $\mathrm{Re}(S_{21})$ with the same parameters as in Fig. 2.4(a).

From Fig. 2.3(a), I find that the voltage across the LC resonator can be written as

$$\begin{aligned} V_{LC}(\omega) &= \frac{Z_0 + 1/i\omega C_{\rm out}}{Z_0 + Z_{\rm Th}} V_{\rm Th} = \frac{2Y_{\rm in}}{Y_{\rm int} + Y_{\rm out} + Y_{\rm LC}} 2V_{\rm in} \\ &\approx \frac{-i2\omega^2 LC_{\rm in}}{1/Q + 2i(\omega - \omega_0)/\omega_0} V_{\rm in} \end{aligned} \tag{2.25}$$

The magnitude of the voltage across the LC resonator at the resonance frequency $\omega = \omega_0$ can be written as

$$\begin{aligned} |V_{LC}(\omega_0)| &= \frac{2\omega_0 LC_{\rm in}}{1/Q} |V_{\rm in}| \\ &= 2Q \left(\frac{P_{\rm in}}{Q_{\rm in}} \right)^{1/2} \left(\frac{L}{C + C_{\rm in} + C_{\rm out}} \right)^{1/4}. \end{aligned} \tag{2.26}$$

using the definitions of $1/Q_{\rm in}$, ω_0, and $P_{\rm in}$. From this, the power absorbed by the resistance R in the circuit diagram can then be written as

$$\begin{aligned} P_R &= \frac{|V_{LC}(\omega_0)|^2}{R} = \frac{4Q^2 P_{\rm in}}{Q_{\rm in} R} \sqrt{\frac{L}{C + C_{\rm in} + C_{\rm out}}} \\ &= \frac{4Q^2}{Q_i Q_{\rm in}} P_{\rm in}. \end{aligned} \tag{2.27}$$

Note that P_R is the power absorbed by all internal sources of loss in the resonator.

If $\langle n \rangle$ is the average number of photons in the resonator, the average total energy stored in the resonator can be written as

$$\langle n \rangle \hbar\omega_0 \;=\; \left\langle \frac{1}{2}(C + C_{\rm in} + C_{\rm out})|V_{LC}(\omega_0)|^2 \right\rangle \;+\; \left\langle \frac{1}{2} L |I_L(\omega_0)|^2 \right\rangle, \tag{2.28}$$

where I_L is the current at inductor L and I now have to include the overall capacitance. Here I have ignored the zero-point energy. The first term on the right hand side is the average energy stored in the capacitors and the second term is the average energy stored in the inductor. From the Virial theorem, the two terms are equal. Eq. 2.28 can then be rewritten as

$$\langle n \rangle \hbar\omega_0 \;=\; \left\langle (C + C_{\rm in} + C_{\rm out})|V_{LC}(\omega_0)|^2 \right\rangle. \tag{2.29}$$

Using the definition of ω_0 and Eq. 2.26, I find

$$\langle n \rangle \;=\; \frac{4Q^2 P_{\rm in}}{Q_{\rm in} \hbar \omega_0^2}. \tag{2.30}$$

2.2 Two-Level Systems

2.2.1 TLS Overview

Two-level systems (TLSs) are a major source of loss for superconducting qubits and resonators, especially at low drive powers. TLSs effects in dielectrics were observed as far back as the 1950's. In the 1970's Zeller and Pohl, for example, described how TLSs in various glasses caused the thermal conductivity and specific heat to deviate from the standard Debye model [111]. A common type of TLS is

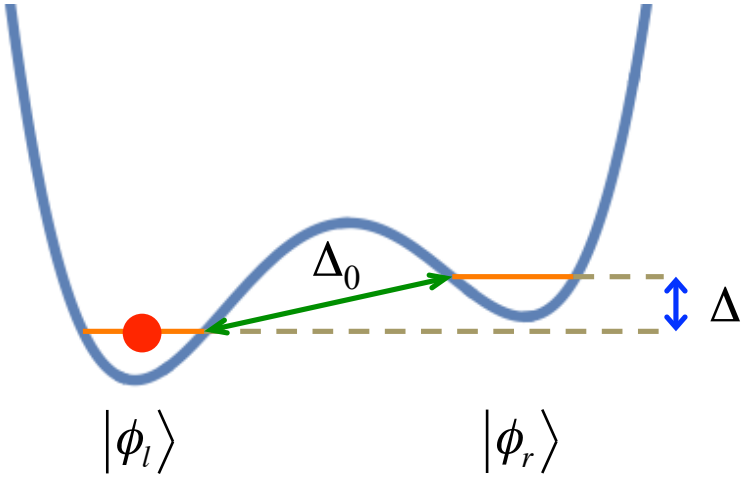

Figure 2.5: A TLS is modeled as a particle in an asymmetric double well potential.

thought to be a dangling OH^- ion in or on the surface of a dielectric [19, 112]. A key signature of TLS behavior is the saturation of loss under a sufficiently large driving field. In my experiment the driving field was a microwave electric field, but similar situation of loss can be observed under acoustic fields [113].

In superconducting resonators and qubits, TLSs can be located in surface oxides that grow on the superconductor, at the substrate-metal boundaries, at substrate-air boundaries, in the Josephson junction oxides, and in the dielectric in any parallel plate capacitors [19, 41, 114]. In recent years, major reductions in TLS loss in resonators and qubits have been achieved by using better dielectrics [19], removing unnecessary dielectrics [114, 115], using better and cleaner fabrication techniques [39, 116], and by using architectures such as 3d cavities [49] and whispering gallery mode resonators [117, 118] that minimize surface effects.

Phillips [119–121] and Anderson *et al.* [122] developed the now-standard theo-

retical model for describing TLS behavior. In the standard model, a TLS is treated as a particle that is trapped in an asymmetric double-well potential (Fig. 2.5). I now consider just the lowest lying state in each well $|\phi_l\rangle$ for the left well and $|\phi_r\rangle$ for the right well. In this picture Δ is the asymmetry of the well, which is the energy difference between the two basis states. The tunneling rate between the two sites is Δ_0. In this basis, the Hamiltonian can be written as

$$\mathcal{H}_{\mathrm{TLS},0} \;=\; \frac{1}{2}\begin{pmatrix} -\Delta & \Delta_0 \\ \Delta_0 & \Delta \end{pmatrix}. \tag{2.31}$$

The eigenvalues $E_\pm$ and eigenstates $|\psi_\pm\rangle$ of the Hamiltonian can be found by diagonalizing Eq. 2.31. The eigenvalues are given by

$$E_\pm \;=\; \pm\frac{1}{2}\sqrt{\Delta^2+\Delta_0^2} \;=\; \pm\frac{1}{2}\mathcal{E}, \tag{2.32}$$

where $\mathcal{E} \equiv E_+ - E_- = \sqrt{\Delta^2+\Delta_0^2}$. The eigenstates are given by

$$|\psi_+\rangle \;=\; \sin\alpha|\phi_l\rangle \;+\; \cos\alpha|\phi_r\rangle \tag{2.33}$$

$$|\psi_-\rangle \;=\; \cos\alpha|\phi_l\rangle \;-\; \sin\alpha|\phi_r\rangle, \tag{2.34}$$

where $\tan(2\alpha) = \Delta_0/\Delta$. In the eigenstate $|\psi_\pm\rangle$ basis, the Hamiltonian can then be written as

$$\mathcal{H}_{\mathrm{TLS},0} \;=\; \frac{1}{2}\sigma_z\mathcal{E}, \tag{2.35}$$

where σ_z is one of the Pauli matrices, which are given by

$$\sigma_x \;=\; \begin{pmatrix} 0 & 1 \\ 1 & 0 \end{pmatrix}, \qquad \sigma_y \;=\; \begin{pmatrix} 0 & i \\ -i & 0 \end{pmatrix}, \qquad \sigma_z \;=\; \begin{pmatrix} 1 & 0 \\ 0 & -1 \end{pmatrix}. \tag{2.36}$$

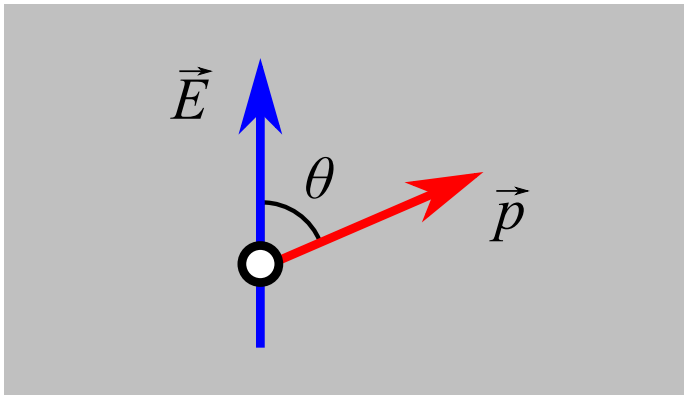

Figure 2.6: Illustration of a TLS with dipole moment $\vec{p}$ under electric field E, with angle θ between $\vec{p}$ and $\vec{E}$.

2.2.2 Effects of Individual TLS

Figure 2.6 shows a TLS under an electric field $\vec{E}$. In the figure $\vec{p}$ is the electric dipole moment of the TLS, and θ is the angle between $\vec{E}$ and $\vec{p}$. If the TLS is an ion with charge q that is displaced by $\vec{l}$ when it changes from state $|\phi_l\rangle$ to $|\phi_r\rangle$ then $\vec{p} = q\vec{l}/2$. Reported values of $|\vec{p}|$ in dielectric materials used in superconducting resonators, for example Si_3N_4, are around 5-10 Debye [19, 113, 123]. Debye is a non-SI unit and I note that 1 Debye ≈ 0.21 eÅ. A charged TLS interacts with the electric field and as a result the Hamiltonian of the TLS is perturbed an interaction Hamiltonian by $\delta\mathcal{H}_{\text{int}}$ and $\mathcal{H}_{\text{TLS}} = \mathcal{H}_{\text{TLS},0} + \delta\mathcal{H}_{\text{int}}$. In the $|\phi_l\rangle$, $|\phi_r\rangle$ basis, $\delta\mathcal{H}_{\text{int}}$ can be written as

$$\delta\mathcal{H}_{\text{int}} = \frac{1}{2}\begin{pmatrix} -\delta\Delta & \delta\Delta_0 \\ \delta\Delta_0 & \delta\Delta \end{pmatrix}. \tag{2.37}$$

The interaction with external field is mainly thought to be changing the asymmetry Δ, and any effect on Δ_0 is typically ignored [124, 125]. Accordingly I will take

$\delta\Delta_0 = 0$. The change in Δ is then given by

$$\delta\Delta \;=\; 2\vec{p}\cdot\vec{E}. \tag{2.38}$$

In the eigenstate basis, it can be shown that the interaction Hamiltonian can then be written as [121]

$$\delta\mathcal{H}_{\text{int}} \;= \frac{1}{\mathcal{E}}\begin{pmatrix} \Delta & -\Delta_0 \\ -\Delta_0 & -\Delta \end{pmatrix}\left(\vec{p}\cdot\vec{E}\right) \tag{2.39}$$

$$= \frac{\Delta}{\mathcal{E}}\sigma_z\left(\vec{p}\cdot\vec{E}\right) \;-\; \frac{\Delta_0}{\mathcal{E}}\sigma_x\left(\vec{p}\cdot\vec{E}\right). \tag{2.40}$$

The overall Hamiltonian of a driven TLS in the eigenstate basis can then be written as

$$\mathcal{H} \;=\; \frac{1}{2}\sigma_z\mathcal{E} \;+\; \frac{\Delta}{\mathcal{E}}\sigma_z\left(\vec{p}\cdot\vec{E}\right) \;-\; \frac{\Delta_0}{\mathcal{E}}\sigma_x\left(\vec{p}\cdot\vec{E}\right). \tag{2.41}$$

It has been noted [126] that the Hamiltonian given by Eq. 2.41 is analogous to the Hamiltonian of a spin-1/2 particle under a magnetic field [18]

$$\mathcal{H} \;=\; \hbar\gamma\vec{B}\cdot\vec{S} \;=\; \hbar\gamma\left(\vec{B}_0 + \vec{B}'\right)\cdot\vec{S}. \tag{2.42}$$

where γ is the gyromagnetic factor, $\vec{B}_0$ is the static magnetic field, $\vec{B}'$ the (time-dependent) perturbation magnetic field, and $\vec{S} = \vec{\sigma}_2$ the spin. Comparing Eqs. 2.41 and 2.42, I can identify

$$\hbar\gamma\vec{B}_0 \;=\; (0,\, 0,\, \mathcal{E}) \tag{2.43}$$

$$\hbar\gamma\vec{B}' \;=\; \left(2\frac{\Delta_0}{\mathcal{E}}\vec{p}\cdot\vec{E},\, 0,\, 2\frac{\Delta}{\mathcal{E}}\vec{p}\cdot\vec{E}\right). \tag{2.44}$$

If there is no dephasing and the spin has infinitely long lifetime, the spin is known to follow the equation of motion [18]

$$\frac{d}{dt}\vec{S}(t) \;=\; \gamma\,\vec{S}\times\vec{B}. \tag{2.45}$$

When loss and spin lifetime are taken into account, the averaged spin $\langle\vec{S}\rangle$ of an ensemble of spin-1/2 particles follow a set of equation called Bloch's equations. Bloch's equations were developed by Felix Bloch in 1946 to describe nuclear magnetic resonance (NMR) [127]. Bloch's equations are

$$\frac{d}{dt}\langle S_x(t)\rangle = \gamma\left(\langle\vec{S}\rangle\times\vec{B}\right)_x - \frac{\langle S_x\rangle}{T_2} \tag{2.46}$$

$$\frac{d}{dt}\langle S_y(t)\rangle = \gamma\left(\langle\vec{S}\rangle\times\vec{B}\right)_y - \frac{\langle S_y\rangle}{T_2} \tag{2.47}$$

$$\frac{d}{dt}\langle S_z(t)\rangle = \gamma\left(\langle\vec{S}\rangle\times\vec{B}\right)_z - \frac{\langle S_z\rangle - S_{z,eq}[B_z(t)]}{T_1}, \tag{2.48}$$

Here $S_{z,eq}[B_z(t)]$ is the instantaneous value of $\langle S_z\rangle$ in thermal equilibrium

$$S_{z,eq}[B_z(t)] = \frac{1}{2}\tanh\left(\frac{\hbar\gamma B_z(t)}{2kT}\right), \tag{2.49}$$

where T is the TLS temperature, T_1 is the TLS relaxation time, and T_2 is the TLS coherence time. The two characteristic times are related by

$$\frac{1}{T_2} = \frac{1}{2T_1} + \frac{1}{T_\phi}, \tag{2.50}$$

where T_ϕ is the dephasing time.

One can use Bloch's equations and the analog between the TLS Hamiltonian and spin Hamiltonian to calculate the loss due to TLS that is being driven by an oscillating electric field. For the loss from a single TLS, one can use specific values of Δ, Δ_0, θ, T_1, and T_2. Assuming $T = 0$, the quality factor from a single TLS as a function of rms electric field drive strength $\langle E\rangle$, is given by [121, 128]

$$\frac{1}{Q_{\mathrm{TLS,s}}}(\langle E\rangle) = \frac{T_2}{\hbar\epsilon V}\left(\frac{p\Delta}{2\mathcal{E}}\right)^2\frac{1}{[1+(\langle E\rangle/E_{c,s})^2]}, \tag{2.51}$$

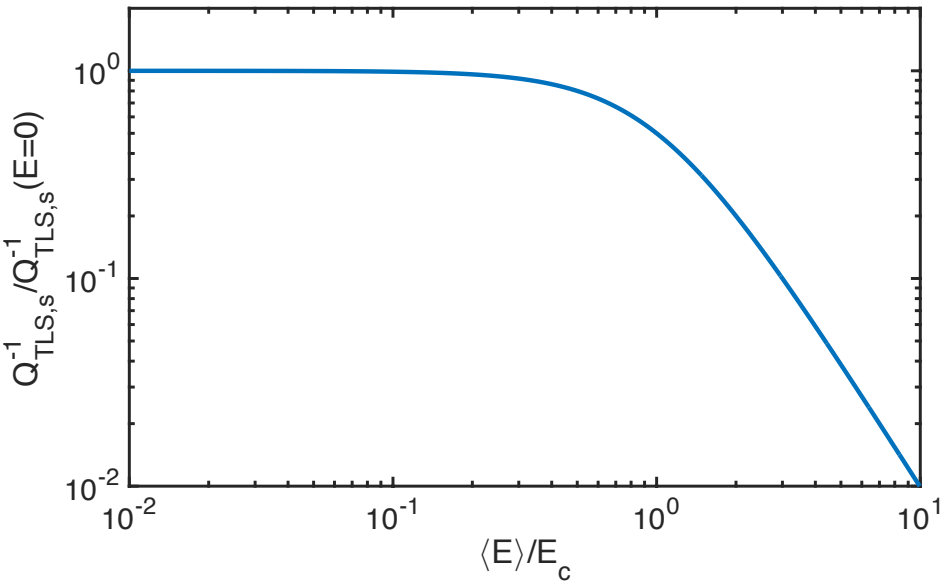

Figure 2.7: Normalized inverse quality factor $Q^{-1}_{TLS,s}/Q^{-1}_{TLS,s}(\langle E\rangle = 0)$ from a single TLS plotted as a function of normalized electric field strength $\langle E\rangle/E_{c,s}$ showing the TLS saturation behavior.

where ϵ is the dielectric permittivity, V is the resonator mode volume, and the critical electric field $E_{c,s}$ is given by

$$E_{c,s} = \frac{2\hbar\mathcal{E}}{p\cos\theta\Delta_0\sqrt{T_1T_2}}. \tag{2.52}$$

Figure 2.7 shows the behavior of $1/Q_{\mathrm{TLS,s}}$ as a function of scaled electric field $\langle E\rangle/E_c$. For fields below $\langle E\rangle/E_c \ll 1$, $1/Q_{\mathrm{TLS,s}}$ approaches

$$\frac{1}{Q_{\mathrm{TLS,s}}}(\langle E\rangle = 0) = \frac{T_2}{\hbar\epsilon V}\left(\frac{p\Delta}{2\mathcal{E}}\right)^2. \tag{2.53}$$

At around $\langle E\rangle \approx E_c$, $1/Q_{\mathrm{TLS,s}}$ starts decreasing rapidly. This is due to "saturation", which means that at high powers the TLS is equally likely to be in the ground state or excited state and therefore cannot absorb energy on average.

Bloch's equations are classical equations and do not provide a complete or completely accurate description of TLS behavior. It is well-known that a TLS coupled to a resonator forms a Jaynes-Cummings system [129]. Bhattacharya *et al.* developed a quantum theory to explain the behavior of a TLS that is strongly coupled to a resonator in the quantum regime [128]. They found that the loss follows closely the classical Bloch's equations in the weak coupling regime. In the strong coupling regime $1/Q_{\mathrm{TLS,s}}$ follows the general electric field $\langle E \rangle$ dependence of Eq. 2.51. However at low power $1/Q_{\mathrm{TLS,s}}$ from quantum theory is smaller compared to that found from the classical theory using Bloch's equations.

One signature of a Jaynes-Cummings system in the strong coupling regime with very small detuning is the "vacuum Rabi splitting" in the energy spectrum, where the energy eigenstates of the system showed increased separation compared to the uncoupled energies due to the strong coupling. For example, Walraff *et al.* observed vacuum Rabi splitting of the qubit in circuit QED systems by [36]. Recently Sarabi *et al.* reported observations of vacuum Rabi splitting in a TLS-resonator system [100, 101], which confirms that the quantum mechanical model can be used to explain the behavior of TLS. For weaker coupling or larger detuning, vacuum Rabi splitting might not appear, but one can expect to see a shift in the resonator resonance frequency due to coupling to a TLS. In the case of superconducting qubits, avoided level crossings have been observed when the qubit energy is tuned close to a TLS energy [19]. The TLSs in this case are thought to be located in the aluminum oxide of the Josephson junction.

2.2.3 Effects of an Ensemble of TLSs

In a macroscopic dielectric region, one should expect there can be many TLSs with different values of θ, Δ, Δ_0, T_1, T_2 and p. To simplify things, the characteristic times T_1 and T_2, as well as the magnitude of the electric dipole moment p of the TLS ensemble are often assumed to be constant. In the standard model of TLS loss [130], the orientation of the TLS is assumed to be uniformly distributed. Also the distribution of asymmetry energy Δ is assumed to be uniform in Δ, while the distribution of tunneling rate Δ_0 is assumed to be uniform in $\log \Delta_0$ [121]. The resulting standard distribution yields the number d^2P of dipoles with asymmetry energy between Δ and $\Delta + d\Delta$, tunneling energy between Δ_0 and $\Delta + d\Delta_0$ given by

$$d^2P \;=\; \frac{P_0}{\Delta_0}\, d\Delta\, d\Delta_0. \tag{2.54}$$

P_0 has been reported to be of order 10^{44} /J m^3 [121, 123].

From the distribution $d^2P/d\Delta\, d\Delta_0$ one can calculate the quality factor from an ensemble of TLS as a function of rms electric field strength $\langle E \rangle$ one finds[19, 121]

$$\frac{1}{Q_{\mathrm{TLS,e}}}(E) \;=\; \frac{\tan(\delta)\, \tanh(\hbar\omega/2k_BT)}{\sqrt{1 + (\langle E \rangle / E_{c,d})^2}}. \tag{2.55}$$

where ω is the microwave drive frequency and the loss tangent $\tan(\delta)$ is

$$\tan(\delta) \;\equiv\; \frac{\pi P_0 p^2}{3\epsilon}, \tag{2.56}$$

and the characteristic field $E_{c,d}$ is given by

$$E_{c,d} \;=\; \frac{\hbar\sqrt{3}}{2p\sqrt{T_1T_2}}. \tag{2.57}$$

At low electric fields and low temperatures, $1/Q_{\mathrm{TLS,e}}$ goes to $\tan\delta$, saturation starts around $\langle E\rangle \approx E_{c,d}$ and $k_B T \sim \hbar\omega$.

I note that the electric field dependence of the saturation in Eq. 2.55 is slower compared to that in Eq. 2.53 due to a single TLS. In Fig. 2.8 I compare the normalized $1/Q_{\mathrm{TLS}}$ from a single TLS and from an ensemble of TLSs as a function of normalized field $\langle E\rangle/E_c$. The slower saturation for TLS ensemble case is evident. I note here that the value of E_c depends on the microscopic parameters of the TLSs and the material. Even though the average microwave photon occupation number $\langle n\rangle$ doesn't appear explicitly in the expression for quality factor, it is proportional to rf drive power, and hence to $\langle E\rangle^2$. Equivalently, I can define the critical photon occupation number n_c where saturation starts to occur. The value of n_c has typically been reported to be around 1-1000 for a range of materials and designs [39, 114, 131–133].

The hyperbolic tangent factor in Eq. 2.51 describes the dependence of TLS loss on temperature. The result is that $1/Q_{TLS,e}$ decreases with increasing temperature, due to saturation of TLSs from thermal excitation.

The interaction between a resonator and a distribution of TLSs also causes a shift in the resonance frequency of the resonator. Similar to the loss, the shift in resonance frequency depends on temperature and electric field strength. As discussed by Gao, the expression for the electric field dependence is complicated but relatively weak [126]. At weak electric field strength, the fractional frequency shift

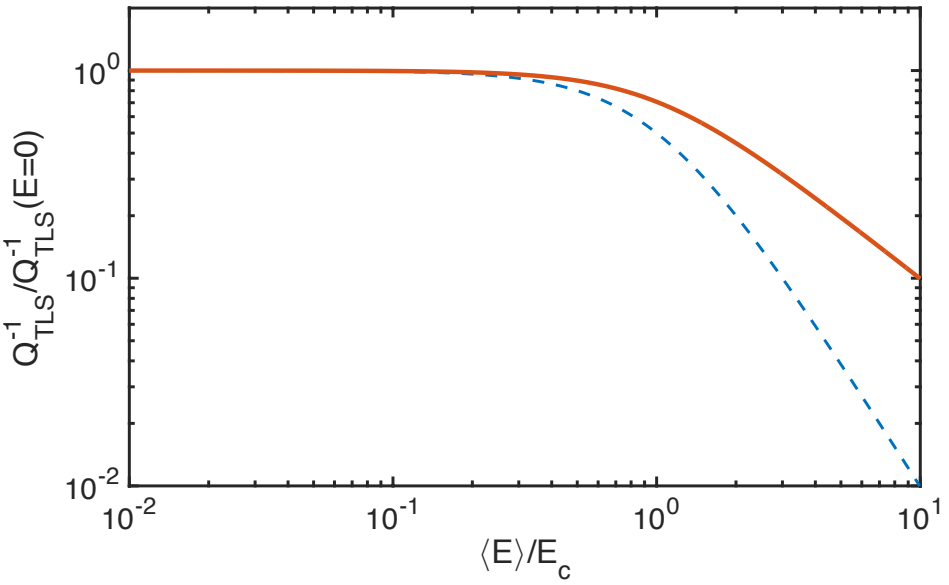

Figure 2.8: Comparison between normalized TLS inverse quality factor $Q^{-1}_{\mathrm{TLS}}/Q^{-1}_{\mathrm{TLS}}(\langle E\rangle = 0)$ between a single TLS (dashed blue curve) and the standard TLS ensemble (solid red curve) as a function of normalized electric field $\langle E\rangle/E_c$, showing slower saturation behavior for the case of an ensemble of TLSs.

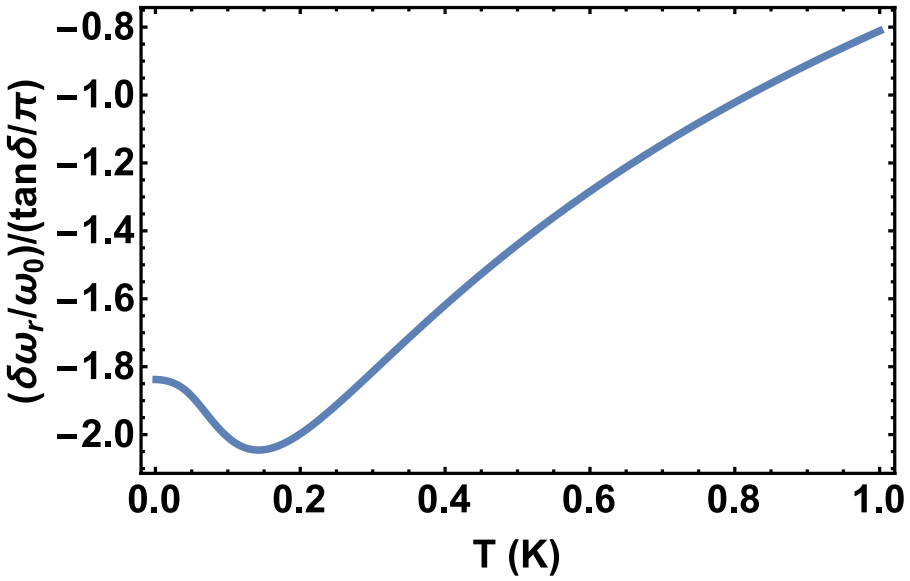

Figure 2.9: Fractional frequency shift $\delta\omega_r/\omega_0$ from a standard TLS ensemble (with fill factor $F = 1$) as a function of temperature T for a resonator with $\omega/2\pi = 5$ GHz.

is [41, 121]

$$\frac{\delta\omega_r}{\omega_0} = \frac{\tan\delta}{\pi}\left\{\mathrm{Re}\left[\Psi\left(\frac{1}{2}+\frac{\hbar\omega}{2\pi i k_B T}\right)\right] - \ln\left(\frac{\hbar\omega}{k_B T}\right)\right\}, \tag{2.58}$$

where ω_0 is the resonance frequency when there is no TLS effect and Ψ is the complex digamma function [134]. Figure 2.9 shows the fractional shift as a function of temperature for $\omega/2\pi = 5$ GHz. The frequency initially decreases with increasing temperature at very low temperatures, then increases with increasing temperature at higher temperatures.

The above results have implicitly assumed that the electric field is completely confined inside the dielectric and is uniform. This is only true for resonators with parallel plate capacitors filled with dielectric. However for lumped-element resonators I used, there is a significant field in vacuum outside the dielectric, and the

field is non-uniform inside and outside the dielectric. This changes the expressions for the quality factor and frequency shift due to the TLSs. The key insight is to define the filling factor F as the ratio of the electrical energy stored in the dielectric compared to the total stored electrical energy. The expression for F is [41]

$$F \;=\; \frac{\int_{V_d} \epsilon_d(\vec{r})|\vec{E}(\vec{r})|^2\, d^3\vec{r}}{\int_{V_{\rm all}} \epsilon(\vec{r})|\vec{E}(\vec{r})|^2\, d^3\vec{r}}, \tag{2.59}$$

where the numerator is integrated over the volume of the dielectric V_d and the denominator is integrated over the entire volume $V_{\rm all}$. Electric field simulations of coplanar waveguide resonators have shown that the largest contributor to the fill factor comes from the metal-substrate interface, followed by the air-substrate interface, while the contribution from the metal-air interface is about an order of magnitude lower than the previous two [116, 135]. This assumes an equal density of dipoles at these different interfaces, which may not be true in real devices.

Thus for my resonators, the frequency shift due to TLS becomes [41]

$$\frac{\delta\omega_r}{\omega_0} \;=\; \frac{F\tan\delta}{\pi}\left\{\mathrm{Re}\left[\Psi\left(\frac{1}{2}+\frac{\hbar\omega}{2\pi i k_B T}\right)\right] \;-\; \ln\left(\frac{\hbar\omega}{k_B T}\right)\right\}, \tag{2.60}$$

and the quality factor becomes [136]

$$\frac{1}{Q_{\rm TLS,e}}(V) \;=\; \frac{F\,\tan\delta\,\tanh(\hbar\omega/2k_BT)}{\sqrt{1+(\langle V\rangle/V_c)^{\beta}}}. \tag{2.61}$$

I note in Eq. 2.61 that because of the non-uniform nature of the electric field in my resonators, the relevant experimental parameter is the rms voltage across the capacitor $\langle V\rangle$ instead of $\langle E\rangle$. Consequently, the characteristic scaling factor is the characteristic voltage V_c instead of E_c. Depending on the geometry of the resonator, the saturation behavior may also change somewhat, represented by the exponent

β with $\beta = 2$ for the uniform field case. For coplanar waveguides, Wang *et al.* calculated $\beta \approx 1.6$ using simple approximations of electric field strength [136].

In contrast, Macha *et al.* [137] and Khalil *et al.*[138] have measured much lower β values, as low as 0.03-0.4, in coplanar waveguide and lumped-element resonators on bare substrate. In an attempt to explain this behavior, Faoro and Ioffe developed a model that they call interacting TLSs [139, 140]. In this model, the energy distribution of the TLS is modified to

$$\frac{d^2P}{d\Delta\, d\Delta_0} = \begin{cases} (1+\mu)\left(\frac{\Delta}{\Delta_{\max}}\right)^{\mu} \frac{P_0}{\Delta_0}, & \text{for } \Delta \leq \Delta_{\max} \\ 0, & \text{otherwise.} \end{cases} \tag{2.62}$$

with $\mu \approx 0.3$. The interacting TLS model is consistent with the observations of weaker saturation behavior. However, as I discuss in Section 2.3, non-equilibrium distribution of quasiparticles can create rf drive power dependent loss and may also be able to explain such behavior, especially at higher drive powers.

2.3 Quasiparticles

2.3.1 Quasiparticles Overview

The BCS theory of superconductivity [141, 142] revealed that superconductivity is caused by the creation of bound n pairs of electrons at low temperatures, commonly known as Cooper pairs [143]. Breaking Cooper pairs requires at least 2Δ of energy, where Δ is the superconducting gap. For a superconductor in the weak coupling BCS limit, the superconducting critical temperature T_c is related to the gap by $\Delta = 1.76 k_B T_c$, where k_B is the Boltzmann constant. Pair breaking can be

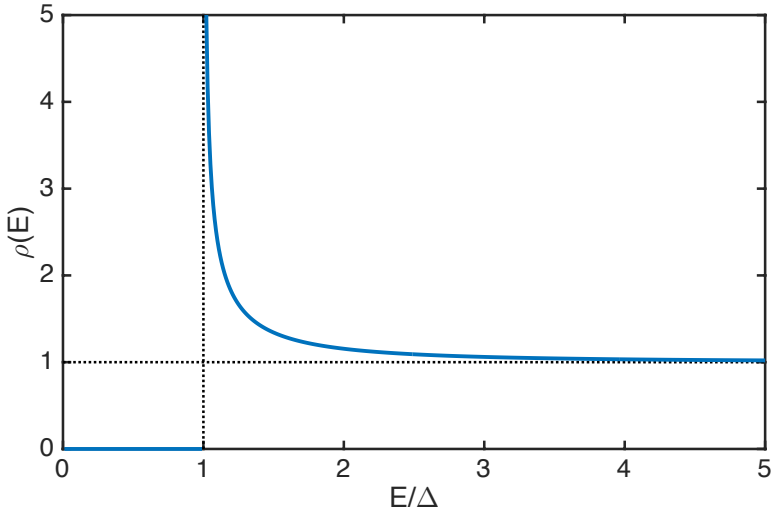

Figure 2.10: The solid blue curve is the normalized quasiparticle density of states $\rho(E)$ as a function of normalized quasiparticle energy E/Δ. The vertical dotted line shows $\rho(E)$ diverged to $+\infty$ at $E = \Delta$ and the horizontal dotted line shows the asymptotic value of $\rho(E) \to 1$ for $E \to +\infty$.

caused by many factors, including thermal fluctuations, a strong microwave drive, or optical illumination, which I describe in the following sections. A broken Cooper pair leaves two excitations known as Bogoliubov quasiparticles, which I will call simply quasiparticles.

When a Cooper pair breaks into quasiparticles, the energy is split between the two quasiparticles and the minimum energy of each quasiparticle E is at least Δ. I define $f(E)$ as the energy distribution of quasiparticles, *i.e.* it is the probability that a quasiparticle state of energy E is occupied. Another important quasiparticle function from BCS theory is the normalized density of states of quasiparticles, given

by [144]

$$\rho(E) \;=\; \begin{cases} 0, & \text{for } E < \Delta \\ \dfrac{E}{\sqrt{E^2 - \Delta^2}}, & \text{for } E > \Delta. \end{cases} \tag{2.63}$$

Figure 2.10 shows the density of states $\rho(E)$ as a function of E/Δ. The value of $\rho(E)$ diverges at $E = \Delta$, then decreases rapidly and approaches 1 for $E \to \infty$. From the distribution and the density of states, one can calculate the total density of quasiparticles $n_{\rm qp}$ using the expression

$$n_{\rm qp} \;=\; 4N_0V \int_{\Delta}^{\infty} f(E)\,\rho(E)\,dE, \tag{2.64}$$

where N_0 is the single spin density of states at the Fermi surface. I note here that the superconducting gap Δ is not a constant, but depends on the quasiparticle distribution and is determined by the self-consistency equation [142]

$$\frac{1}{N_0V_{\rm BCS}} \;=\; \int_{\Delta}^{\infty} \frac{\rho(E)}{E}\,\left[1 - 2f(E)\right]\,dE, \tag{2.65}$$

where $V_{\rm BCS}$ is the BCS interaction parameter. However, for sufficiently low temperatures, low rf powers, and low optical intensities, one finds $f(E) \ll 1$ and Eq. 2.65 gives Δ independent of temperature to a high order.

In 1958 Mattis and Bardeen derived an expression for the complex conductivity $\sigma = \sigma_1 - i\sigma_2$ of a superconducting film that was subjected to an oscillating electromagnetic field with frequency ω [145]. I typically use an rf drive frequency $f = \omega/2\pi$ that is in the 4-8 GHz range. This is smaller than $2\Delta/h$ of my superconducting aluminum, which is around 40 GHz. In this limit, the relevant Mattis-

Bardeen expression is

$$\frac{\sigma_1(\omega)}{\sigma_n} = \frac{2}{\hbar\omega}\int_{\Delta}^{\infty} dE\,[f(E) - f(E+\hbar\omega)]\,h_+(E, E+\hbar\omega)\,\rho(E) \tag{2.66}$$

$$\frac{\sigma_2(\omega)}{\sigma_n} = \frac{1}{\hbar\omega}\int_{\Delta-\hbar\omega}^{\Delta} dE\,[1 - 2f(E+\hbar\omega)]\,h_+(E, E+\hbar\omega)\,\frac{E}{\sqrt{\Delta^2 - E^2}}, \tag{2.67}$$

where σ_n is the normal state conductivity and the coherence factors are

$$h_{\pm}(E, E') = \left(1 \pm \frac{\Delta^2}{EE'}\right)\rho(E'). \tag{2.68}$$

The quality factor and frequency shift of a thin film resonator from quasiparticles can then be calculated from σ_1 and σ_2. One finds [42, 126]

$$\frac{1}{Q_{\mathrm{TLS}}} = \alpha\,\frac{\sigma_1}{\sigma_2} \tag{2.69}$$

$$\frac{\delta\omega}{\omega_0} = -\frac{\alpha}{2}\,\frac{\delta\sigma_2}{\sigma_2}. \tag{2.70}$$

In the above expression ω_0 is the resonance frequency assuming no quasiparticle effect, $\delta\sigma_2 = \sigma_2 - \sigma_{2,0}$, and $\sigma_{2,0}$ is the imaginary component of σ_2 assuming zero temperature, no rf drive, and no optical illumination. Here I also have defined the kinetic inductance ratio α_k as

$$\alpha_k = \frac{L_k}{L_k + L} \tag{2.71}$$

where L_k is the kinetic inductance due to Cooper pairs and L is the geometric inductance of the resonator.

2.3.2 Thermal Quasiparticles

Quasiparticles are fermions, hence when the resonator is in thermal equilibrium at temperature T the distribution of the quasiparticles $f(E)$ follows the Fermi-Dirac

distribution [142]

$$f(E) \;=\; \frac{1}{e^{E/k_BT}+1}, \tag{2.72}$$

where E is measured from the Fermi level. Using this distribution, the quasiparticle density $n_{\rm qp}$, the superconducting gap Δ, and the complex conductivities σ_1 and σ_2 can be numerically calculated using Eqs. 2.64, 2.65, 2.66, and 2.67, respectively. However when $k_BT \ll \Delta$ and $\hbar\omega \ll \Delta$, the following approximate analytical expressions can be found [42]

$$n_{\rm qp} \;= 2N_0\sqrt{2\pi k_BT\Delta_0}\, e^{-\frac{\Delta_0}{k_BT}} \tag{2.73}$$

$$\frac{\sigma_1}{\sigma_n} \;= \frac{4\Delta_0}{\hbar\omega}\, e^{-\frac{\Delta_0}{k_BT}}\, \sinh\left(\frac{\hbar\omega}{2k_BT}\right)\, K_0\left(\frac{\hbar\omega}{2k_BT}\right) \tag{2.74}$$

$$\frac{\sigma_2}{\sigma_n} \;= \frac{\pi\Delta_0}{\hbar\omega}\, \left[1-\sqrt{\frac{2\pi k_BT}{\Delta_0}}e^{-\frac{\Delta_0}{k_BT}} - 2e^{-\frac{\Delta_0+(\hbar\omega/2)}{k_BT}} I_0\left(\frac{\hbar\omega}{2k_BT}\right)\right] \tag{2.75}$$

where Δ_0 is the superconducting gap at zero temperature, I_n and K_n are nth order modified Bessel function of the first and second kind, respectively. Most of my data was taken in the limit where these equations are good approximations.

Figure 2.11 shows the normalized complex conductivities σ_1/σ_n and σ_2/σ_n as a function of temperature T using the analytical approximations Eqs. 2.74 and 2.75. The parameters I used in these plots are for typical aluminum resonators with $\omega/2\pi = 5$ GHz and $\Delta_0 = 180$ μeV, which gives a critical temperature $T_c \approx 1.19K$. σ_1/σ_n is zero at zero temperature, but increases rapidly to 1 as the temperature increases toward T_c. The imaginary part σ_2/σ_n is $\pi\Delta_0/\hbar\omega$ at zero temperature, and decreases with increasing temperature. Note that because I use the approximation, the plotted result should be expected to deviate from the actual conductivities at temperatures approaching T_c. From these results, it is straightforward to conclude

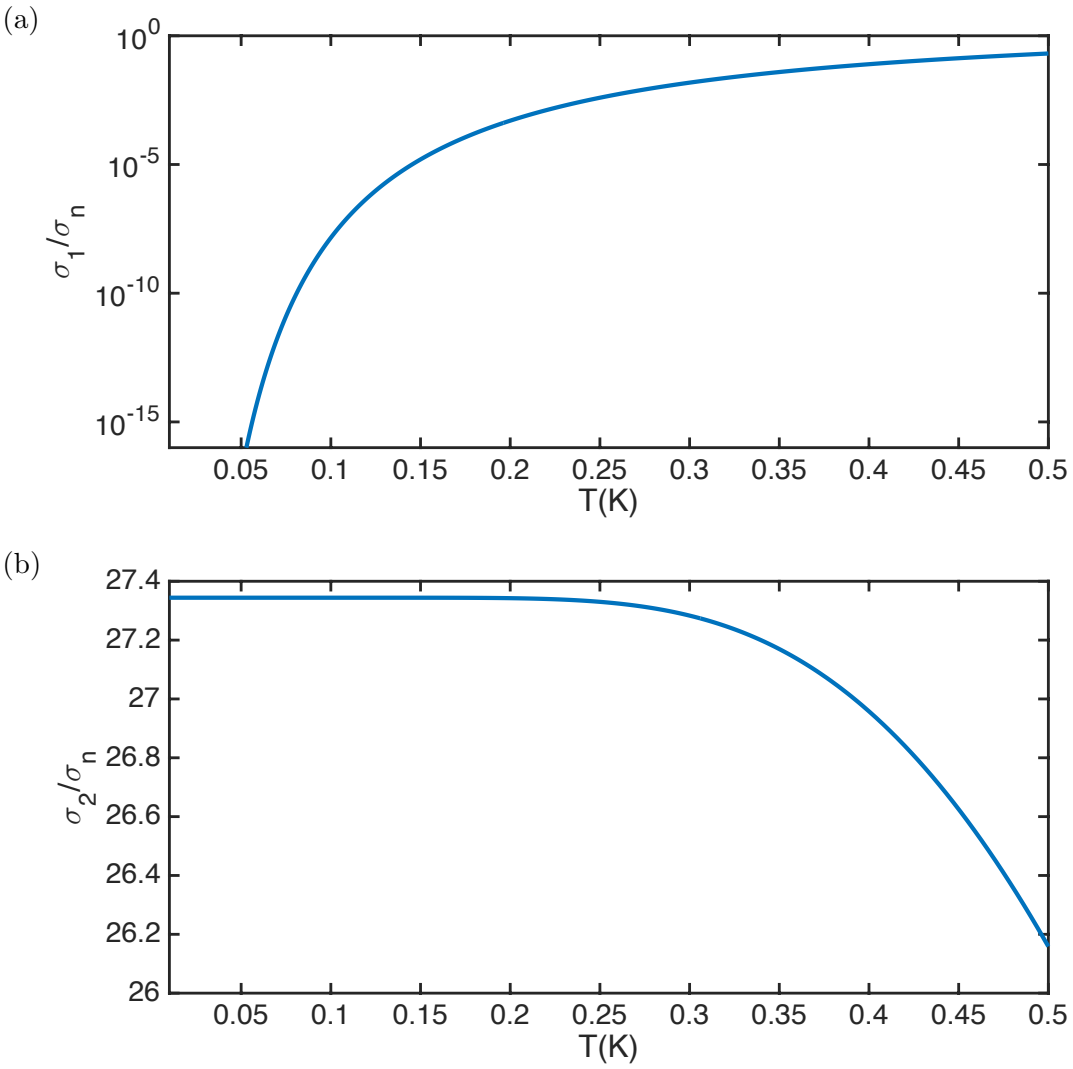

Figure 2.11: (a) Real conductivity σ_1/σ_n vs temperature T using Eq. 2.74. (b) Imaginary conductivity σ_2/σ_n vs temperature T using Eq. 2.75. The parameters are $\omega/2\pi = 5$ GHz and $\Delta_0 = 180$ μeV.

that quasiparticles should cause the inverse quality factor $1/Q$ to increase with increasing temperature and the resonance frequency ω_r to decrease with increasing temperature.

2.3.3 Non-Equilibrium Distribution of Quasiparticles

To understand the effect of rf drive and optical illumination on quality factor and frequency shift, I need to take into account how they influence σ_1 and σ_2. In 1967 Rothwarf and Taylor developed a set of equations that describes the behavior of the quasiparticle density n_{qp} under external injection of quasiparticles [146]. However as can be seen in the expressions for n_{qp} and σ, n_{qp} by itself is not sufficient to calculate σ. What is needed is the quasiparticle distribution $f(E)$.

In 1977 Chang and Scalapino derived a set of kinetic equations that can be used to calculate $f(E)$ [147, 148]. In the kinetic equations, the quasiparticle can be injected or driven by an external source, scatter due to absorption/emission of a phonon, recombine into Cooper pairs, and Cooper pairs can break to generate quasiparticles. In the BCS theory, Cooper pairs are caused by an electron-phonon interaction [143]. As a result, most of the mechanisms above will involve the phonon distribution $n(\Omega)$, where Ω is the phonon energy. In the kinetic model, the phonons can interact with quasiparticles during scattering, pair breaking, and recombination. Additionally, an injection source can inject phonons and phonons can escape to a thermal bath.

All these processes can be summarized in the block diagram shown in Fig. 2.12.

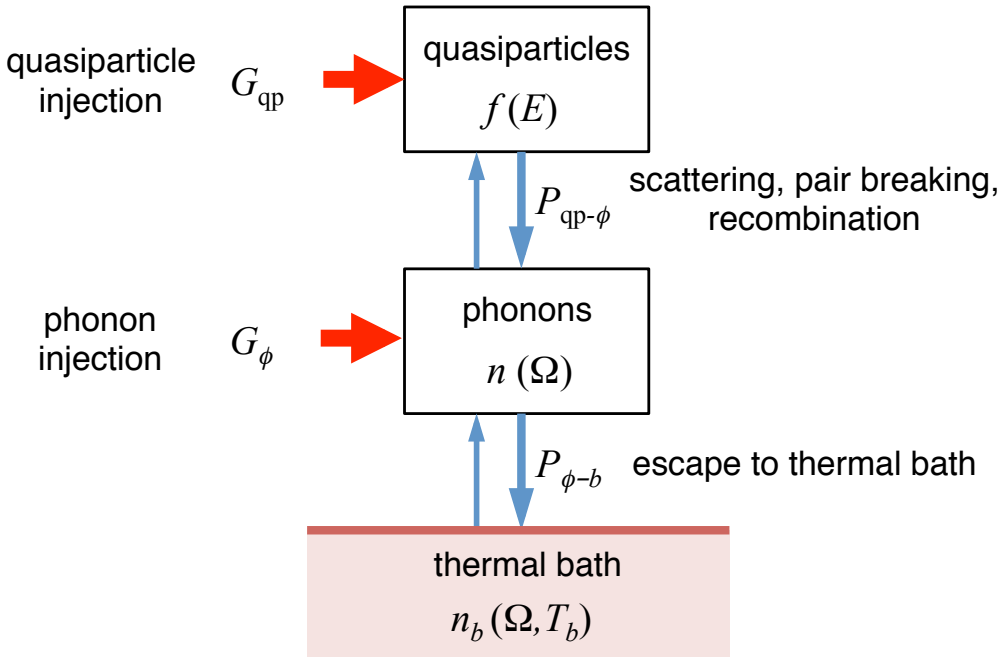

Figure 2.12: Block diagram showing the processes included in the Chang & Scalapino kinetic equations.

When integrated over the energies E and Ω, the Chang and Scalapino kinetic equations results in the Rothwarf-Taylor equations [147]. It is also possible to work out equations to handle the situations where the distributions $f(E)$ and $n(\Omega)$ depend on position. These will be needed if quasiparticle and phonon diffusion needs to be taken into account. Here I have assumed uniform distributions and ignore diffusion.

The quasiparticles distribution $f(E)$ obeys the kinetic equation [147, 149]

$$\begin{aligned}\frac{df(E)}{dt} &= G_{qp}(E) - \frac{1}{\tau_0(k_B T_c)^3}\left\{\int_0^\infty d\Omega\,\Omega^2\, h_-(E, E+\Omega)\right. \\ &\times \Big(f(E)[1-f(E+\Omega)]n(\Omega) - [1-f(E)]f(E+\Omega)[n(\Omega)+1]\Big) \\ &+ \int_0^{E-\Delta} d\Omega\,\Omega^2\, h_-(E, E-\Omega) \\ &\times \Big(f(E)[1-f(E-\Omega)][n(\Omega)+1] - [1-f(E)]f(E-\Omega)n(\Omega)\Big)\end{aligned}$$

$$+\int_{E+\Delta}^{\infty} d\Omega\,\Omega^2\,h_+(E,\Omega-E)$$
$$\times\Big(f(E)f(\Omega-E)[n(\Omega)+1]-[1-f(E)][1-f(\Omega-E)]n(\Omega)\Big)\Big\} \quad (2.76)$$

Here $G_{\rm qp}$ is a term that represents quasiparticle "injection", which may include external microwave drive (Section 2.3.4) as well as direct injection through tunneling processes. τ_0 is the characteristic time constant for quasiparticle-phonon scattering [150]. The first two integral terms represents quasiparticle scattering due to absorption and emission of a phonon. The third integral term represents recombination and pair breaking processes.

The phonon distribution $n(\Omega)$ obeys the kinetic equation [147, 149]

$$\begin{aligned}\frac{dn(\Omega)}{dt} &= G_\phi(\Omega)-\frac{1}{\pi\tau_\phi\Delta}\Big\{2\int_{\Delta}^{\infty} dE\,\rho(E)\,h_-(E,E+\Omega)\\
&\quad\times\Big(f(E)[1-f(E+\Omega)]n(\Omega)-[1-f(E)]f(E+\Omega)[n(\Omega)+1]\Big)\\
&\quad+\int_{\Delta}^{\Omega-\Delta} dE\,\rho(E)\,h_+(E,\Omega-E)\\
&\quad\times\Big([1-f(E)][1-f(\Omega-E)]n(\Omega)-f(E)f(\Omega-E)[n(\Omega)+1]\Big)\Big\}\\
&\quad+\frac{n_b(\Omega,T_b)-n(\Omega)}{\tau_e} \qquad (2.77)\end{aligned}$$

Here $G_\phi(\Omega)$ represents phonon injection, which may include optical illumination (Section 2.3.5) as well as direct injection from a heater. τ_ϕ is the characteristic phonon-quasiparticle scattering time [150] and τ_e is the escape time for phonons to leave the superconductor and go into the substrate [151]. The first integral term represents quasiparticle scattering due to both absorption and emission of a phonon. The second integral term represents recombination and pair breaking processes. The final term on the right hand side represents phonon escape to a thermal bath, where

the phonon distribution of the thermal bath $n_b(\Omega, T_b)$ at bath temperature T_b is given by the Bose-Einstein distribution

$$n_b(\Omega, T_b) \;=\; \frac{1}{e^{\Omega/k_B T_b} - 1}. \tag{2.78}$$

Within the kinetic model, power balance needs to be satisfied. Power can be absorbed by the system and flows from the quasiparticle to the phonon. The power flow from the quasiparticles at energy E to $E + dE$ to the phonons is given by [149]

$$\begin{aligned} dP_{\mathrm{qp}-\phi}(E) \;=& \frac{4N_0 E\rho(E)V}{\tau_0(k_B T_c)^3}\Bigg\{ \int_0^\infty d\Omega\, \Omega^2\, h_-(E, E+\Omega) \\ & \times \Big(f(E)[1-f(E+\Omega)]n(\Omega) - [1-f(E)]f(E+\Omega)[n(\Omega)+1]\Big) \\ & + \int_0^{E-\Delta} d\Omega\, \Omega^2\, h_-(E, E-\Omega) \\ & \times \Big(f(E)[1-f(E-\Omega)][n(\Omega)+1] - [1-f(E)]f(E-\Omega)n(\Omega)\Big) \\ & + \int_{E+\Delta}^\infty d\Omega\, \Omega^2\, h_+(E, \Omega-E) \\ & \times \Big(f(E)f(\Omega-E)[n(\Omega)+1] - [1-f(E)][1-f(\Omega-E)]n(\Omega)\Big)\Bigg\}\, dE, \end{aligned} \tag{2.79}$$

where V is the total superconductor volume of the resonator and a positive value means power flows from the quasiparticles to the phonons for that value of E. The total power flowing between quasiparticles and phonons is then given by

$$P_{\mathrm{qp}-\phi} \;=\; \int_\Delta^\infty \frac{dP_{\mathrm{qp}-\phi}(E)}{dE}\, dE. \tag{2.80}$$

The power flow between the phonons and the bath at energy Ω is given by [149]

$$dP_{\phi-b}(\Omega) \;=\; D(\Omega)\,\Omega\, V\, \frac{n_b(\Omega, T_b) - n(\Omega)}{\tau_e}\, d\Omega, \tag{2.81}$$

where $D(\Omega)$ is the phonon density of states. Using the Debye model, I can write

$$D(\Omega) \;=\; \frac{9N_i\Omega^2}{\Omega_D^3}, \tag{2.82}$$

where N_i is the atomic density of the superconductor and Ω_D is the Debye energy. A positive value in Eq. 2.81 means that power is flowing from the phonons to the thermal bath. The total power flowing between the phonons and the thermal bath is then given by

$$P_{\phi-b} \;=\; \int_0^{\Omega_D} \frac{dP_{\phi-b}(\Omega)}{d\Omega}\, d\Omega. \tag{2.83}$$

I note that the parameters τ_0 and τ_ϕ appearing in the kinetic equations above are not independent parameters, but satisfy the relation [149]

$$\frac{2\pi N_0\tau_\phi\Delta_0\Omega_D^3}{9N_i\tau_0(k_BT_c)^3} \;= 1. \tag{2.84}$$

If interaction between the quasiparticles and phonons is sufficiently strong, the superconducting gap Δ may become complex and dependent on quasiparticle energy E. In this case the quasiparticle density of states $\rho(E)$ of Eq. 2.63 becomes [144, 152]

$$\rho(E) \;=\; \mathrm{Re}\left(\frac{E}{\sqrt{E^2-[\Delta(E)]^2}}\right). \tag{2.85}$$

This reduces to Eq. 2.63 if Δ is real and independent of E. Eq. 2.85 typically causes discontinuity in $\rho(E)$ at $E=\Delta$ to smear out and $\rho(E)$ becomes a continuous function with small nonzero values of $\rho(E)$ for $E<\Delta$. This effect was first observed by Giaever *et al.* in Pb [153] and theoretically described by Schrieffer *et al.* [152].

For simplicity I assumed Δ to be independent of E but retained a small imaginary component [149] to prevent divergence at $E=\Delta$. In this case $\rho(E)$ can be

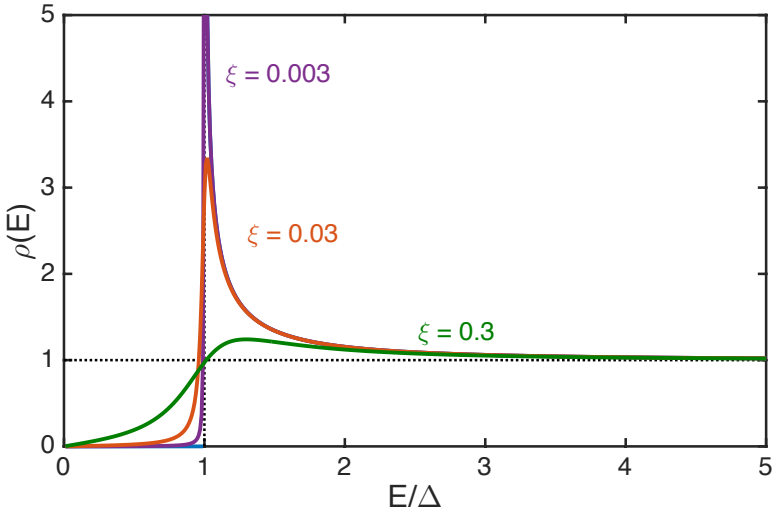

Figure 2.13: Modified quasiparticle density of states $\rho(E)$ of Eq. 2.86 as a function of normalized quasiparticle energy E/Δ for several values of ξ: $\xi = 0.003$ (purple curve), $\xi = 0.03$ (red curve), $\xi = 0.003$ (green curve).

written as

$$\rho(E) \;=\; \mathrm{Re}\left(\frac{E}{\sqrt{E^2-\Delta^2(1+i\xi)^2}}\right), \tag{2.86}$$

where Δ is a real constant and ξ is a small dimensionless parameter. Figure 2.13 shows $\rho(E)$ of Eq. 2.86 as a function of E/Δ for several values of ξ between 0.003 and 0.3. All the curves show smearing of the peak and nonzero values of $\rho(E)$ for $E < \Delta$, as expected. The largest deviation compared to the original expression for $\rho(E)$ of Eq. 2.63 occurs for the largest value of ξm also as as expected. Typically in the model I used $\xi = 0.001$ to prevent divergences at $E = \Delta$ and used $E = \Delta$ as lower limit of integration for quasiparticle distribution.

It is not immediately obvious that the kinetic equations of Eqs. 2.76 and 2.77 will result in a Fermi-Dirac distribution at temperature T_b for the quasiparticle

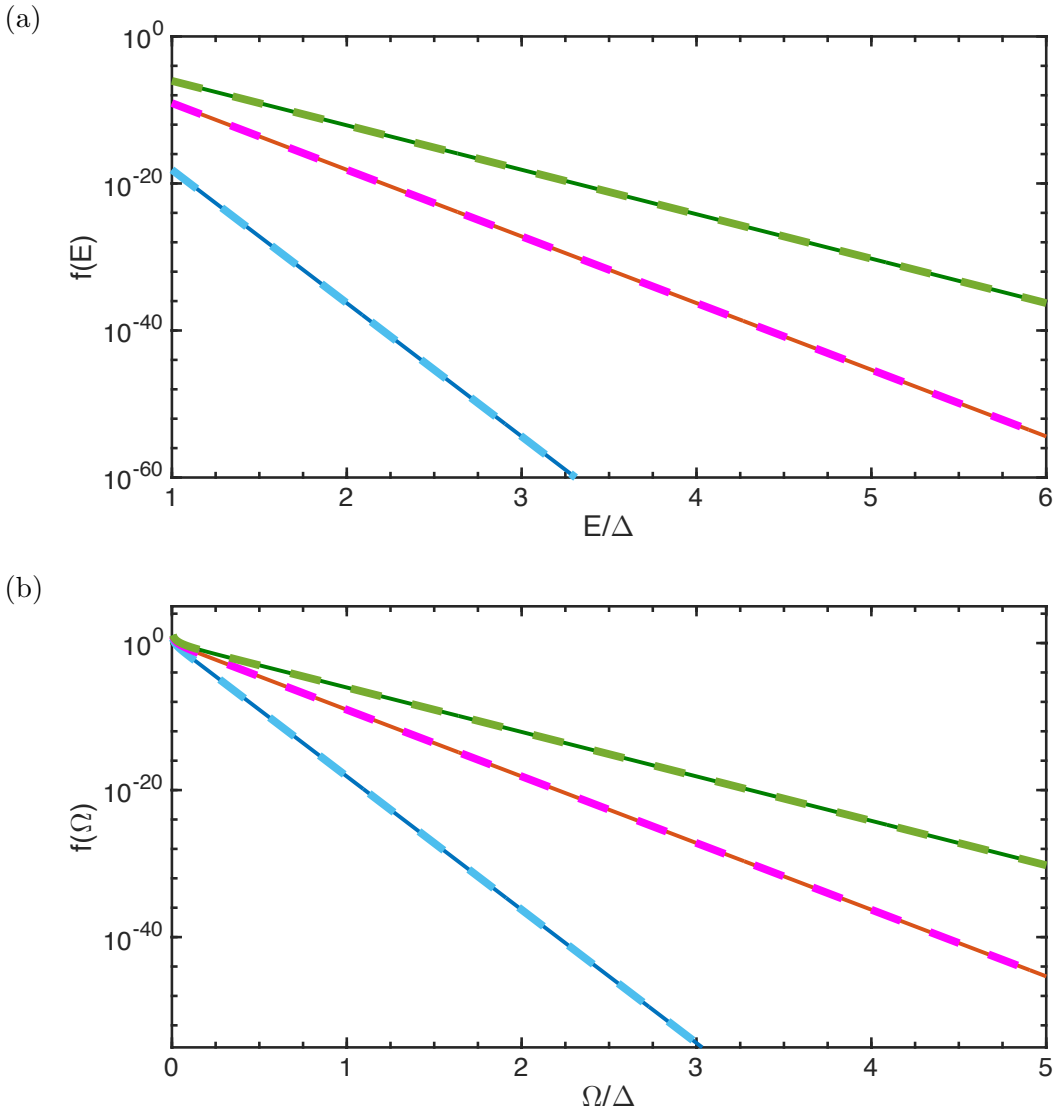

Figure 2.14: (a) Plot of $f(E)$ vs E/Δ and (b) $n(\Omega)$ vs Ω/Δ. Solid curves are from numerical simulations and dashed curves are from using the analytical expression for the thermal distribution. The temperatures are 50 mK (blue and light blue curves), 100 mK (red and magenta curves), and 150 mK (green and light green curves), and the superconducting gap was set to $\Delta = 180$ μeV.

distribution $f(E)$ when the bath temperature is at T_b and there are no contributions from the quasiparticle or phonon injection terms. Due to the direct connection between the phonons and the thermal bath, it is easier to see that the phonon distribution $n(\Omega)$ will be equal to the bath distribution $n_b(\Omega, T_b)$. To verify the behavior of the equations, I performed a numerical simulation to find the steady state equilibrium $f(E)$ and $n(\Omega)$ for a range of temperature values and no drive terms. I used a modified version of the simulation method I will describe in detail in the next section. For these tests, I set $\Delta = 180$ μeV. I found that the $f(E)$ and $n(\Omega)$ obtained from the simulations were practically indistinguishable from thermal distributions. Figures 2.14 show a comparison between $f(E)$ and $n(\Omega)$ from the simulation and the thermal distributions. This result was also a useful check on the routine I used to solve the kinetic equations.

2.3.4 Non-Equilibrium Distribution from rf Drive

According to Chang and Scalapino's kinetic model, applying a microwave drive to a superconductor creates an effective quasiparticle injection or excitation [147]. They defined an injection term $G_{\rm qp}(E)$ that gives the rate at which quasiparticles with energy E are changing occupancy due to the rf drive. For a drive frequency ω_r, $G_{\rm qp}(E)$ is given by [147]

$$\begin{aligned} G_{\rm qp}(E,\omega_r) \; = & 2B \Big\{ h_+(E, E+\hbar\omega_r) \left[f(E+\hbar\omega_r) - f(E) \right] \\ & - \; h_+(E, E-\hbar\omega_r) \left[f(E) - f(E-\hbar\omega_r) \right] \Big\}. \end{aligned} \tag{2.87}$$

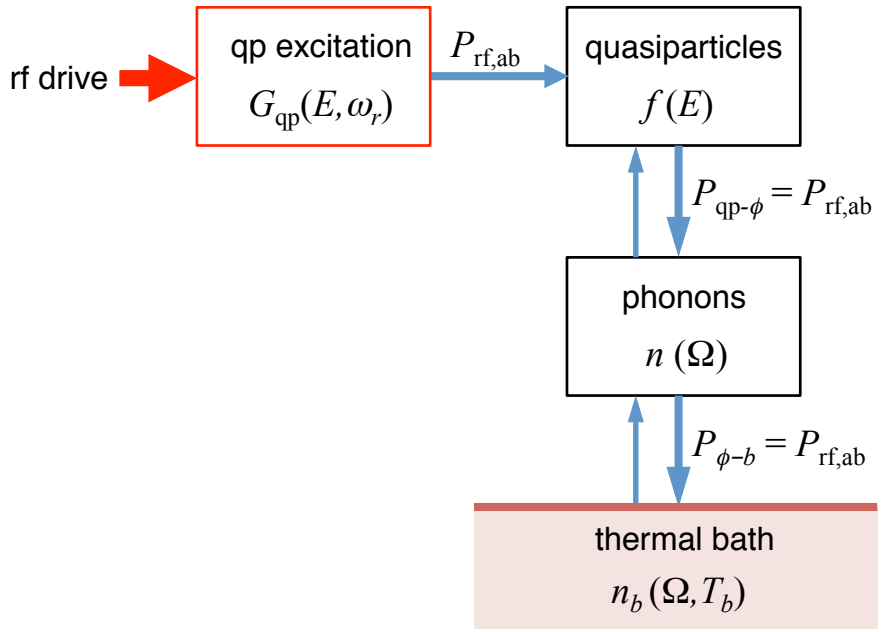

Figure 2.15: Block diagram showing the power flow in the quasiparticle-phonon system under rf drive.

The coefficient B is expected to be proportional to the absorbed rf drive power $P_{\mathrm{rf,ab}}$ [147, 149], which will be defined below.

Figure 2.15 shows a block diagram for the power flows in the system when an rf drive is applied. From the kinetic equations, the total power absorbed by the quasiparticles is given by [149]

$$P_{\mathrm{rf,ab}} = 4N_0V \int_{\Delta}^{\infty} dE\, G_{\mathrm{qp}}(E, f_r)\, E\, \rho(E). \tag{2.88}$$

The power $P_{\mathrm{rf,ab}}$ absorbed by the quasiparticles is not in general the same as the applied rf power P_{rf}, which is defined as the power at the input port. To find how $P_{\mathrm{rf,ab}}$ and P_{rf} are related, note that Eq. 2.27 is an expression for P_R, which is the power absorbed by all internal sources. To take into account the power absorbed by quasiparticles only, I need to find the fraction of the total internal loss that is due

to quasiparticles. For simplicity, I will assume equal or balanced input and output coupling so that $Q_{\rm in} = 2Q_e$. Finally, I have defined $P_{\rm rf} = P_{\rm in}$ as the total applied power. With these assumptions, the power absorbed by the quasiparticles from the rf drive is

$$P_{\rm rf,ab} \;=\; P_R\,\frac{1/Q_{\rm qp}}{1/Q_i} \;=\; \frac{2P_{\rm rf}Q^2}{Q_iQ_e}\,\frac{Q_i}{Q_{\rm qp}} \;=\; \frac{2P_{\rm rf}Q^2}{Q_{\rm qp}Q_e}. \tag{2.89}$$

To calculate the nonequilibrium distributions $f(E)$ and $n(\Omega)$, as well as the complex conductivities σ_1 and σ_2, I follow the numerical procedure described by Goldie and Withington [149] and solve Eqs. 2.76, 2.77, and 2.88 for $f(E)$, $n(\Omega)$, and B for the steady state condition $df(E)/dt = 0$ and $dn(\Omega)/dt = 0$. Also from Eq. 2.88, I defined a 'power error' term $\delta P_{\rm rf,ab}$ as

$$\delta P_{\rm rf,ab} \;=\; 4N_0V\int_\Delta^\infty dE\,G_{\rm qp}(E,f_r)\,E\,\rho(E) \;-\; P_{\rm rf,ab}, \tag{2.90}$$

with $\delta P_{\rm rf,ab} = 0$ for the correct set of solutions. I then discretize the problem so as to evaluate $f(E)$ on $N = 1000$ points from $E = \Delta$ to $\Delta + (N-1)$ μeV in steps of 1 μeV and $n(\Omega)$ on $N = 1000$ points from $\Omega = 1$ μeV to N μeV in steps of 1 μeV. For typical values of Δ for Al resonators, the upper limit of E evaluated was about 7Δ and the upper limit of Ω evaluated was about 6Δ. Eqs. 2.76, 2.77 and 2.90 yield $2N + 1 = 2001$ simultaneous equations which we then solve using Newton-Raphson method [154], which will be described below. Since the energies are discrete I confine the values of Δ and $\hbar\omega$ to be integer multiples of grid size 1 μeV. As I discussed previously, Δ depends on $f(E)$, due to Eq. 2.65. However, I found that for the range of parameters I was interested in, Δ changed by much less than the grid size. Hence confining Δ only to integer multiple values was acceptable.

In the numerical simulation, I define $f_j = f(\Delta + (j-1)\ \mu\text{eV})$ and $n_j = n(j\ \mu\text{eV})$ with $j = 1, \ldots, N$. For the lth iteration of the simulation, I define the solution vector γ_l and the error vector ζ_l

$$\gamma_l = \begin{pmatrix} f_1 \\ \vdots \\ f_N \\ B \\ n_1 \\ \vdots \\ n_N \end{pmatrix}, \qquad \zeta_l = \begin{pmatrix} df_1/dt \\ \vdots \\ df_N/dt \\ \delta P_{\text{rf,ab}} \\ dn_1/dt \\ \vdots \\ dn_N/dt \end{pmatrix}. \tag{2.91}$$

The Newton-Raphson method, or Newton's method, is a numerical iteration method used to find zeros of an equation or a set of equations [154]. For the initial condition, I usually chose thermal distributions with temperature $2T_b$ for f_j and n_j. For the initial guess for B, I chose a value of B that satisfied Eq. 2.88 for the initial distribution. For each iteration, I evaluated

$$\gamma_{l+1} = \gamma_l - \chi\,[J(\gamma_l)]^{-1}\zeta_l. \tag{2.92}$$

Here $0 \leq \chi \leq 1$ is the convergence parameter. I typically used $\chi = 1$. $J(\gamma_l)$ is the $(2N+1) \times (2N+1)$ Jacobian matrix

$$J(\alpha_l) = \begin{pmatrix} \frac{\partial(df_1/dt)}{\partial f_1} & \cdots & \frac{\partial(df_1/dt)}{\partial f_N} & \frac{\partial(df_1/dt)}{\partial B} & \frac{\partial(df_1/dt)}{\partial n_1} & \cdots & \frac{\partial(df_1/dt)}{\partial n_N} \\ \vdots & \ddots & \vdots & \vdots & \vdots & \ddots & \vdots \\ \frac{\partial(df_N/dt)}{\partial f_1} & \cdots & \frac{\partial(df_N/dt)}{\partial f_N} & \frac{\partial(df_N/dt)}{\partial B} & \frac{\partial(df_N/dt)}{\partial n_1} & \cdots & \frac{\partial(df_N/dt)}{\partial n_N} \\ \frac{\partial\delta P_{\text{rf,ab}}}{\partial f_1} & \cdots & \frac{\partial\delta P_{\text{rf,ab}}}{\partial f_N} & \frac{\partial\delta P_{\text{rf,ab}}}{\partial B} & \frac{\partial\delta P_{\text{rf,ab}}}{\partial n_1} & \cdots & \frac{\partial\delta P_{\text{rf,ab}}}{\partial n_N} \\ \frac{\partial(dn_1/dt)}{\partial f_1} & \cdots & \frac{\partial(dn_1/dt)}{\partial f_N} & \frac{\partial(dn_1/dt)}{\partial B} & \frac{\partial(dn_1/dt)}{\partial n_1} & \cdots & \frac{\partial(dn_1/dt)}{\partial n_N} \\ \vdots & \ddots & \vdots & \vdots & \vdots & \ddots & \vdots \\ \frac{\partial(dn_N/dt)}{\partial f_1} & \cdots & \frac{\partial(dn_N/dt)}{\partial f_N} & \frac{\partial(dn_N/dt)}{\partial B} & \frac{\partial(dn_N/dt)}{\partial n_1} & \cdots & \frac{\partial(dn_N/dt)}{\partial n_N} \end{pmatrix}. \tag{2.93}$$

Table 2.1: Parameters used by de Visser *et al.* in their nonequilibrium simulations [48]. I used these values to test my simulation routine.

Symbol	Parameter	Value
Δ	superconducting gap	177 μeV
$\hbar\omega_r$	rf photon energy in simulation	23 μeV
V	resonator Al volume	1770 μm^3
Q_e	external quality factor	20100
$1/Q_{\mathrm{TLS}}$	TLS loss component	0
$1/Q_{\mathrm{qp}}$	quasiparticle loss component	varies
$1/Q_0$	power-independent loss component	0
N_0	single spin density of states at Fermi level	1.74×10^{10} /eV μm^3
τ_0	quasiparticle-phonon time	438 ns
τ_ϕ	characteristic phonon time	0.26 ns
τ_e	phonon escape time	0.17 ns

The expression for each element of the Jacobian can be derived by taking partial derivatives of Eq. 2.90 and discretized versions of Eqs. 2.76 and 2.77 (see Appendix A). Typically I needed about 20 to 30 iterations to converge to a solution for γ.

To check the simulation and understand what the kinetic model predicts for the behavior of $1/Q$ and ω_r under rf drive, I checked against the published results. The behavior I describe below was first reported by de Visser *et al.* in Al resonators [48]. The parameters I used in the simulation are listed in Table 2.1 and are the parameters de Visser et al. *et al.* reported for their simulations on their resonators. The Q_i values used in these simulations were the measured Q_i, which varied with temperature T_b and rf drive powers P_{rf}. The range of P_{rf} corresponded to photon

occupation numbers between approximately 10^4 and 10^8, much higher photon numbers than the TLS critical photon numbers, sp that the TLS loss should be small in this regime.

Figures 2.16 show some examples of $f(E)$ and $n(\Omega)$ from the simulations. Here I set $T_b = 120$ mK and chose three drive powers. The corresponding distributions for $T_b = 320$ are shown in Fig. 2.17. Both $f(E)$ and $n(\Omega)$ show striking deviations from thermal distributions (dashed curves), with stronger drive powers showing larger deviations. In particular, peaks appear every $\hbar\omega$ due to the microwave drive term at frequency $\omega \approx \Delta/8\hbar$. For $T = 120$ mK, there are significant jumps in $n(\Omega)$ at $\Omega = 2\Delta$ and smaller jumps in $f(E)$ at $E = 3\Delta$ for lower $P_{\rm rf}$. This is caused by the pair breaking and recombination term.

In experiments below about 200 mK, de Visser *et al.* reported that the loss $1/Q$ increased with increasing drive power, while ω_r decreased with increasing drive. The reason for this behavior can be seen in the plot for $f(E)$ shown in Fig. 2.16(a). Notice that $f(E)$ increases with increasing rf drive power for all values of E; the drive increases the number of quasiparticles. The effect of increasing drive power on $f(E)$ in this regime is similar to an increase in T_b (see Fig. 2.14). From Eq. 2.64, I can also show that quasiparticles are created with increasing drive in this regime.

On the other hand, at temperatures above around 200 mK, they reported that $1/Q$ decreased with increasing drive, while ω_r increased with increasing drive. The distribution $f(E)$, as shown in Fig. 2.17(a) and (c) increases with increasing drive only for $E > \Delta + \hbar\omega$, while it actually decreases for $\Delta < E < \Delta + \hbar\omega$. By applying Eq. 2.64, one can show that no quasiparticles are created by the drive

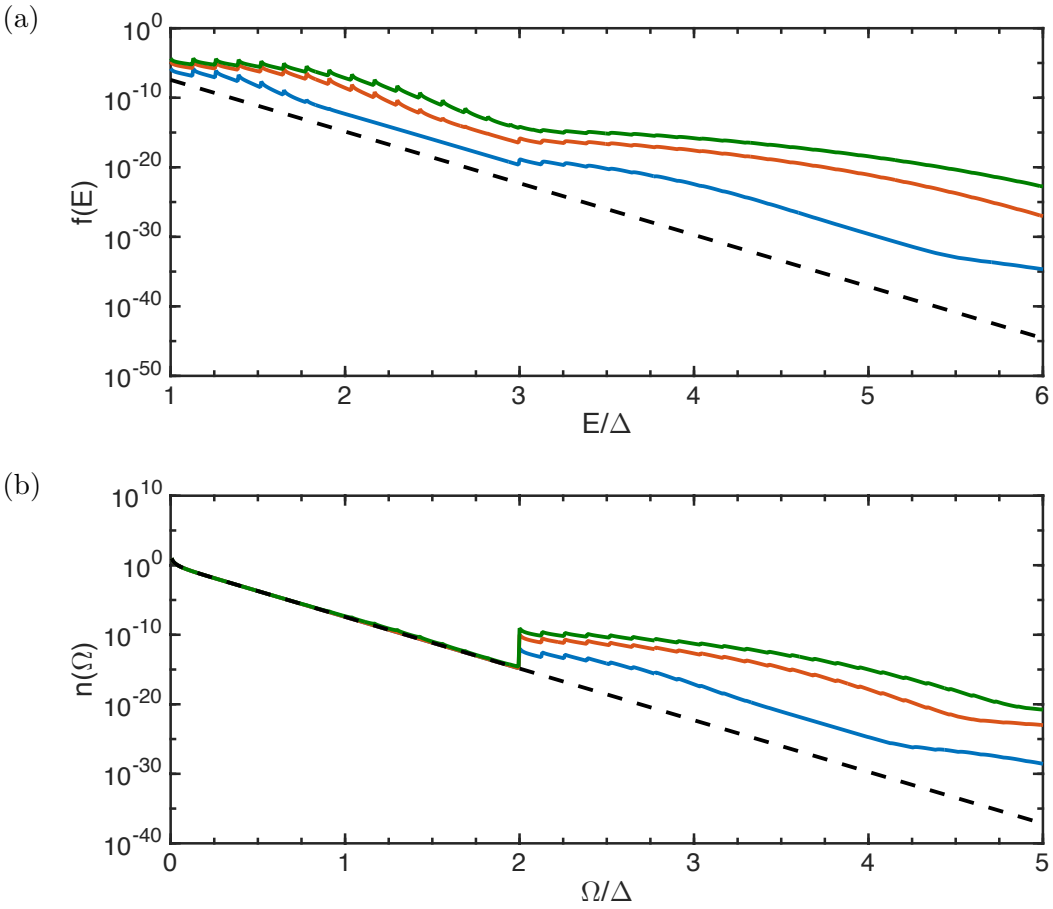

Figure 2.16: (a) Simulated quasiparticle distribution $f(E)$ vs normalized energy E/Δ and (b) simulated phonon distribution $n(\Omega)$ vs normalized energy Ω/Δ, both for bath temperature $T_b = 120$ mK and for rf drive powers $P_{\rm rf}$ of -100 dBm (blue curve), -80 dBm (red curve), and -72 dBm (green curve). Other parameters are shown in Table 2.1. The black dashed curve was found assuming a thermal distribution with $T_b = 120$ mK.

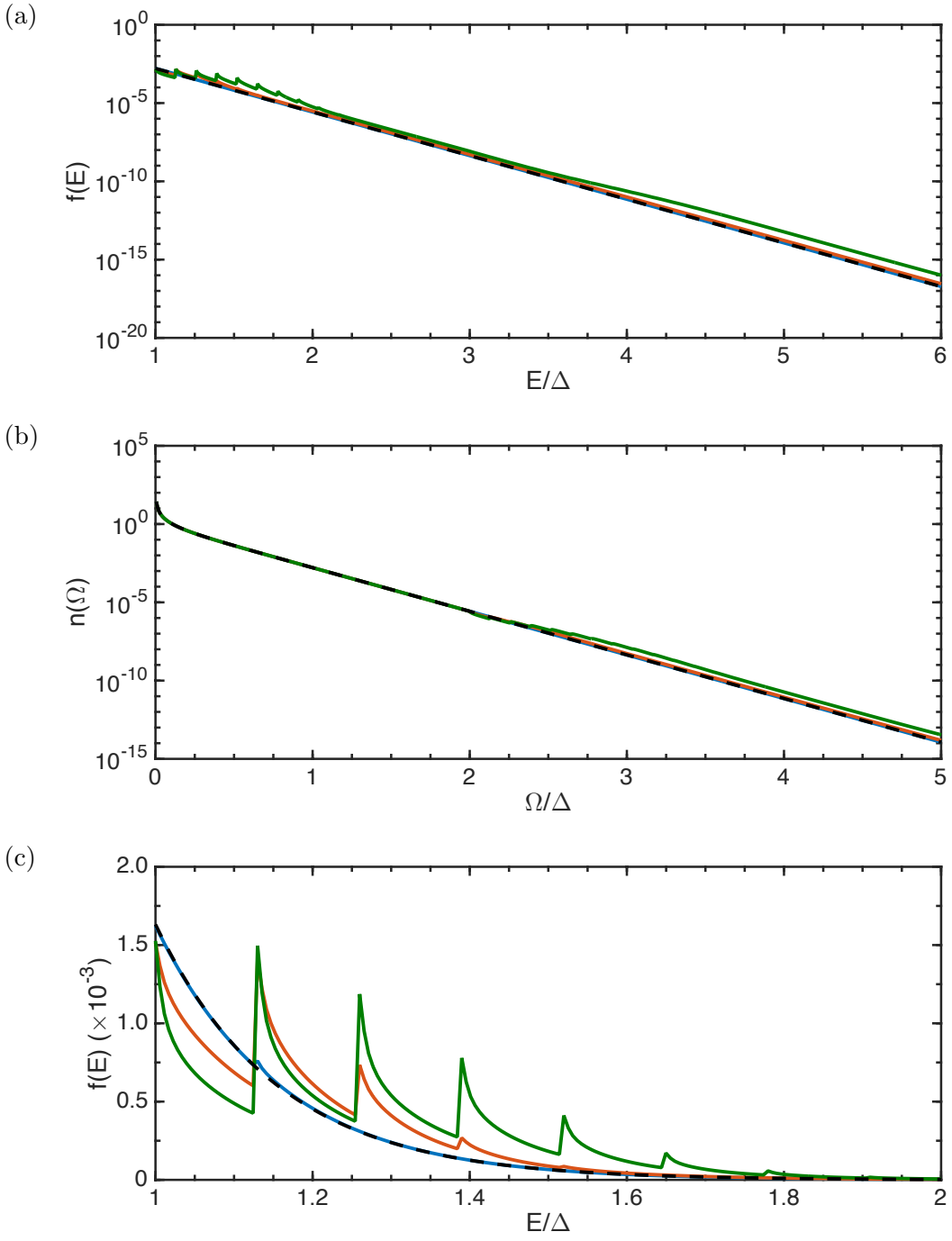

Figure 2.17: (a) Simulated quasiparticle distribution $f(E)$ vs normalized energy E/Δ and (b) simulated phonon distribution $n(\Omega)$ vs normalized energy Ω/Δ, both for bath temperature $T_b = 320$ mK and for rf drive powers $P_{\rm rf}$ of -100 dBm (blue curve), -80 dBm (red curve), and -72 dBm (green curve). Other parameters are shown in Table 2.1. The black dashed curve was found assuming a thermal distribution with $T_b = 320$ mK. (c) Linear plot of $f(E)$ between $E = \Delta$ and $E = 2\Delta$.

in this range. Instead, the rf drive just redistributes the quasiparticles from lower energies to higher energies. According to Eq. 2.66, σ_1 depends on the difference factor $f(E) - f(E + \hbar\omega)$. The redistribution of quasiparticles causes this factor to decrease with increasing drive, which in turn causes σ_1 to decrease with increasing drive. From Eq. 2.67, σ_2 depends on $1 - 2f(E + \hbar\omega)$, however the limits of the integration ensure that only $f(E)$ values for $\Delta < E < \Delta + \hbar\omega$ are included in the integration. Since $f(E)$ decreases with increasing drive for this range of E, the factor, and in turn σ_2 increases with increasing drive.

For an Al resonator, de Visser *et al.* reported that the boundary between the two regimes was around $T_b \approx 220$ mK [48]. This behavior can also be seen in my simulations in the plots of σ_1/σ_n and σ_2/σ_n shown in Figs. 2.18. I note that when I used even higher powers in the simulation than the powers reported, $f(E)$ in the higher temperature regime starts to show behavior similar to the lower temperature behavior, *i.e.* an increase in loss due to the rf-drive generating additional quasiparticles. Of course, this is what one should expect at sufficiently high power.

2.3.5 Non-Equilibrium Distribution from Optical Illumination

Guruswamy, Goldie and Withington also extended their approach to include effects of pair breaking due to photons with energies up to about 10Δ [155, 156]. Unfortunately, in my experiments I used optical photons of energy ≈ 1.6 eV, which is approximately 9000Δ. For such energetic photons the effects on the superconductor are similar to adding a source of heating [42, 107, 156–158]. Accordingly, here I used

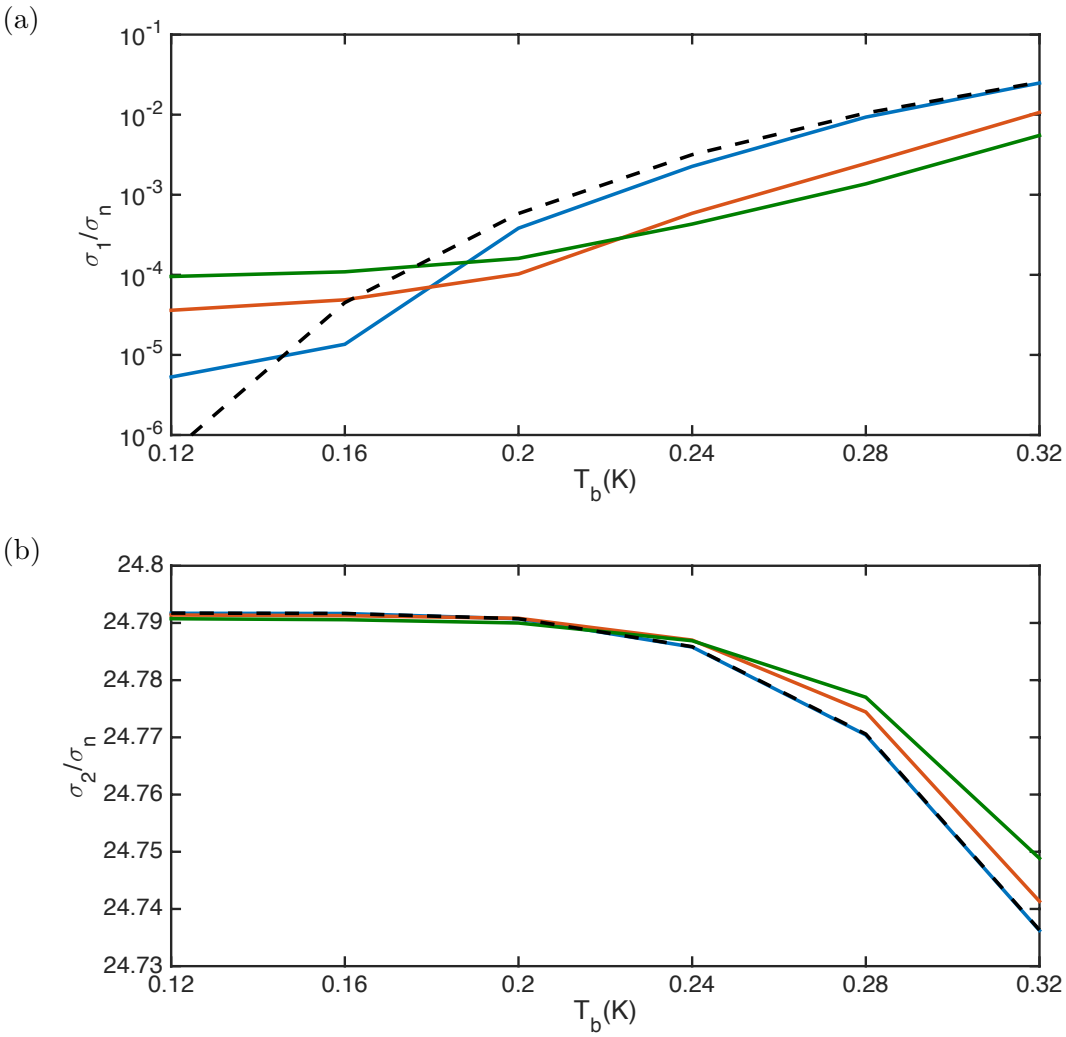

Figure 2.18: (a) Scaled real component of conductivity σ_1/σ_n vs bath temperature T_b and (b) scaled imaginary component of conductivity σ_2/σ_n vs bath temperature T_b, both for rf drive powers P_{rf} of -100 dBm (blue curve), -80 dBm (red curve), and -72 dBm (green curve). Other parameters are shown in Table 2.1. The black dashed curve was found by assuming a thermal distribution at temperature T_b for $f(E)$.

a modification of the Parker heating model [107] that accounts for optical radiation by introducing a phonon generating term with an effective temperature determined by the optical power (see Fig. 2.19).

To proceed, I define a phonon generation term due to photons

$$G_\phi(\Omega) \;=\; \frac{n_{\rm opt}(\Omega, T_{\rm eff})}{\tau_e}. \tag{2.94}$$

Here $n_{\rm opt}(\Omega, T_{\rm eff})$ is an effective source of hot phonons with effective temperature $T_{\rm eff}$ that is determined by the optical intensity. I used a variation on Parker's model and set [107]

$$n_{\rm opt}(\Omega, T_{\rm eff}) \;=\; \begin{cases} 0, & \text{for } \Omega < 2\Delta \\ \dfrac{1}{e^{\Omega/k_B T_{\rm eff}} - 1} & \text{for } \Omega > 2\Delta. \end{cases} \tag{2.95}$$

Although $n_{\rm opt}$ takes the form of a Bose-Einstein thermal distribution for $\Omega > 2\Delta$ it is not a thermal distribution since $n_{opt} = 0$ for $\Omega < 2\Delta$.

Fig. 2.19 shows the block diagram for the power flows in the superconductor when there are an applied rf drive and optical illumination. Assuming the light is normally incident on the superconductor, the optical power absorbed by the system is

$$P_{\rm opt} \;= \varepsilon I_{\rm opt} A, \tag{2.96}$$

where ε is the emissivity of the aluminum film, $I_{\rm opt}$ is the incident optical intensity, and A is the illuminated area of the resonator. In the steady state, this optical power must equal the power transferred to the phonon distribution $n(\Omega)$ by $n_{\rm opt}$,

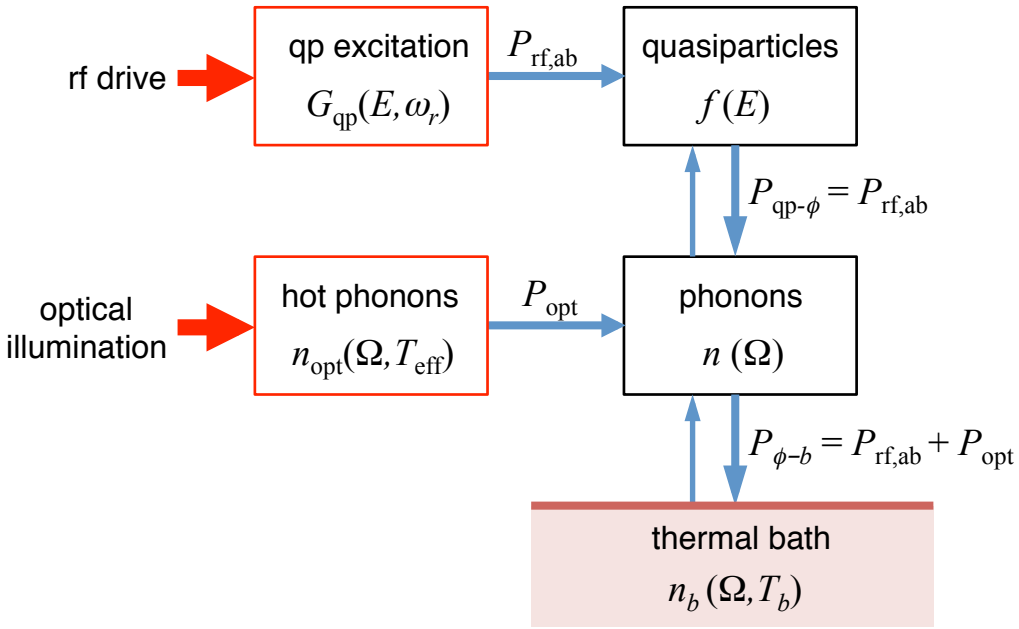

Figure 2.19: Block diagram showing the power flow in the quasiparticle-phonon system under rf drive and optical illumination.

which is given by

$$P_{\rm opt}(T_{\rm eff}) = V\int_0^\infty d\Omega\, D(\Omega)\,\Omega\,\frac{n_{\rm opt}(\Omega,T_{\rm eff})}{\tau_e}. \tag{2.97}$$

With the addition of the phonon generating term, the numerical simulation proceeded as detailed in the previous section to find $f(E)$, $n(\Omega)$, σ_1 and σ_2. I typically choose a starting $f(E)$ distribution that was thermal with a temperature T_b and $T_{\rm eff}$. For $n(\Omega)$, I choose $n_b(\Omega,T_b) + n_{\rm opt}(\Omega,T_{\rm eff})$ as an initial distribution. Figure 2.20 shows $f(E)$ and $n(\Omega)$ using the parameters listed in Table 2.1, and temperatures $T_b = 50$ mK and $T_{\rm eff} = 280$ mK. Examination of Fig. 2.20 reveals a jump in $n(\Omega)$ at $\Omega = 2\Delta$ and a jump in $f(E)$ at $E = 3\Delta$. The nonequilibrium $n(\Omega)$ distributions appear to follow the thermal distribution with $T = T_{\rm eff}$ closely for energies $\Omega > 2\Delta$, especially for lower $P_{\rm rf}$. A similar behavior is seen for $f(E)$

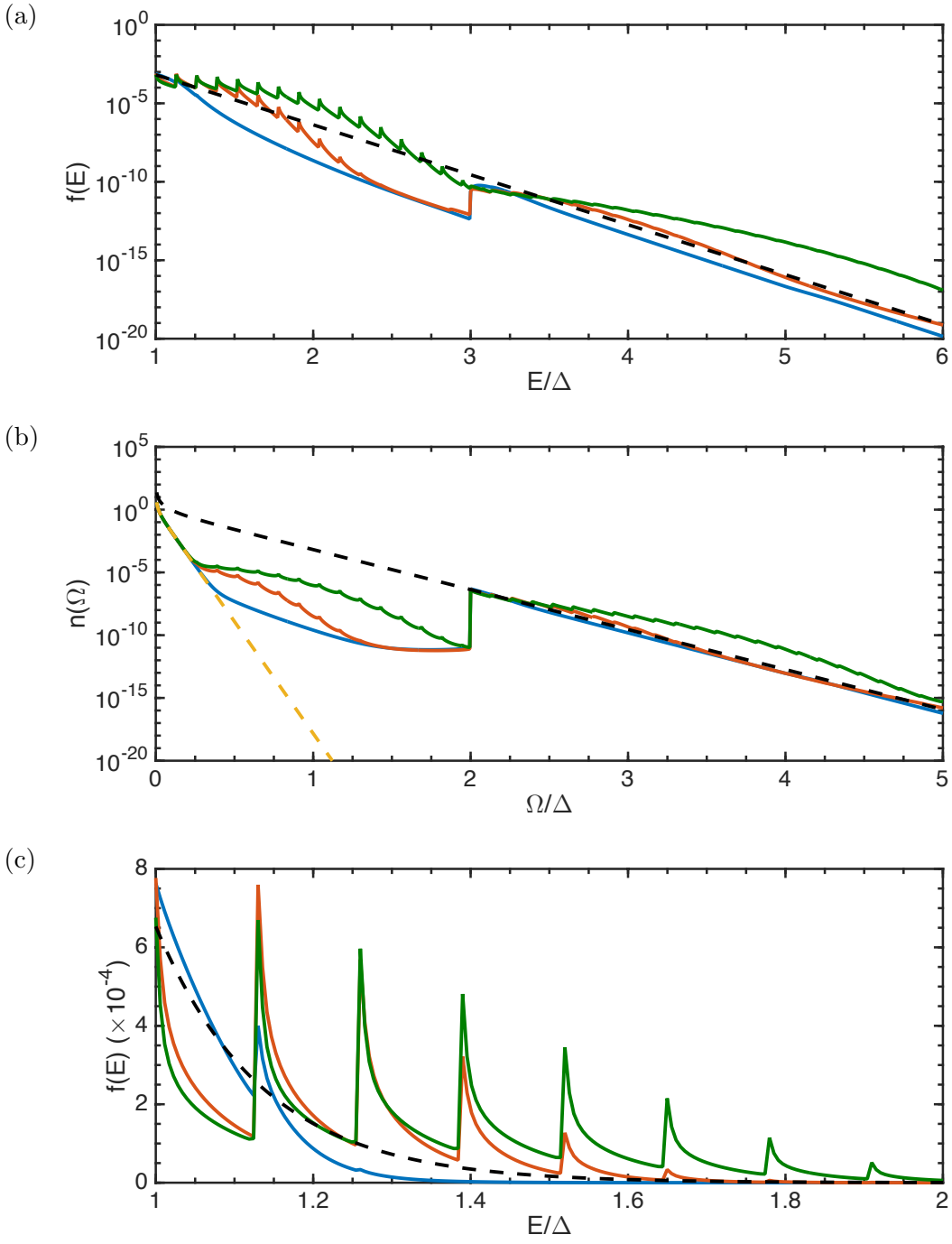

Figure 2.20: (a) Simulated quasiparticle distribution $f(E)$ vs normalized energy E/Δ and (b) simulated phonon distribution $n(\Omega)$ vs normalized energy Ω/Δ using the illumination model with bath temperature $T_b = 50$ mK, effective temperature $T_{\text{eff}} = 280$ mK, and rf drive powers P_{rf} of -100 dBm (blue curve), -80 dBm (red curve), and -72 dBm (green curve). Other parameters are shown in Table 2.1. The yellow dashed curve is the thermal distribution for $T = 50$ mK and the black dashed curve is the thermal distribution for $T = 280$ mK. (c) Linear plot of $f(E)$ between $E = \Delta$ and $E = 2\Delta$.

for $E > 3\Delta$. Comparison with Figs. 2.16 and 2.17 supports the conclusion that the jumps are mainly due to the discontinuity in $n_{\rm opt}$ at $\Omega = 2\Delta$, while pair breaking and recombination contribute to a lesser extent, as discussed previously for the no illumination case.

2.3.6 Using Simulation to Fit Data

It turns out some additional complications arise when the nonequilibrium model with rf drive and illumination is used to fit data. To fit to real data, I first need to assume initial values for all of the model parameters. In the simulations, $P_{\rm rf,ab}$ is calculated using Eq. 2.20 and 2.89. However to complete this calculation I need Q_i, but Q_i is what I am trying to find in the simulation. To proceed, I used the measured values of $P_{\rm rf}$, Q, Q_i, and Q_e, while Q_0 (see Eq. 2.20) was a fit parameter and I assumed $1/Q_{\rm TLS} = 0$. I performed the simulation for a range of $P_{\rm rf}$, T, and $I_{\rm opt}$, and then compared the results to the measured value of $1/Q$ and $\delta f_r/f_r$. In general, the input Q_i and output Q_i will differ unless all the parameters are chosen correctly. I then adjusted one or more of the parameters and repeated the entire process to fit the model to the data.

For the range of optical intensities $I_{\rm opt}$ and rf powers $P_{\rm rf}$ I used (see Chapters 4 and 5), the effective temperature $T_{\rm eff}$ and inverse quality factor $1/Q$ increased with increasing $I_{\rm opt}$, while the resonance frequency ω_r decreased with increasing $I_{\rm opt}$. For the same $I_{\rm opt}$, $1/Q$ decreases with increasing $P_{\rm rf}$. I discussed the reason for this decrease, but the detailed behavior of the distributions and $1/Q$ are different. I will

discuss them in my discussion of my data in more detail in Chapter 5.

I note here that my model for optical illumination is still relatively simple in its treatment of optical effects. I believe this picture can be improved using a more complete model that includes, among other things, the optical photon energies and the time dynamics of quasiparticles and phonons after photon absorption. However, as I will show in Chapters 4 and 5, this model appears to explain our results very well.

2.4 Other Sources of Loss

In addition to TLSs and quasiparticles, there are other sources of loss in superconducting resonators and qubits. I briefly discuss some of the sources below.

2.4.1 Other Microwave Lines

A resonator may couple to input/output lines, bias line, or other external lines, whether those lines are added intentionally (*e.g.* flux or other bias lines) or unintentionally. If the line is known to be present, it should be included in the external quality, *i.e.*

$$\frac{1}{Q_e} = \frac{1}{Q_{\rm in}} + \frac{1}{Q_{\rm out}} + \frac{1}{Q_{\rm line}}, \tag{2.98}$$

where $Q_{\rm line}$ is the coupling quality factor to this external line. If the resonator is capacitively coupled to this line with capacitance $C_{\rm line}$, I can use a similar definition to the definition of $Q_{\rm in}$ and $Q_{\rm out}$ (Eqs. 2.16 and 2.17) and write

$$\frac{1}{Q_{\rm line}} \equiv \omega_0^3 C_{\rm line}^2 L Z_0. \tag{2.99}$$

If the line is not explicitly included in Q_e, the additional loss it causes may be attributed to an unknown internal loss mechanism.

2.4.2 Other Microwave Modes

A resonator or qubit may also couple to additional microwave resonance modes in the system. For example, in my system the resonator is embedded inside a 3d cavity which has many microwave modes. All of these modes of the 3d cavity can couple to the resonator. I can define g as the coupling strength between the two modes, ω_r as the frequency of the resonator, ω_c as the frequency of the cavity mode, and $\Delta\omega = \omega_c - \omega_r$ as the detuning between the two modes. When the coupling between the modes is strong, that is $g > |\Delta\omega|$, the two modes cannot be considered independent. In this case, the measured frequencies would be the eigenmodes of the coupled system. By making a two-level approximation, the eigenvalues can be found by diagonalizing the matrix

$$\begin{pmatrix} \omega_r & g \\ g & \omega_c \end{pmatrix} = \left(\frac{\omega_r + \omega_c}{2}\right)\mathcal{I} + \begin{pmatrix} -\Delta\omega/2 & g \\ g & \Delta\omega/2 \end{pmatrix}, \tag{2.100}$$

where $\mathcal{I}$ is the 2×2 identity matrix. The eigenmodes $\omega_\pm$ are then given by

$$\omega_\pm = \left(\frac{\omega_r + \omega_c}{2}\right) \pm \sqrt{(\Delta\omega/2)^2 + g^2}. \tag{2.101}$$

To calculate the quality factor of the coupled modes, a similar calculation can be done with the loss components. The quality factor of each eigenmode then is found to depend on both the quality factor of the cavity and resonator.

When the coupling is weak, $g \ll |\Delta\omega|$, the modes can be considered independent with a small correction factor. The modified resonator frequency ω_r' and the

modified cavity frequency ω_c' are then given by

$$\omega_r' = \omega_r - \frac{g^2}{\Delta\omega} \tag{2.102}$$

$$\omega_c' = \omega_c + \frac{g^2}{\Delta\omega}. \tag{2.103}$$

In this regime, loss from the cavity contributes an additional component to the resonator loss. This is called the Purcell effect and was discovered by Purcell in spontaneous emission rates [159]. If γ_{cavity} is the decay rate of the cavity then the Purcell decay rate γ_{Purcell} is given by [160]

$$\gamma_{\text{Purcell}} = \left(\frac{g}{\Delta\omega}\right)^2 \gamma_{\text{cavity}}. \tag{2.104}$$

Since $\gamma = \omega/Q$, then if Q_{cavity} is the quality factor of the cavity, the Purcell quality factor Q_{Purcell} is given by

$$\frac{1}{Q_{\text{Purcell}}} = \left(\frac{g}{\Delta\omega}\right)^2 \frac{\omega_c}{\omega_r} \frac{1}{Q_{\text{cavity}}}. \tag{2.105}$$

The experiments I describe in Chapters 4 and 5 were in the weak coupling regime $g \ll |\Delta\omega|$. Also, I found that the quality factor of the fundamental mode my 3d cavities was independent of rf drive power for applied rf power P_{rf} in the range of about -110 dBm to -50 dBm. Hence in my system, I typically assumed the cavity mode contribution to resonator or transmon loss was rf power independent and relatively weak. Of course, there are many cavity modes, not just the fundamental mode, and they can contribute to resonator or transmon loss as well.

2.4.3 Trapped Vortices

Magnetic flux vortices trapped in a superconducting film can magnetically couple to the resonator and cause additional loss and frequency shift [85]. Vortices can be trapped in the superconducting film of the resonator if it is cooled below T_c in an ambient magnetic field, or if a strong enough magnetic field is applied to the resonator even for a brief amount of time. Several well-known methods has been used to mitigate vortex loss. These methods include introducing narrow slots [161] or holes [162, 163] in the superconducting films which in effect trap the vortices, and better magnetic shielding of devices to reduce the number of trapped vortices.

More recently, Nsanzineza and Plourde managed to trap a single vortex at the current antinode of a coplanar waveguide resonator [164] and found that the vortex did not induce an additional loss because the coupling between the vortex and the resonator was very weak. In fact, they reported a reduction in loss which they attributed to the vortex acting as a quasiparticle trap that produced a net decrease in the quasiparticle density near the vortex.

2.5 Summary

In this chapter, I discussed the circuit representation of an LC resonator. Using circuit analysis, I derived the transmission S_{21} as a function of frequency. I also defined the internal and external quality factors in terms of the circuit model parameters. I then described sources of loss in superconducting resonators, and focused on the two main loss sources: TLSs and quasiparticles. I described the physical model

of a TLS, and how a single TLS and an ensemble of TLSs contribute to loss. I then discussed loss due to quasiparticles, including how an rf drive and optical illumination affects quasiparticles. I introduced a nonequilibrium quasiparticle model and described how to simulate the effects of rf drive and illumination. Finally, I briefly described other sources of loss in resonators, including trapped vortices and loss due to coupling to microwave lines and other microwave modes.

Chapter 3: Experimental Details: Resonator

In this chapter, I describe the experimental details for experiments in which I applied optical illumination to a thin-film superconducting microwave resonator. I discuss the design choices and fabrication steps for building the resonator, the design choices and machining steps for the 3d cavity in which the resonator is mounted, and the wiring setup for the microwave lines and the optical illumination line. Finally, I discuss how I subtract the background from the raw data and how I fit the resonance to extract the resonance parameters.

3.1 Resonator Design Considerations

As discussed in Chapter 1, to achieve strong coupling between trapped atoms and a resonator we need a resonator with a high quality factor Q and strong magnetic field to couple to the magnetic moment of the atoms. A strong magnetic field can be achieved by having a small magnetic mode volume of the resonance. Additionally, we also would like the resonant frequency to be near the 6.83 GHz Rb resonance, although this is more essential for a proof of principle experiment.

There are many different physical arrangements to make a superconducting resonator, but not all of them are viable candidates for use in the proposed hybrid

system. For example, superconducting and normal metal 3d cavities recently became popular due to long coherence times achieved by superconducting qubits mounted inside 3d cavities [49, 165]. 3d cavities made from aluminum can reach internal quality factor $Q_i > 10^6$ at base temperature [49, 166]. However, due to the large volume of the cavity ($\sim$ 5000 mm^3) and the fact that the electric and magnetic fields are spread out over the cavity volume, the magnetic field is too small to achieve strong coupling. As discussed in Section 3.3, we will still use a 3d cavity in the experiment, but this is not the resonator for a hybrid system. Instead, the resonators for a hybrid system will be mounted inside a 3d cavity.

Another commonly used resonator design for superconducting qubits is a coplanar waveguide (CPW) resonator [36]. A CPW resonator typically consists of a single superconducting strip, surrounded by ground plane and coupled to microwave drive typically by capacitive coupling. The resonant frequency is determined by the length of the line. CPW resonators have both electric and magnetic field spread over the entire length of the resonator, with the fields confined between the center strip and ground plane. A 7 GHz $\lambda/2$ CPW resonator has a typical mode volume of $\sim 10^{-3}$ mm^3, which is about 10^6 times smaller than the mode volume of a 3d cavity with a 7 GHz TE$_{101}$ mode frequency.

We chose to use lumped-element LC resonators, described in Ch. 2. Multiple groups have studied the loss characteristics of lumped-element resonators [132, 138], and Ben Palmer's group at LPS have used lumped-element resonators in superconducting qubit readout [167]. Lumped-element resonators have well defined inductors and capacitors, the magnetic field is concentrated in the inductor and the electric

field is concentrated in the capacitor. The inductor may have some self-capacitance, and the capacitor may have some self-inductance, but as shown by de Visser *et al.* they constitute only small percentage of the total capacitance and inductance [132].

The resonators used in some of my measurements were originally designed by Zaeill Kim for the resonator tuning experiment [104]. Zaeill designed the resonators to have a resonance frequency $f_r = \omega_r/2\pi \approx 6.7$ GHz, so that he could tune it up to the ^{87}Rb hyperfine splitting frequency of 6.83 GHz using the tuning pin. He also found the expected resonant frequency from Microwave Office simulations [168]. The initial design was a conventional lumped-element planar resonator, embedded inside a ground plane and coupled to microwave drive by transmission line (Fig. 3.1). The interdigitated capacitor had 40 fingers, with a 5 μm finger width and gap, and a finger length of 50 μm. The meandering inductor had a line width 5 μm and a total line length of about 4 mm. The resonators were fabricated with several design variations. By varying the length of the last finger, the resonant frequency was varied slightly. All the resonators in the mask were coded MWX-Y, where X was a number representing the variant of the resonator and Y was a number representing the position in the mask. A separate mask was also made for the gold alignment marker.

3.2 Resonator Fabrication

Zaeill performed the initial fabrication steps [130], which were as follows. 215 nm Al was deposited on a 3-inch sapphire wafer using the thermal evaporator at

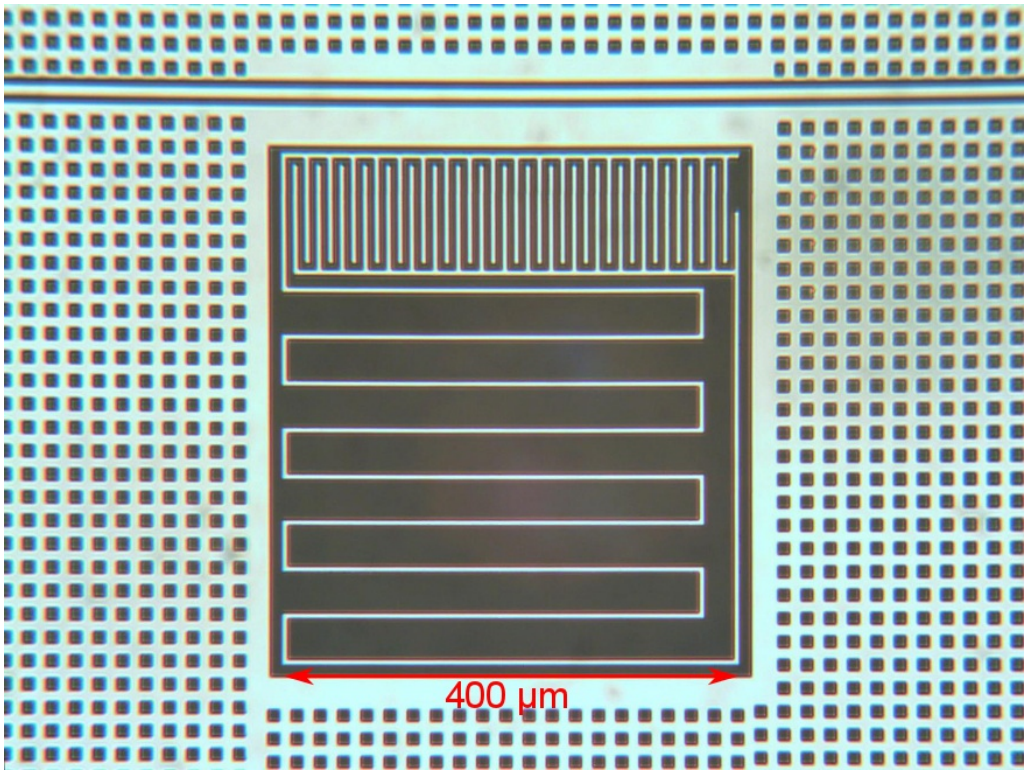

Figure 3.1: Photograph of LC resonator MW2-14 as fabricated by Zaeill Kim before ground plane etching. The light area is Al, the dark area is sapphire substrate. This resonator was used in the experiments described in Chapters 4 and 5.

LPS, followed by depositions of Ti (for adhesion layer for Au) and Au (for alignment marker). After spinning and patterning layer a of photoresist using photolithography, the metal was wet etched away. After spinning a protective photoresist layer, the wafer was then diced into 5 mm $\times$ 5 mm chips and stored for safe keeping.

Starting with a single resonator chip, I needed to remove all the metal except the resonator itself. Jared Hertzberg, Kristen Voigt, and I developed the process and the three of us alternately performed the fabrication described below in the Fablab clean room in the Kim Engineering Building.

First, we removed the protective resist on the chosen chip by placing it in a beaker of remover PG [169] heated to 95°C for 15 minutes. We then rinsed with isopropyl alcohol (IPA), then with DI water, and finally dried the chip using N_2. To ensure that there was no water remaining on the surface of the chip, the chip was then pre-baked on a hot plate at 130°C for 10 minutes. After baking, we set the chip on the spinner, and made sure the chip was centered. If the chip is slightly off center it can cause the chip to detach while spinning. We applied HMDS (hexamethyldisilazane) on the chip and spun at 4000 rpm for 60 s. The purpose of the HMDS layer was to improve adhesion between the substrate surface and photoresist. We then applied Shipley S1813 photoresist, and spun at 4000 rpm for another 60 s. Since the chip was small and square shaped, beads of thicker photoresist tend to form on the corners of the chip. We used a razor blade to remove the corner beads. We then soft baked the chip on a hot plate at 95°C for 5 minutes.

To hold the chip during patterning, we taped the chip on a microscope slide. We initially used white clean room tape, however we observed that the chip could

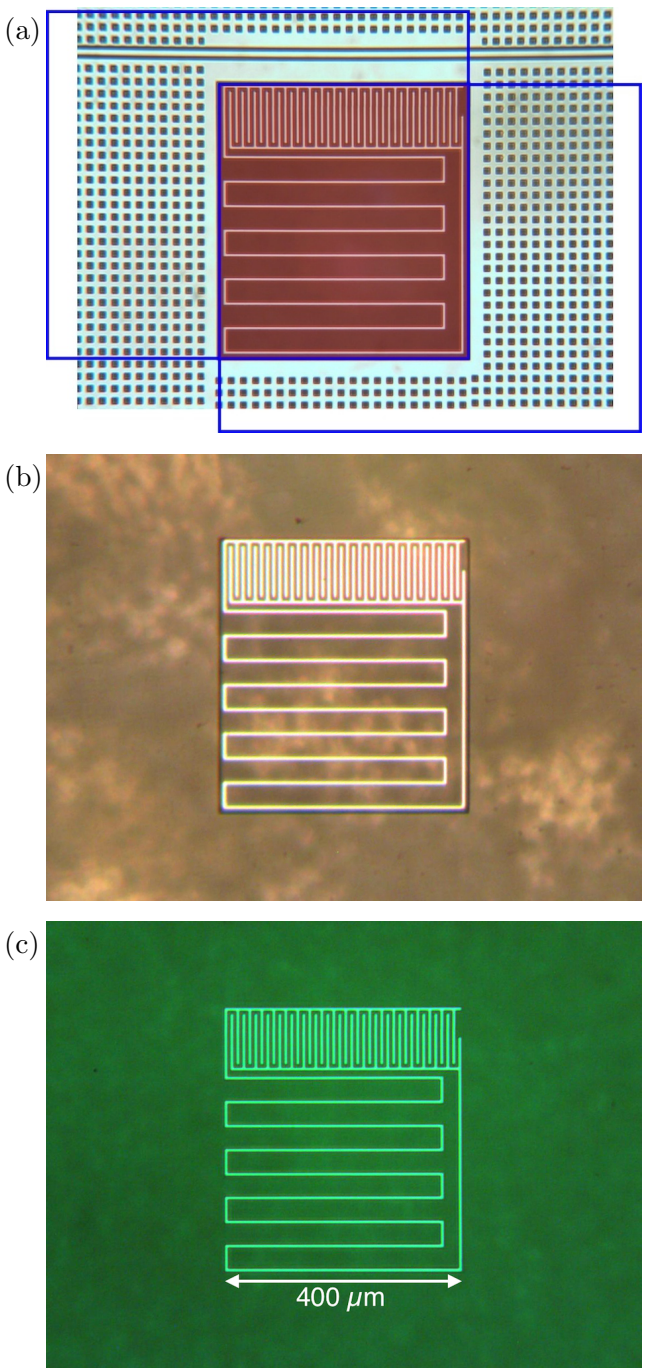

Figure 3.2: Photograph of LC resonator MW2-14 at different fabrication steps: (a) Before resist spin and exposure. The two blue rectangles are approximate position of rectangular structure in photomask during exposure. The resist will remain in the overlap region between the two rectangles (shaded red area). (b) After metal etching. The rectangle around the resonator is the photoresist. (c) After removing photoresist layer.

still move during alignment and exposure, resulting in generally poor alignment. We found that double sided Cu tape fixed the alignment issue, although more work was needed to clean the chip's back surface. We repurposed an older photomask (DS10_nitrite_10/12/2010) from previous phase qubit experiments [31, 170] in the photolithography process. Before putting the mask on the mask aligner, we cleaned the mask with acetone, methanol, IPA, followed by DI water, and then dried the mask with N_2.

To pattern, we mounted the chip and the mask on a Karl Suss MJB-3 Mask Aligner that let us align the resonator structure to a dark rectangular pattern on the mask (see Fig. 3.2(a)). The structure has dimensions of 1000 μm $\times$ 600 μm, which is larger than the size of the resonator. As a result, we aligned twice and exposed twice for 10 s, with the alignment as shown in Fig. 3.2(a), so that all regions except the resonator was exposed to light.

We developed the resist using Shipley 352 developer for 45 s, then rinsed it using DI water, and finally dried with N_2. We next examined the chip under an optical microscope to check the alignment. We wanted the resonator to still be completely covered by photoresist and no resist layer above the ground planes. If the alignment was not good, we removed the photoresist using acetone and DI water and started over. If there were no issues, we proceeded to etch the metal.

For the etching step, we first prepared two large beakers by filling them with DI water for rinsing. We started by etching the Al layer using Transene Al Etchant Type A [171]. We kept the chip in the etchant until all the exposed Al was etched away; this usually took about 9 minutes. We then quickly put the chip in the first

water beaker. After 3 minutes, we transferred the chip to the second beaker, keeping it there for another 3 minutes, after which we dried the chip using N_2. This was followed by etching Au layer using Transene TFA Etchant [171] for 60 s, and then etching Ti layer using Transene TFT Etchant [171] for 15 s. After each etch, we rinsed the chip with DI water using the process described above. We then removed the remaining photoresist layer by putting the chip in Remover PG heated to 95°C for 7 minutes, followed by our standard rinsing and drying process.

Finally, we cleaned the adhesive from the back of the chip using acetone applied on swabs, followed by the standard rinsing process. If acetone did not completely remove the adhesive, we put the chip in Remover PG heated to 95°C for about 10 minutes, followed by another rinsing. Once this was done, the chip was stored for safe-keeping in a dry box until it was ready to be put in the cavity.

The chip used in the experiment described in Chapters 4 and 5 was device MW2-14. It was first built in 2011, the ground plane was removed in July 2013, and it was stored for several days before being put into the cavity.

3.3 3D Cavity

Similar to the setup used by 3d transmons [49], we mounted the resonator inside a 3d cavity. A cavity and transmon can couple strongly and create a Circuit QED system [36, 172], with an approximate Jaynes-Cummings Hamiltonian [129]. For the experiments in Chapters 4 and 5, we used the cavity to couple microwave input and output lines to the resonator. Due to the resonator's small size compared

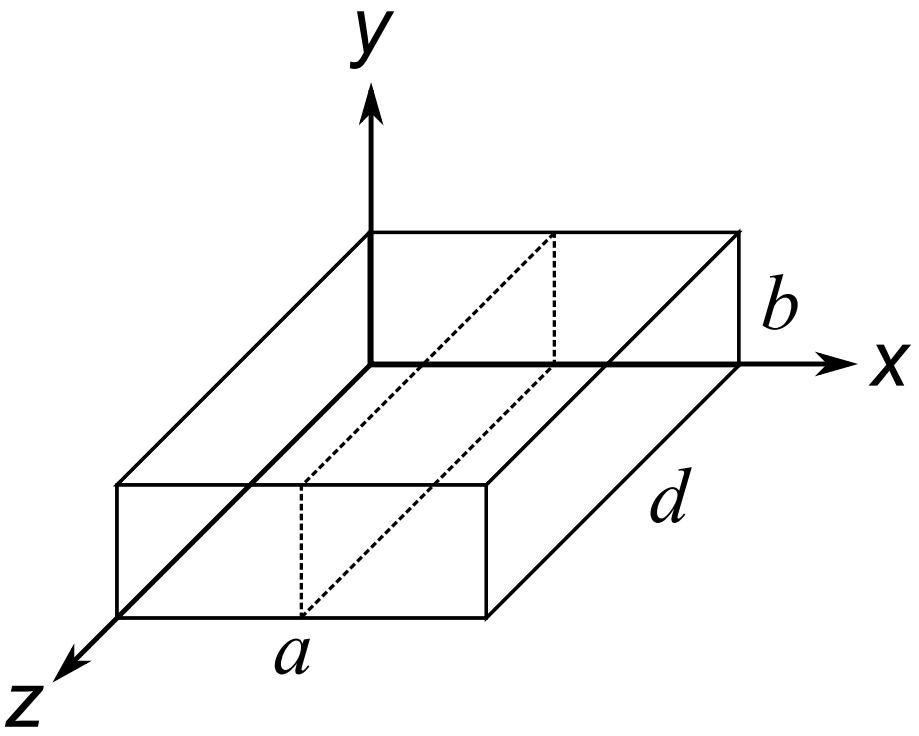

Figure 3.3: Illustration of a 3d cavity with the dimensions labeled a, b, and d following Pozar [173]. The dashed rectangle represent where the cavity separates into two halves.

to a typical transmon size, the coupling was expected to be very weak and we could treat the cavity and resonator as effectively independent modes.

In the following discussion of the modes of a 3d cavity, I follow Pozar [173] closely. I define the inner dimensions of the cavity as a along the x-axis, b along the y-axis, and d along the z-axis, with $b < a < d$ (as shown in Fig. 3.3). The resonant modes of the electric field $\vec{E}$ and magnetic field $\vec{B}$ reside inside the cavity are determined by solving the Maxwell's equations and imposing boundary conditions for the fields for all cavity surfaces, which result in standing wave behavior of the fields. The modes inside the cavity include the TE_{mnl} and TM_{mnl} modes, where m, n, and

l indicate the indices in x-, y-, and z-axes respectively. The TE (transverse electric) modes have no electric field component along the z-axis, i.e $E_z = 0$. Similarly the TM (transverse magnetic) modes have $B_z = 0$. The frequency of the TE_{mnl} and TM_{mnl} modes are given by [173]

$$f_{mnl} = \frac{c}{2\sqrt{\mu_r \epsilon_r}} \sqrt{\left(\frac{m}{a}\right)^2 + \left(\frac{n}{b}\right)^2 + \left(\frac{l}{d}\right)^2}, \tag{3.1}$$

where c is the speed of light, and μ_r and ϵ_r are the relative permittivity and permeability of the dielectric inside the cavity, respectively. My cavity was filled with vacuum or air, and thus $\mu_r = 1$ and $\epsilon_r = 1$. The actual cavities usually had rounded edges instead of sharp edges, but this has only a small effect on the mode frequencies. The lowest mode of the cavity, and the mode that we mainly care about is the TE_{101} mode, and using Eq. 3.1 the frequency of this mode is given by

$$f_{101} = \frac{c}{2}\sqrt{(1/a)^2 + (1/d)^2}. \tag{3.2}$$

When a chip is put in the middle of the cavity, due to the higher ϵ_r of the substrate (sapphire has $\epsilon_r \approx 10$) the frequency will be shifted down by a small amount Δf_{101},

$$\Delta f_{101} \approx 2 f_{101} (\epsilon_r - 1) \frac{V_{\mathrm{chip}}}{V_{\mathrm{cav}}} \tag{3.3}$$

where V_{chip} is the volume of the chip and $V_{\mathrm{cav}} \equiv abd$ is the volume of the cavity. This correction can be estimated using cavity perturbation theory [173] or finite element field solvers.

The 3d cavity I used in the experiment is described in Chapters 4 and 5 was Cavity SI-1 "Space Invaders", due to the similar appearance to the aliens in the video game with that name [174]), and it was made from Al-6061 alloy. I initially

(a)

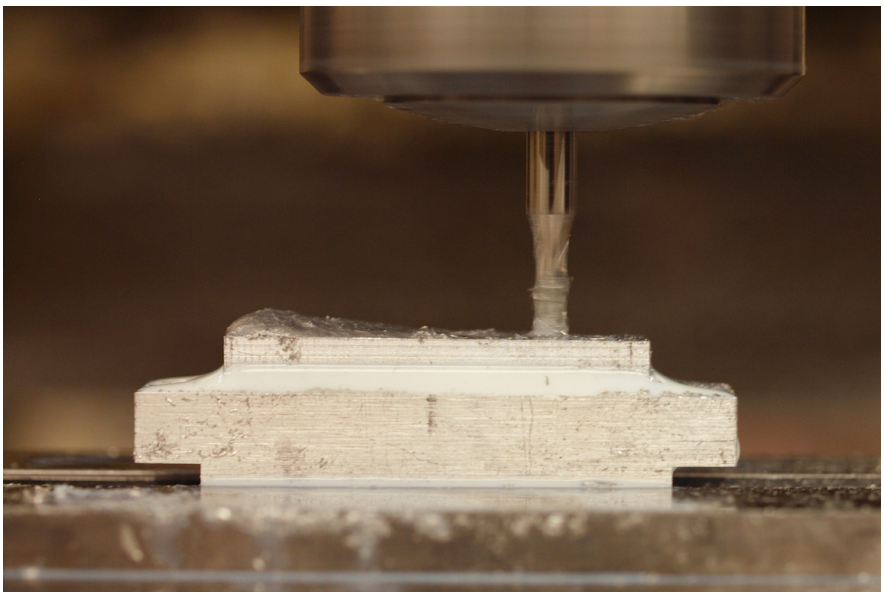

(b)

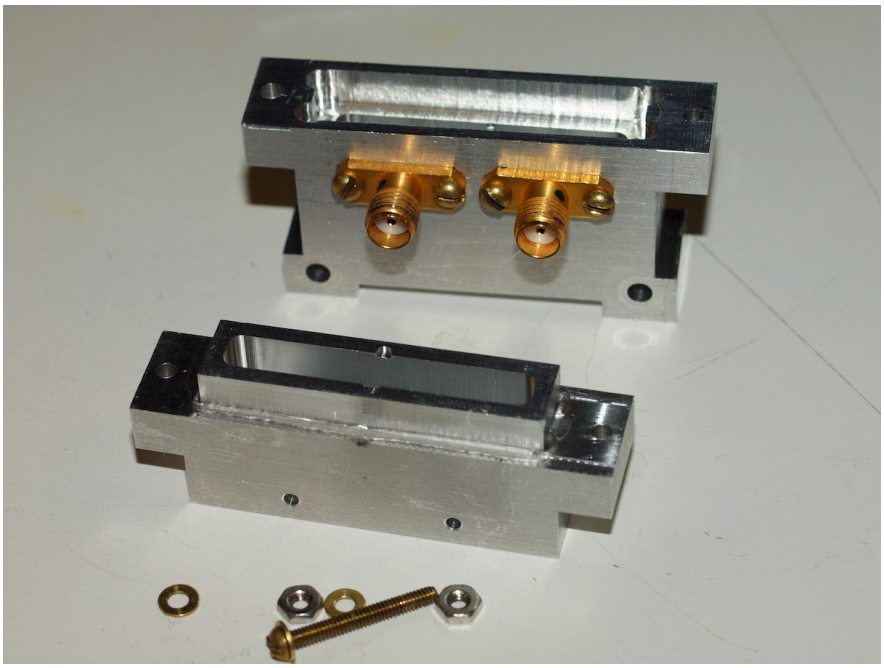

Figure 3.4: Cavity SI-1 at different steps during machining. (a) Milling of the cavity space. (b) After milling of the upper and lower halved of the cavity. The SMA terminal connectors are attached on the upper half of the cavity.

designed the cavity to have the dimensions $a = 1.0$ inch $= 25.4$ mm, $b = 5$ mm, and $d = 1.4$ inch $= 35.6$ mm, which gave the expected TE_{101} mode frequency of $f_{101} = 7.25$ GHz. Cody Ballard machined the cavity in the Physics Student Machine Shop. Unfortunately $b = 5$ mm was slightly too large to hold a resonator chip in the standard orientation, where two of the sides of the chip sit between the two sides of the cavity. Instead, I rotated the chip by 45 degrees so that two corners were on the two sides of the cavity and Cody milled a slot for the chip for this orientation (see Fig. 3.6). The center of the chip was located roughly at center of the cavity, where the electric field is strongest and there is no magnetic field for the lowest mode. Finally, Cody also drilled holes for mounting the input and output pins that couple the cavity to the microwave lines. Once this was done, Cody and I cleaned the cavity by first washing it with water and soap, followed by a bath of acetone with sonication for several minutes. We considered cleaning it further using an electropolish, but decided not to.

I connected the cavity to input and microwaves line by attaching SMA terminal connectors (typically from Pasternack [175]) to the outside of the cavity (see Fig. 3.4(b)). Each connector has a pin that extended inside the cavity, coupling the line to the cavity. The coupling strength is determined by the position and the length of the pins. The connectors were attached to the surface parallel to the $x - z$ plane, roughly at $x = a/2$ and $z = d/4$ for the first pin and at $x = a/2$ and $z = 3d/4$ for the second pin (see Fig. 3.3). Both pin locations are in between the node and antinode of the TE_{101} mode, at the antinode of the TE_{102} mode, and at the node of the TE_{201} mode, where the electric field is zero. This should result in

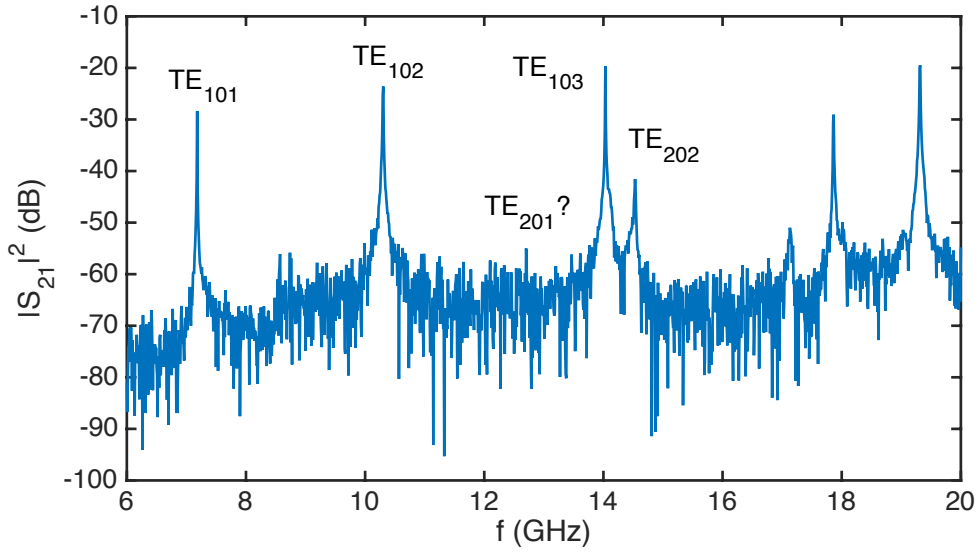

Figure 3.5: $|S_{21}|^2$ vs applied frequency f of cavity SI-1 (before shaving part of lip) at room temperature. Several of the lowest modes are labeled. The TE_{201} mode, which is expected to be at 12.5 GHz is not seen.

relatively strong coupling to the TE_{102} mode, almost no coupling to the TE_{201} mode, and moderate coupling to the TE_{101} mode, which is the lowest frequency mode. I adjusted the input and output coupling by adjusting the length of pins, with longer pins give stronger coupling. I tried using several different connector models, with different pin lengths and diameters. All of the connectors came with the pins partially surrounded by teflon, I usually removed the teflon, as it is a lossy dielectric, using a razor blade. For smaller pin diameters, fine adjustments could be done by cutting the pin length using a wire cutter, or increasing the length by soldering a small wire to the pin.

Figure 3.5 shows a log plot of $|S_{21}|^2 = P_{\text{out}}/P_{\text{in}}$ versus frequency for cavity SI-1 from 6 GHz to 20 GHz. This trace was taken at room temperature using an Agilent

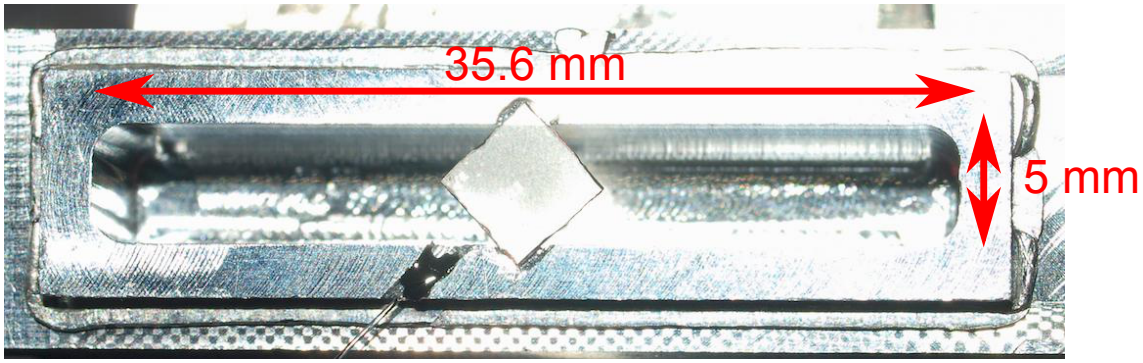

Figure 3.6: Lower half of cavity SI-1 with test chip mounted upside down in the cavity. At the center of the chip the resonator can be seen. To the lower left of the chip one of the optical fibers used in the illumination measurements can be seen.

E5071C vector network analyzer (VNA), discussed in detail in the next section. For this measurement, no chip was inside the cavity. Several of the modes are labeled. The TE_{101} mode was located at 7.18 GHz, close to the expected value. We also saw a strong peak for the TE_{102} mode at 10.3 GHz, but we didn't see a peak at the expected TE_{201} peak at 12.5 GHz. This was consistent with the expected coupling strengths to the different modes, as discussed in the previous paragraph.

Putting a 5 mm $\times$ 5 mm $\times$ 0.5 mm sapphire chip inside the cavity typically brings the TE_{101} mode frequency down by about 200 MHz to about 7.0 GHz, in addition to some reduction in quality factor. Since the 7.0 GHz shifted frequency could have ended up very close to the expected resonator frequency of 6.7 GHz, we decided to increase the TE_{101} mode frequency by reducing the cavity volume. To do this, Cody shaved 0.1 inch of aluminum from the lip where the two halves of the cavity connect, resulting in $a = 0.9$ inch and the expected TE_{101} mode frequency of about 7.8 GHz without a chip, and 7.6 GHz with a chip. This change also resulted

in the chip being slightly off-center.

For the experiment described in Chapter 4 and 5, I chose the pins such that the cavity TE_{101} mode had approximately balanced input and output coupling, $Q_{\mathrm{in,cav}} \approx Q_{\mathrm{out,cav}} \approx 2.6 \times 10^5$ so the external quality factor was $Q_{\mathrm{e,cav}} = (1/Q_{\mathrm{in,cav}} + 1/Q_{\mathrm{out,cav}})^{-1} \approx 1.3 \times 10^5$. To accommodate optical fibers, Cody drilled some additional holes through the cavity walls (see Section 3.5). I observed no major effect on the mode frequencies and quality factors with the addition of the holes.

To mount a chip in the cavity, I placed the chip on the slot and secured the corners with chunks of indium wire (see Fig. 3.6). The chip was mounted upside down such that the chip was directly illuminated from one of the fibers (see Section 3.5) instead of through the sapphire substrate. I then placed a ring of indium wire on the base of the inner lip, to act as an rf-tight gasket and reduce gaps between the two halves. Finally, I attached the two halves of the cavity and secure them tightly.

3.4 Microwave Setup

Microwave wiring for the experiments described in Chapters 4 and 5 is shown in upper part of Fig. 3.7. Zaeill Kim installed many of the components at the beginning of the project, especially the ones inside the dilution refrigerator. The refrigerator is an Oxford Triton 200 cryogen-free refrigerator with a cooling power of 200 μW at 100 mK [176]. Jared Hertzberg, Kristen Voigt, Liam Fowl, and I made subsequent additions and modifications over time as needed for different experiments.

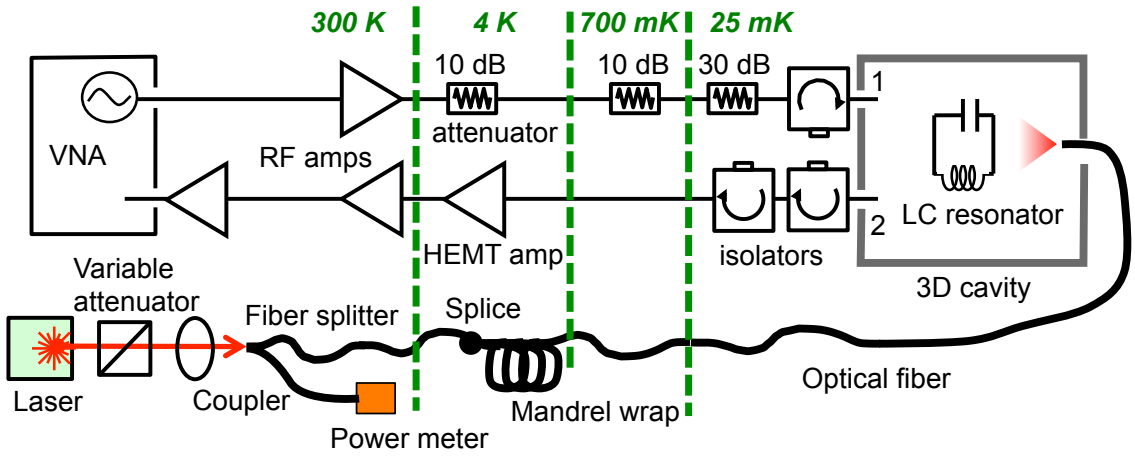

Figure 3.7: Diagram of microwave wiring (upper part) and optical wiring (lower part) wiring used in the optical illumination experiments.

Microwave signals were supplied by an Agilent E5071C Vector Network Analyzer (VNA) [177], with the range of possible frequencies between 300 kHz and 20 GHz and the range of possible powers between -85 and 10 dBm. The drive came out of port 1 of the VNA. In some experiments we wanted to supply higher powers to the resonator, and we connected the output of port 1 to an rf amplifier for this purpose. One we used was a Mini-Circuits ZX60-14012-L+ amplifier [178], with a wide bandwidth (300 kHz - 14 GHz), about 11-12 dB gain, and a 1 dB compression point of about 11 dBm. For even higher powers, we used a Mini-Circuits ZRON-8G+ amplifiers [178] with 2-8 GHz bandwidth, 20 dBm gain, and a 1 dB compression point of 20 dBm. From the VNA or amplifier output, the signal then goes to a flexible SMA coaxial cable to a SMA feedthrough port at the screen room wall. Inside the screen room the feedthrough connects to a long SMA coaxial cable to the top of the refrigerator, where it went to another feedthrough inside the refrigerator.

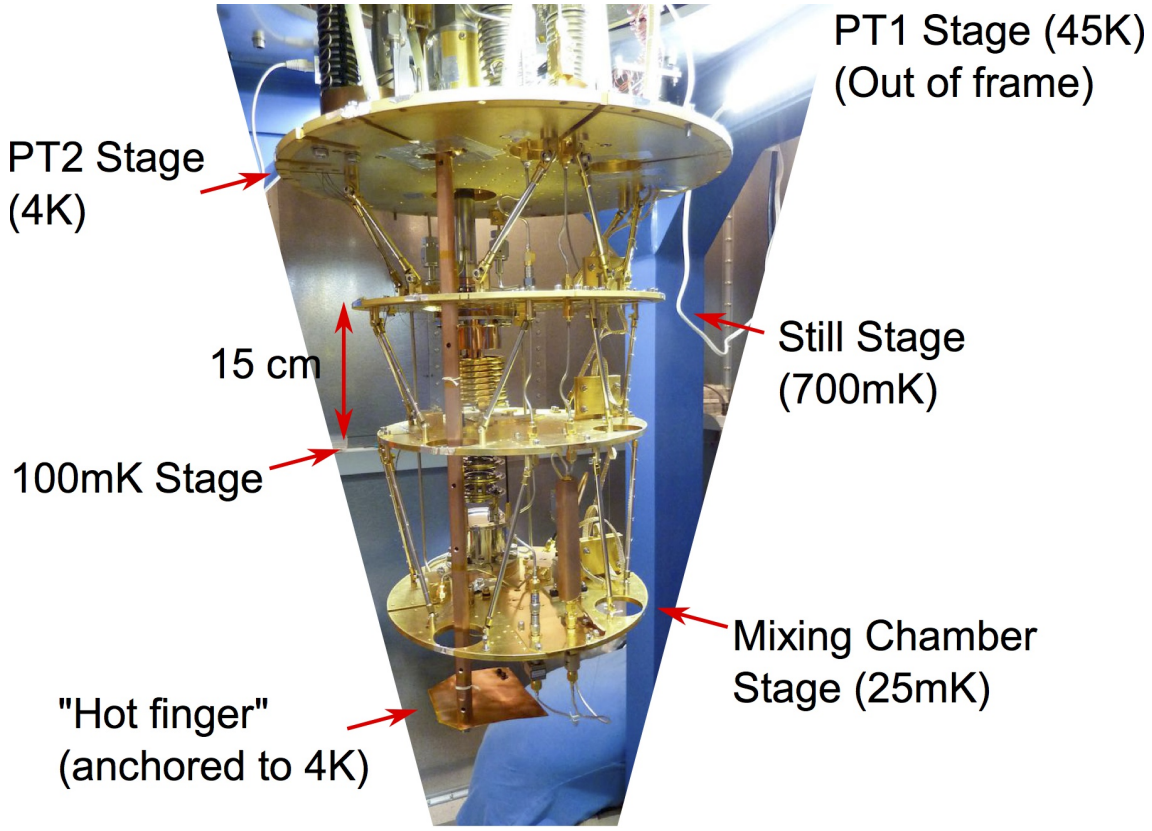

Figure 3.8: Picture of dilution refrigerator, with different temperature stages labeled. First pulse tube stage, at 45 K, is located just out of frame. A 'hot finger', anchored to 4K stage, was used for some separate heat load experiments, is placed under the mixing chamber.

The microwave line inside the fridge was separated into short segments between each temperature stage. Each segment consisted of a $\sim$ 0.2 m length of UT-85 SS/SS coaxial cable, with a stainless steel inner and outer conductors. This cable was chosen to reduce thermal links between stages because stainless steel has a relatively low thermal conductivity. Midwest Microwave cryogenic attenuators [179] were added between some of the segments, thermally anchored to the stages, to reduce Johnson-Nyquist noise. Specifically, 10 dB was located at the second pulse tube plate (at 4-5 K), 10 dB at the still stage (typically around 700 mK), and 30 dB total at the mixing chamber stage (at base temperature at 10-20 mK) (see Fig. 3.8). From the last attenuators we used a UT-85 Flexi coaxial cable, with silver-plated copper inner and outer conductors, to connect to a Pamtech CTH1365KS cryogenic isolator [180] mounted on the mixing chamber stage. In some cool downs we added a isolator because we were concerned about the presence of cable self-resonances from impedance mismatches in the lines. The isolator had a frequency range of 4-8 GHz and about 18 dB of isolation within this range. The output port of the isolator was connected directly to the input port of the 3d cavity, mounted on the mixing chamber stage. The total attenuation on the input line from the VNA to the cavity, not including the rf amplifiers, was about 65 dB around 6-7 GHz (see Fig. 3.9).

The output port of the cavity was connected to another set of cryogenic isolators at the mixing chamber by a segment of UT-85 Flexi coaxial cable. Here we used Pamtech CTH1409KS isolators [180] with a 4-8 GHz range and 18 dB isolation. The role of these circulators was to reduce noise and other stray microwaves coming down the output lines, without attenuating the output signal from the cavity. At 4

K stage, a high-electron-mobility transistor (HEMT) amplifier amplified the rf output from the cavity. The amplifier was a CITCRYO4-12A amplifier, made by the Weinreb group at Caltech [181], with frequency range 4-12 GHz, less than 5 K noise temperature, and maximum gain of about 32 dBm. Zaeill found that the HEMT tended to show self-oscillation behavior due to mismatched impedance outside of the circulator band width. To prevent self-oscillation, Zaeill added a 3 dB cryogenic attenuator at the input of the HEMT [130].

We used a Miteq AMF-3F-04000800-07-10P room temperature low-noise amplifier [182], located just on top of the fridge, to amplifiy the output signal from of the cavity. The amplifier has a 4-8 GHz frequency range and about 30 dB gain. The output signal then passed through a similar coax setup as the input line to reach the outside of the screen room. A Mini Circuits ZX60-14012L+ [178] provided the final 11 dB amplification before the signal went into port 2 of the VNA. The VNA then typically measures the complex transmission $S_{21} = V_2/V_1$ as a function of frequency.

The VNA was connected to a Stanford FS725 Rb Frequency Standard [183] at its 10 MHz input port to provide an accurate frequency calibration. A GPIB cable connected the VNA to a Dell Windows PC that has a National Instruments PCI-GPIB card [184]. This allows us to automate the data taking process (VNA setup and S_{21} readout) using either LabVIEW or Matlab. I mainly used a Matlab control program E5071C_multiplepowertraces_singlespan_header.m, which will be discussed in Section 3.6.

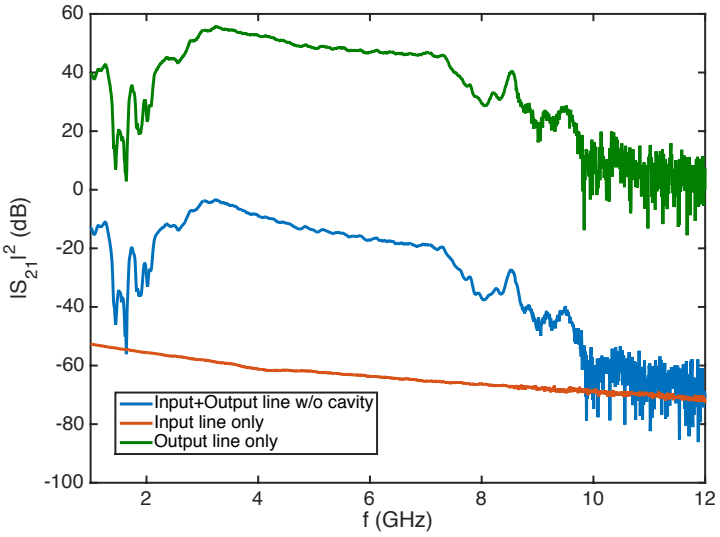

Figure 3.9: $|S_{21}|^2$ vs applied frequency f of microwave lines at room temperature. The value will differ somewhat when the refrigerator is in operation. No rf amplifier was used in the input line and the HEMT, Miteq, and Mini Circuits amplifiers were used on the output line.

3.5 Optical Illumination Setup

The lower part of Fig. 3.7 shows a simplified diagram for the optical illumination setup. Most of the setup outside the refrigerator was done by the people working on the atomic side of the Atoms on SQUIDs project, Jeff Grover, Pablo Solano, and Jon Hoffman.

We used a diode laser to supply light with 780 nm wavelength, one of the wavelengths needed for our ^{87}Rb atom trapping experiment [81, 83]. This light reflected off several mirrors mounted on an optical table and then passed through an acousto-optic modulator (AOM). The AOM allowed us to pulse the light (see Section 5.3.3 for example). To prevent thermal drifts, we set the AOM to a duty

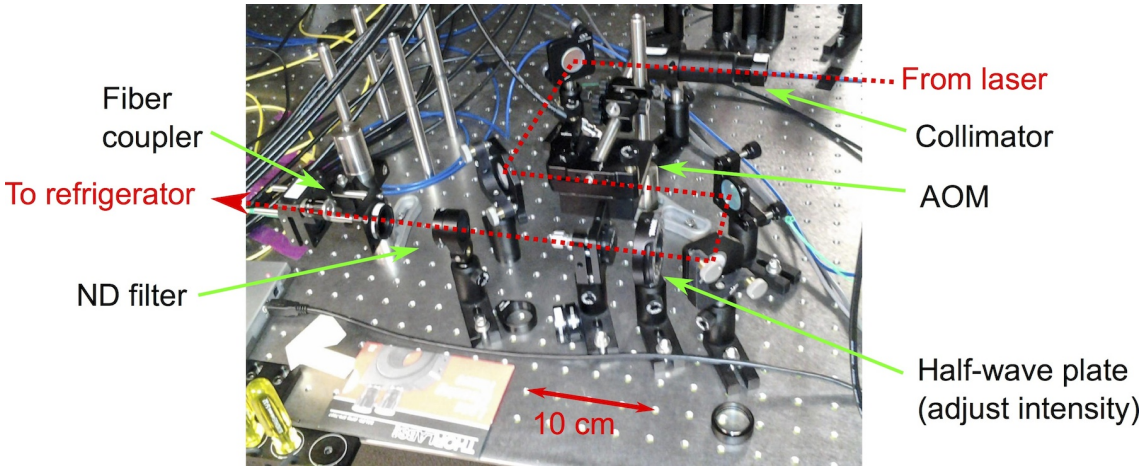

Figure 3.10: Photograph of part of the illumination line on the optical table. Red dotted line shows the path of the photons.

cycle that was about 90 % on. This required some adjustment in measurement timing. The pulse timing was controlled by a TTL signal from a Stanford DG535 pulse generator [183]. After the AOM, the light passed through a half-wave plate. We rotated the wave plate to adjust the intensity of the light passing through.

For some experiments where we changed the polarization of the light (see Section 5.3.2 for example), we added a quarter-wave plate followed by a half-wave plate. This arrangement allowed us to adjust the polarization by rotating both wave plates. These two wave plates were not used otherwise. I note that the optical fibers used (see below) did not preserve the polarization and thus I expected the polarization of light hitting the resonator to be slightly different from the polarization set by the wave plates.

Because the total power at the output of the laser was high ($\sim$ 5 mW), we sent the light through an ND filter to reduce the power. We varied the ND filter

depending on the attenuation needed. The light then passed through a lens which couples the light to a single-mode optical fiber (see Fig. 3.10).

A Thorlabs FC 780-50P-APC fiber splitter [185] then divided the power from the laser to two branches. One branch went to a Thorlabs S140C power meter [185] which we used to measure the optical power P_{opt}, the other branch continued to the fridge. The splitting ratio $\eta \equiv P_{\text{refrigerator}}/P_{\text{meter}}$ of the splitter was not exactly unity, and drifted slowly over time, with a typical value of around $0.9 - 0.95$. At the beginning of cool downs, we measured the splitting ratio by comparing the power passing through both branches for several optical powers. The branch that goes to the refrigerator then went to a connector on the screen room wall.

For some experiments, I used two illumination lines in the refrigerator. Each line can be connected at the screen room wall to the single line outside the screen room. For experiments where we compared the effects produced by illumination from one or the other of the two lines (Sections 5.3.1 and 5.3.2), we swapped the connections at the screen room wall. However, we found that disconnecting and reconnecting the lines could introduce additional loss, likely from variations in the connection or dust getting on the connectors. To avoid such variations, for most of the measurements we avoided disconnecting the connections. To get to the inside of the refrigerator vacuum space, the two lines go through vacuum feedthroughs on the refrigerator top plate.

Inside the refrigerator, we spliced the fiber from the feedthrough to another section of the fiber that was connected to the cavity using a fusion splicer. We taped the splice point, as well as additional fiber lengths, on the 4 K stage using Kapton

tape. To prevent light in the jacket from reaching the cavity, we wrapped the fiber around a ~ 1 inch diameter post at least 20 times. at the 4 K stage. Finally, the fibers entered the cavity at the mixing chamber through holes drilled in the cavity. We secured the fibers using Stycast 2850 epoxy, one of them directly to the cavity, the other to an Al mounting bracket attached to the cavity (see Figs. 3.11).

The two lines were used to illuminate the cavity differently, one line was oriented perpendicular to the surface of the chip, and the other roughly parallel to the surface (see Fig. 3.11). Light came out of the end of the fiber and formed a cone with opening angle of approximately 10°. For the perpendicular fiber, the end of the fiber was located about 8 mm from the chip surface. This resulted in a spot of light with a diameter of approximately $d_{\text{spot}} = 1.4$ mm. The resonator, about 0.4 mm in size, was significantly smaller than the spot size and located roughly at the center of the spot. As a result we expected that the resonator was exposed to uniform light of intensity

$$I_{\text{opt}} \approx \frac{4\eta P_{\text{opt}}}{\pi d_{\text{spot}}^2}. \tag{3.4}$$

For the parallel fiber, the end of the fiber was about 2 mm from the edge of the chip and the LC resonator was located a further 2 mm away (see Fig. 3.6 for example). The edge of part of the inductor line saw the fiber. For a perfect alignment of the fiber and chip, only this edge was illuminated. Of course, we can expect slight error in the alignment.

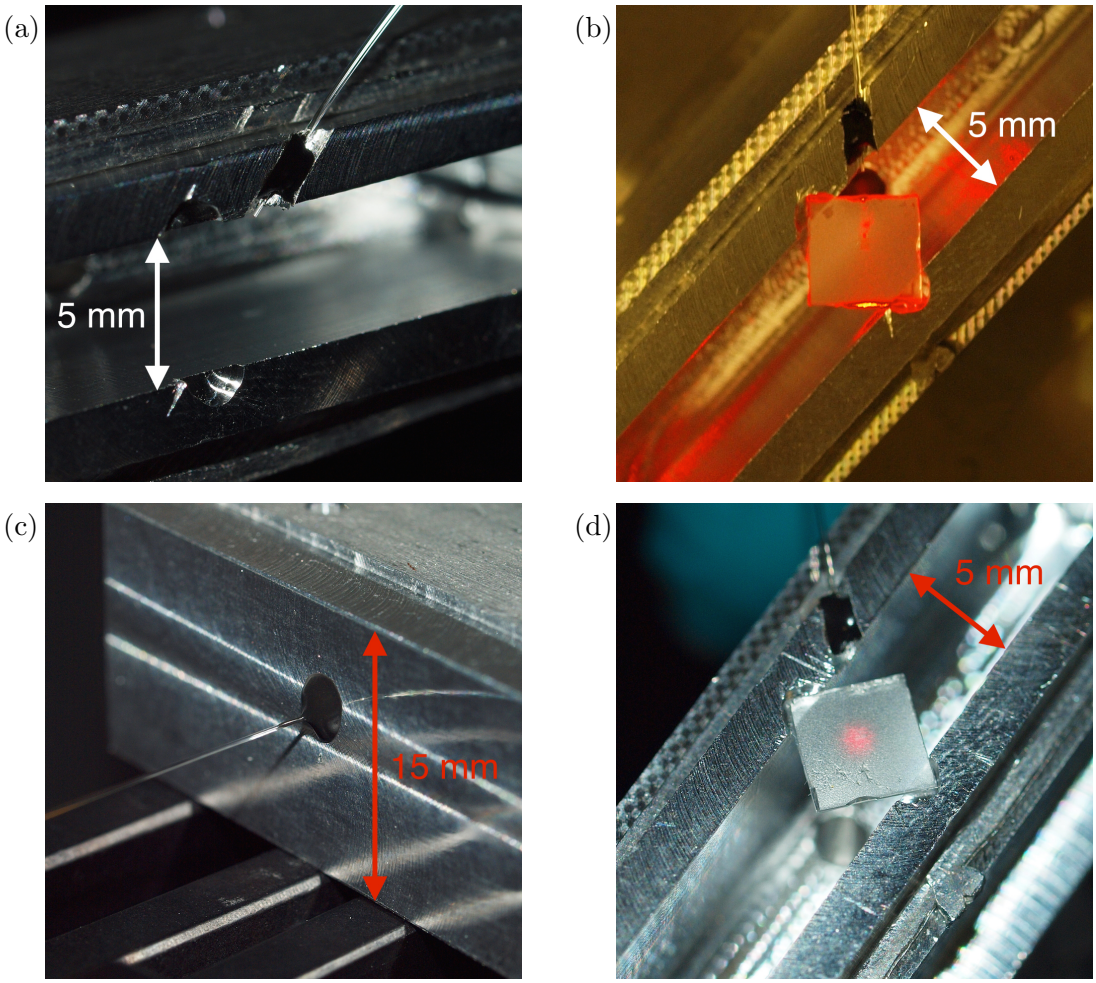

Figure 3.11: Pictures of chip illumination lines in the 3d cavity. (a) Parallel line. (b) Parallel line illuminating a test chip. (c) The epoxy point of perpendicular line on a mounting bracket attached to the cavity (d) Perpendicular line illuminating a test chip. For the test illuminations, we used visible red laser diode instead of the actual 780 nm laser.

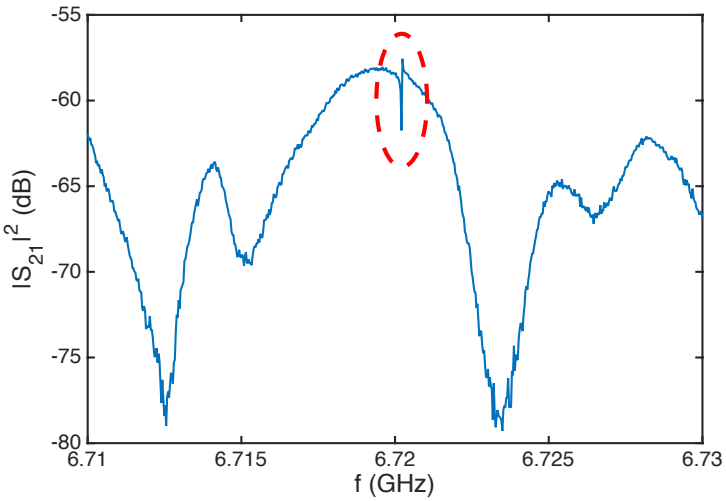

Figure 3.12: $|S_{21}|^2$ vs frequency f near resonance peak (located inside dashed ellipse), showing the presence of cable resonances with line widths > 1 MHz.

3.6 Background Subtraction and Peak Fitting

As I discussed in Section 3.4, I automated the data taking process using Matlab. The routine that I mainly used is the E5071C_multiplepowertraces_singlespan_header.m, which set most of the typical S_{21} measurement parameters for its input parameters and allowed me to take multiple rf powers in sequence. The trace was then saved in a tab-delimited file format with 3 columns and the number of rows is the number of points in the trace (typically 1601, which was the maximum value allowed by the VNA). The first column was the frequency, the second column was the $|S_{21}|^2$ in dB, and the third column was phase of the complex S_{21}. We could then calculate the real and imaginary components of S_{21}.

As discussed, we attempted to reduce the effects of cable self-resonance, in-

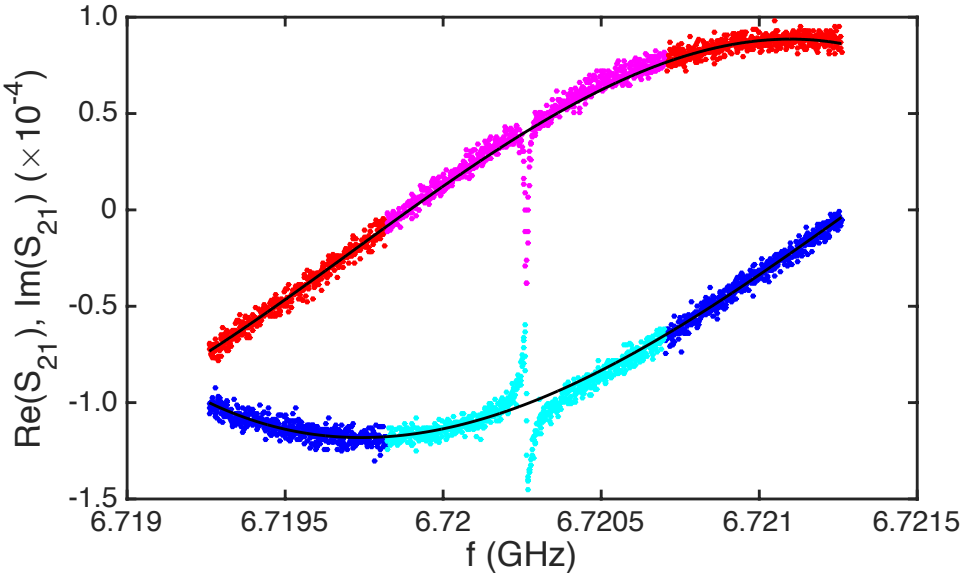

Figure 3.13: Real and imaginary components S_{21} vs frequency f of a sample background trace, showing the polynomial fit for background subtraction. Blue dots are part of real component data used in fit, cyan dots are part of real component data not used in fit. Red dots are part of imaginary component data used in fit, magenta dots are part of imaginary component data not used in fit. The two black lines are the results of the polynomial fit.

cluding by adding an additional isolator in the input of the cavity. However, we still observed self-resonances with line widths 1 MHz or above, including near the LC resonance of 6.720 GHz (See Fig. 3.12). This resulted in the resonance located on a non-flat background which needed to be subtracted.

To subtract the background, I took an S_{21} trace with ≈2 MHz span around the resonance with a relatively high rf power to reduce noise. This span was much larger than the line width of the resonance, which ranges between 3 kHz to 60 kHz depending on the parameters used. I ignored the middle ∼900 kHz where the resonance was located, and fit the real and imaginary components of S_{21} to

a 4th order polynomial using a Matlab script peakBGfitter.m. This script gave 8 fit parameters that defined the functional form of the background components of $\mathrm{Re}(S_{21})$ and $\mathrm{Im}(S_{21})$ as a function of frequency f,

$$\mathrm{Re}[S_{21}(f)]_{\mathrm{bg}} = A_{\mathrm{Re}} + B_{\mathrm{Re}} f + C_{\mathrm{Re}} f^2 + D_{\mathrm{Re}} f^3, \tag{3.5}$$

$$\mathrm{Im}[S_{21}(f)]_{\mathrm{bg}} = A_{\mathrm{Im}} + B_{\mathrm{Im}} f + C_{\mathrm{Im}} f^2 + D_{\mathrm{Im}} f^3. \tag{3.6}$$

Here A, B, C, and D are the fit parameters, with the subscript determining whether it is the real or imaginary component. I then subtracted the real and imaginary component of the background from the S_{21} trace. The background level didn't drift much over time, but I typically took the background trace every several hours. When I added microwave components (e.g room temperature amplifiers), changed temperature (including temperature cycling), or applied optical light, the background level would jump to a different value, which means I needed to take a new background trace.

I fit the subtracted S_{21} to the Lorentzian of Eq. 2.21. However, I needed to take into account the loss in the input line and the gain in the output line, phase the signal can gain in propagation, as well as possible remaining offsets. The expression for the complex S_{21} becomes

$$S_{21}(f) \;=\; |S_{21,\mathrm{in}}|\,|S_{21,\mathrm{out}}| \left(e^{i\phi} \frac{2Q/\sqrt{Q_{\mathrm{in}} Q_{\mathrm{out}}}}{1 + 2iQ\frac{(f-f_r)}{f_r}} + C_0 \right), \tag{3.7}$$

where $|S_{21,\mathrm{in}}|$ is the transmission of the input line, $|S_{21,\mathrm{out}}|$ is the transmission of the output line, ϕ is the phase, Q is the quality factor, Q_{in} is the input coupling quality factor, Q_{out} is the output coupling quality factor, and C_0 is a complex offset.

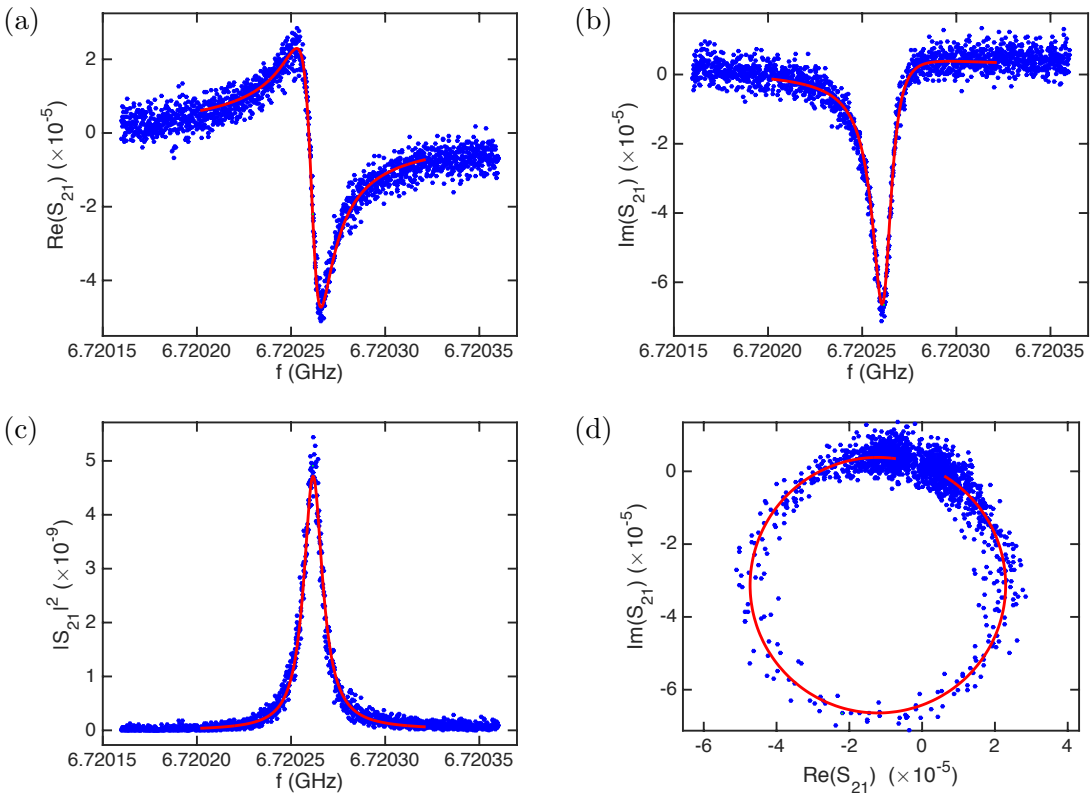

Figure 3.14: Lorentzian fit of resonance peak. Blue dots are the data, red line is the fit of the data to Eq. 3.7 (a) Re(S_{21}) vs frequency. (b) Im(S_{21}) vs frequency. (c) $|S_{21}|^2$ vs frequency. (d) Im(S_{21}) vs Re(S_{21}). The resonance peak forms a circle in the complex plane of S_{21}

I calculated $|S_{21,\text{in}}|$ from the loss in the input line and $|S_{21,\text{out}}|$ from the gain in the output line. C_0 should be negligible after background subtraction. I then fit two curves simultaneously, the real and imaginary components of S_{21} (see Figs. 3.14(a) and (b)), to obtain six fitting parameters: ϕ, Q, $\frac{1}{2}\sqrt{Q_{\text{in}}Q_{\text{out}}}$, f_r, and the real and imaginary components of C_0. As I discussed in Section 2.1.2, plotting the S_{21} in the complex plane results in a circle, as shown in Fig. 3.14(d). The diameter of the circle is

$$d_p = |S_{21,\text{in}}||S_{21,\text{out}}|2Q/\sqrt{Q_{\text{in}}Q_{\text{out}}}. \tag{3.8}$$

We have $Q_{\text{in}} \approx Q_{\text{out}}$, hence the external quality factor $1/Q_e = 1/Q_{\text{in}} + 1/Q_{\text{out}} \approx 2/Q_{\text{in}}$, and $\frac{1}{2}\sqrt{Q_{\text{in}}Q_{\text{out}}} \approx \frac{1}{2}Q_{\text{in}} \approx Q_e$.

At higher drive powers, we found that the shape of the peak deviated from Lorentzian, and the peak circle in complex S_{21} became elongated (see Fig. 3.15). Because of the very weak coupling between the microwave line and the resonator, $Q_e \gg Q_i$, which meant that the total Q was limited by the internal quality factor Q_i. While Q_e was expected to be constant, Q_i depended strongly with drive power, or rf photon occupation, as we will discuss in detail in Chapters 4 and 5. The rf photon occupation inside the resonator when the rf drive was detuned from resonance would be less compared to when it was driven at resonance. For the range of our measurements we had Q_i increasing with increasing drive power, or photon occupation. Hence we had a frequency dependent-Q_i, where the Q_i was highest at resonance, and getting lower with increasing detuning $\delta f \equiv f - f_r$. This dependence would result in the elongated shape of the peak as we saw.

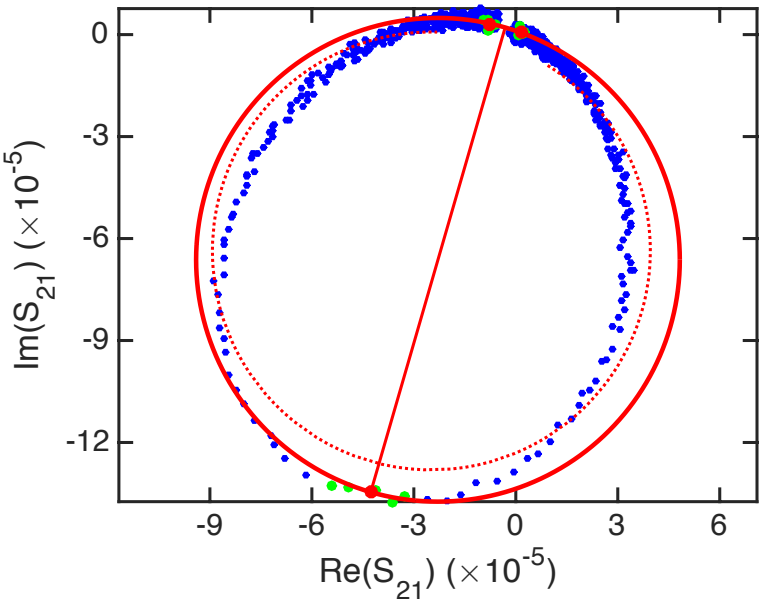

Figure 3.15: Im(S_{21}) vs Re(S_{21}), showing the failure of Lorentzian fit at high rf powers, and the 3-point fitting method. The peak is elongated in the complex S_{21} plane. Blue dots are the data. The red dotted circle is an attempt to fit the data to Eq. 3.7. The green dots are the data points used in the 3-point fit method, the three red points are there resulting averaged points. The solid red circle is the circle where the three points are located, obtained from Eq. 3.9.

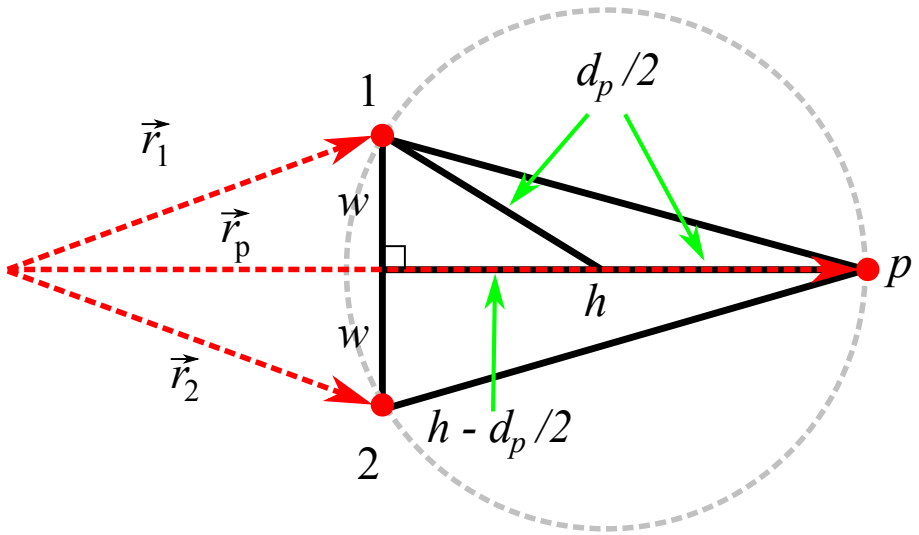

Figure 3.16: Illustration for the 3-point fitting scheme. The three red dots are the three averaged points, the two wings (1 and 2), and the peak (p), located at $\vec{r}_1$, $\vec{r}_2$, and $\vec{r}_p$, respectively. The distance between points 1 and 2 is $2w$, and the distance between p and the midpoint between the two wings is h. The diameter of the circle is $d_p/2$.

One way to improve the fitting of the peak in this regime is by introducing the frequency dependence, $Q_i(f)$, in the fit formula of Eq. 3.7 then solve for this dependence, probably using some iterative method. However, the method that I actually employed used the fact that at f_r, the Q_i is the highest in the curve and also the main Q_i value that we actually care about. I found that the unmodified fit routine to fit to Eq. 3.7 gave the correct value of f_r. I chose several points around the peak in the trace then average their location in the S_{21} complex plane. I wanted to have enough points to average so I could get the accurate peak position, but not too many such that points that were too far away from the peak were included. Additionally, I also averaged the location of several points at or near the beginning of the trace, as well as several points at or near the end of the trace (the "wings"). I

wanted the detuning from f_r of these two averaged points to be the same. All three averaged points should be on the perimeter of the circle with the diameter d_p of Eq. 3.8 with $Q \approx Q_i(f_r)$, as shown in Fig. 3.16. The definitions shown in Fig. 3.16 are as follows: $\vec{r}_1$ and $\vec{r}_2$ are the position of the wings in the complex plane, $\vec{r}_p$ is the position of the peak, $2w = |\vec{r}_1 - \vec{r}_2|$ the distance between the wings, $\vec{r}_m = (\vec{r}_1 + \vec{r}_2)/2$ the position of the midpoint between the two wings located w distance away, and $h = |\vec{r}_p - \vec{r}_m|$ the distance between the midpoint and the peak. I can then calculate d_p by

$$\begin{aligned} (d_p/2)^2 &= w^2 + (h - d_p/2)^2 \\ d_p &= \frac{w^2 + h^2}{h}. \end{aligned} \tag{3.9}$$

Jared wrote a Matlab script LorzReIm3Pt.m that automated this process, requiring a S_{21} trace array and resonance frequency obtained from standard fit, and calculated the diameter of the circle. From the diameter, I calculated the $Q \approx Q_i$ by using Eq. 3.8 and the averaged value of $\frac{1}{2}\sqrt{Q_{\text{in}}Q_{\text{out}}}$ from Lorentzian fit.

3.7 Summary

In this chapter, I discussed the design and fabrication of the thin-film resonators and 3d cavity. I then discussed the experimental setup, which includes the microwave drive and readout lines, and the optical illumination lines. Finally, I described the standard process of the data analysis, which includes the background subtraction, fitting of data to Lorentzian, and the 3-point fit method for higher rf power data.

Chapter 4: Resonator Results: Without Optical Illumination

In this chapter, I present and discuss my results from measurements on resonator MW2-14 when no optical illumination was applied. At base temperature and low drive powers, the resonance showed signs of strong coupling to a single TLS. At higher drive powers, quasiparticle effects dominated. For temperatures between 25 and 300 mK, the results at high powers can be fit well to the nonequilibrium quasiparticle model discussed in Chapter 2. I discuss the parameters from the fit and how they compare to the expected physical and design parameters. Finally, I discuss the behavior of the 3d cavity during the measurements.

4.1 Properties of Resonator at Base Temperature

4.1.1 Measurement Details

Jared Hertzberg and I measured resonator MW2-14 inside the dilution refrigerator between late July and late November 2013. The base temperature of 20-25 mK was slightly higher than the typical base temperature of the refrigerator, which was about 10-15 mK. The reason for this was likely because in the same cooldown Jared mounted a hot finger, which was anchored at 4 K, and extended inside the

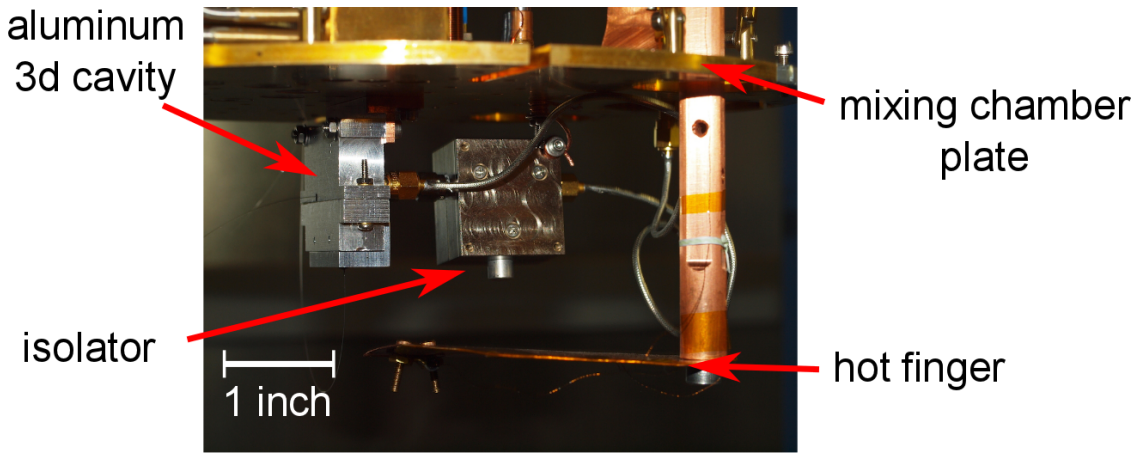

Figure 4.1: Photograph of the hot finger anchored at 4 K next to the 3d cavity, under the mixing chamber plate.

inner shield of the refrigerator to within a few inches of the cavity (see Fig. 4.1). This hot finger had a resistor attached to it, and was used to perform heat load experiments in preparation for mounting the magneto-optical trap (MOT) inside the refrigerator. Slight touches between the hot finger and lower temperature stages, as well as blackbody radiation coming from the hot finger, may have caused the increase in the refrigerator temperature. In fact, during the first attempt to cool down the resonator, the refrigerator only reached about 150 mK because of a touch between the hot finger and one of the coaxial lines. The hot finger may also have introduced some additional complications, as I discuss in Section 4.2.3.

During the cooldown over an interval of 4 months, the refrigerator was cycled 3 times above the critical temperature of Al ($\approx$ 1.2 K). The resulting data from the cooldown can thus be separated into 4 sessions. For example, Figs. 4.2 and 4.3 show the inverse quality factor $1/Q$ and resonance frequency f_r of the resonator,

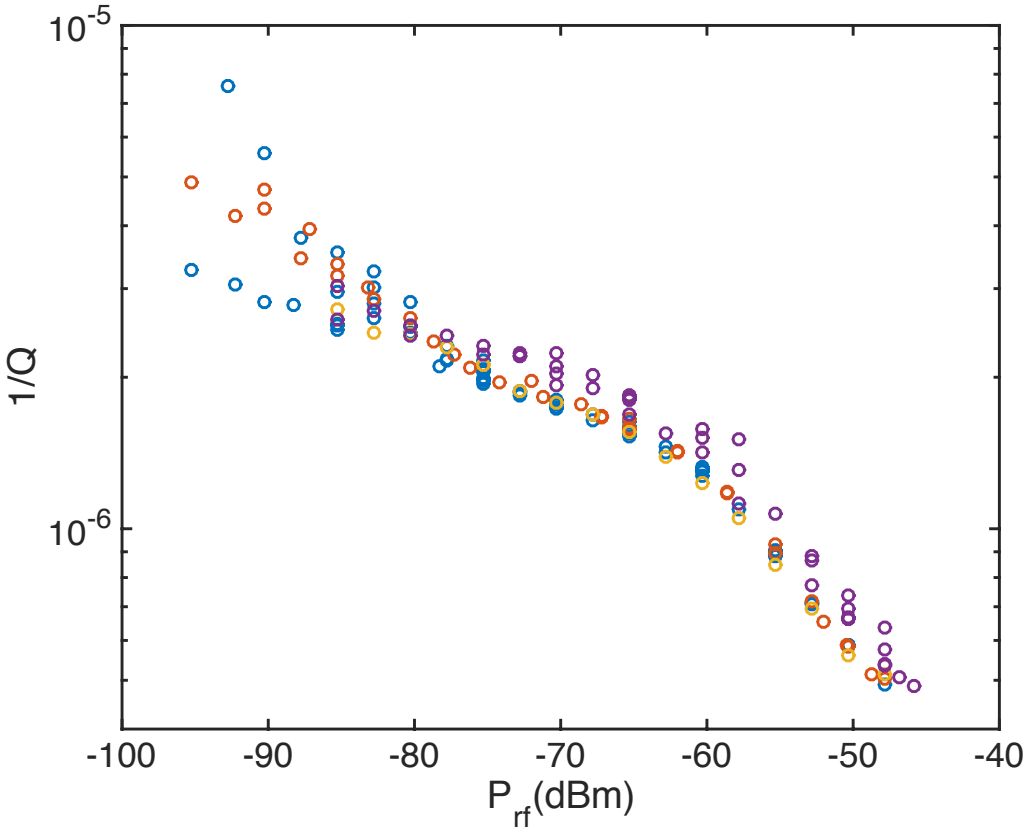

Figure 4.2: Inverse quality factor $1/Q$ vs rf drive power P_{rf} for base temperature for the entire cooldown. Different sessions are in different colors: blue for the first session, red for the second session, orange for the third session, and purple for the fourth session.

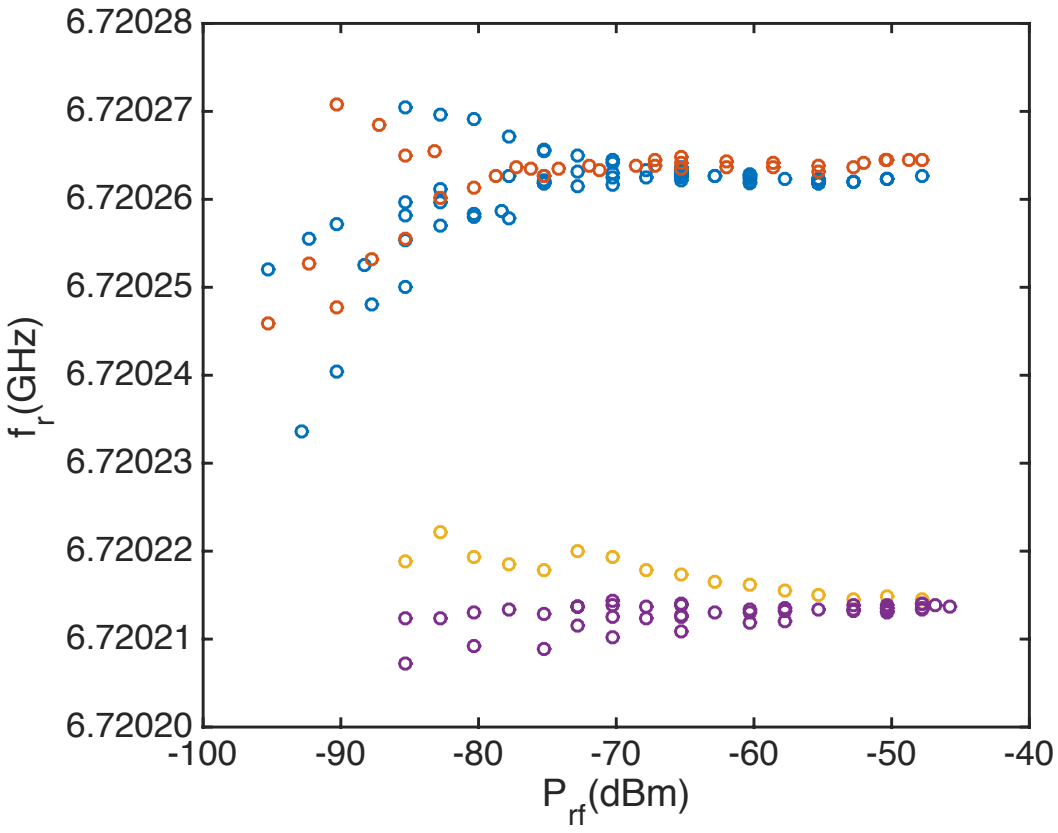

Figure 4.3: Resonance frequency f_r vs rf drive power P_{rf} for base temperature for the entire cooldown. Different sessions are in different colors: blue for the first session, red for the second session, orange for the third session, and purple for the fourth session.

obtained from fits described in Section 3.6, as a function of rf power reaching the input port of the cavity $P_{\rm rf}$ at base temperature, with each session shown with different color. Within the same session we sometimes measured the same values of $P_{\rm rf}$ multiple times, several days apart. We found that $1/Q$ and f_r for higher powers ($P_{\rm rf} \gtrsim -70$ dBm) varied by a small percentage during any one session. For lower powers ($P_{\rm rf} \lesssim -70$ dBm), we saw multiple branches in $1/Q$ and f_r even during the same session, which I will discuss in Section 4.1.2.

The blue open circles are the results from the first session. At high powers $f_r \approx$ 6.720263 GHz. The first temperature cycling happened in September 10, 2013. For this cycle we set the refrigerator mixing chamber to 1.5 K, then put a μ-metal shield around the refrigerator and cooled it back down to base temperature. The red open circles are the result from the second session, *i.e.* after the first cycle. Compared to the first session, the $1/Q$ for the second session was basically unchanged, while f_r at high power shifted up by about 1 kHz to about $f_r \approx$ 6.720264 GHz. The second temperature cycling happened in October 21, 2013, when the house chilled water that supplied our refrigerator failed overnight, bringing the mixing chamber temperature to about 80 K. We brought the refrigerator back to base temperature after the chilled water system was fixed during the day. The orange open circles are the result from the third session, *i.e.* after the second cycle. Compared to the second session, the $1/Q$ for the third session was again unchanged, however f_r at high power actually shifted down by about 50 kHz to about $f_r \approx$ 6.720214 GHz. The third temperature cycling happened three days after the second, due to another chilled water failure. The refrigerator again warmed to about 80 K for several hours.

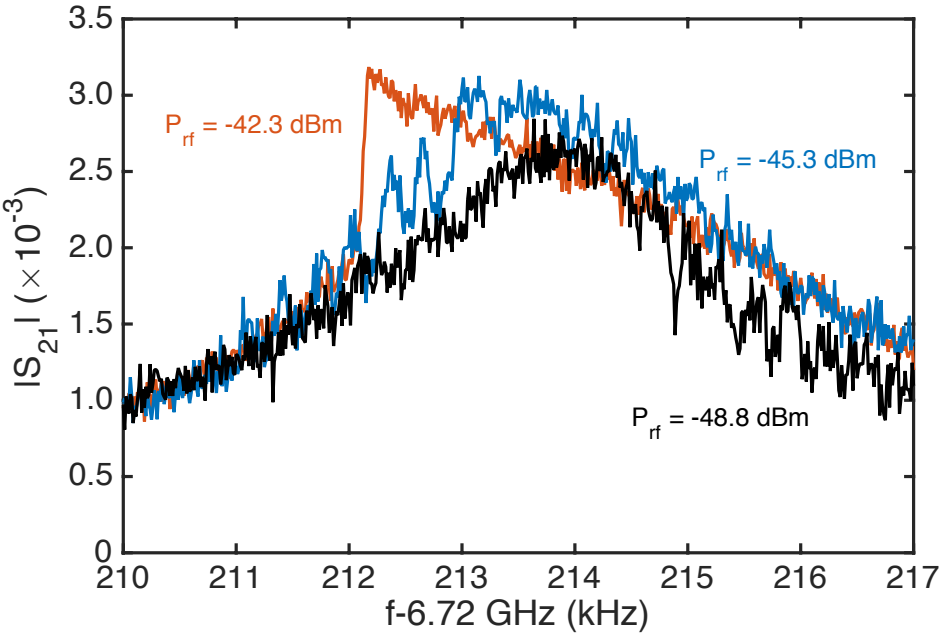

Figure 4.4: Transmission $|S_{21}|$ vs frequency f for traces with very high $P_{\rm rf}$, showing the onset of distortion in $|S_{21}|$. Black curves has $P_{\rm rf} = -48.8$ dBm, where there are no noticeable distortion. Blue curves has $P_{\rm rf} = -45.3$ dBm, where distortions started to appear for $f < f_r$. Red curves has $P_{\rm rf} = -42.3$ dBm, where there is a significant jump in S_{21} at $f \approx 6.720212$ GHz.

The purple open circles are the result from the fourth session, *i.e.* after the third cycle. In this session, the variations in $1/Q$ and f_r for the same $P_{\rm rf}$ seemed to be somewhat larger compared to the previous sessions, up to about $\pm 8\%$ in $1/Q$. In the previous sessions, the variations were at most about $\pm 2\%$ in $1/Q$. Compared to the third session, $1/Q$ for the fourth session were typically slightly higher, while f_r was unchanged. Examination of all of the $1/Q$ data in Fig. 4.2 gives about 8% uncertainty in $1/Q$ due to session-to-session variation.

The range of $P_{\rm rf}$ in the measurements was between -95 dBm to -45 dBm. This corresponds to $\langle n \rangle$, which is the rms number of microwave photons inside the

resonator, between about 20 and 2×10^8. The lower limit of $P_{\rm rf}$ was limited by the averaging time to get a reasonable signal. S_{21} traces with $P_{\rm rf} = -95$ dBm required an averaging time of several hours, and attempting to measure even lower powers would require even longer averaging time. Above $P_{\rm rf} \approx -45$ dBm, distortions in the resonance shape started to appear, and this sets the upper limit of the measurement. Figure 4.4 shows several $|S_{21}|^2$ vs f traces for $P_{\rm rf} > -45$ dBm with the distortion visible in the resonance. These distortions appear to be due to the onset of nonlinear effects, which may come from heating, nonlinearity of the kinetic inductance, or possibly nonequilibrium quasiparticle effects [186, 187].

4.1.2 Low Power Regime: Effects of TLS

As I mentioned in the previous subsection, the curves for f_r vs $P_{\rm rf}$ and $1/Q$ vs $P_{\rm rf}$ seemed to have multiple branches for lower $P_{\rm rf}$. The branches were especially apparent in f_r of the first two time sessions (blue and red open circles), as can be seen in Fig. 4.3. For the first session (blue open circles) the branches in f_r could be seen appearing below $P_{\rm rf} \approx -70$ dBm, and for the second session (red open circles) the branches in f_r could be seen appearing below $P_{\rm rf} \approx -80$ dBm. f_r differed by up to 20 kHz between branches for $P_{\rm rf}$ values about 10 dB lower than where the branches start to appear. For the third session (orange open circles), while it may appear that f_r started to shift below about $P_{\rm rf} \approx -60$ dBm, we didn't see a second branch. For the fourth session, branches seemed to appear below $P_{\rm rf} \approx -65$ dBm, however f_r were only separated by about 5 kHz by $P_{\rm rf} \approx -85$ dBm. In contrast,

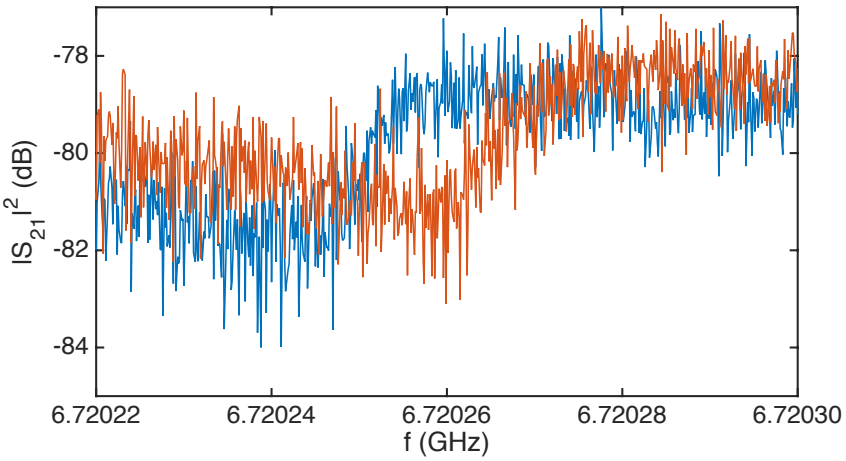

Figure 4.5: Comparison of two $|S_{21}|^2$ vs f plots traces taken four days apart: blue curve was taken on 8/6/13, red curve was taken on 8/10/13. $P_{\mathrm{rf}} = -85.3$ dBm for both traces, and other measurement parameters were identical. The traces shown are raw traces from VNA, before background subtraction. The resonant frequencies f_r extracted from fit of the two traces were 6.7202506 GHz and 6.7202664 GHz, indicating a shift of 15.8 kHz.

the resonant frequency f_r seemed to be fairly independent of P_{rf} for higher powers, and we did not see multiple branches.

We found that f_r typically followed one branch for multiple measurements in the same day, but would jump to a different branch efter several days. For example, Fig. 4.5 shows two $|S_{21}|^2$ vs f traces taken at $P_{\mathrm{rf}} = -85.3$ dBm using the VNA. All other measurement settings were identical but the two traces were taken 4 days apart (08/06/13 and 08/10/13). The resonant frequencies f_r extracted from fit of the two traces differed by 16 kHz. This was fairly typical for the shifts we saw.

For comparison, the $1/Q$ vs P_{rf} plot appears to show two distinct branches in the first session below $P_{\mathrm{rf}} \approx -75$ dBm (see Fig. 4.2). The lower branch followed the

trend of the $P_{\rm rf}$ dependence from higher powers, while for the upper branch the loss $1/Q$ increased rapidly with decreasing $P_{\rm rf}$ below -80 dBm. For the second session, $1/Q$ vs $P_{\rm rf}$ seemed to follow the first session's upper branch, although the $1/Q$ values at the lowest values of $P_{\rm rf}$ were about $\approx 40\%$ lower than the corresponding $1/Q$ values from the upper branch. For the next two sessions, we did not measure Q at low enough $P_{\rm rf}$ to be certain if there were multiple branches or which branch was present.

To check whether each branch in $1/Q$ corresponded to a specific branch in f_r, I plotted $1/Q$ and f_r vs $P_{\rm rf}$ for the first session (see Fig. 4.6). The blue closed circles represent points taken when $1/Q$ vs $P_{\rm rf}$ followed the upper branch, while the black open circles represent points taken when $1/Q$ vs $P_{\rm rf}$ followed the lower branch. It seems that the lower (black) branch in $1/Q$ showed a smaller frequency shift δf_r at lower $P_{\rm rf}$ compared to higher values of $P_{\rm rf}$. However, while the largest shifts δf_r came from the upper branch, many points in the upper branch had a shift that was comparable to the points in the lower branch. Hence it was hard to conclude that the branches in $1/Q$ correspond to branches in f_r.

I note that the regime where we saw multiple branches corresponded to the regime with relatively low microwave photon numbers $\langle n \rangle \approx 20 - 2000$. The fact that in this regime we generally found $1/Q$ to decrease rapidly with increasing $P_{\rm rf}$ suggests that this behavior was due to two-level systems (TLSs). In Section 2.2, I discussed the effects of both a single TLS and an ensemble of TLSs. Since f_r jumped between branches every few days, this suggests it was not caused by an ensemble of TLSs, as it would require the entire TLS ensemble to reorganize at the same time

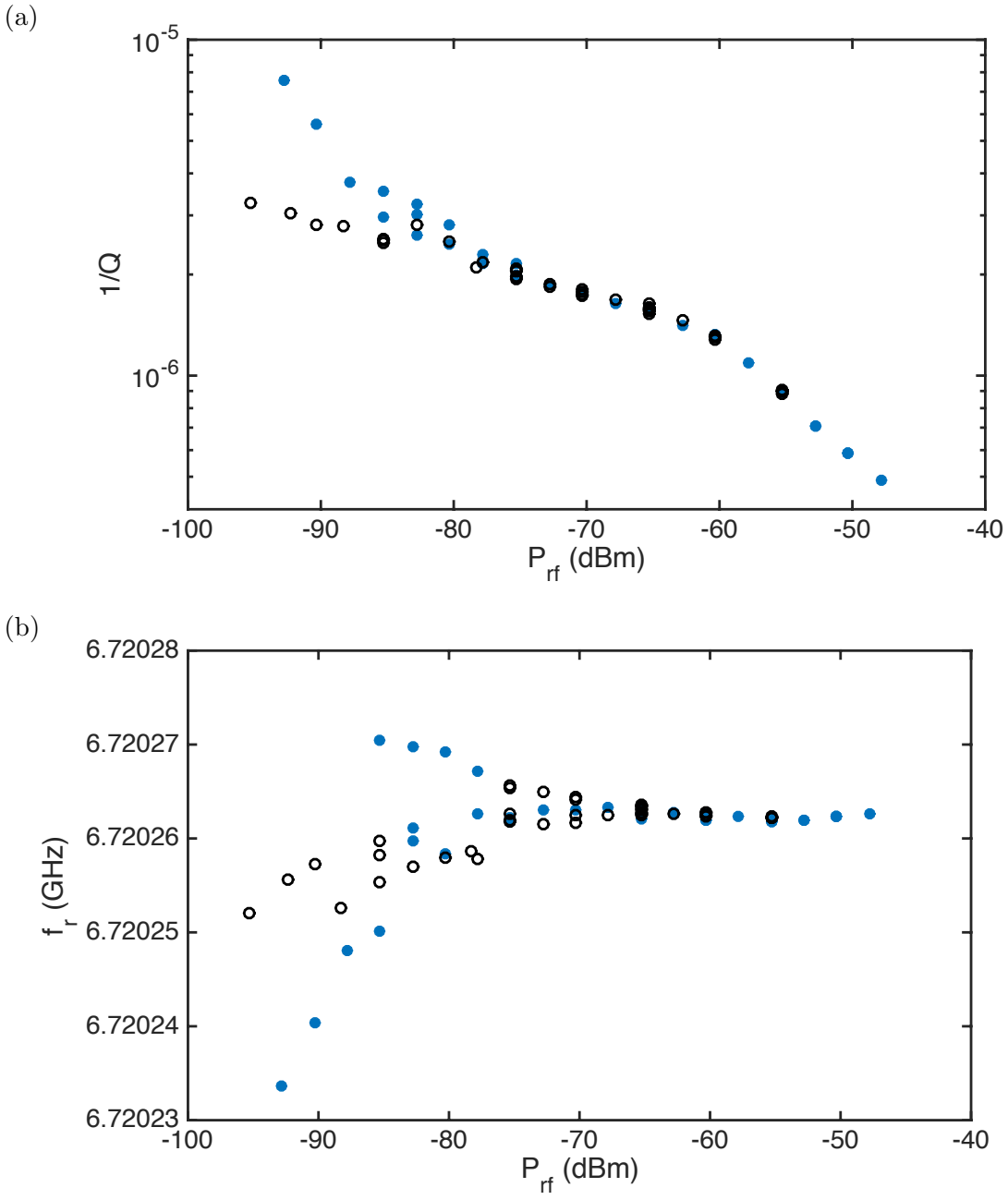

Figure 4.6: (a) Inverse quality factor $1/Q$ vs rf drive power $P_{\rm rf}$. (b) Resonance frequency f_r vs rf drive power $P_{\rm rf}$. Both data sets were taken for the first session at the base temperature of 25 mK. Closed blue circles represent measurements taken when $1/Q$ appeared to follow the upper branch, open black circles represent measurements taken when $1/Q$ appeared to follow the lower branch.

every few days. On the other hand, it is entirely plausible that a single TLS could change its energy or orientation every few days due to some microscopic change in the dielectric local environment. It is also possible that the resonator coupled to a different TLS when branch jumping occured. Hence it is reasonable to assume that the presence of branches was caused by coupling to a single TLS, or at most a few TLSs.

If the branches effects were caused by coupling/decoupling to a single TLS, it would be reasonable to fit $1/Q$ vs $P_{\rm rf}$ to Eq. 2.51 for loss due to a single TLS. Since the electric field in the capacitor is not uniform, the expression should be modified slightly to depend on voltage instead of the electric field, *i.e.*

$$\frac{1}{Q_{\rm TLS,s}}(\langle V\rangle) \;=\; \frac{T_2}{\hbar\epsilon V}\left(\frac{p\Delta}{2\mathcal{E}}\right)^2 \frac{1}{[1+(\langle V\rangle/V_{c,s})^2]}, \tag{4.1}$$

where $\langle V\rangle$ is the rms voltage across the interdigitated capacitor and $V_{c,s}$ is the characteristic voltage. Equations 2.52 and 2.53 show that the low power inverse quality factor value $1/Q_{\rm TLS,s}(\langle E\rangle = 0)$ and characteristic electric field $E_{c,s}$ depend on the individual TLS parameters. These include the well asymmetry Δ, tunneling rate Δ_0, TLS energy $\mathcal{E} = \sqrt{\Delta^2+\Delta_0^2}$, TLS orientation angle θ, dipole moment p, relaxation time T_1, and coherence time T_2. All of these parameters can differ between TLSs, and hence each branch would need to be separately fitted. Additionally, it doesn't appear that we applied low enough $P_{\rm rf}$ such that $1/Q$ reached the regime where it is flat. This makes it difficult to fit to Eq. 4.1 and extract accurate physical parameters.

Recently, Sarabi *et al.* reported observations of strong coupling between a

superconducting resonator and a single TLS located in silicon nitride dielectric used in the parallel plate capacitor of a resonator [100, 101]. I noticed several similarities between their results and the low power behavior in the resonator we measured. For example, in both devices the resonance frequency f_r was independent of rf drive power at strong drive, and f_r could shift at weak drive. f_r at low power also seemed to drift around and ocassionally would jump to a new value. These similarities again suggest that the effects that we saw were caused by coupling to a single TLS.

In some of their resonators, Sarabi *et al.* could apply a dc voltage bias to their resonators. Applying dc bias changes the well asymmetry Δ of the TLSs, and subsequently the TLS energy $\mathcal{E}$. Using this they could adjust the detuning between the resonator and each TLSs, and control which TLS couples to the resonator [101].

Our setup lacked the capability to apply a dc bias to the capacitor, but we looked at several possible methods to bias or excite the TLSs, or otherwise cause f_r or $1/Q$ to jump to a different branch. First, we found that applying high optical intensity ($I_{\rm opt} \approx 0.2$ pW/μm^2) for several minutes may have caused f_r to jump to a different branch. This was probably equivalent to heating the TLSs. However, the optical intensity was so high (250 times higher than the highest intensity we applied in Chapter 5) that we could not observe the resonance during illumination because the quality factor of the resonator degraded so much or the frequency decreased too much. We also attempted a two-tone experiment in which we drove the TLSs using an rf tone supplied by an Agilent 83731B signal generator with frequencies near the resonator resonance frequency $f_r \approx 6.72026$ GHz, while continuously probing the resonance with the VNA. While initial scans suggested a jump in f_r when the

second tone was driven around 6.68 GHz, subsequent repeated measurements failed to recreate the jump. This suggests that the jump we saw was not caused by the second rf tone, but was instead a random jump, similar in nature to the ones that occured every several days.

To check whether it was reasonable for our resonator to be coupled to a single TLS, I used the expression derived by Sarabi for the number of TLSs N_{TLS} with energies within the bandwidth of the resonator, given by [101]

$$N_{\mathrm{TLS}} \;=\; P_0 h B V \,\ln\left(\sec\eta_m + \tan\eta_m\right), \tag{4.2}$$

where P_0 is the TLS density of states, $B = f_r/Q$ is the resonator bandwidth, V is the dielectric volume, and $\eta_m \approx 0.9\pi/2$. For this estimate, I assumed the typical number $P_0 \approx 10^{44}$ / J m^3 and used $1/Q \approx 5\times10^{-6}$, which is the inverse quality factor values at the lowest powers we applied. In Section 2.2.3, I noted that for coplanar waveguide resonators, the fill factor F is largest at the metal-substrate interface and at the air-substrate interface, while the contribution from the metal-air interface is much smaller. I performed a finite element simulation using COMSOL [188] to find the approximate electric fields in an interdigitated capacitor and found that this is the case as well for interdigitated capacitors. This suggests the TLS loss may be dominated by dielectric at the metal-substrate interface and the air-substrate interface. Hence for volume V in Eq. 4.2, I tried using the estimated total volume of dielectric in the metal-substrate interface and the air-substrate interface, but did not include the dielectric volume at the metal-air interface. The total aluminum film area for the interdigitated capacitor was $\approx 2 \times 10^4$ μm^2. As the gap between

capacitor fingers was the same as the finger width, the total area of the substrate between the fingers was comparable to the capacitor Al film area $\approx 2 \times 10^4$ μm^2. I assumed a typical thickness of the interface of 5 nm. This gives $V \approx 200$ μm^3. Using all these numbers, I find $N_{\mathrm{TLS}} \approx 1.3$. Note that I used approximate values for many of the parameters in Eq. 4.2 and hence this calculation is at best an order of magnitude estimate for N_{TLS}. Nevertheless, this result confirms that the resonator should be expected to be coupled to a single or a few TLSs.

4.1.3 High Power Regime: Effects of Quasiparticles

I now focus on the $P_{\mathrm{rf}} \gtrsim -70$ dBm range where multiple branches did not seem to appear. I often took multiple measurements with the same P_{rf}, and for the following data analysis I averaged the $1/Q$ values from those measurements for use in subsequent fits. Between -70 dBm and -45 dBm, $1/Q$ decreased with increasing P_{rf}. In principle, this could be due to TLS effects, nonequilibrium quasiparticle or both. If I assumed this behavior to be caused by an ensemble of TLSs, I could extract a characteristic microwave photon number $n_c \approx 10^6$ where the loss saturated. This was many orders of magnitude larger than the typically reported values of $n_c \approx 1 - 100$ [39, 131, 136]. This suggests that this behavior was unlikely to be caused by TLSs.

Assuming the behavior was caused by nonequilibrium quasiparticles, I could obtain good fits to $1/Q$ vs P_{rf} with reasonable fit parameters. Figure 4.7 shows examples of such fit. The colored open circles represent the individual measurements, with different colors represent different sessions, as described in Section 4.1.1. The

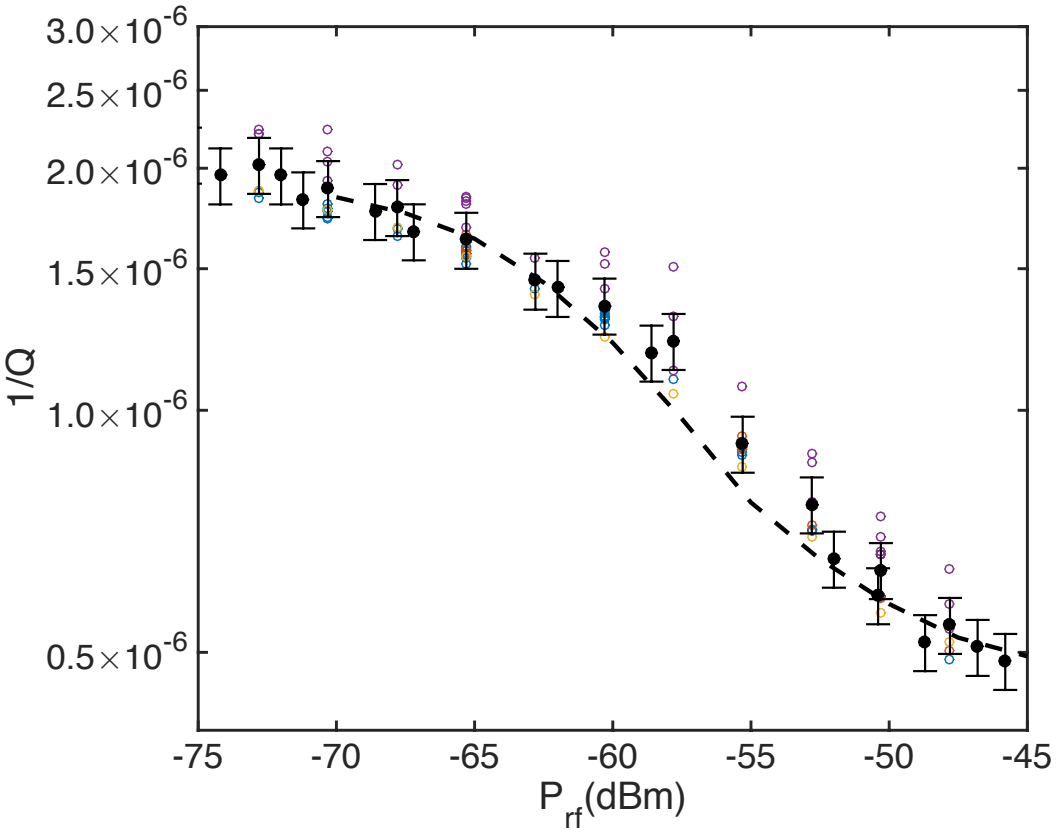

Figure 4.7: Inverse quality factor $1/Q$ vs rf drive power P_{rf} for a base temperature of 25 mK and no optical power. The colored open circles represent different time sessions: blue for first session, red for second session, orange for third session, and purple for fourth session. The black closed circles are the averaged $1/Q$ values for multiple measurements with the same P_{rf}. The black dashed curve is the fit to nonequilibrium quasiparticle model.

black dots are the averaged value of $1/Q$ while the black dashed curve is the fit to the nonequilibrium quasiparticle model. To extract the complete set of fit parameters, I needed to fit $1/Q$ and f_r vs $P_{\rm rf}$ curves at higher temperatures as well as under optical power, and I will discuss the fitting method and the fit parameters in detail in Subsections 4.2.2 and 4.2.3.

4.2 Properties of the Resonator at Higher Temperatures

4.2.1 Measurement Details

To set the mixing chamber temperature of the refrigerator above its base temperature of 25 mK, we input the desired temperature into the PID (Proportional / Integral / Derivative) temperature control at the refrigerator control computer. The refrigerator applied power to heater resistors located at the mixing chamber plate and adjusted the power to keep the temperature at the desired temperature. Oxford claims that the temperature stability is ± 1 mK for temperatures below 1 K [86]. We typically waited at least 30 minutes after the refrigerator reached the desired temperature before performing measurements, to make sure the temperature had stabilized inside the cavity.

We performed transmission measurements of the resonance at higher temperatures in two sessions. The first session was in early October 2013, at the same time as the second session of base temperature measurements (red open circles in Fig. 4.2 and 4.3). Here the highest temperature was 320 mK, with the $P_{\rm rf}$ range between -70 and -50 dBm.

The second session was in early November 2013, at the same time as the fourth session of base temperature measurements (purple open circles in Fig. 4.2 and 4.3). In this session the highest temperature was 300 mK. Originally we intended to increase the range of $P_{\rm rf}$ at each temperature to be comparable to the range of $P_{\rm rf}$ at base temperature. We found that the resonance drifted when driven strongly ($P_{\rm rf} \gtrsim -55$ dBm) for temperatures above 230 mK, with the frequency shift and loss increasing with the length of time the power was applied. For $P_{\rm rf} \approx -55$ dBm this drift was relatively slow, with f_r shifting comparable to $10 - 15\%$ of the resonance linewidth after 10 minutes. However at much higher powers the drift is much more rapid, with f_r shifting by up to 2 times the resonance linewidth in less than 5 minutes when driven at $P_{\rm rf} \approx -47$ dBm.

The drifts suggest that the resonator heated up when driven strongly. As a result, we set the limit of $P_{\rm rf}$ in our measurements to be between -65 dBm and -55 dBm for temperatures above 230 mK and we tried to keep the averaging time short. I note that the mixing chamber stage temperature did not seem to increase when we applied strong drive at these high temperatures. This suggests that the heating effect was localized near the resonator. While we did not notice this self heating behavior during the first high temperature session, it was possible the effect was present in the measured S_{21} traces. Because of this, the results from the first session may not be reliable and I will focus on the results from the second session only.

4.2.2 Fit to Nonequilibrium QP Model

From the discussion in Chapter 2, I expected the TLS loss to decrease with increasing temperature and the quasiparticle loss to increase with increasing temperature. The range of $P_{\rm rf}$ in our measurements at higher temperatures was about 10 to 20 dB higher than where we expected TLS effects to dominate, as discussed in Section 4.1.2. Hence one should expect TLS effects to be negligible or small in this power range and quasiparticle effects to dominate.

Figures 4.8 and 4.9 show $1/Q$ and f_r vs $P_{\rm rf}$ for several temperatures between 25 mK and 300 mK. For the 25 mK data, the $1/Q$ plot showed the averaged $1/Q$ for each $P_{\rm rf}$ from all four base temperature sessions and f_r plot showed the averaged $1/Q$ for each $P_{\rm rf}$ from the fourth base temperature session only. We found that both $1/Q$ and f_r did not appear to depend on temperature from base temperature up to about 230 mK. Above 230 mK, $1/Q$ increased with increasing temperature and f_r decreased with increasing temperature, as expected from quasiparticle loss. I note that the self-heating effects discussed in the previous subsection seem to appear above 230 mK as well.

To figure out if this behavior was due to quasiparticles, I needed to fit the nonequilibrium quasiparticle model discussed in Section 2.3 to my $1/Q$ and f_r data. As the nonequilibrium model does not provide an analytical expression for $Q_{\rm qp}$ or the fractional frequency shift $\delta f_r/f_r$, and there are multiple physical parameters to fit, attempting to do standard least-squares fitting would be computationally time-consuming and technically challenging. Instead I assumed initial values for all

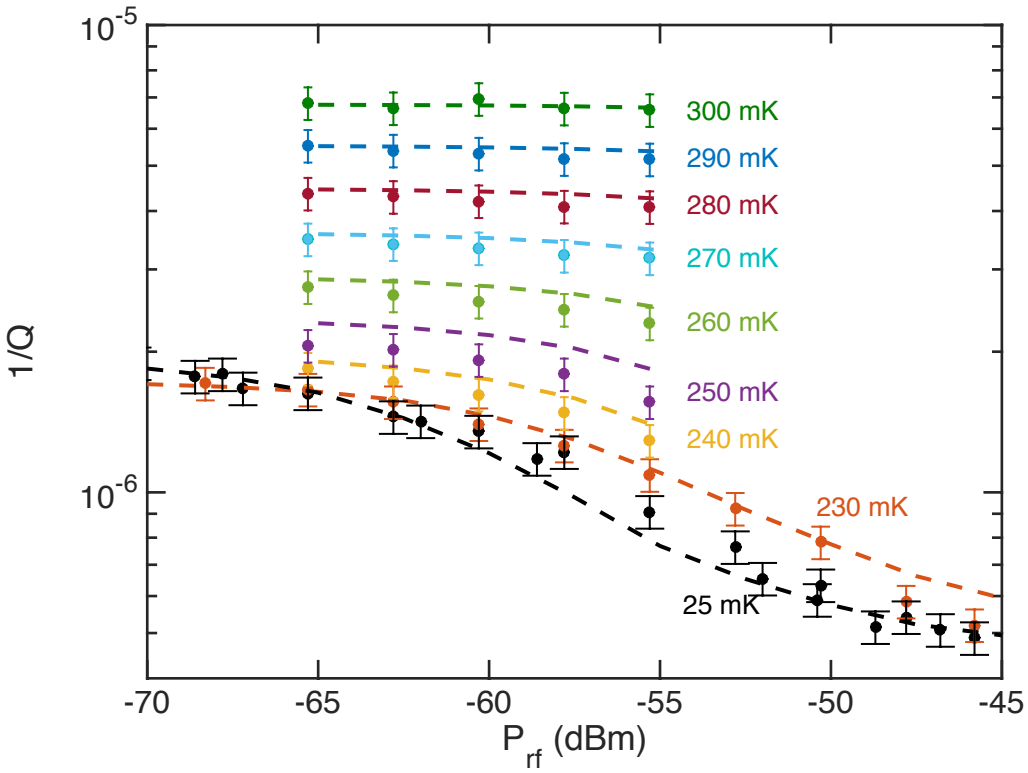

Figure 4.8: Inverse quality factor $1/Q$ vs rf drive powers $P_{\rm rf}$ for different temperatures and no applied optical power. Solid circles are data. Dashed curves are fit to nonequilibrium quasiparticle model with background illumination represented by an effective temperature $T_{\rm eff,0} = 236$ mK.

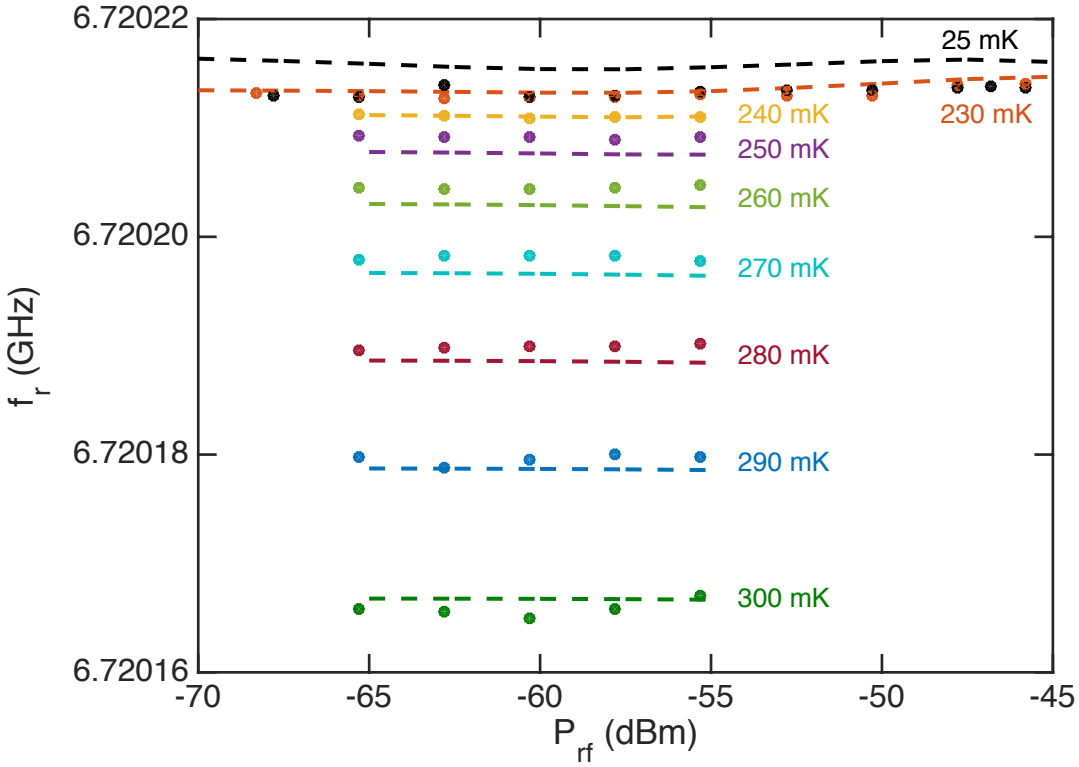

Figure 4.9: Resonance frequency f_r vs rf drive powers $P_{\rm rf}$ for different temperatures and no applied optical power. Solid circles are data. Dashed curves are fit to nonequilibrium quasiparticle model with background illumination represented by an effective temperature $T_{\rm eff,0} = 236$ mK.

of the model parameters (see Table 4.1), then used the Newton-Raphson method discussed in Chapter 2 to find the solutions for quasiparticle distribution $f(E)$, phonon distribution $n(\Omega)$, and rf drive proportionality factor B. From $f(E)$, I calculated the conductivities σ_1 and σ_2 using Eq. 2.66 and 2.67. I repeated the process for a range of rf drive powers $P_{\rm rf}$ and refrigerator temperature T_b. Here I assumed the phonon bath temperature equals the refrigerator temperature. I then compared the simulation results to our measured value of $1/Q$ and $\delta f_r/f_r$ vs $P_{\rm rf}$. I adjusted the parameters (see Table 4.1) and repeated the entire process to find a reasonable fit of the model to the data.

In the simulations, the rf power absorbed by quasiparticles $P_{\rm rf,ab}$ was calculated using Eq. 2.89. For this step I used the measured values of rf drive power $P_{\rm rf}$, overall quality factor Q, internal quality factor Q_i and external quality factor Q_e. Of course, Q_i was what I was trying to simulate, so this procedure was potentially circular. I discuss this issue in Chapter 2. Here I also assumed no TLS loss, *i.e.* $1/Q_{\rm TLS} = 0$, while the inverse quality factor from other sources $1/Q_0$ was a fit parameter. The superconducting gap Δ was a fit parameter and single-valued, as I expected the change in Δ to be much smaller than the grid size 1 μeV. In the simulations I used $\hbar\omega_r = 28$ μeV $= h \times 6.77$ GHz, which is the closest integer multiple of 1 μeV from $\hbar\omega_r$ values for rf drive frequencies ≈ 6.72 GHz. I used a quasiparticle-phonon scattering time of $\tau_0 = 438$ ns, which is the τ_0 for aluminum in Ref. [150] and phonon-quasiparticle scattering time of $\tau_\phi = 0.26$ ns which is the τ_ϕ for aluminum in Ref. [149]. I treated the phonon escape time τ_e as a fit parameter, and I actually needed to fit to also optical illumination results in Chapter 5 to obtain a value for

Table 4.1: Parameters used in nonequilibrium simulations for resonator MW2-14

.

Symbol	Parameter	Value	Source
Δ	superconducting gap	167 μeV	fit parameter
$\hbar\omega_r$	rf photon energy in simulation	28 μeV	closest 1 μeV multiple
		($h \times 6.77$ GHz)	to measured frequencies
A	resonator Al surface area	4.18×10^4 μm^2	design parameter
V	resonator Al volume	8.99×10^3 μm^3	design parameter
Q_e	external quality factor	4.9×10^9	fit to S_{21}
N_0	single spin density of states	1.74×10^{10} eV$^{-1}\mu$m^{-3}	Ref. [149]
	at Fermi level		
N_i/Ω_D^3	atomic density/(Debye frequency)^3	1.41×10^{15} (eV μm)$^{-3}$	Eq. 2.84
τ_0	quasiparticle-phonon time	438 ns	Ref. [150]
τ_ϕ	phonon-quasiparticle time	0.26 ns	Ref. [149]
τ_e	phonon escape time	8.96 ns	fit parameter (Ch. 5)
ϵ	Al absorption coefficient	$\approx 15\%$	nominal
$1/Q_{\rm TLS}$	TLS loss component	0	nominal
$1/Q_0$	power independent loss component	2.5×10^{-7}	fit parameter
α_1	$1/Q$ scaling factor	0.61%	fit parameter
α_2	$\delta f_r/f_r$ scaling factor	0.88%	fit parameter
f_0	baseline LC resonator frequency	6.720225 GHz	fit parameter
$T_{\rm eff,0}$	effective temperature	236 mK	fit parameter
	of background radiation		

τ_e. The resonator surface area was $A = 4.18 \times 10^4$ μm^2, and the thickness of the Al film was measured using a profilometer to be (215 ± 5) nm. This gives the resonator volume $V = 8.99$ μm^3. Finally, I used an approximate nominal value for the Al emissivity of $\varepsilon \approx 15\%$.

All the parameters used in the simulation are shown in Table 4.1. The dashed curves in Figs. 4.8 and 4.9 show best fit results for $1/Q$ and f_r from the nonequilibrium model using these parameters. To get fits that were this good, I found that I

had to include the effect of a background illumination with $T_{\mathrm{eff},0} = 236$ mK. Overall the simulation does a very good job of capturing the behavior of $1/Q$ and f_r with changing rf drive and temperature well. There are small discrepancies between the simulation and data, in particular in the $240 - 260$ mK range, which may be due to the approximate nature of the n_{opt} model which I used to include a background illumination.

4.2.3 Discussions: Fit Parameters

Finding the uncertainties of each of the fit parameters in Table 4.1 would require simultaneously varying all the fit parameters and then performing the nonequilibrium simulations for all rf powers, temperatures, and optical intensities for each set of parameters. In Section 5.2.3 I discuss my attempt to estimate the uncertainty of Δ, however finding the uncertainties for all of the fit parameters would be very time-consuming.

I can make some remarks about the values of some of the fit parameters shown in Table 4.1. The superconducting gap $\Delta = 167$ μeV is close to the 170 μeV expected value of the superconducting gap in Al. Goldie and Withington [149] and de Visser *et al.* [48] assumed phonon escape time $\tau_e \approx \tau_\phi$ for 100 nm thick Al films. τ_e is proportional to film thickness [151], and the Al thickness of our resonator is 215 nm. As a result I initially expected $\tau_e \approx 2.2\tau_\phi$. However I found $\tau_e = 8.96$ ns $\approx 34\tau_\phi$ was needed to maintain power balance for the absorbed optical power for $\varepsilon \approx 15\%$ (Chapter 5). This value is about an order of magnitude larger than the expected

value, however it is within the reasonable range of values of τ_e for Al on sapphire substrate, as discussed by Kaplan [151]. I found that relatively large changes in τ_e only resulted in small changes in σ_1 and σ_2.

I found that both the scaling factors α_1 and the frequency scaling factor α_2 were slightly less than 1%. In Section 2.3 I stated that α_1 and α_2 were expected to be equal to the kinetic inductance ratio α_k. I estimated the kinetic inductance for our resonator using the expression derived by Gao to estimate the kinetic inductance of coplanar waveguide resonators [126],

$$L_k = \frac{\mu_0 \lambda_{\text{eff}} l}{4a(1-k^2)K^2(k)} \left\{ (1+k) \left[\pi - \log\left(\frac{1+k}{1-k}\right) \right] + \log\left(\frac{4\pi a}{t}\right) + k \log\left(\frac{4\pi b}{t}\right) \right\}. \tag{4.3}$$

Here $2a$ is the width of the center strip, $2b$ is the separation between the two ground planes, $k = a/b$, t is the film thickness, l is the length of the strip, λ_{eff} is the effective penetration depth, and $K(k)$ is the complete elliptic integral of the first kind given by

$$K(k) = \int_0^{\pi/2} \frac{d\theta}{\sqrt{1 - k^2 \sin^2\theta}}. \tag{4.4}$$

Equation 4.3 is supposed to be valid for $t \ll a$. For our lumped-element resonator without ground planes, I used $2a = 5$ μm, $2b = \infty$, $k = 0$, $t = 215$ nm, and $l \approx 3.5$ mm. I also used Gao's calculated values of λ_{eff} for $t \approx 200$ nm, which is $\lambda_{\text{eff}} \approx 60$ nm [126], as well as the estimate of the geometric inductance of the resonator $L \approx 5$ nH. This gives an estimate of the kinetic inductance ratio of $\alpha_k \approx 1.7\%$. I note that this is a very rough estimate, and hence the scaling factor values $\alpha_1 = 0.61\%$ and $\alpha_2 = 0.88\%$ were actually quite reasonable. What is unexpected is that α_1 and

α_2 differs somewhat, with $\alpha_1 \approx 0.7\alpha_2$. Gao also discussed that for thicker films (t comparable to the mean free path), the scaling factors can deviate by up to a factor of 2/3 [126]. It is possible that the onset of the deviation in α_1 is slightly different than in α_2.

In the model I found that I had to include a rf power-independent inverse quality factor term $1/Q_0 = 2.5 \times 10^{-7}$ to get a good fit to the data. I note here that I have plotted $1/Q$ instead of $1/Q_i$. However since $1/Q_e = 2.0 \times 10^{-10}$ it was clear that I could not assign this power-independent $1/Q_0$ to the input and output lines. It was also unlikely there were additional external lines with such strong coupling to the resonator. As shown by the base temperature results, this power-independent loss $1/Q_0$ was not affected by temperature cycling and addition of a μ-metal shield, which meant it was unlikely it was due to trapped vortices. However it was possible the small increase and slight drift in $1/Q$ after the final temperature cycling was caused by trapped vortices. In the following section I report the cavity inverse quality factor $1/Q_{\text{cavity}} \approx 1.1 \times 10^{-5}$. Unfortunately I did not make a precise independent calculation of the coupling between the cavity and resonator g. Typically a 1 mm long 3d transmons mounted in the center of a 3d cavity has $g/2\pi \approx 120-150$ MHz [49, 189]. Since the scaling should scale with the length of the device, I can estimate for our 0.4 mm resonator $g/2\pi < 60$ MHz. Using Eq. 2.105, I can calculate the Purcell contribution for loss as $1/Q_{\text{Purcell}} \lesssim 7 \times 10^{-8}$. This is only about 30% of $1/Q_0$ and suggests there are additional loss sources contributing to the power-independent loss.

To get a reasonable fit to the data, I also had to include a constant background

illumination, as represented by the optically generated effective temperature $T_{\mathrm{eff},0} = 236$ mK. As shown by the model curves in Figs. 4.8 and 4.9, this was needed to account for why $1/Q$ and f_r did not change much between base temperature and 230 mK. I also note that for my fits $f_0 = 6.720225$ GHz was the resonance frequency assuming zero temperature, no rf drive, and no illumination. This value was 11 kHz higher than the measured f_r values at base temperature.

Given T_{eff}, I can use Eqs. 2.96 and 2.97 to find $P_{\mathrm{opt}}(T_{\mathrm{eff}})$ and evaluate

$$P_{\mathrm{opt}}(T_{\mathrm{eff},0}) \;=\; \varepsilon I_{\mathrm{opt},0} A \tag{4.5}$$

to find the background optical intensity $I_{\mathrm{opt},0}$. An effective temperature of $T_{\mathrm{eff},0} = 236$ mK gives $I_{\mathrm{opt},0} = 22$ aW/μm^2. While it was possible broadband light with this intensity was coupled to the cladding at the fiber input on the optical table, a significant fraction of the light should be attenuated by the mandrel wrap located at 4 K. It is more likely that there is a different source of this illumination. In Section 4.1.1 I noted the presence of a hot finger which was anchored at 4 K and extended inside the inner shield of the refrigerator to within a few inches of the cavity (see Fig. 4.1). I expected the temperature of the hot finger to be at or near 4 K. Using the Stefan-Boltzmann law, the intensity of black-body radiation from a black 4 K source is $I_{\mathrm{bb}} \approx 15$ aW/μm^2, which is comparable to $I_{\mathrm{opt},0}$. However, the resonator was not directly exposed to the hot finger, but instead was embedded inside the 3d aluminum cavity.

I can approximate the effect of a 4 K source on the cavity using the Parker heating model. I assume the phonon ballistic limit, where τ_e is proportional to

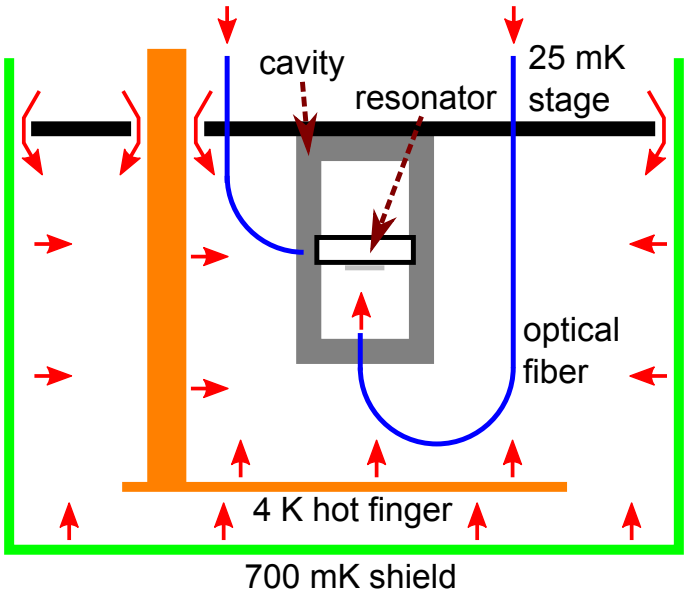

Figure 4.10: Illustration of possible sources (red arrows) of background illumination inside the dilution refrigerator. Illustration not to scale.

thickness [151], and also assume that the volume of Al forming the cavity is proportional to the illuminated area. With these assumptions, Eq. 2.97 yields an effective temperature that is independent of the cavity dimensions. Using $I_{\rm opt} = 15$ aW/μm^2 for black-body radiation from the 4 K hot finger I find the effective temperature in the Parker model to be $T_{\rm eff,c} \approx 231$ mK which is remarkably close to the value from the fit to the data especially considering the simplicity of the assumptions. This suggests the hot finger caused a nonequilibrium distribution of phonons in the cavity and resonator, even though the resonator was not directly exposed to the 4 K radiation.

Additionally, this suggested that we need to consider other possible sources of radiation, as shown by the red arrows in Fig. 4.10. These include black-body radiations from the 700 mK shield or from higher temperature stages passing through

gaps or holes in the mixing chamber plate. However, the hot finger was the hottest radiation source close to the resonator, and hence it was most likely the dominant source of background radiation.

4.2.4 Discussions: Nonequilibrium Distributions $f(E)$ and $n(\Omega)$

In this section, I discuss the quasiparticle distribution $f(E)$ and phonon distribution $n(\Omega)$ in several interesting temperature regimes. The first regime is when the bath temperature T_b is much less than the optically generated phonon effective temperature $T_{\rm eff}$. The solid curves in Figs. 4.11 show simulated results $f(E)$ and $n(\Omega)$ as a function of normalized energy for $T_b = 25$ mK and $T_{\rm eff,0} = 236$ mK for several values of $P_{\rm rf}$. These are clearly nonequilibrium distributions with peaks appearing every hf_r/Δ due to the microwave drive term. We also see jumps in $f(E)$ at $E = 3\Delta$ and in $n(\Omega)$ at $\Omega = 2\Delta$. These jumps come from the discontinuity in $n_{\rm opt}$ (see Eq. 2.95) as well as pair breaking and recombination. $f(E)$ generally increases with increasing $P_{\rm rf}$, except in parts between $E = \Delta$ and $E = \Delta + hf_r$ where it decreases instead. As discussed previously, this behavior causes $1/Q_{qp}$ to decrease with increasing rf drive power $P_{\rm rf}$. However I note here for E slightly less than $\Delta + hf_r$, $f(E)$ appears to increase with increasing $P_{\rm rf}$, unlike the no illumination case.

For comparison, the purple dashed curves in Figs. 4.11 show $f(E)$ and $n(\Omega)$ for a thermal distribution with $T = T_b = 25$ mK and the yellow dashed curves show $f(E)$ and $n(\Omega)$ for a thermal distribution with $T = T_{\rm eff,0} = 236$ mK. The

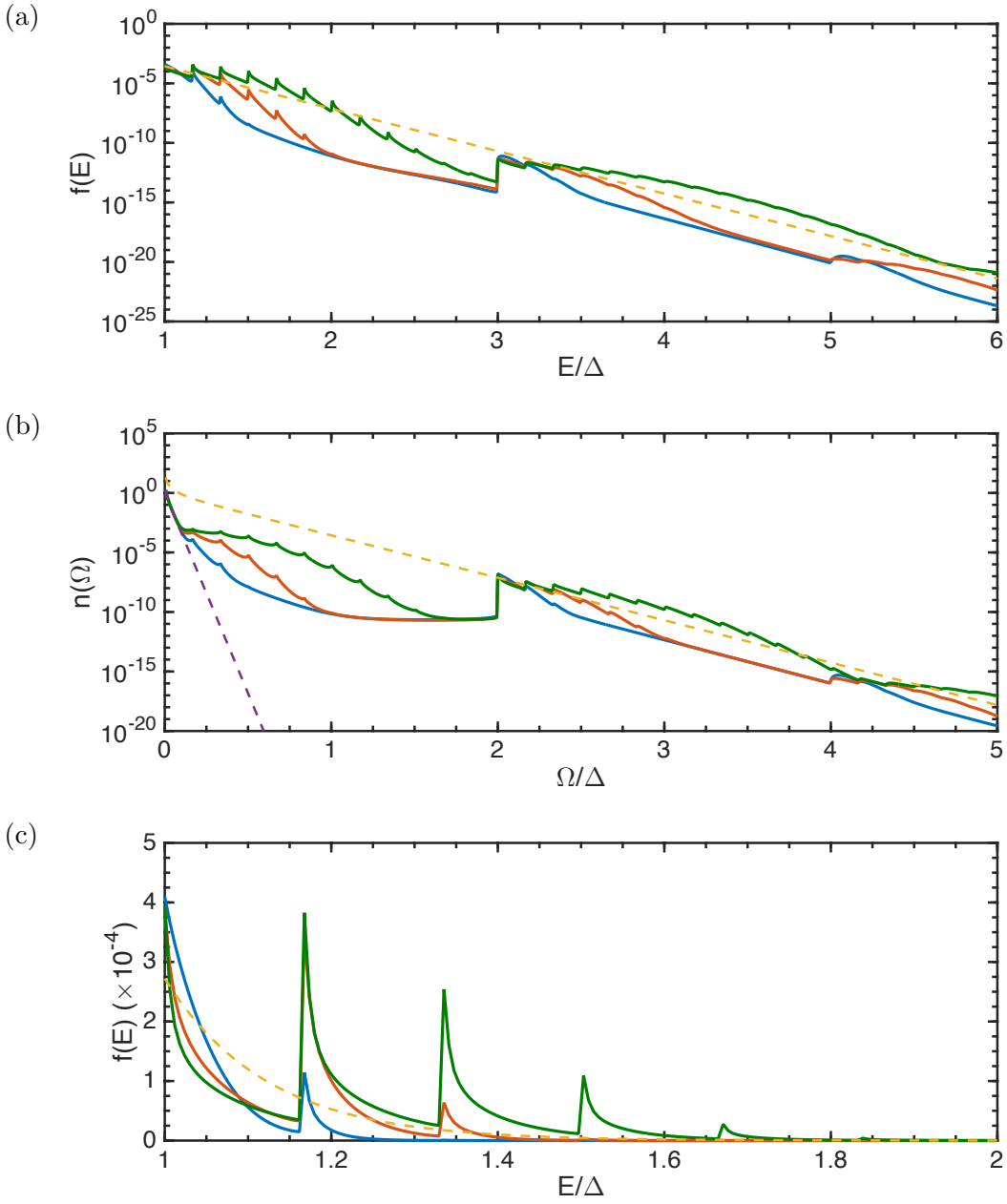

Figure 4.11: (a) Simulated quasiparticle distribution $f(E)$ vs normalized energy E/Δ and (b) Simulated phonon distribution $n(\Omega)$ vs normalized energy Ω/Δ, both for illumination model with bath temperature $T_b = 25$ mK and effective optical illumination background temperature $T_{\text{eff},0} = 236$ mK and several rf drive powers P_{rf}: -65 dBm (blue curve), -55 dBm (red curve), and -45 dBm (green curve). Other parameters are shown in Table 4.1. The purple dashed curve is the thermal distribution for $T_b = 25$ mK and the yellow dashed curve is the thermal distribution for $T_{\text{eff},0} = 236$ mK. (c) Linear plot of $f(E)$ between $E = \Delta$ and $E = 2\Delta$.

purple curve is located outside the figure limits for the quasiparticle distribution $f(E)$. For Ω near 0, $n(\Omega)$ follows the T_b thermal distribution very closely for up to $\Omega \approx hf_r$ before deviating significantly for all $P_{\rm rf}$. Although this is a very coarse log scale, the nonequilibrium $n(\Omega)$ distributions appear to follow the $T_{\rm eff,0}$ thermal distribution for $\Omega > 2\Delta$, as would be expected due to the $n_{\rm opt}$ source term. $f(E)$ distributions appear to roughly follow $T_{\rm eff,0}$ thermal distribution for $E > 3\Delta$ as well. This behavior was not obvious in the kinetic equations.

The second regime of interest is when T_b is comparable to $T_{\rm eff}$. The solid curves in Figs. 4.12 show $f(E)$ and $n(\Omega)$ as a function of normalized energy for $T_b = 230$ mK and $T_{\rm eff,0} = 236$ mK for several values of $P_{\rm rf}$. The difference in $f(E)$ between different $P_{\rm rf}$ values is much less compared to the difference for $T_b = 25$ mK for the same $P_{\rm rf}$ values. The jumps in $n(\Omega)$ at $\Omega = 2\Delta$ is still visible, although the height of the jump appears to be much less than the jumps for $T_b = 25$ mK. Similarly, if there is a jump in $f(E)$ at $E = 3\Delta$ it is so small it is not visible.

For comparison, the purple dashed curves in Figs. 4.12(a) and 4.12(b) show $f(E)$ and $n(\Omega)$ for a thermal distribution with $T = T_b = 230$ mK and the yellow dashed curves show $f(E)$ and $n(\Omega)$ for a thermal distribution with $T = T_{\rm eff,0} = 236$ mK. $f(E)$ at the lower $P_{\rm rf}$ values appears to follow closely the effective temperature $T_{\rm eff}$ distribution. For all $P_{\rm rf}$ values, $n(\Omega)$ follows the bath temperature distribution T_b up to the jump at $\Omega = 2\Delta$. For lower $P_{\rm rf}$ values, $n(\Omega)$ closely follows the effective temperature $T_{\rm eff}$ distribution above the jump at $\Omega = 2\Delta$.

The last regime of interest is when T_b is significantly larger than $T_{\rm eff}$. The solid red curves in Figs. 4.13 show $f(E)$ and $n(\Omega)$ as a function of normalized energy for

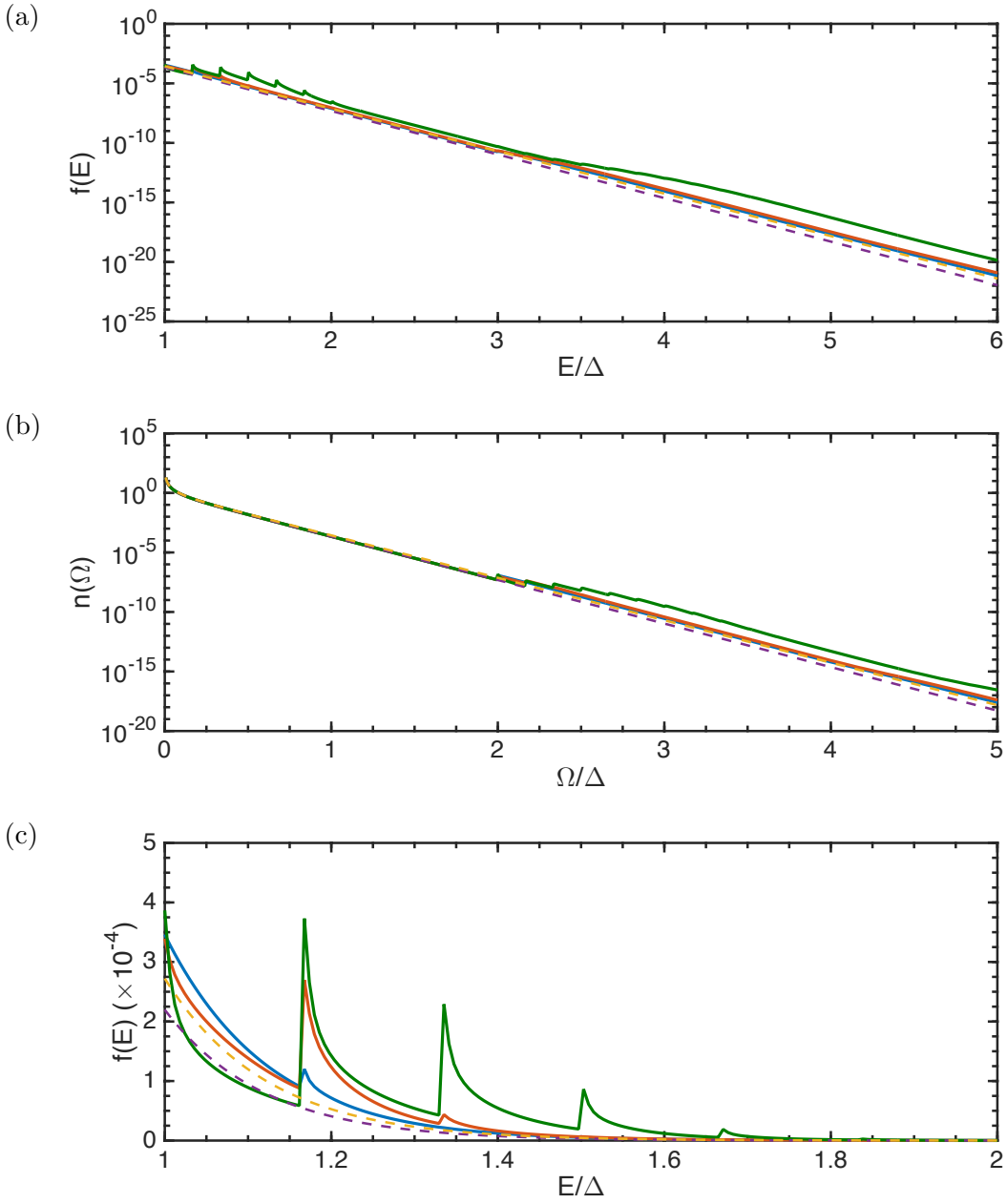

Figure 4.12: (a) Simulated quasiparticle distribution $f(E)$ vs normalized energy E/Δ and (b) Simulated phonon distribution $n(\Omega)$ vs normalized energy Ω/Δ, both for illumination model with bath temperature $T_b = 230$ mK and effective optical illumination background temperature $T_{\text{eff},0} = 236$ mK and several rf drive powers P_{rf}: -65 dBm (blue curve), -55 dBm (red curve), and -45 dBm (green curve). Other parameters are shown in Table 4.1. The purple dashed curve is the thermal distribution for $T_b = 230$ mK and the yellow dashed curve is the thermal distribution for $T_{\text{eff},0} = 236$ mK. (c) Linear plot of $f(E)$ between $E = \Delta$ and $E = 2\Delta$.

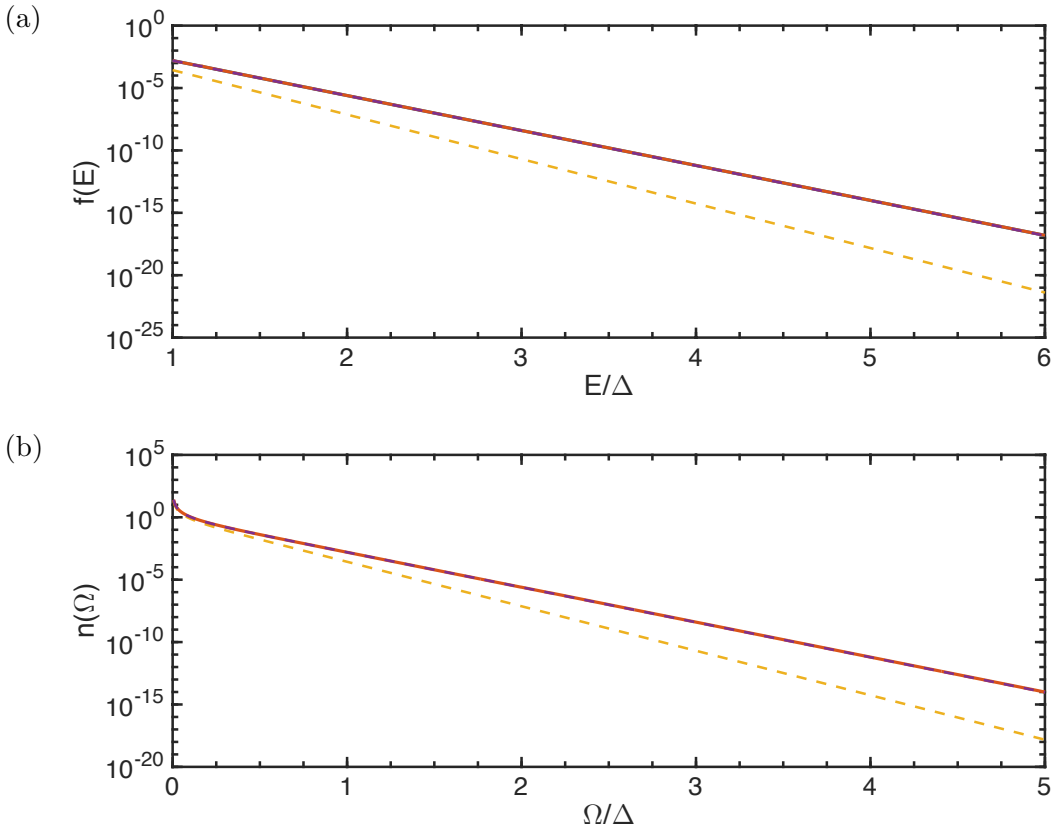

Figure 4.13: (a) Simulated quasiparticle distribution $f(E)$ vs normalized energy E/Δ and (b) Simulated phonon distribution $n(\Omega)$ vs normalized energy Ω/Δ, both for illumination model with bath temperature $T_b = 300$ mK and effective optical illumination background temperature $T_{\text{eff},0} = 236$ mK and $P_{\text{rf}} = -55$ (red curve). Other parameters are shown in Table 4.1. The purple dashed curve is the thermal distribution for $T_b = 300$ mK and the yellow dashed curve is the thermal distribution for $T_{\text{eff},0} = 236$ mK.

$T_b = 300$ mK and $T_{\text{eff},0} = 236$ mK for $P_{\text{rf}} = -55$ dBm. I only plotted one P_{rf} because between the range of measured P_{rf} values (-65 to -55 dBm) the distributions at other P_{rf} values were almost indistinguishable. This independence from P_{rf} is also seen as a flat $1/Q$ vs P_{rf} curve, as shown by the 300 mK (dark green) data and curve in Fig. 4.8. For comparison, the purple dashed curves in Figs. 4.13(a) and 4.13(b) show $f(E)$ and $n(\Omega)$ for a thermal distribution with $T = T_b = 300$ mK and the yellow dashed curves show $f(E)$ and $n(\Omega)$ for a thermal distribution with $T = T_{\text{eff},0} = 236$ mK. Here both $f(E)$ and $n(\Omega)$ appear to follow the bath temperature T_b thermal distribution for the entire range of energies.

4.3 Properties of the 3D Aluminum Cavity

While the properties of the 3d cavity were not the focus of my measurements, we did take some S_{21} traces around the cavity resonance frequency using the VNA. At the 25 mK base temperature the 3d cavity has a resonance frequency $f_c = 7.501$ GHz and a quality factor $Q \approx 9.1 \times 10^4$. By fitting to S_{21} at 300 K, we found the cavity to have $\frac{1}{2}\sqrt{Q_{\text{in}}Q_{\text{out}}} \approx 1.3 \times 10^5$. We chose the input and output pins to have an approximately balanced coupling, *i.e.* $Q_{\text{in}} \approx Q_{\text{out}}$ and from the relations between the Q values, I found an internal quality factor $Q_i \approx 3 \times 10^5$. This value was relatively low for a typical Al 3d cavity used in transmon experiments. A more typical value would be $Q_i \gtrsim 10^6$. However this lower value was not unreasonable since we did not perform extensive cleaning of the cavity (see Section 3.3). During this cooldown we did not perform P_{rf} dependent studies of the 3d cavity, however

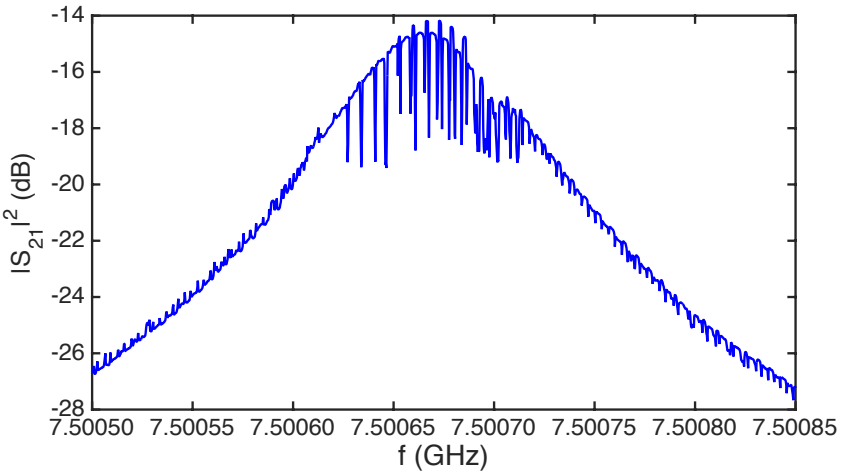

Figure 4.14: Transmission $|S_{21}|^2$ vs frequency f of cavity TE101 mode at base temperature 25 mK, showing apparent periodic jitter.

in other cooldowns we observed that the Q_i of the cavity was independent of P_{rf} for several orders of magnitude range in P_{rf}, between about -110 dBm and -50 dBm.

One problem we found was that the cavity resonance showed jitter, for example in the S_{21} vs f plot (see Fig. 4.14). From Fig. 4.14 it is apparent that the jitter was periodic. In Fig. 4.15, I plot S_{21} value as a function of time at the peak frequency, as well as both 70 kHz and 370 kHz above and below the peak. In Figs. 4.15(b) and 4.15(c), red is below resonance, and blue is above resonance. We found that the jitter occurred every 14 ms (or 70 Hz), although it does not always happen and the apparent strength varied. The effect of the jitter appeared to be strongest about 70 kHz above the resonance, and got significantly weaker further away. I Note that these plots were not taken at the same time, hence the jitter occurrence times did not exactly align with each other.

The nature, low-frequency, and the periodicity of the jitter suggested mechan-

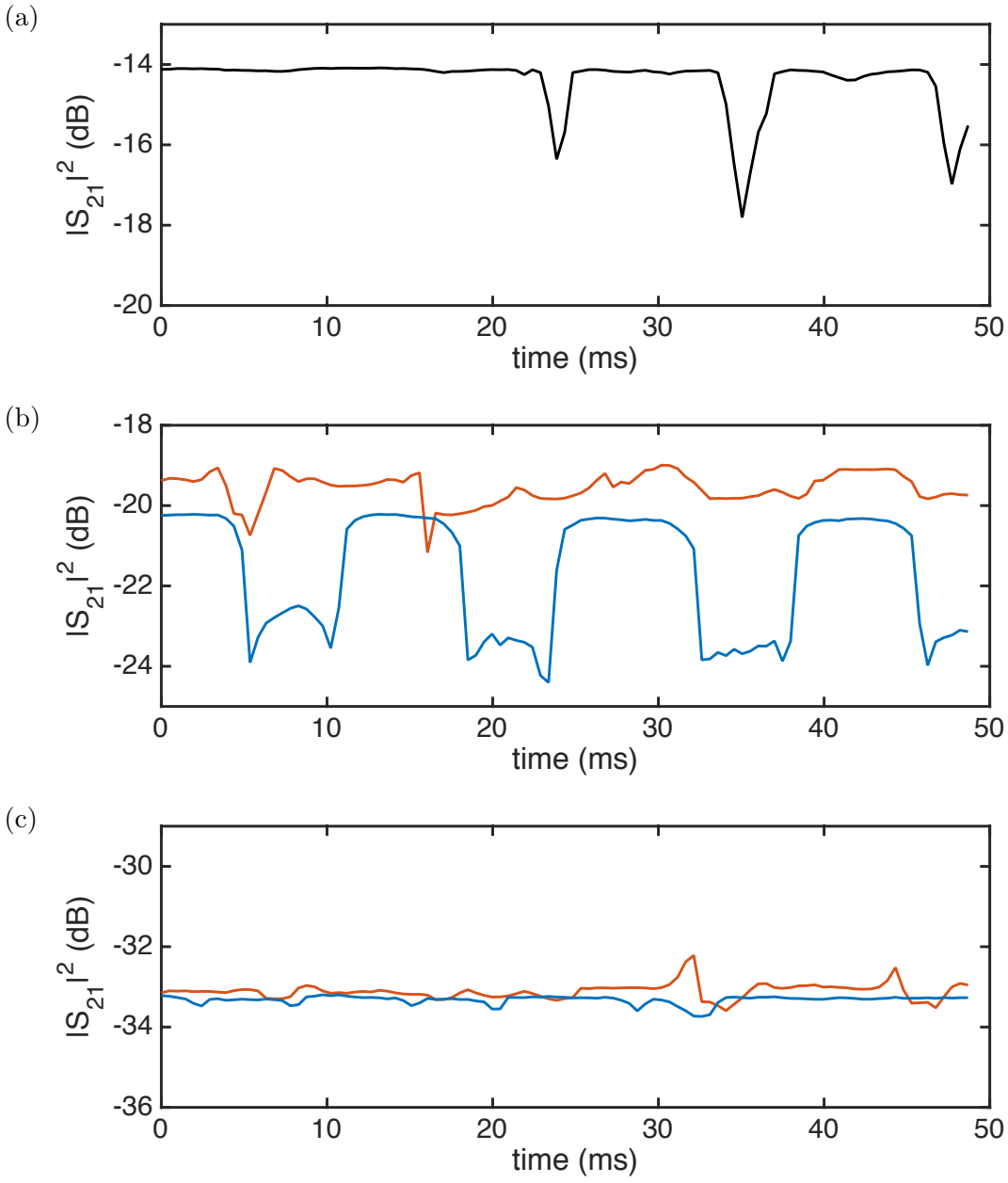

Figure 4.15: Transmission $|S_{21}|^2$ vs time t of cavity TE101 mode at different frequencies: (a) at resonance of frequency of 7.500670 GHz, (b) 70 kHz above and below resonance, and (c) 370 kHz above and below resonance. For (b) and (c), red is below resonance, and blue is above resonance. The periodic jitter can be seen.

ical movement inside the cavity. One of the component in the cavity that could move were the optical fibers. Each fiber had one point where it was secured with Stycast epoxy to the cavity or the bracket. For the perpendicular fiber, the end of the fiber was located about 1 cm from this point, while for the parallel fiber it was approximately 1 mm. These fibers could act as a cantilever beam and vibrate. The fiber dielectric would then interact with the electric field inside the cavity and perturb the TE101 mode frequency of the cavity. One end of the perpendicular fiber was located where the TE101 mode electric field strength was a minimum and should have produced only very small effect on the TE101 mode. On the other hand, the perpendicular fiber was in a location where there was a significant electric field gradient. The parallel fiber was located closer to the field strength maximum, but with much shorter length, the effect should be very small and we would expect a much higher frequency.

I can estimate the natural frequencies of vibration of these fiber by using the expression for the n-th mode frequency f_n of a cantilever beam, which is given by [190]

$$f_n \;=\; \frac{(\beta_n l)^2}{2\pi l^2}\sqrt{\frac{EI}{\rho A}}, \tag{4.6}$$

where here E is the Young's modulus, ρ is the mass density, I is the second moment of area, A is the cross-sectional area of the beam, l is the length of the beam, and $(\beta_n l)$ is a solution for the equation of motion of the beam. For $n = 1$, the equations of motion give the solution $(\beta_1 l)^2 \approx 3.52$. For a cylindrical beam with a diameter d, $A = \pi d^2/4$ and $I = \pi d^4/64$. This lowest mode frequency of a cylindrical beam is

then given by

$$f_1 \approx \frac{3.52}{2\pi}\sqrt{\frac{Ed^2}{16\rho L^4}}. \tag{4.7}$$

For our optical fibers, I have $d = 125$ μm, and used the parameters for fused silica, where $\rho = 2200$ kg/m^3 and $E = 72$ GPa. For the 1 mm long parallel fiber, the lowest mode frequency is $f_1 \approx 100$ kHz, while for the 1 cm long perpendicular fiber, $f_1 \approx 1$ kHz. The frequency of the perpendicular fiber was only one order of magnitude larger than the jitter frequency.

In Fig. 4.16(a), I have plotted another measurement of $|S_{21}|^2$ vs time t, this time with a better time resolution so that one can better see the behavior during a jitter. Between 2 and 5 ms there appeared to be a damped oscillation with a frequency ≈ 4 kHz. Figure. 4.16(b) shows a spectrogram representation of Fig. 4.16(a) found using a code written by Jonathan Hoffman [82]. A spectrogram is a representation of the spectrum of a signal as they vary with time. The signal was binned into multiple overlapping time windows and a Fast Fourier Transform (FFT) was performed to obtain the spectrum within these windows. In the spectrogram, brighter means stronger signal at that frequency. From the spectrogram, I can also see that $|S_{21}|^2$ had an oscillation with a 4 kHz frequency from 2 up to 10 ms, and there may be oscillations at 8 kHz. It is possible that these frequencies come from the fiber vibrations discussed above and suggests that the jitter is actually due to an external kick that causes the fibers to vibrate. However, the shape of the signal varies a good deal and does not exactly follow this behavior.

A possible source of kick or vibrations in the refrigerator would be the turbo

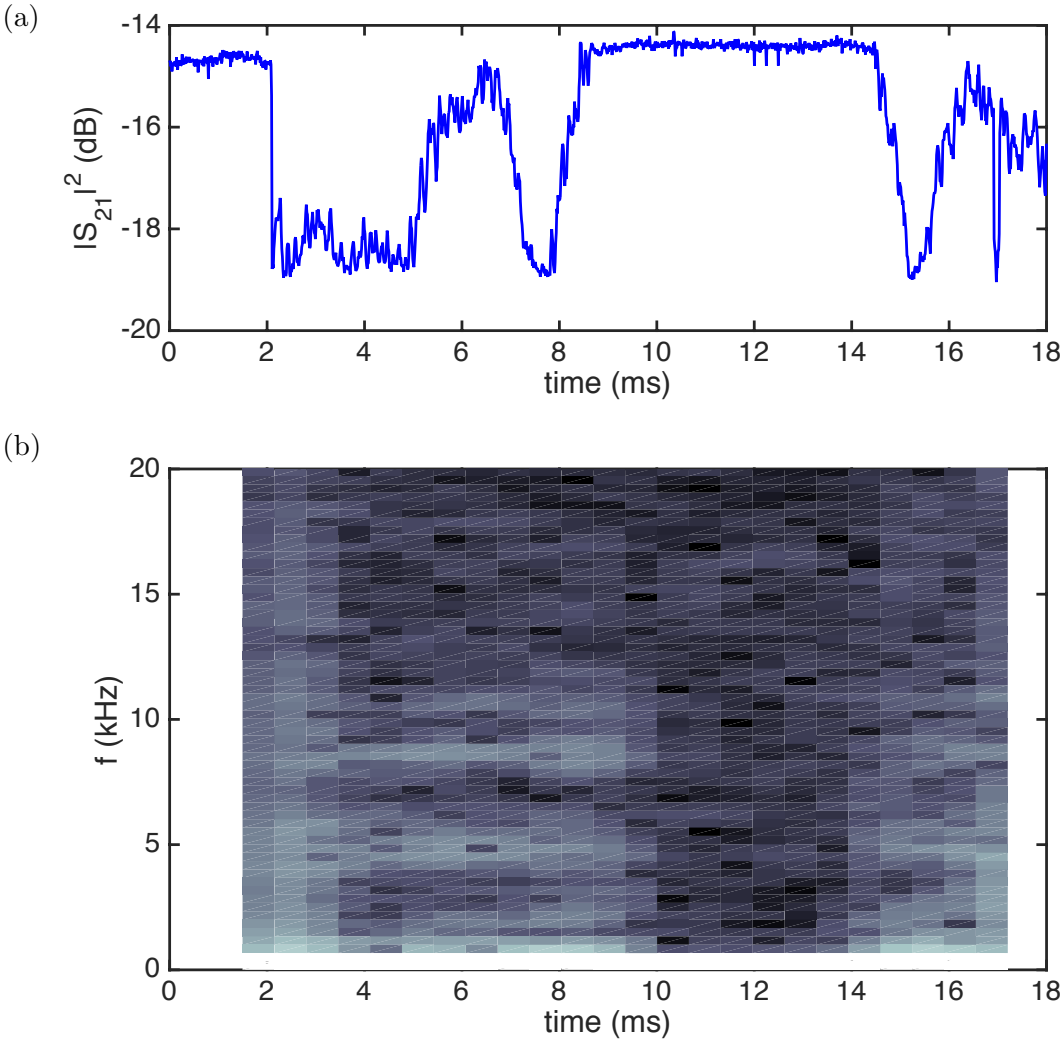

Figure 4.16: (a) Transmission $|S_{21}|^2$ vs time t of cavity TE101 mode at frequency 7.500670 GHz. (b) Associated spectrogram representation of (a). Brighter means stronger signal.

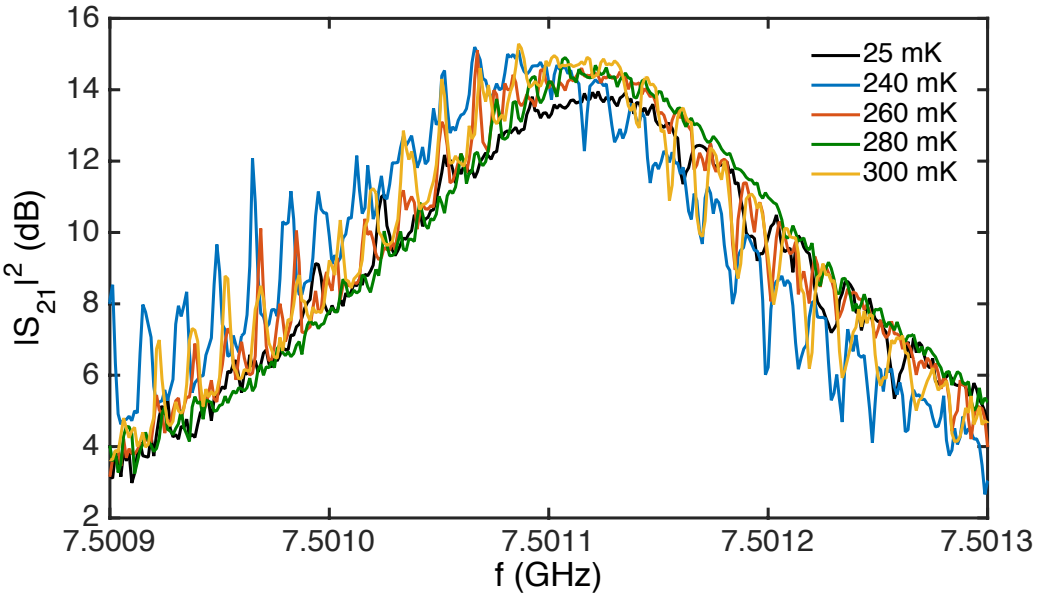

Figure 4.17: Transmission $|S_{21}|^2$ vs frequency f of cavity TE101 mode at several temperatures: 25 mK (black curve), 240 mK (blue curve), 260 mK (red cuve), 280 mK (green curve), 300 mK (yellow curve).

pump and the pulse tube running the refrigerator. We turned off both and this caused the refrigerator temperature to drift up to about 400 mK over 30 minutes. This appeared to reduce the jitter greatly, however the 70 Hz jitter frequency appeared to be unchanged. We also tried tapping the frame of the refrigerator, which caused the jitter to become stronger again, with the same 70 Hz frequency. This suggests that the source of the jitter was not completely removed with the pumps turned off, although the vibration of the pumps may have amplified them. However the ultimate source of the jitter was unclear.

When we turned off the pumps and the refrigerator temperature drifted up to 400 mK, the resonance frequency f_r and internal quality factor Q_i did not seem to change much. We also performed measurements of the cavity when the refrigerator

was set at elevated temperatures, as discussed in Section 4.2. Fig. 4.17 shows several $|S_{21}|^2$ vs f traces of the cavity TE101 mode at several temperatures. The shape of the resonance did not seem to change much with temperature, and there did not seem to be any trend in S_{21} with increasing temperature. Here the turbo pump and the pulse tube were running and jitter effects appear in the entire range of temperature. Again, this made detailed study of the cavity difficult. Fortunately, the jitter did not seem to occur in the LC resonance, which was our main quantity of interest.

4.4 Summary

In this chapter, I discussed measurement results on resonator MW2-14 when no optical illumination was applied. First, I discussed the behavior of the inverse quality factor $1/Q$ and resonance frequency f_r at the base temperature of about 25 mK. At low rf drive powers $P_{\rm rf}$, we saw multiple branches in both $1/Q$ and f_r, as well as a substantial decrease in $1/Q$ with increasing power. I argued that many of the behavior at low powers can be explained by coupling between the resonator and a single TLS.

At higher $P_{\rm rf}$, we also saw a decrease in $1/Q$ with increasing $P_{\rm rf}$. The behavior in this regime can be explained by nonequilibrium quasiparticles, although I had to include background radiation represented by an effective temperature $T_{\rm eff,0} =$ 236 mK. By fitting the base temperature and the higher temperature results to the nonequilibrium quasiparticle model, I extracted the physical parameters of the

resonator. The parameters were generally close to their expected values. I discussed the possible sources of background radiation, which most likely came from blackbody radiation from a hot finger creating nonequilibrium distribution of phonons in the cavity and the resonator. Finally, I discussed the shape of the quasiparticle distribution $f(E)$ and phonon distribution $n(\Omega)$ at several temperature regimes.

Finally, I discussed the jitter we observed in the 3d cavity resonance. I discussed the possible sources of the jitter, which seemed to be enhanced by the operation of the pumps and was possibly caused by the vibration of the perpendicular fiber within the cavity.

Chapter 5: Resonator Results: Optical Illumination of Resonator

In this chapter, I discuss my results on measurements of resonator MW2-14 at base temperature under optical illumination. The behavior of the quality factor as a function of rf drive powers under continuous illumination appeared very similarly to what I expected for TLS loss, however the TLS loss increased under illumination. This was not what I expected as I discuss below. In contrast I was eventually able to show that the quality factor and resonance frequency could be fit well to the nonequilibrium quasiparticle model discussed in Chapter 2. This made more sense and also required fewer *ad hoc* assumptions. I also compare the effect of illumination between the perpendicular fiber and parallel fiber, and the effect of light polarization on the response. Finally, I discuss the effect of applying pulsed light on the response.

5.1 Expected Result of Illumination

In Section 2.3.5 I discussed how optical illumination of a superconductor generates quasiparticles. In my nonequilibrium quasiparticle model, optical illumination effectively acts as a source of nonequilibrium phonons with energy greater than 2Δ, parameterized by an effective temperature $T_{\rm eff}$. Increasing illumination intensity $I_{\rm opt}$ increases $T_{\rm eff}$. Since phonons with energy greater than 2Δ can break pairs and

generate quasiparticles, the quasiparticle density increases due to illumination. This causes the loss factor $1/Q_{\rm qp}$ to increase and the resonance frequency f_r to decrease with increasing $I_{\rm opt}$. Of course, the effect of the rf drive is also important in the nonequilibrium model. This will introduce an rf power $P_{\rm rf}$ dependence in $1/Q_{\rm qp}$ and f_r. In fact, as I discussed in Chapter 4, I had to include a contribution from background illumination to understand the response of the resonator to rf power. This illumination was likely caused by background blackbody radiation from the 4 K hot finger. At base temperature with this background illumination, we found $1/Q_{\rm qp}$ decreased with increasing $P_{\rm rf}$.

On the other hand, the loss from TLS, as discussed in Section 2.2, doesn't appear to have an explicit $I_{\rm opt}$ dependence. However, one might expect that optical illumination would increase the temperature of the TLS ensemble. This would decrease the loss factor $1/Q_{\rm TLS,e}$ due to the $\tanh(\hbar\omega/2k_BT)$ factor in Eq. 2.55. For typical resonator parameters, increasing TLS temperature would also generally increase f_r except at the lowest temperatures, as shown in Fig. 2.9. In fact, this frequency increase has been reported by Wang *et al.* in Nb resonators on Si substrate under 635 nm optical illumination [191]. They were able to observe this increase in frequency in Nb because Nb has a critical temperature $T_c \approx 9$ K, and typically thermal quasiparticle effects only become significant for temperatures above about 10% T_c. As a result, one can observe an increase in f_r with increasing temperature due to TLS below 1 K in Nb without the effect being hidden by quasiparticles [41]. Al on the other hand has $T_c \approx 1.2$ K. Below about 150 mK, the TLS actually causes f_r to decrease with increasing temperature as shown in Fig. 2.9, and above that

changes from the loss in quasiparticles tend to dominate. In addition, the presence of background radiation must be taken into account. As a result I expected it to be difficult in my aluminum resonators to see a clear signature of the frequency increase due to TLS under illumination in our resonator.

As I discussed in Section 4.1.2, our resonator was likely coupled to only a few TLSs within the bandwidth of the resonator. One might also expect that photoabsorption by a TLS could activate a TLS that was otherwise not contributing to the loss. However, photoabsorption could also remove TLSs from the bandwidth of the resonator, leading to reduced loss. Since the distribution of TLS asymmetry energy is expected to be uniform [121], we would not expect photoabsorption to produce a net change in the number of active TLSs in the bandwidth of the resonator. Taking the above considerations into account, I thus concluded that loss from TLSs should decrease or show no change with optical illumination.

5.2 Resonator Properties Under Continuous Illumination

5.2.1 Measurement Details

Jared Hertzberg and I performed the resonator illumination measurements. I described the optical illumination setup in Section 3.5. We used a range of optical illumination powers from 0.1 to 4.0 μW at 780 nm, as measured at the power meter when no ND filter was applied. For this experiment, we used a Thorlabs NE60A neutral density filter [185], with a measured transmission of 0.034% for 780 nm light. Taking into account the splitting ratio of the fiber splitter, and the distance

between the resonator and the end of the fiber (see Section 3.5), this range of optical power corresponds to a range of optical intensities $I_{\rm opt}$ between 20 and 812 aW/μm^2 incident at the chip surface. This corresponds to roughly 80 to 3200 optical photons per second per μm^2 striking the Al surface of the LC resonator. Of course not all of these would be absorbed as aluminum is quite reflective.

The power from the laser tended to drift, typically by a small amount. After passing the ND filter the powers were smaller than, or of order of the 1nW resolution of the power meter. This made continuous measurement of the optical power difficult. Instead, at the beginning of a set of measurements, we measured the initial optical power without the ND filter. After about 1 hour of measurement, we measured the power again without the ND filter. If the power drifted by more than 5%, we retook the measurements. In practice, this happened very rarely. This process was repeated every hour that we took data.

We performed transmission measurements of the resonance under illumination in two sessions. In both sessions, the temperature of the refrigerator was kept at base of about 25 mK. The first session was between October 2, 2013 and October 19, 2013, between the first and second temperature cycles. During this session, we focused on lower and intermediate rf drive power $P_{\rm rf}$ regime.

The closed circles in Figs. 5.1 and 5.2 show the inverse quality factor $1/Q$ and resonance frequency f_r as a function of $P_{\rm rf}$ for all applied optical intensities from the first session, with different color representing different intensities. In both plots, the black closed circles represent the measurements when no optical illumination was applied taken during the same session.

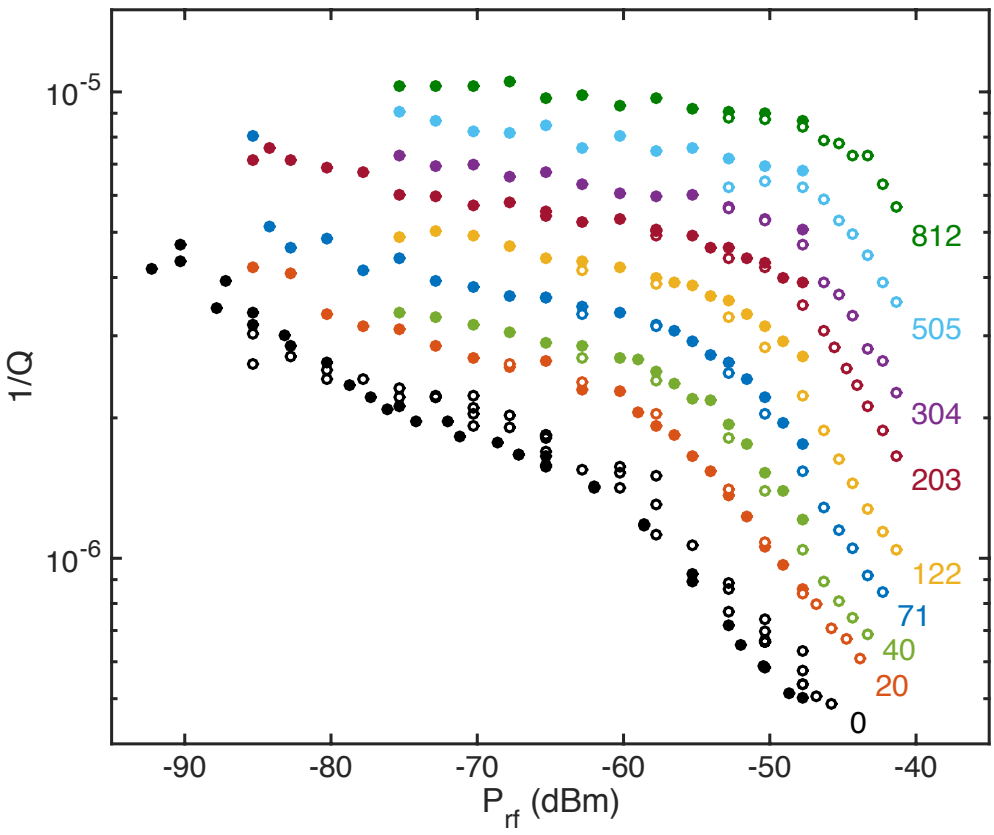

Figure 5.1: Inverse quality factor $1/Q$ vs rf drive powers $P_{\rm rf}$ at base temperature 25 mK under 780 nm optical illumination for intensities $I_{\rm opt}$ as indicated with units of aW/μm^2. The closed circles were taken during the first illumination session, the open circles were taken during the second session.

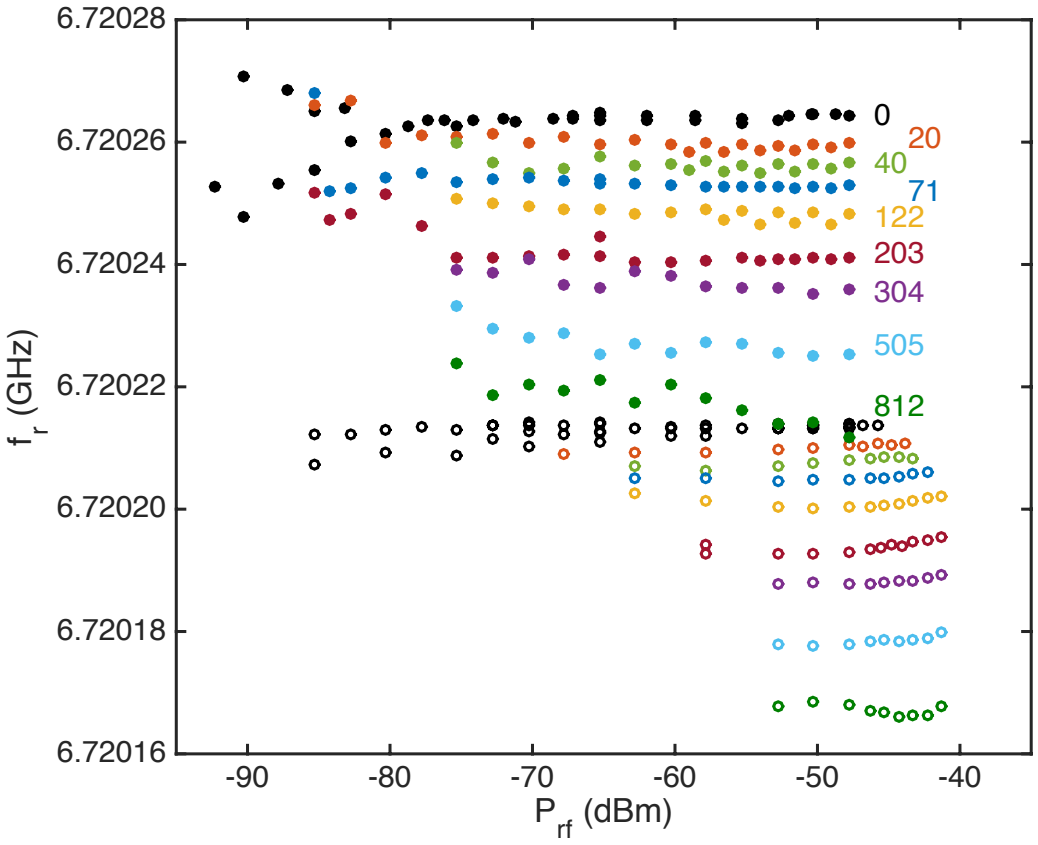

Figure 5.2: Resonance frequency f_r vs rf drive powers $P_{\rm rf}$ at base temperature 25 mK under 780 nm optical illumination for intensities $I_{\rm opt}$ as indicated with units of aW/μm^2. The closed circles were taken during the first illumination session, the open circles were taken during the second session.

The second session was between Novermber 7, 2013 and November 9, 2013, after the third temperature cycle. As I discussed in Section 4.1.1, the resonance frequency at base temperature during this session was shifted down by about 50 kHz compared to the early October session. The second session was performed after we added the Mini-Circuits ZRON-8G+ high power amplifier at the input line, and we focused our measurements on higher values of P_{rf}. At lower optical intensities, the maximum P_{rf} value was limited by the onset of distortion, similar to the ones we observed at base temperature and discussed in Section 4.1.1. The P_{rf} values where the distortion started to appear increased with increasing I_{opt}. At higher optical intensities, the maximum P_{rf} value was around -40 dBm, limited by the compression point of the amplifiers.

The open circles in Figs. 5.1 and 5.2 show the inverse quality factor $1/Q$ and resonance frequency f_r as a function of P_{rf} for all applied optical intensities from the second session, with different color representing different intensities. In both plots, the black open circles represent the measurements when no optical illumination was applied taken during the same session. As can be seen in Fig. 5.1, the $1/Q$ values from the two sessions overlap well for the same I_{opt}. On the other hand, for the same I_{opt}, f_r values for the second session was shifted down from f_r values for the first session by exactly 50 kHz as would be expected, as can be seen in Fig. 5.2.

5.2.2 Initial Interpretation of Results

Examination of Fig. 5.1 reveals that the loss $1/Q$ increases with increasing $I_{\rm opt}$ and decreases with increasing $P_{\rm rf}$. Above a a certain power level, $1/Q$ starts decreasing faster with increasing $P_{\rm rf}$. This point depends on $I_{\rm opt}$ and increases with increasing $I_{\rm opt}$. Figure 5.2 shows that f_r decreases with increasing $I_{\rm opt}$. For the highest values of $P_{\rm rf}$ taken during the second session, f_r appears to slightly increase with increasing $P_{\rm rf}$. For intermediate values of $P_{\rm rf}$, f_r seems to be independent of $P_{\rm rf}$.

At low $P_{\rm rf}$ values the resonance frequencies f_r appeared to shift from the values at intermediate powers. This occurred at all optical powers, but is most obvious in Fig. 5.2 at $I_{\rm opt} = 0$ (black filled circles). Additionally, there appeared to be a jump between branches for $I_{\rm opt} = 71$ aW/μm^2 (see dark blue filled circles). This suggests that the coupling between the resonator and a few TLS, as discussed in Section 4.1.2, is still significant at low rf drive powers under illumination. However, the low $P_{\rm rf}$ values where f_r started to shift appeared to increase with increasing $I_{\rm opt}$.

Generally loss from a distribution of TLSs depends on the electric field in the dielectric, the rms voltage across the capacitor V_{LC}, or the average rf photon number $\langle n \rangle$, which is related to V_{LC} by Eq. 2.29. Here I plotted both $1/Q$ and f_r vs rf drive power $P_{\rm rf}$ at the input of the cavity . V_{LC} is related to $P_{\rm in}$ by Eq. 2.26, and $\langle n \rangle$ is related to $P_{\rm in}$ by Eq. 2.30. I note that $\langle n \rangle$ only depends on directly measured parameters, while V_{LC} requires assumptions on values of input and output

capacitances $C_{\rm in}$ and $C_{\rm out}$. For $Q_{\rm in} = Q_{\rm out} = 2Q_e$, Eq. 2.30 can be rewritten as

$$\langle n \rangle \;=\; \frac{2Q^2 P_{\rm in}}{Q_e \hbar \omega_0^2} \;=\; \frac{Q^2 P_{\rm in}}{\pi Q_e h f_r^2}. \tag{5.1}$$

As I've discussed, Q_e is constant while Q_i varies with $P_{\rm rf}$. f_r also varies, however in my resonators $\delta f_r / f_r \ll 1$. For many resonators used in circuit QED, $Q_e \ll Q_i$ and $Q \approx Q_e$, hence $\langle n \rangle$ is

$$\langle n \rangle_{\rm typ} \;\approx\; \frac{Q_e P_{\rm in}}{\pi h f_r^2} \;\propto\; P_{\rm in}. \tag{5.2}$$

Hence $\langle n \rangle$ increases with increasing $P_{\rm rf}$, and all measurements with the same $P_{\rm rf}$ has the same $\langle n \rangle$. However, in the resonator I used, I have $Q_i \ll Q_e$ and $Q \approx Q_i$, and one finds

$$\langle n \rangle_{\rm us} \;\approx\; \frac{Q_i^2 P_{\rm in}}{\pi Q_e h f_r^2} \;\propto\; Q_i^2 P_{\rm in}. \tag{5.3}$$

Thus $\langle n \rangle$ depends strongly on Q_i in my device. For the same $P_{\rm rf}$, Q_i decreases with increasing bath temperature T_b or optical intensity $I_{\rm opt}$. This means for the same $P_{\rm rf}$, $\langle n \rangle$ decreases with increasing bath temperature T_b or optical intensity $I_{\rm opt}$.

Figures 5.3(a) and 5.3(b) show measured values for $1/Q$ and f_r as a function of $\langle n \rangle$. For Fig. 5.3(b), I only show f_r from the first illumination session. The dashed vertical line in Fig. 5.3(b) at $\langle n \rangle = 2 \times 10^3$ shows the estimated upper limit of the multiple branch behavior under no illumination. While we did not take too many measurements at low power, it seems under illumination the branching behavior also appeared at roughly the same $\langle n \rangle$ value of a few thousand. This is consistent with the branching due to coupling to TLS, as described earlier.

The shape of the measured $1/Q$ vs $\langle n \rangle$ curves in Fig. 5.3(a) appear very similarly to what one expects for $1/Q$ from an ensemble of TLSs (Eq. 2.55), which may

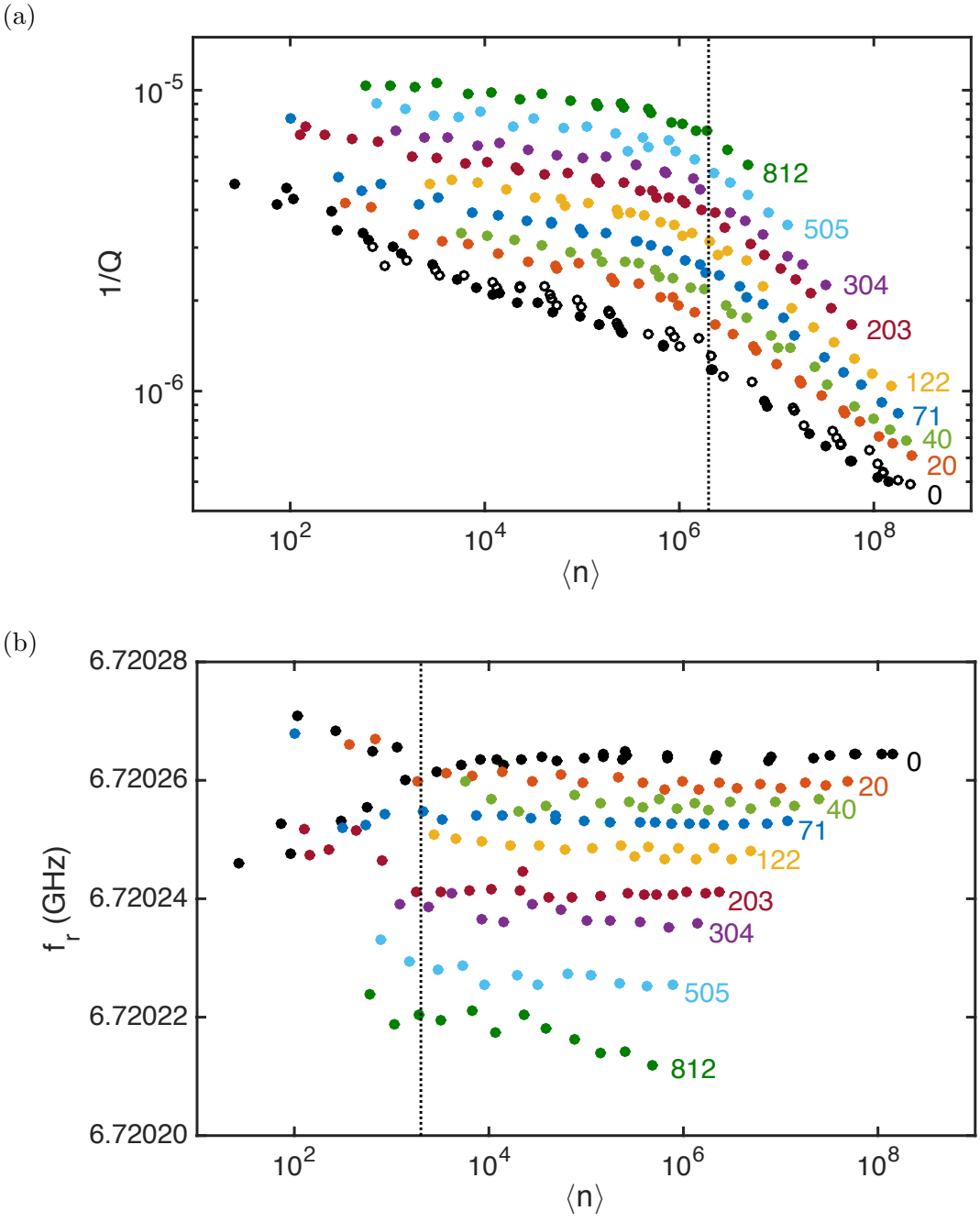

Figure 5.3: (a) Inverse quality factor $1/Q$ and (b) resonance frequency f_r, both vs average rf photon numbers $\langle n \rangle$ at base temperature 25 mK under 780 nm optical illumination for intensities I_{opt} shown in Figure with units of aW/μm^2. The vertical dashed line in (a) was $\langle n \rangle = 2 \times 10^6$ where $1/Q$ start decreasing more rapidly with increasing $\langle n \rangle$, and the vertical dashed line in (b) was $\langle n \rangle = 2 \times 10^3$, which was an estimated upper limit of multiple branch behavior in f_r.

lead one to think that the significant loss component was due to TLSs in this regime. I note however that the point where $1/Q$ starts decreasing more rapidly with increasing $\langle n \rangle$ appears to be about the same for all $I_{\rm opt}$ and is at $\langle n \rangle = 2 \times 10^6$. This is represented by the dashed vertical line in Fig. 5.3(a). Given that the observed $1/Q$ increases with increasing $I_{\rm opt}$, one may conclude that illumination is creating an increase in TLS loss.

In fact, this was our initial conclusion from these results, even though there were no previously known mechanisms for an increase in TLS loss under illumination, and we actually expected a decrease in TLS loss instead. I note however that the characteristic $\langle n \rangle$ value for the rapid $1/Q$ decrease is much larger than the typical values for Al resonators with comparable size and frequency, which were around 1-100 [39, 131, 136]. Furthermore, examination of the data revealed that $1/Q$ increased with illumination as approximately $I_{\rm opt}^{1/2}$. An $I_{\rm opt}^{1/2}$ dependence is similar to that expected for the number of quasiparticles generated by pair breaking radiation in the steady state [146], which suggests that the increased loss is due to quasiparticles rather than TLSs. As I show in the next ssection, the power dependent behavior of $1/Q$ in this regime can in fact be completely explained by nonequilibrium quasiparticles.

5.2.3 Fit to Nonequilibrium QP Model

The closed circles in Fig. 5.4 show measured values for $1/Q$ vs $P_{\rm rf}$ for several optical intensities $I_{\rm opt}$. For the case of no illumination (black dots), I averaged $1/Q$

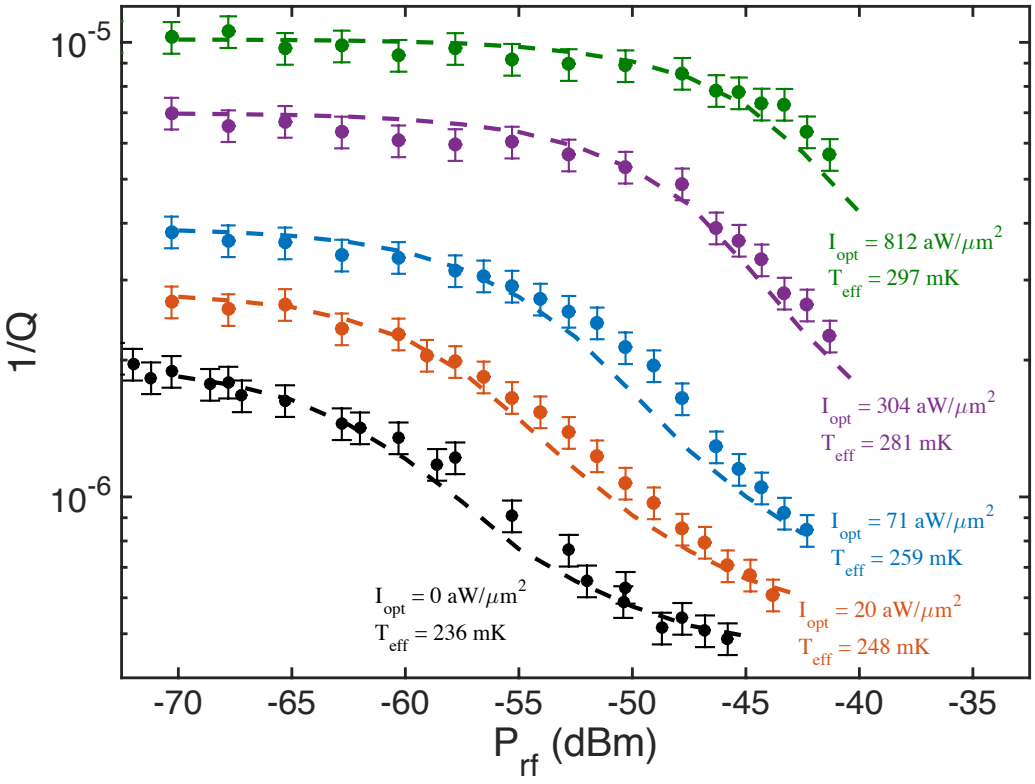

Figure 5.4: Inverse quality factor $1/Q$ vs rf drive powers $P_{\rm rf}$ at 25 mK under optical illumination for intensities $I_{\rm opt}$ as listed. The closed circles are data, the dashed curves were found from the nonequilibrium simulation with $T_b = 25$ mK using the parameters given in Table 5.1. For each optical intensity, the effective temperature $T_{\rm eff}$ was varied in the simulation to find the best fit.

Table 5.1: Parameters used in nonequilibrium simulations for resonator MW2-14.

Symbol	Parameter	Value
Δ	superconducting gap	167 μeV
$\hbar\omega_r$	rf photon energy in simulation	28 μeV
A	resonator Al surface area	4.18×10^4 μm^2
V	resonator Al volume	8.99×10^3 μm^3
Q_e	external quality factor	4.9×10^9
N_0	single spin density of states at Fermi level	1.74×10^{10} eV$^{-1}\mu$m^{-3}
N_i/Ω_D^3	atomic density/(Debye frequency)^3	1.41×10^{15} (eV μm)$^{-3}$
τ_0	quasiparticle-phonon time	438 ns
τ_ϕ	characteristic phonon time	0.26 ns
τ_e	phonon escape time	8.96 ns
ϵ	Al absorption coefficient	$\approx 15\%$
$1/Q_{\mathrm{TLS}}$	TLS loss component	0
$1/Q_0$	power independent loss component	2.5×10^{-7}
α_1	$1/Q$ scaling factor	0.61%
α_2	$\delta f_r/f_r$ scaling factor	0.88%
$f_{0,1}$	baseline resonance frequency (1$^{\mathrm{st}}$ session)	6.720275 GHz
$f_{0,2}$	baseline resonance frequency (2$^{\mathrm{nd}}$ session)	6.720225 GHz
$T_{\mathrm{eff},0}$	effective temperature of background radiation	236 mK

from multiple measurements with the same P_{rf}, similar to the analysis in Chapter 4. The dashed curves in Fig. 5.4 show best fit results to the nonequilibrium quasiparticle model of Section 2.3. For these curves, I fixed $T_b = 25$ mK and only varied T_{eff}. The range of T_{eff} I obtained was between 236 mK and 297 mK. Other parameters are identical to the parameters used to fit higher temperature results listed in Table 4.1, and I include them here in Table 5.1 for completeness.

Illumination also causes a shift in the resonance frequency of the resonator.

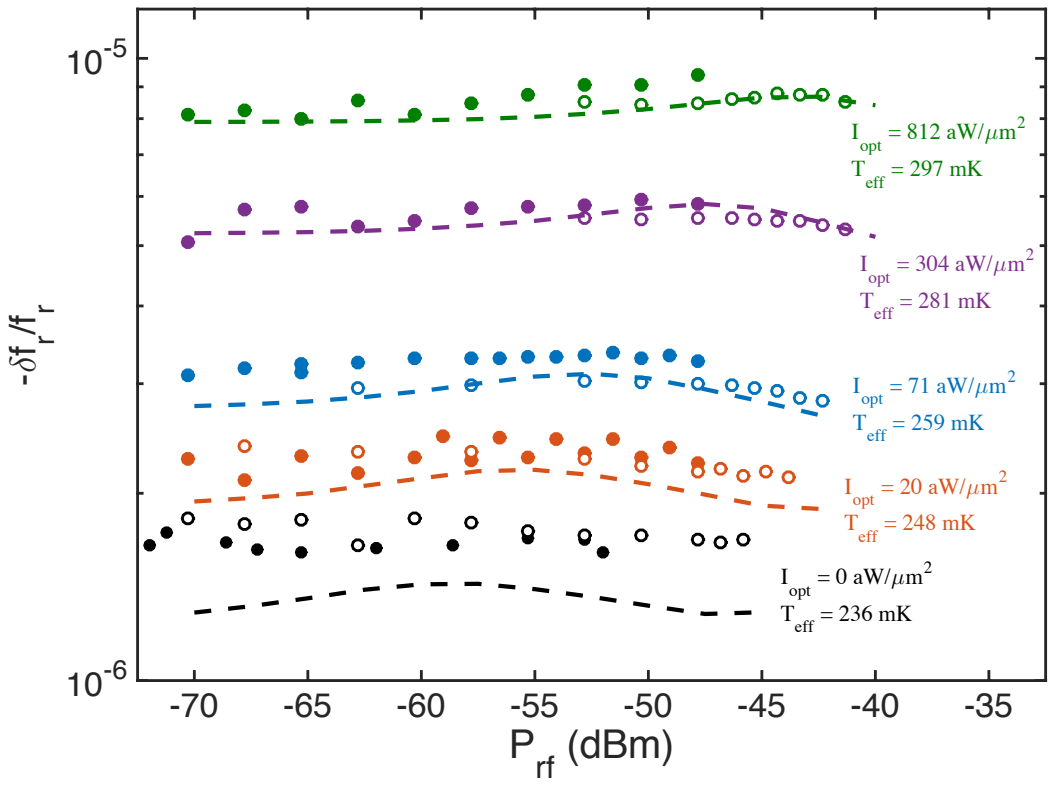

Figure 5.5: Fractional frequency shift $-\delta f_r/f_r$ vs rf drive powers $P_{\rm rf}$ at 25 mK under optical illumination for intensities $I_{\rm opt}$ as listed. The closed circles are data from the first session, the open circles are data from the second session, and the dashed curves were found from the nonequilibrium simulation with $T_b = 25$ mK. For each optical intensity, the effective temperature $T_{\rm eff}$ was varied in the simulation to fit the $1/Q$ data (Fig. 5.4)

In Fig. 5.5, I compare the measured $\delta f_r/f_r$ values (circles) with the values from the nonequilibrium simulation (dashed curves). The closed circles are data from the first session, and the open circles are data from the second session. For the simulation, I used a fixed value of $T_b = 25$ mK and used the corresponding values for $T_{\rm eff}$ that I obtained from fitting $1/Q$ in Fig. 5.4. I note that this fit required only one additional parameter, the baseline resonance frequency for the first illumination session $f_{0,1} =$ 6.720275 GHz. For the baseline frequency for the second session $f_{0,2}$, I used the same value as the baseline frequency value found in the higher temperature measurements f_0 (Table 5.1) because the two measurements were done at overlapping times. The data and simulation agree well at the higher $I_{\rm opt}$ values. For lower $I_{\rm opt}$ values, the simulation predicted slightly lower shifts than what were measured. For the no illumination case, the difference between the measured frequency and expected frequency from simulations was about 2-3 kHz. This discrepancy was also seen seen in Fig. 4.9. In Fig. 4.9, I used the same base temperature data and simulations (black in Fig. 4.9) as the $I_{\rm opt} = 0$ aW/μm^2 second session data and simulations (black) in Fig. 5.5. I note here that I have in effect used the resonator $1/Q$ to predict f_r using the nonequilibrium quasiparticles model. This is strong support for the loss being from nonequilibrium quasiparticles.

It is interesting to note that the nonequilibrium simulations actually predicted that $-\delta f_r/f_r$ varies slightly with rf drive power $P_{\rm rf}$. At the lowest powers, $-\delta f_r/f_r$ slowly increases with increasing $P_{\rm rf}$, before turning around and decreasing with increasing $P_{\rm rf}$. At $I_{\rm opt} = 0$ and 20 aW/μm^2, there are signs that the curve turns around for a second time, and starts to increase with increasing $P_{\rm rf}$. However, the

change in $-\delta f_r/f_r$ with $P_{\rm rf}$ were much less than the change in $1/Q$ with $P_{\rm rf}$. It is also comparable to the magnitude of variations in measured $-\delta f_r/f_r$, especially at lower $P_{\rm rf}$ values. As a result it is hard to observe the $P_{\rm rf}$ dependence of $-\delta f_r/f_r$ at very low microwave power. Also, as I previously noted, f_r appeared to increase (or $-\delta f_r/f_r$ decreased) with increasing $P_{\rm rf}$ at the highest $P_{\rm rf}$ values. These aligned well to where the simulations predicted $-\delta f_r/f_r$ to decrease with increasing $P_{\rm rf}$. Although the response is weak, the data is consistent and this suggests that the f_r dependence on $P_{\rm rf}$ at the highest powers was caused by nonequilibrium quasiparticles.

In Section 4.2.3 I discussed that finding the uncertainties for all of the model fit parameters would be very time-consuming because this would require simultaneously varying all the fit parameters and then performing the nonequilibrium simulations for all rf powers, temperatures, and optical intensities for each set of parameters. Instead, I estimated the uncertainty in just the superconducting gap Δ by performing nonequilibrium simulations for several Δ values near 167 μeV, while keeping the other parameters fixed at the values shown in Table 5.1. From the resulting $f(E)$ distribution, I calculated $1/Q$ values for each $P_{\rm rf}$, T_b, and $I_{\rm opt}$. I then calculated χ^2 using

$$\chi^2 = \sum_i \left(\frac{(1/Q)_{{\rm model},i} - (1/Q)_{{\rm data},i}}{\sigma_{1/Q,i}} \right)^2 . \tag{5.4}$$

Here $(1/Q)_{{\rm model},i}$ is the i-th $1/Q$ value from the model, $(1/Q)_{{\rm data},i}$ is the i-th measured $1/Q$ data point, and $\sigma_{1/Q,i}$ is the uncertainty in $(1/Q)_{{\rm data},i}$. From the approximately 8% fluctuations in $1/Q$ values (see Section 4.1.1), I have $\sigma_{1/Q,i} = 8\% \times (1/Q)_{{\rm data},i}$. Of course it is possible that different $(1/Q)_{{\rm data},i}$ have different

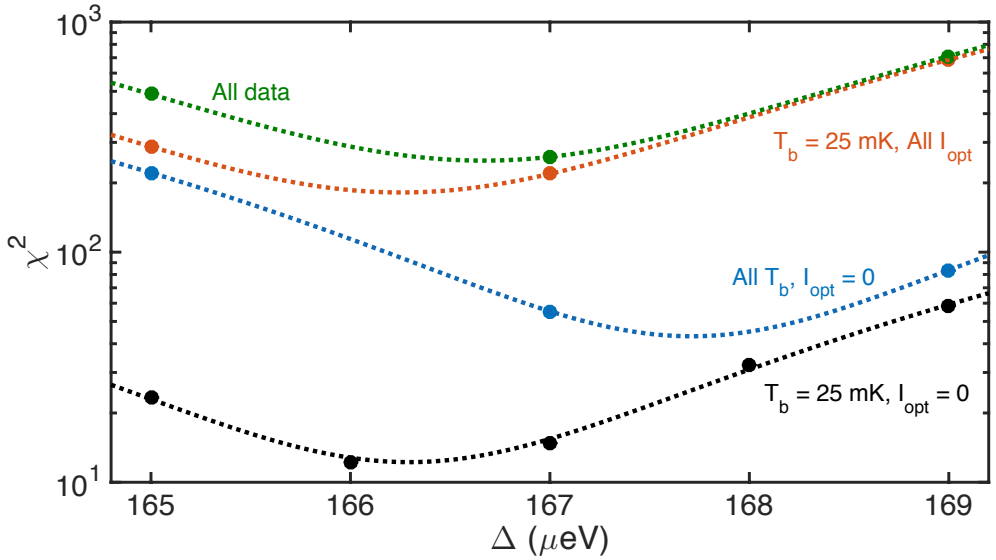

Figure 5.6: χ^2 of $1/Q$ as a function of superconducting gap Δ value used in simulation. Different colors represent different data sets. The dots are the calculated χ^2 values, and the dotted curves are a 2nd order polynomial fit to the calculated χ^2.

$\sigma_{1/Q,i}$ values but examination of the scatter in $1/Q$ data in Fig. 5.1 suggests this is a reasonable estimate. I also note that I did not perform the simulations for some $P_{\rm rf}$ values where I have data. For those $P_{\rm rf}$ values, I used a spline interpolation to obtain the $(1/Q)_{{\rm model},i}$ value.

In Eq. 5.4, the sum is taken over all the points in all the data sets, but it is interesting to also compare χ^2 for the different $1/Q$ data sets. Figure 5.6 shows χ^2 values as a function of Δ, and different colors corresponding to different data sets. The black dots show the χ^2 values for the data set taken at base temperature ($T_b = 25$ mK) and no illumination ($I_{\rm opt} = 0$) data, corresponding to the black dots in Figs. 4.7, 4.8, and 5.4. I found that the calculated χ^2 was lowest for $\Delta = 166$ μeV, with $\chi^2 \approx 12$. χ^2 should be minimized for the best fit value, and I can approximate

the behavior of χ^2 near the minimum with a second order polynomial. The black dotted curve is the 2nd order polynomial fit to the calculated χ^2 points. The fit curve reveals that χ^2 is minimized with $\chi^2 = 12.2$ at $\Delta = 166.3$ μeV. The uncertainty in Δ can then be found from the change in Δ that cause χ^2 to increase by 1 from the minimum value. In the fit curve, this occurs at $\Delta = 165.9$ μeV and 166.7 μeV. Hence this data set gives $\Delta = (166.3 \pm 0.4)$ μeV.

For the subsequent data sets, I performed nonequilibrium simulations for fewer values of Δ. The blue dots in Fig. 5.6 used the no illumination data, which includes the data where the temperature was varied (all dots in Fig. 4.8). The blue dotted curve is the corresponding 2nd order polynomial fit to χ^2. Here χ^2 gave a best fit $\Delta = (167.7 \pm 0.2)$ μeV. The red dots in Fig. 5.6 show χ^2 for data sets where $I_{\rm opt}$ was varied at 25 mK (dots in Fig. 5.5 as well as other intensities not shown) and the red dotted curve is the corresponding 2nd order polynomial fit to χ^2. Here χ^2 gave a best fit $\Delta = (166.3 \pm 0.1)$ μeV. The green dots in Fig. 5.6 used all the data from the previously described sets and the green dotted curve is the corresponding fit. Here χ^2 gave a best fit value $\Delta = (166.7 \pm 0.1)$ μeV. I note that this value of Δ is consistent with the $\Delta = 167$ μeV I used in the simulated curves shown in Figs. 4.7, 4.8, 4.9, 5.4, and 5.5 as well as Table 5.1, and the fact that in the simulations I constrained Δ to be integer multiples of 1 μeV. I note that this analysis assumed that the other fit parameters (τ_e, α_1, α_2, $1/Q_0$, and f_0) had no uncertainty. When the uncertainties of other parameters are taken into account as well, the uncertainty in Δ should increase.

Finally, I note that for the four curves shown in Fig. 5.6, χ^2 has minimum

values of 12.2, 43.1, 182, and 250. The corresponding degrees of freedom ν were 18, 64, 166, and 213. The corresponding values for $p(\chi^2, \nu)$ are 0.84, 0.98, 0.19, and 0.038. The first three of these values fell within the 5% to 95% window corresponding to a good fit of the model to the data. The last value lie outside the window, but not by a significant amount.

5.2.4 Discussions: Validity of Effective Heating Model

In Fig. 5.7(a), I plot the best fit effective temperature $T_{\rm eff}$ as a function of illumination intensity $I_{\rm opt}$ for all applied $I_{\rm opt}$ values. The points are from my fits to the $1/Q$ vs $P_{\rm rf}$ data and the solid curve is a fit of the points to the expression for absorbed optical power

$$P_{\rm opt}(T_{\rm eff}) \;=\; P_{\rm opt}(T_{\rm eff,0}) + \gamma I_{\rm opt}, \tag{5.5}$$

where $P_{\rm opt}$ is numerically calculated from Eq. 2.97, and γ is a fit parameter. This equation just says that the total optical power is the sum of the applied optical power and a background optical power $P_{\rm opt}(T_{\rm eff,0})$. I find excellent agreement between data and simulation with fit parameters $T_{\rm eff,0} = 238$ mK and $\gamma \approx 6.8 \times 10^3$ μm^2. From the data itself I had found $T_{\rm eff,0} = 236$ mK, and from Eq. 2.96, I expected $\gamma = \varepsilon A = 6.3 \times 10^3$ μm^2. The 10% discrepancy between the expected and the fit values of γ is less than the uncertainty in the surface emissivity ϵ and the incident optical intensity $I_{\rm opt}$.

In Fig. 5.7(b), I compare the measured $1/Q$ values (dots) and the $1/Q$ values from the simulation (solid curves) as a function of $I_{\rm opt}$ for $P_{\rm rf} = -65$ dBm and -45

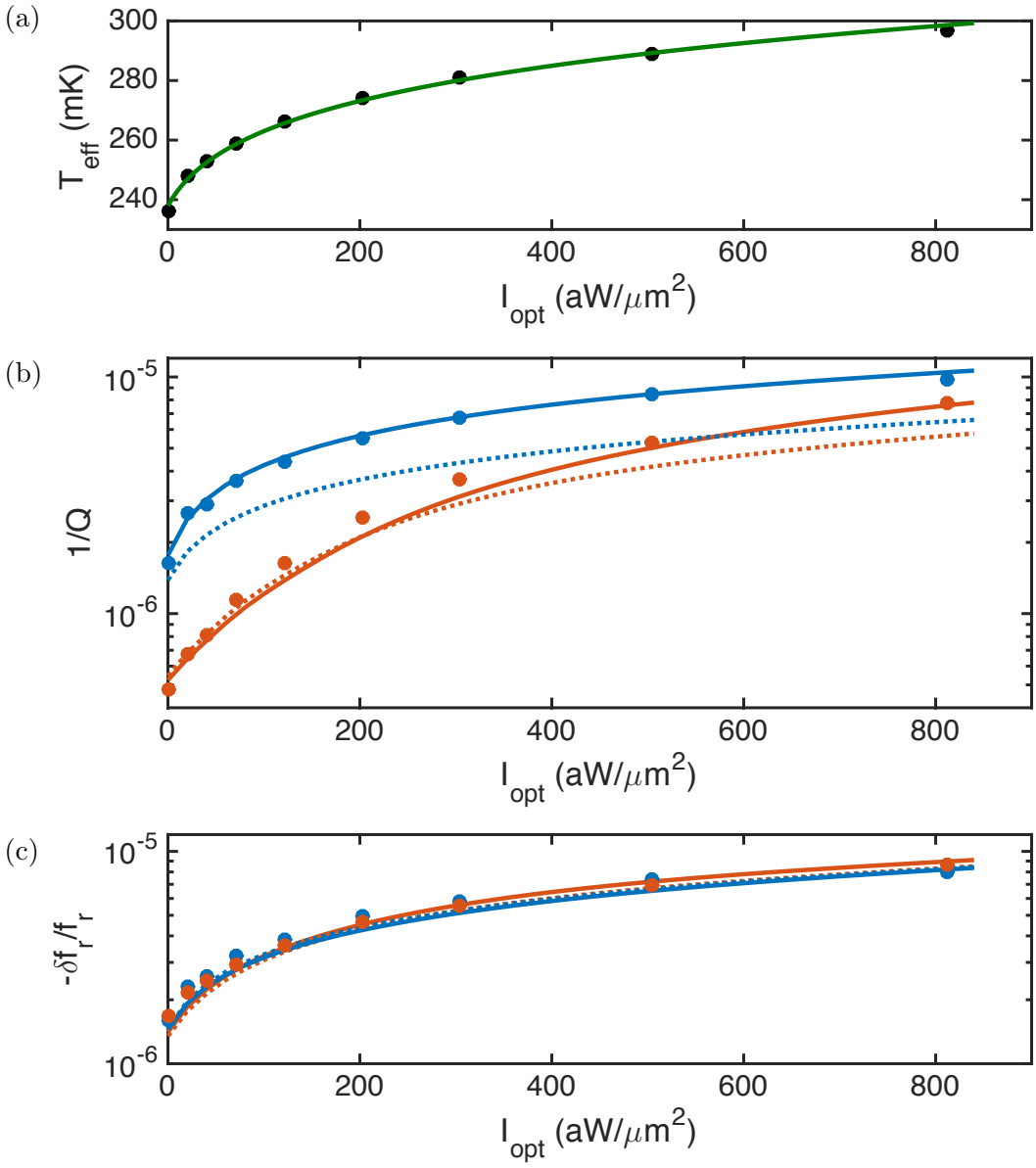

Figure 5.7: (a) Effective temperature $T_{\rm eff}$ vs optical illumination intensity $I_{\rm opt}$. The black circles are extracted from fit to data shown in Fig. 5.4. The green curve is a fit to Eq. 5.5. (b) Inverse quality factor $1/Q$ and (c) fractional frequency shift $-\delta f_r/f_r$ vs $I_{\rm opt}$ for $P_{\rm rf} = -65$ dBm (blue) and -45 dBm (red). In each plot, the closed circles are measured and the solid curves are from the nonequilibrium simulation with $T_b = 25$ mK and $T_{\rm eff}$ using the fit values in (a). For comparison, the dotted curves in (b) and (c) are from the nonequilibrium simulation assuming simple heating with $T_b = T_{\rm eff}$ from fit in (a) and no illumination ($P_{\rm opt} = 0$).

dBm. Here I used the nonequilibrium simulation with $T_b = 25$ mK and $T_{\rm eff}$ values obtained from the fit shown in Fig. 5.7(a). I used simulated values for $1/Q$ only for the nine $I_{\rm opt}$ values where I had data, and performed spline interpolation for other values of $I_{\rm opt}$. The data and simulation agree well for both $P_{\rm rf}$ values. I show the corresponding comparison for the frequency shift in Fig. 5.7(c). The measured $-\delta f_r/f_r$ values are shown as dots and the values from simulation are shown as solid curves. For $P_{\rm rf} = -65$ dBm, I used the data from the first illumination session while for $P_{\rm rf} = -45$ dBm, I used the data from the second illumination session. Again the data and simulations agree well. The largest disagreement is a small discrepancy in $-\delta f_r/f_r$ at the lowest $I_{\rm opt}$ values, as discussed in the previous section.

Gao *et al.* have suggested that pair-breaking radiation produces nearly the same effect on $1/Q$ and f_r as an increase in temperature [42]. Comparing our measured $1/Q$ and f_r values at higher temperatures with values obtained under illumination between $P_{\rm rf} = -65$ dBm and -55 dBm, I find that for comparable values of $\delta f_r/f_r$, the $1/Q$ values under illumination are higher than the $1/Q$ values at the same increased bath temperatures.

To compare this increased temperature model with our model for optical illumination, in Fig. 5.7(b) and (c), the dotted curves show $1/Q$ and $\delta f_r/f_r$ for the increased temperature model. Here I used the nonequilibrium simulation with T_b values equal to the $T_{\rm eff}$ fit values in Fig. 5.7(a) and $n_{\rm opt} = 0$. The discrepancy in $\delta f_r/f_r$ between the two models is small for both values of $P_{\rm rf}$, as shown in Fig. 5.7(c). On the other hand, Fig. 5.7(b) shows that for $P_{\rm rf} = -65$ dBm the $1/Q$ from the increased temperature model is smaller than that from the data or the full model

for the entire range of $I_{\rm opt}$. For $P_{\rm rf} = -45$ dBm, the difference between the two models are negligible below $I_{\rm opt} \approx 300$ aW/μm^2 and the $1/Q$ from the increased temperature model is again smaller above the same $I_{\rm opt}$. This comparison suggests that the non-equilibrium model for $n_{\rm opt}$ is better than the increased temperature model for simulating effects produced by optical illumination.

In summary, I note that the illumination model for the nonequilibrium quasiparticle distribution can explain our results well and that our model is still relatively simple in its treatment of optical effects. I believe this picture can be improved using a more complete model that includes, among other things, the system's microscopic response to the absorption of optical photon energy and the time dynamics of quasiparticles and phonons after photon absorption [157, 158].

5.2.5 Discussions: Rolloff Behavior in $1/Q$ vs $P_{\rm rf}$

I mentioned earlier that the inverse quality factor from quasiparticles $1/Q_{\rm qp}$ in this regime has a behavior that is very similar to the inverse quality factor from TLSs. In our resonators, I can distinguish the two by fitting the $1/Q$ vs $P_{\rm rf}$ curves at different temperatures and optical intensities. However in the past the superconducting qubit community usually assumed that TLS loss was dependent on $P_{\rm rf}$, but that quasiparticle loss was independent of $P_{\rm rf}$. It is possible that this may have caused some confusion in the past. For example, the weak $P_{\rm rf}$ dependence of TLS loss reported by Macha *et al.* [137] and Khalil *et al.* [138] may actually come from quasiparticles or a combination of quasiparticles and TLSs.

The dependence of $1/Q_{\mathrm{TLS}}$ on the drive is parameterized by a characteristic field E_c or a characteristic voltage V_c, which can be rescaled into a characteristic rf photon occupation n_c. Due to the similarity to the rolloff in the loss due to quasiparticles, one can define a similar characteristic variable for quasiparticle $1/Q_{\mathrm{qp}}$. However, since $1/Q_{\mathrm{qp}}$ does not have an analytical expression in the nonequilibrium model, determining this characteristic variable is an open question. In addition to rf photon occupation, another possible candidate for the characteristic variable is the absorbed rf power $P_{\mathrm{rf,ab}}$.

5.3 Additional Illumination Measurements

5.3.1 Comparison Between Parallel and Perpendicular Lines

In Section 3.5 I mentioned that there were two optical fiber lines in the system, one aligned perpendicular to the resonator surface, the other parallel to the resonator surface. All of the illumination measurements discussed in the previous sections were done using the perpendicular line. We also performed some illumination measurements using the parallel line and compared the response between the two lines.

As discussed previously, to first order, $1/Q$ increases approximately proportional to the number of quasiparticles generated by pair-breaking radiation, which is proportional to $P_{\mathrm{opt}}^{1/2}$ [146]. As before, I will define $P_{\mathrm{opt}} = \varepsilon I_{\mathrm{opt}} A$ as the absorbed optical power, ε is the emissivity, I_{opt} is the illumination intensity, and A is the area of the resonator perpendicular to illumination.

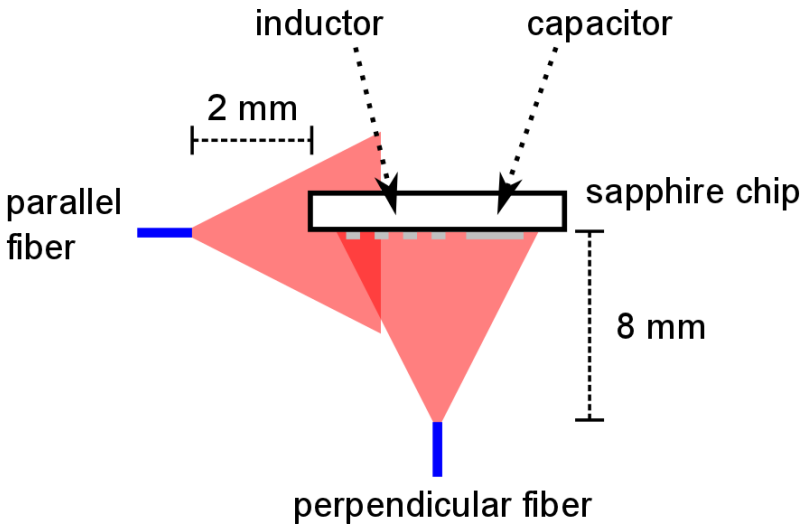

Figure 5.8: IIllustration of chip illumination from both fiber perpendicular and parallel lines. Figure not to scale.

Figure 5.8 shows an illustration of the illumination coming from the two fibers. For the same optical intensity I_{opt} the absorbed optical power is then proportional to εA where $A = A_{\perp}$ for the perpendicular fiber and $A = A_{\parallel}$ for the parallel fiber. The emissivity ε can depend on the roughness of the surface, with rougher surface having higher emissivity. It is possible the edge surfaces of the resonator have higher roughness than the top surface, due to the etching process. However, I will assume here that they have similar emissivity. This means that P_{opt} mainly depends on the illuminated area A. What this means is that the parallel and perpendicular illumination are expected to give the same response when the ratio of the applied intensities is $I_{\parallel}/I_{\perp} = A_{\perp}/A_{\parallel}$. Here $I_{\perp}$ is the intensity of perpendicular illumination hitting the top surface, while $I_{\parallel}$ is the intensity of the parallel illumination hitting the edge surface of the inductor line closest to the fiber.

As discussed in the previous sections, the illuminated area of the perpendicular

illumination is $A_\perp = 4.18 \times 10^4\ \mu\text{m}^2$. When the parallel fiber is perfectly aligned, the edge surface of the inductor line closest to the fiber is the only surface illuminated. For perfect alignment, the illuminated area is given by the product of the film thickness (215 nm) and the length of the illuminated inductor line (400 μm), which gives $A_\parallel = 86\ \mu\text{m}^2$. This gives the ratio of the cross sections $A_\parallel/A_\perp \approx 1/500$. Of course, there may be slight errors in the alignment of the fibers.

If the perpendicular fiber is misaligned by a small angle $\theta_\perp$, the cross-section area of the top surface is multiplied by the factor $\cos\theta_\perp$. For very small angles, $\cos\theta_\perp \to 1$. The edge surfaces may absorb some of the radiation as well, but since the area of these surfaces is much smaller than the top surface, and it is multiplied by the factor $\sin\theta_\perp \to 0$, it is negligible. Hence $A_\perp$ will change very little with slight misalignment. On the other hand, if the parallel fiber is misaligned by a small angle $\theta_\parallel$, there will be absorption from either the top surface or the bottom surface of the resonator aluminum film, as well as edge surfaces located further away. Even though the intensities reaching the top and bottom surfaces are reduced on account being further away and $\theta_\parallel$ small, the much larger top surface area means this can be a large contribution and the effective cross-section $A_{\parallel,\text{eff}} \equiv \int I.dA/I_{\text{opt}}$ can increase by a significant amount. From these results, I can conclude that slight errors in the alignment of the fibers can result in a significant increase in the ratio of the cross-sections $A_{\parallel,\text{eff}}/A_\perp$ and thus I expect $A_\parallel/A_\perp \gtrsim 1/500$.

Figure 5.9 shows the measured $1/Q$ vs illumination intensity I_{opt} for illumination from both fibers. The rf drive power is fixed at $P_{\text{rf}} = -65.3$ dBm. The blue dots are the data for perpendicular fiber and the red dots are data from parallel illumina-

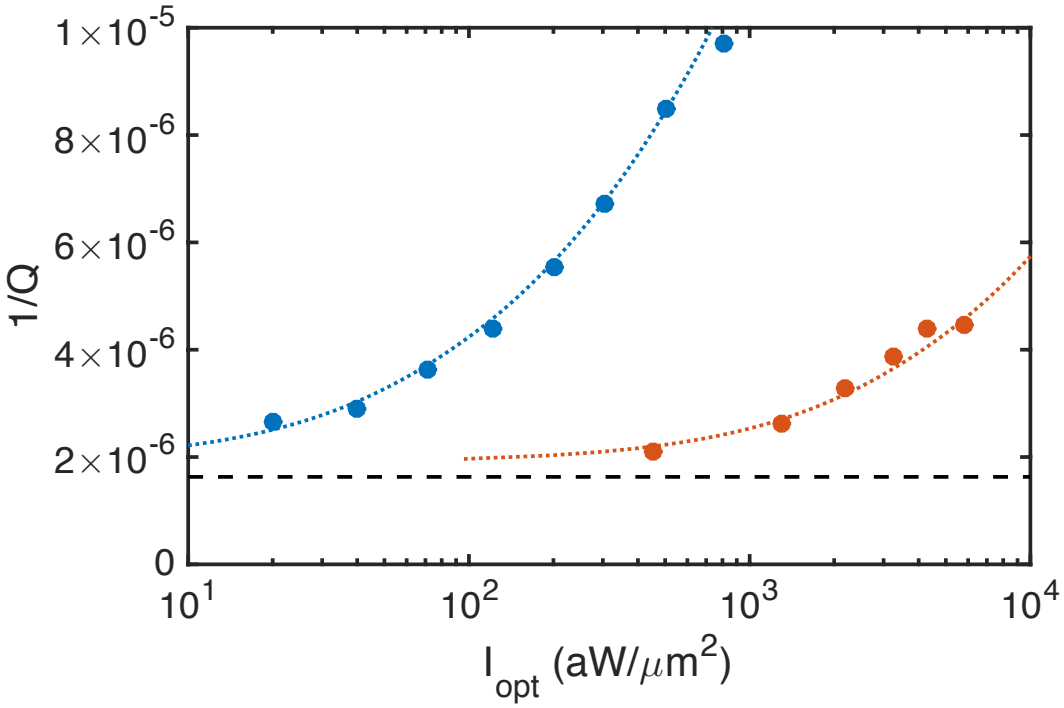

Figure 5.9: Inverse quality factor $1/Q$ vs illumination intensity I_{opt} for $P_{\text{rf}} = -65.3$ dBm for both fiber lines. The blue dots are data from perpendicular illumination, the red dots are data from parallel illumination. The blue dotted curve is fit of nonequilibrium model to the perpendicular data. The red dotted curve is a rescaled version of the blue dotted curve translated by $I_{\text{opt}} \to 48 I_{\text{opt}}$, such that it agrees to parallel data. The black dashed horizontal line is $1/Q = 1.63 \times 10^{-6}$, the averaged measured value of $1/Q$ when $I_{\text{opt}} = 0$ aW/μm^2.

tion. The blue dotted curve is a fit of the perpendicular data to the nonequilibrium model (this curve is the same as the blue solid curve in Fig. 5.7(b)). The red dotted curve is the blue dotted curve rescaled along the x-axis by $I_{\rm opt} \rightarrow 48 I_{\rm opt}$ such that it agrees well to the parallel data. The good agreement means the response from the parallel fiber at intensity $I_{\parallel}$ is comparable to the response from the perpendicular fiber with a ratio of intensities $I_{\parallel}/I_{\perp} \approx 48$. This appears to be consistent with the misalignment picture described above, although the ratio increased by an order of magnitude from the minimum possible value of 1/500. I could then calculate the angle $\theta_{\parallel}$ by solving $\sin\theta_{\parallel} \approx 1/48 - 1/500$, and I found $\theta_{\parallel} \approx 1.1^{\circ}$. As it was entirely possible to misalign the fibers by up to a few degrees, this value of $\theta_{\parallel}$ was reasonable.

In Chapter 3, I noted that disconnecting and reconnecting the fiber connections at the screen room wall could introduce additional losses, likely from variations in the connections or dust getting on the connectors. For the perpendicular fiber, we found that this intensity could be reduced up to a factor of 3. The perpendicular data shown in Fig. 5.9, as well as the ones discussed in the previous sections, were taken after we attempted to minimize the loss as much as possible. However, the parallel fiber measurements were performed only once, and we did not perform any checks whether there were losses on the connection. It is possible that there were some losses, which would cause the real ratio of intensities to be higher than what we measured.

I also note here that the model for the parallel illumination is extremely simplified. For perpendicular illumination, the intensity of light $I_{\perp}$ hitting the top surface is almost uniform, and hence I could assume that the quasiparticle density is inde-

pendent of position in the resonator. However, for parallel illumination, most of the quasiparticles are expected to be generated in the inductor because it is closest to the fiber. For perfect alignment, all of the quasiparticles would be created there. This means the quasiparticle density is not uniform in the resonator. If that is the case, quasiparticle diffusion needs to be taken into account in the nonequilibrium model and I should use the averaged quasiparticle distribution over the inductor.

The knowledge that reduction in cross-section decreases the resonator response to light, although quite obvious, was useful in improving the design for the eventual hybrid system experiment. The initial proposal was to put the tapered optical fiber above the $5 - 10$ μm wide inductor line. The design was changed such that now the tapered fiber is going to be located to the side of the inductor line. This should minimize the cross section of the resonator, and minimize the resonator response to Rayleigh scattering from the fiber. To get this alignment we plan to use x- and z-axis Attocube stages [103] to move the resonator with respect to the fiber while monitoring the response of the fiber (see Section 9.3).

5.3.2 Dependence on Polarization of Light

For superconducting structures with sizes less than or comparable to the wavelength λ of the light, the absorption and resulting response are expected to depend on the polarization of the light. This effect was previously observed in superconducting nanowire single photon detectors (SNSPDs) [192, 193]. SNSPDs are typically of order ≈ 500 μm long, very thin (≈ 5 nm), and very narrow (≈ 100 nm) meandering

superconducting wires. The polarization dependence is due to the interaction between the electric field of the photon and the nanowire. When the optical photon is linearly polarized parallel to the wire, there is no change in photon absorption compared to what one would expect for scaling with the exposed area. On the other hand, when the optical photon is linearly polarized perpendicular to the wire, surface charges causes electric field screening, which results in a reduction in absorption by up to 50% [192, 193].

In our resonator, since the thickness of the film $t = 215$ nm is less than the photon wavelength $\lambda = 780$ nm, we expect the resonator to show a polarization-dependent response to parallel illumination. On the other hand, the smallest structures seen by the perpendicular illumination are 5 μm wide, hence we expect the response from perpendicular illumination is independent of polarization.

The 780 nm light from the laser is linearly polarized. However, we see the scattered light, which has a polarization that depends somewhat on the polarization of the applied light. As I mentioned in Chapter 3, to adjust the polarization I added a quarter-wave plate followed by a half-wave plate in the beam path. The angle of the quarter-wave plate $\theta_{\lambda/4}$ sets the ellipticity of the polarization. When the angle between $\theta_{\lambda/4}$ and the polarization direction of linearly polarized incident light is 0° or 90°, the light coming out of the wave plate is still linearly polarized. When the angle is 45°, the light coming out is circularly polarized. For other angles, the light is elliptically polarized. The angle of the half-wave plate $\theta_{\lambda/2}$ sets the direction of the polarization of linearly or elliptically polarized light. For circularly polarized light, the half-wave plate effectively does nothing. However, since the light still needs to

travel through the fiber from the optical table to the cavity, the polarization of the light illuminating the resonator may be different from what is set at the wave plates, and cannot be independently measured with our setup when it is cold.

For this polarization comparison, I used $P_{\mathrm{rf}} = -65.3$ dBm, where $Q \approx 1.6 \times 10^{-6}$ when no optical illumination was applied. For the optical intensities from the perpendicular and parallel fibers, I chose $I_{\perp} \approx 13$ aW/μm^2 and $I_{\parallel} \approx 450$ aW/μm^2. These intensities were chosen because when the two wave plates were not used, these two intensities gave comparable $1/Q \approx 2.0 \times 10^{-6}$ for $P_{\mathrm{rf}} = -65.3$ dBm. I note that the $1/Q$ from the two illuminations were not exactly equal, with ratio of intensities of only about 35, while we found in the previous section that it needs to be about 48 for it to be equal.

Fig. 5.10(a) shows a false-color plot of $1/Q$ as a function of both wave plate angles for parallel illumination. $1/Q$ clearly shows a dependence on polarization angle. When $\theta_{\lambda/4} \approx 0^{\circ}$ and 80°, the contrast is strongest, and the $1/Q$ dependence on $\theta_{\lambda/2}$ appears to be sinusoidal with minimum value of $1/Q \approx 1.9 \times 10^{-6}$ at about $\theta_{\lambda/2} \approx 50^{\circ}$ and maximum value of $1/Q \approx 2.3 \times 10^{-6}$ at about $\theta_{\lambda/2} \approx 0^{\circ}$. Since $1/Q \approx 1.6 \times 10^{-6}$ for the case of no illumination, the increase in $1/Q$ is reduced by about 60% at minimum $1/Q$ value compared to the maximum $1/Q$ value. This is consistent with the polarization picture described above with a linearly polarized light coming out of the parallel fiber. I assume that when $1/Q$ is at a minimum, the light is polarized perpendicular to the inductor line, and when it is at a maximum, the light is polarized parallel to the line. This means for one of the $\theta_{\lambda/4}$ values, 0° or 80°, the polarization of light from the laser is nearly aligned with the quarter-wave

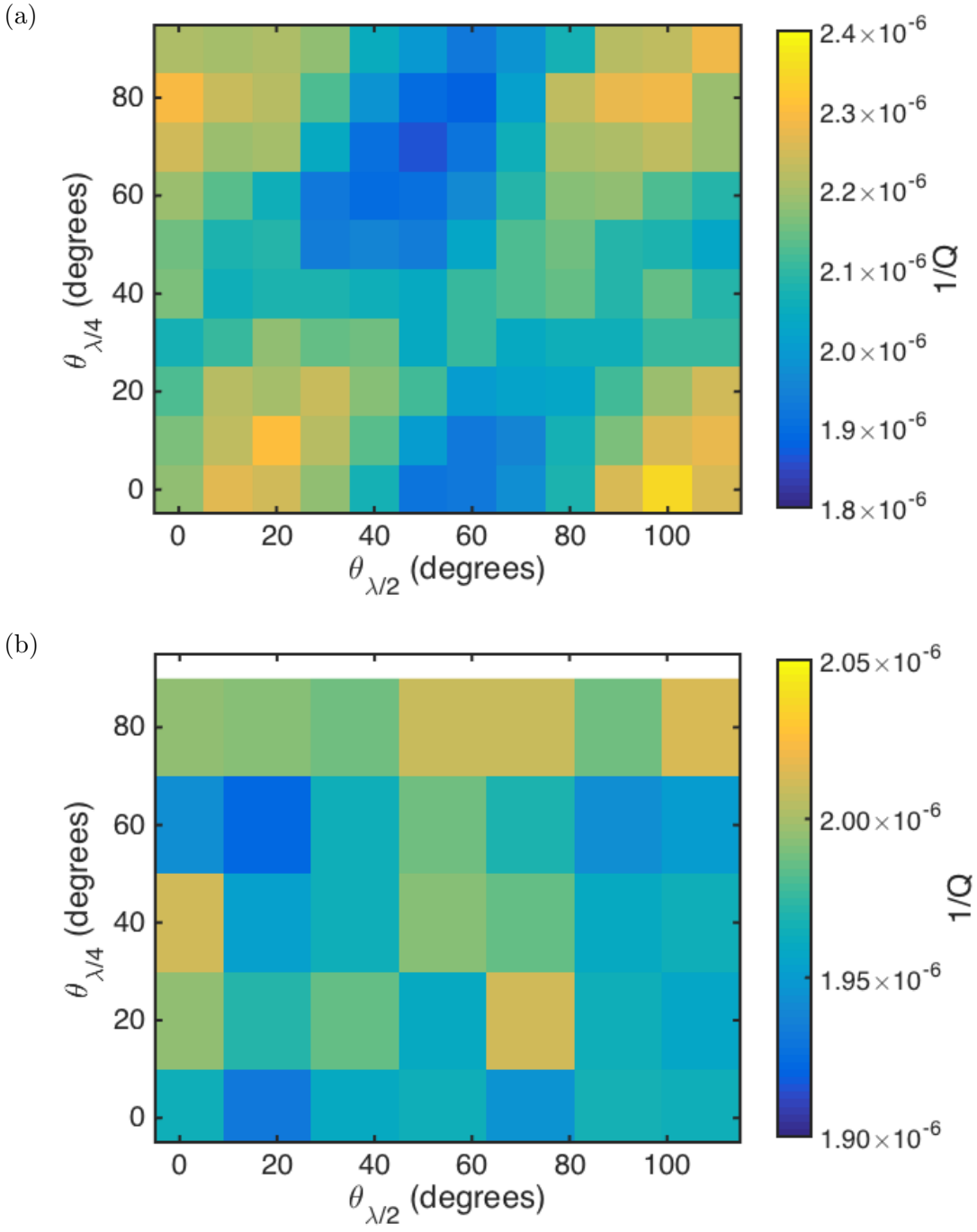

Figure 5.10: False-color plot of inverse quality factor $1/Q$ vs wave plate angles $\theta_{\lambda/2}$ and $\theta_{\lambda/4}$ for (a) parallel illumination and (b) perpendicular illumination.

plate angle. For the other value of $\theta_{\lambda/4}$, the polarization of light from the laser is nearly perpendicular to the quarter-wave plate angle. I note here that the two cases should be separated by 90°, however we have very rough steps between angles at 10°. It is also likely that the contrast is even higher around $-10°$, which we did not measure.

On the other hand, when $\theta_{\lambda/4} \approx 40°$, the dependence is significantly weaker with $1/Q \approx 2.1 \times 10^{-6}$ for all $\theta_{\lambda/2}$ values. This is consistent with a near circularly polarized light coming out of the fiber. Since for circularly polarized light, the half-wave plate does not change the polarization, $1/Q$ should not be dependent on $\theta_{\lambda/2}$.

Figure 5.10(b) shows a false-color plot of $1/Q$ as a function of both wave plate angles for perpendicular illumination. $1/Q$ does not appear to have any dependence on $\theta_{\lambda/4}$ and $\theta_{\lambda/2}$ with $1/Q$ values between 1.9×10^{-6} and 2.05×10^{-6}. This is consistent with what I expected for perpendicular illumination.

I can compare the $\theta_{\lambda/2}$ and $\theta_{\lambda/4}$ dependence results of the parallel illumination with the expected dependence. Pablo Solano performed a simulation to calculate the time-averaged and scaled Poynting energy density I_x only for electric field perpendicular to inductor line (here defined as x-direction) as a function of waveplate angles [194]. Since $I_x \propto \langle |E_x|^2 \rangle_t$ where E_x is the x-component electric field, I_x is the proportional time-averaged intensity from the x-component of the electric field only. In the simulation, the polarization of the scattered light from the fiber is assumed to be identical to the polarization of light coupled to the fiber. He also assumed the initial beam was linearly polarized in the x-direction, which is also aligned with

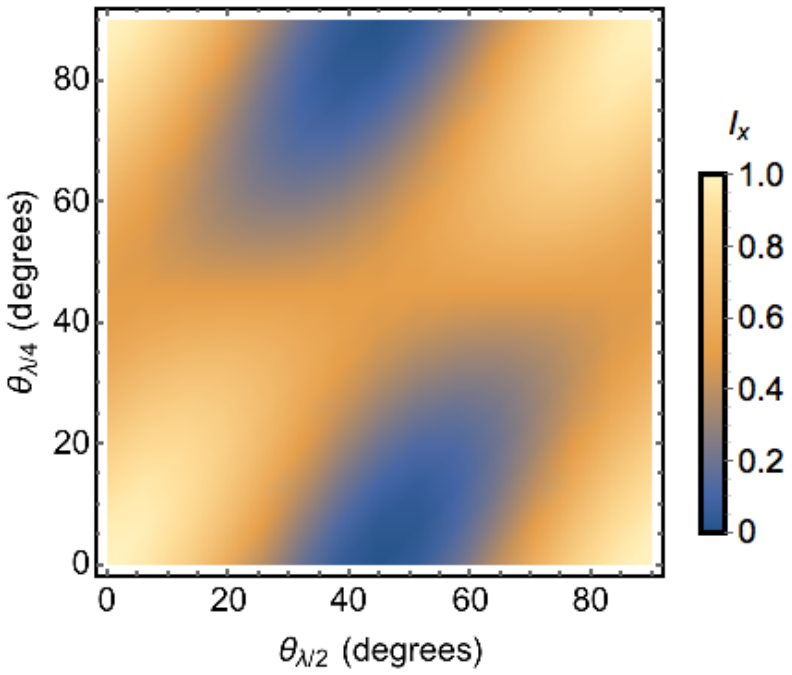

Figure 5.11: Scaled x-component of Poynting energy density I_x vs wave plate angles $\theta_{\lambda/2}$ and $\theta_{\lambda/4}$.

$\theta_{\lambda/4} = 0$ and $\theta_{\lambda/2} = 0$. Figure 5.11 shows the results of Pablo's simulation of I_x vs $\theta_{\lambda/2}$ and $\theta_{\lambda/4}$. The contour of the I_x plot appears to be similar to the contour of $1/Q$ vs $\theta_{\lambda/2}$ and $\theta_{\lambda/4}$ of Fig. 5.10(a). In the simulation, I_x has a 100% contrast, in comparison to the 60% contrast in the increase in loss in measured data. Nevertheless, the simulation suggests that the polarization dependence we see is consistent with the physical picture described at the beginning of this section.

The knowledge that the resonator response to illumination can depend on polarization may be useful to the hybrid system experiment. If the polarization of the Rayleigh scattering from the tapered fiber can be controlled, one can reduce the increase in loss due to optical illumination by up to 60% by arranging the Rayleigh scattered light to be predominantly polarized perpendicular to the inductor.

5.3.3 Pulsed Light Experiments

By using a pulse of optical illumination instead of continuous illumination, we should be able to study the transient behavior of the quasiparticles, specifically right after the pulse is turned on or off. A complete model for the quasiparticle behavior under an optical pulse would require solving the time-dependent nonequilibrium quasiparticle (see Chapter 2). This requires finding the quasiparticle distribution as a function of time $f(E,t)$, which appears to be computationally challenging.

Instead, I considered the total quasiparticle density n_{qp}, which is related to $f(E)$ through Eq. 2.64. While n_{qp} by itself is not sufficient to calculate σ_1 and σ_2, it can be shown that for small changes in n_{qp}, σ_1 and σ_2 change linearly with n_{qp} [42].

$n_{\rm qp}$, as well as the total phonon density n_ϕ for $\Omega > 2\Delta$, obey the Rothwarf-Taylor kinetic equations [146].

The recombination time τ_R is the characteristic time for quasiparticles to interact and form Cooper pairs and this should be one of the key timescale for quasiparticle transient behavior. For a thermal distribution with temperature T_b much lower than the critical temperature T_c, Kaplan *et al.* derived an expression for the τ_R given by [150]

$$\tau_R \;=\; \tau_0 \left(\frac{k_B T_c}{2\Delta_0}\right)^{5/2} \left(\frac{T_c}{\pi T_b}\right)^{1/2} e^{\Delta_0/k_B T_b}, \tag{5.6}$$

where the definitions of the variables are the same as I used in my discussion of nonequilibrium quasiparticles. In Eq. 2.73 I showed that $n_{\rm qp}(T) = 2N_0\sqrt{2\pi k_B T \Delta_0}$ $e^{-\Delta_0/k_B T}$, hence Eq. 5.6 can be rewritten as

$$\tau_R \;=\; \tau_0 \frac{2N_0}{n_{\rm qp}} \frac{(k_B T_c)^3}{(2\Delta)^2} \;=\; \tau_0 \frac{2N_0}{n_{\rm qp}} \frac{k_B T_c}{(3.52)^2}, \tag{5.7}$$

using the relation $2\Delta = 3.52 k_B T_c$. Equation 5.7 depends on $n_{\rm qp}$ but does not have an explicit dependence on temperature T_b, and this let me apply this expression to the case of a nonequilibrium distribution of quasiparticles.

Since taking the entire S_{21} vs f trace would be too slow for pulsed measurements, instead I measured the phase φ of S_{21} at the resonance frequency f_r, where

$$\varphi[S_{21}(f_r)] \;=\; \frac{\mathrm{Re}[S_{21}(f_r)]}{\mathrm{Im}[S_{21}(f_r)]}. \tag{5.8}$$

For small shifts in resonance frequency, the change in phase is proportional to the change in frequency $\delta\varphi \approx 2Q\delta f_r/f_r$. The regime where this is valid is called the linear regime. In practice, I used the VNA to measure φ as a function of time at the resonance frequency f_r.

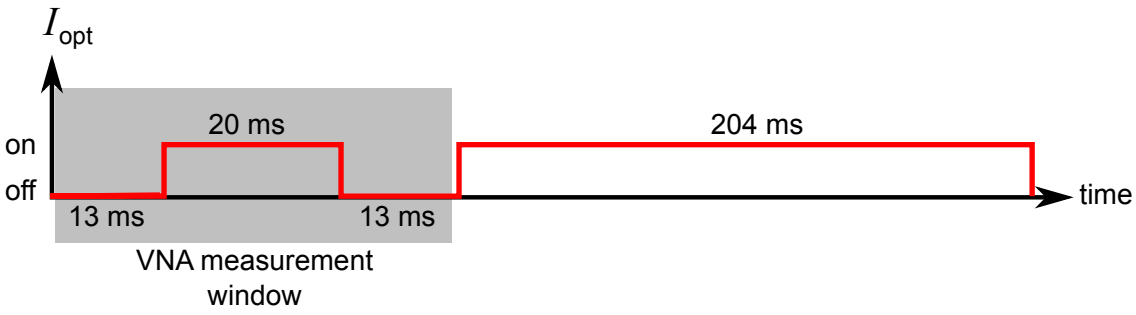

Figure 5.12: Timing sequence of the optical pulse.

As I discussed in Chapter 3, the timing of the optical pulses is controlled by sending voltage pulses to the acousto-optic modulator (AOM). The timing of the optical pulse is shown in Fig. 5.12. At the beginning of the cycle, the light was off for 13 ms, then I applied a 20 ms long optical pulse. The light was switched off for 13 ms and this was followed by a 204 ms pulse with the light on. This pulse was long enough that I could maintain a duty cycle above 90%. This sequence was repeated, resulting in 4 Hz repetition rate. For this measurement, I used the perpendicular illumination. The timing of the VNA measurement was triggered using the same repetition rate as the optical pulse. I then averaged the φ vs time t data for 1000 repetitions. I fit φ vs t at the beginning of the 20 ms pulse to an exponential and extracted the time constant τ_R. I also fit φ vs t right after the pulse was turned off.

Figure 5.13 shows φ vs t for several P_{rf} values. To keep the resonance shift in the linear regime, I chose a very low optical intensity of $I_{\mathrm{opt}} < 2$ aW/μm^2. I note that the I_{opt} values are different for different P_{rf}; each I_{opt} was chosen so that there was roughly the same $\delta\varphi$ between light on and off. For the lower powers, the data appears to be very noisy, and this results in large uncertainties in the extracted

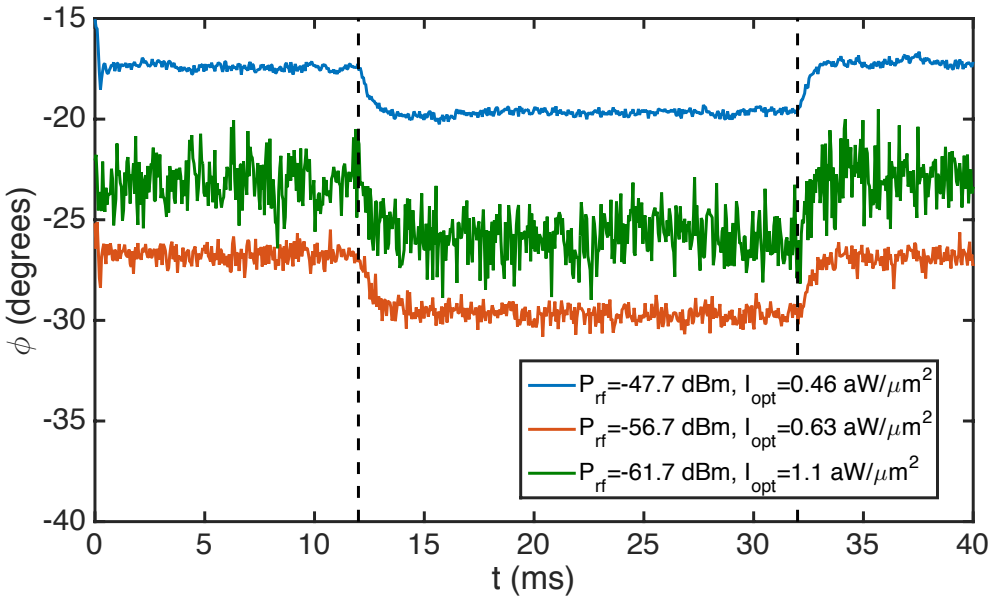

Figure 5.13: Phase φ of S_{21} vs time t for several P_{rf} values for pulsed illumination measurements. The P_{rf} and corresponding I_{opt} value are shown in the legend. The dashed vertical lines indicate the approximate start and end time of the 20 ms optical pulse.

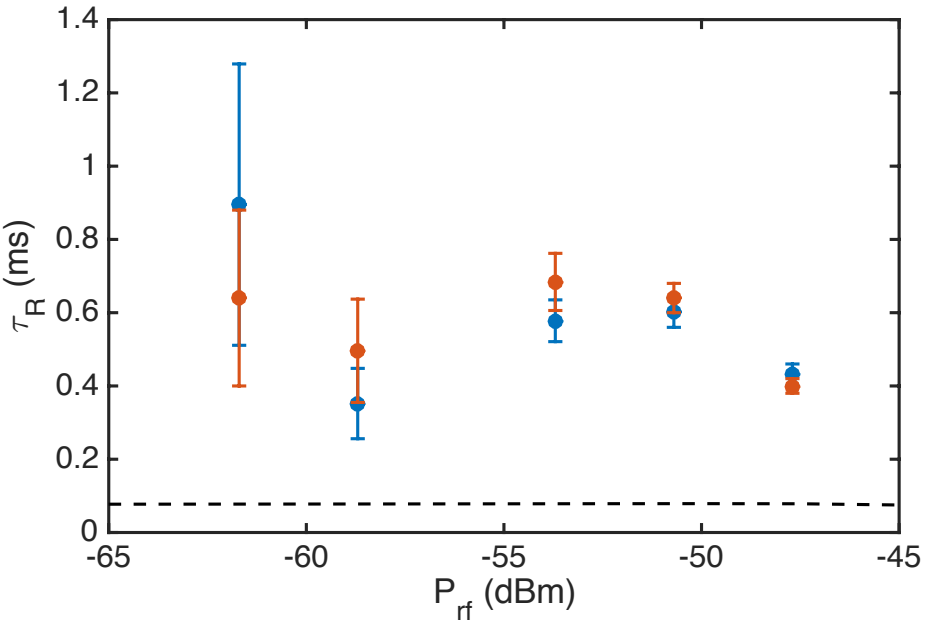

Figure 5.14: Measured recombination time τ_R vs rf power $P_{\rm rf}$ for pulsed optical illumination. Blue dots are for pulse turn on, red dots are for pulse turn off. The dashed black line is the τ_R calculated using Eq. 5.7 and $n_{\rm qp}$ from nonequilibrium simulations.

exponential time scale. The three curves in Fig. 5.13 show very similar behavior, despite the different $I_{\rm opt}$ and $P_{\rm rf}$.

Figure 5.14 shows the extracted τ_R values as a function of $P_{\rm rf}$, with the error bars shown. As I noted, the error bars for the lower $P_{\rm rf}$ values are large. Nevertheless, the τ_R values are about 0.6 ms, with a slightly lower value of about 0.4 ms for the highest $P_{\rm rf}$. τ_R for pulse turn on (red dots) are comparable to τ_R for turn off. I also compared the measured times to τ_R calculated using Eq. 5.7 with $n_{\rm qp}$ values from the nonequilibrium simulations (shown as black dashed line). The calculated value was about 0.08 ms, almost an order of magnitude lower than the measured value.

There are several reasons why the expected and measured value may be dif-

ferent. First, Eq. 5.6 has an exponential dependence on Δ_0. It is possible the actual Δ_0 was slightly higher, which would result in significantly higher τ_R. However this would cause disagreement with the $1/Q$ and δf_r results from continuous illumination and their agreement to the nonequilibrium quasiparticles. It is also possible that Eq. 5.7 is not valid for nonequilibrium distributions. Also, Eq. 5.6 is only approximate for low temperatures. It would be interesting to find τ_R for a nonequilibrium distribution using the transient solutions of the Chang-Scalapino equations [147]. Finally, Rothwarf and Taylor noted that τ_R can also be modified by strong quasiparticle-phonon interactions [146], which should also emerge in the nonequilibrium simulations.

I also note that my measurements were limited by the noise in the φ signal due to weak coupling, which prevented me from making pulsed measurements over a wide range of $P_{\rm rf}$ and T_b values. However, Jared and Kristen have also performed pulsed illumination measurements on a lumped-element resonator coupled to a transmission line, which had about 4-5 orders of magnitude lower value of Q_e. They measured τ_R as a function of temperature T_b, with the results shown in Fig. 5.15. They found that τ_R follows Eq. 5.6 with $\Delta = 200$ μeV above $T_b \approx 220$ mK. Below $T_b \approx 180$ mK, τ_R is constant at about 1 ms. One interesting observation was that at low temperatures they found that turning on light and turning off light resulted in different τ_R, with $\tau_R \approx 1.2$ ms for turn on and 1.4 ms for turn off. The cause for this difference is still unclear.

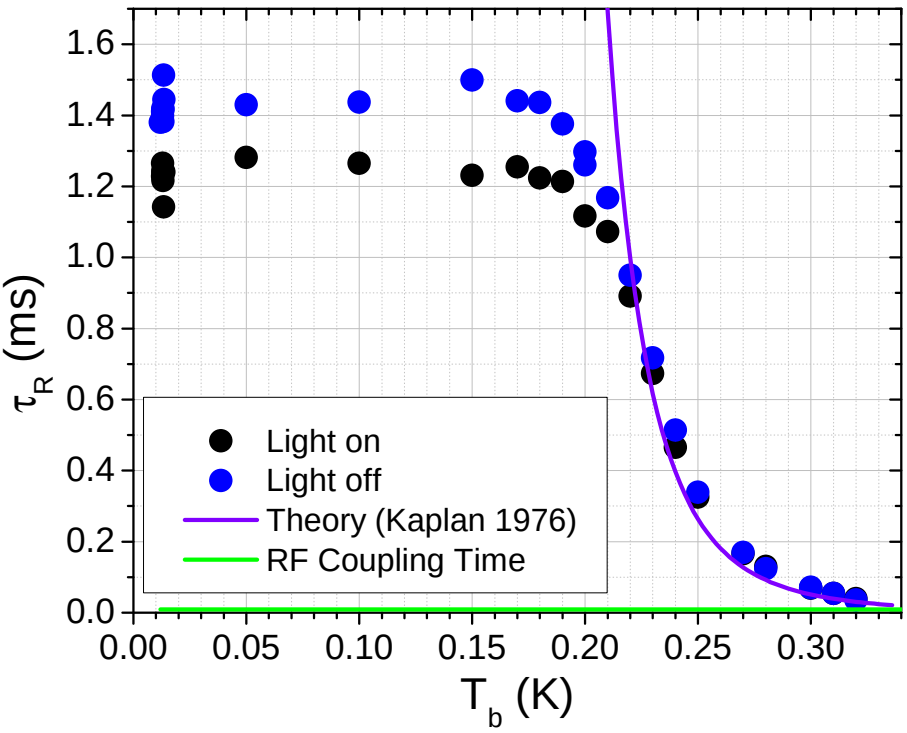

Figure 5.15: Measured recombination time τ_R vs refrigerator temperature T_b for pulsed illumination on a previous resonator, measured by Jared Hertzberg and Kristen Voigt [195]. The purple curve is τ_R calculated using Eq. 5.6 with $\Delta = 200$ μeV. The green curve at the very bottom of the plot is the coupling time of the resonator to the microwave line.

5.4 Summary

In this chapter I discussed measurement results on resonator MW2-14 under optical illumination from the perpendicular fiber. First I discussed the expected TLS and quasiparticle losses under illumination; the loss from TLS should decrease while the loss from quasiparticles should increase with increasing illumination intensity $I_{\rm opt}$.

For the range of parameters in our measurements, it was hard to observe the behavior of the TLS loss. However, the $1/Q$ and $\delta f_r/f_r$ increase with increasing $I_{\rm opt}$ behavior can be explained well by the nonequilibrium quasiparticle distribution. The $T_{\rm eff}$ dependence on $I_{\rm opt}$ is consistent with the optical power absorbed by the resonator. I also showed that the nonequilibrium quasiparticle distribution with the effective heating model explains our results better than a simple heating picture of quasiparticles.

The quasiparticle $1/Q$ show a dependence on $P_{\rm rf}$ that was also seen at refrigerator base temperature and higher temperatures, as discussed in Chapter 4. However, for the illumination case, the shape of the $1/Q$ vs $P_{\rm rf}$ curves appear very similar to the curve for $1/Q$ due to TLS loss. I discussed how we may be able to define a characteristic scale for quasiparticle loss, similar to the characteristic field or voltage for TLS loss. However, due to the nonanalytical nature of the nonequilibrium quasiparticle distribution, I did not obtain an explicit formula for this characteristic field.

I also discussed a comparison between data collected using illumination from

the perpendicular fiber, which we used for most of our measurements, to data collected using illumination from parallel fiber. The difference in response between the two fibers was roughly consistent with the difference in cross-section of the resonator seen by the two illuminations, assuming a small misalignment of the fiber in the parallel case. We also attempted to illuminate the resonator using polarized light from both fibers and varied the polarization ellipticity and angle. The results were as expected, with perpendicular illumination showing no dependence on polarization and parallel illumination showing a strong dependence. The results from these comparison measurements were useful in validating the design of our hybrid system.

Finally, I also measured the phase response of the resonance as a function of time under pulsed illlumination. We measured a recombination time constant of about 0.6 ms. This was about an order of magnitude higher than the expected value, but shorter than what Jared Hertzberg and Kristen Voigt obtained in a similar study in another system. Finally, I discussed the need for a better model which includes the transient behavior of the nonequilibrium quasiparticle distribution.

Chapter 6: Theory of the Transmon

In this chapter, I discuss the theory of transmon qubits. I begin by discussing the background, basic circuit representation and Hamiltonian. I then discuss the Circuit QED system, where the transmon is coupled to a harmonic oscillator, and discuss the resulting Hamiltonian. I then describe two ways to read out the state of a transmon: the low-power readout and the high power readout. Next I discuss dissipation and dephasing in transmons and the underlying sources. I next describe how an applied rf drive affects the state of the qubit, and how the presence of decoherence affects the drive. Finally, I discuss how nonequilibrium quasiparticles may be generated in a transmon, and examine how they affect the relaxation time and transition frequency.

6.1 Transmon Circuit Representation and Hamiltonian

The design of the transmon qubit was based on a previous qubit design, the Cooper-pair box (CPB). The CPB was the first superconducting qubit design that was experimentally realized [17, 24]. The circuit representation of a CPB is shown in Fig. 6.1. It consists of a single ultra-small junction J and a parallel capacitance C_J, which comes from the capacitance of the Josephson junction. The key element

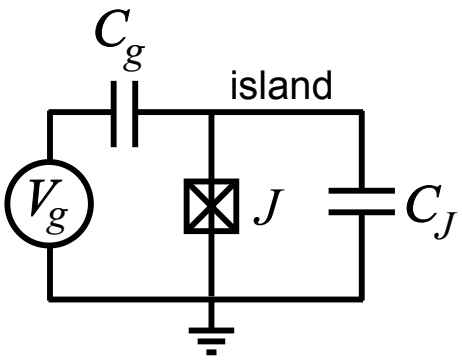

Figure 6.1: Circuit diagram of a Cooper-pair box.

is an island formed by one junction electrode and the associated capacitor plate. Typically CPB's are biased with a gate voltage V_g connected to the junction by a gate capacitance C_g. The Hamiltonian of a CPB can be written as [196]

$$\hat{\mathcal{H}} \;=\; 4E_C(\hat{n} - n_g)^2 \;-\; E_J \cos\hat{\gamma}, \tag{6.1}$$

where n is the excess number of Cooper pairs that have tunneled through the junction and are on the island, $n_g = -C_g V_g/2e$ is the Cooper pair number offset from voltage bias, and γ the phase across the junction. Here I also used the energies E_J and E_C which were also defined in Eqs. 1.8 and 1.9,

$$E_J \;= \frac{\Phi_0 I_0}{2\pi}, \tag{6.2}$$

$$E_C \;= \frac{e^2}{2C_\Sigma}, . \tag{6.3}$$

In the above equations, Φ_0 is the flux quantum, I_0 is the junction critical current, and $C_\Sigma = C_J + C_g$ is the total capacitance of the island. Cooper-pair boxes typically have $E_J \lesssim E_C$ and in this limit the charge on the island is a good quantum variable (except at certain values of n_g). I note here that the operators $\hat{n}$ and $\hat{\gamma}$ are conjugate

variables, and satisfy the commutation relation

$$[\hat{\gamma}, \hat{n}] \; = \; i. \tag{6.4}$$

Using Mathieu functions, the Hamiltonian can be solved exactly in the phase basis, and the energy eigenvalues can be written as [32, 196]

$$E_m \; = \; E_C a_{2[n_g + k(m,n_g)]}(-E_J/2E_C), \tag{6.5}$$

where $m = 0, 1, 2, \ldots$, $a_r(q)$ is the characteristic value for Mathieu cosine function with characteristic exponent r and parameter q, and $k(m, n_g)$ is integer-valued function sorting the order of the eigenvalues. The two lowest energy levels E_0 and E_1, with the qubit transition energy given by the energy separation $E_{01} = E_1 - E_0$, can be used for the qubit ground and excited states.

Figure 6.2 shows E_m for $m = 0, 1$, and 2 for three different values of E_J/E_C, corresponding to the states $|g\rangle$, $|e\rangle$, and $|f\rangle$ of the qubit. For the Cooper-pair box regime $E_J/E_C \lesssim 1$ (Fig. 6.2(a)), the E_m curves depend strongly on bias n_g, while for $E_J/E_C \gg 1$ (Fig. 6.2(c)), the E_m curves appear to be independent of n_g.

CPB qubits have typically been operated at $n_g = \pm 0.5$ where E_{01} is minimum [197]. These points are typically called the "sweet spot" because E_{01} is minimally affected by small fluctuations in n_g, that is, the qubit is protected from charge noise. As dephasing can be caused by low frequency fluctuations that affect E_{01} (see Section 6.5), a CPB will have less charge-noise induced dephasing at the sweet spot. However, away from the sweet spot, the coherence degrades, and this is a problem because larger chargefluctuations will move the qubit away from the sweet spot.

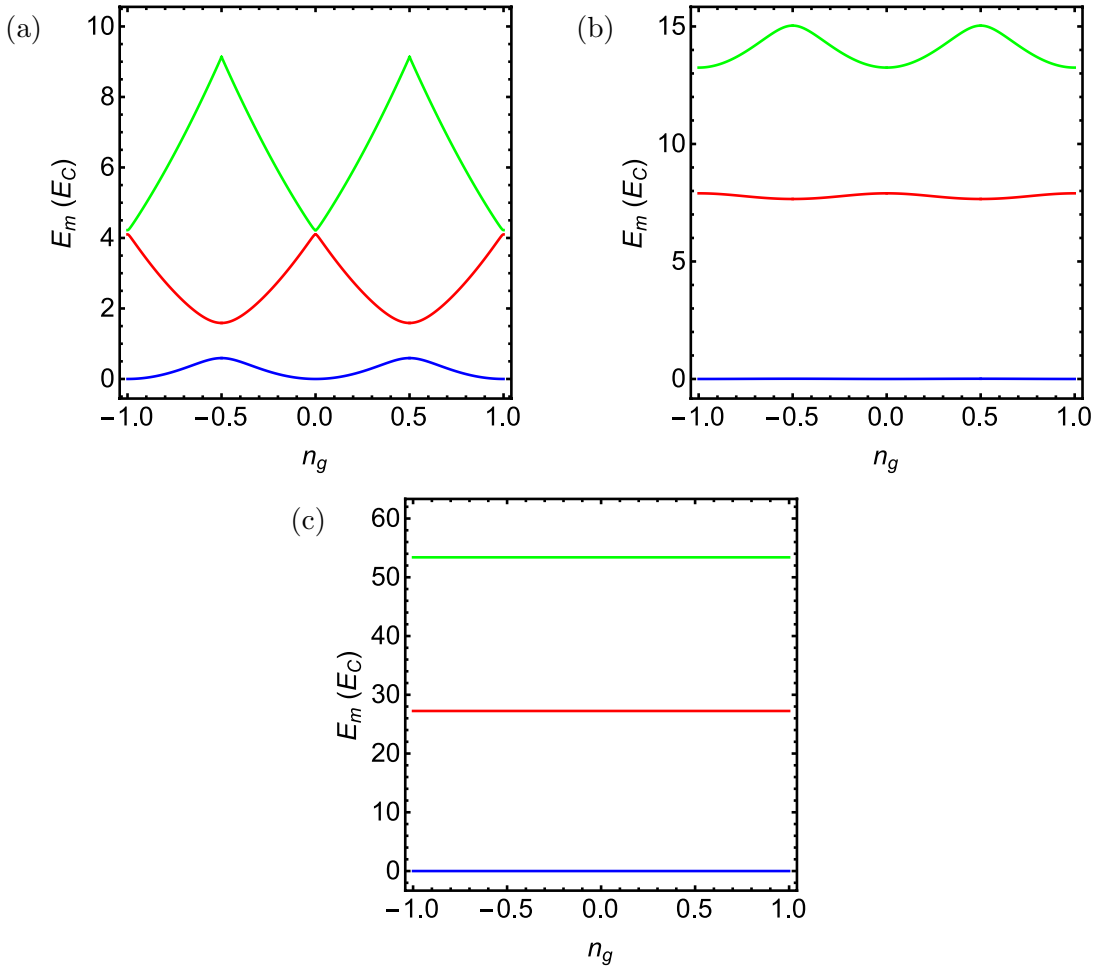

Figure 6.2: Energy eigenvalues for Cooper-pair box for (a) $E_J/E_C = 1$, (b) $E_J/E_C = 10$, and (c) $E_J/E_C = 100$. For all plots, the blue curve corresponds to E_0, the red curve corresponds to E_1, and the green curve corresponds to E_2.

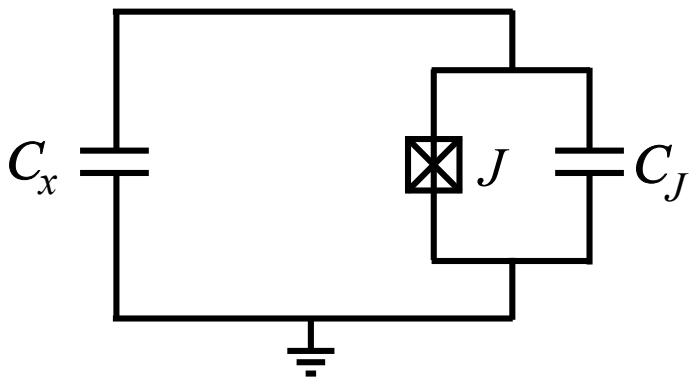

Figure 6.3: Circuit diagram of an isolated transmon.

The dephasing in the CPB was so large, even at the sweet spot, that it is no longer considered a viable qubit candidate, and this was the motivation for the design of the transmon, which was theoretically proposed by Koch *et al.* [32]. As shown in Fig. 6.2(c), for $E_J/E_C \gg 1$, the E_m's are independent of n_g and hence E_{01} is independent of n_g as well. This means that device in this regime are protected by charge noise and that they cannot be tuned by means of bias voltage.

The transmon regime can be achieved by adding a shunting capacitor C_x parallel to the junction to reduce E_C, as shown by the circuit diagram of Fig. 6.3. In the figure the gate voltage V_g is removed as now the qubit energy cannot be tuned by changing V_g. By using a dc SQUID instead of a single junction, one can vary E_J and hence the qubit energy by applying flux bias. Since this also couples in flux noise, it is not necessarily desirable and the transmon I discuss in Chapter 8 has a single junction and it is not tunable.

The Hamiltonian of the transmon is esentially the same as the Hamiltonian of an unbiased phase qubit or of a CPB as given by Eq. 6.1, except I set $n_g = 0$

and take $C_\Sigma = C_x + C_J$. The second term (phase term) of the Hamiltonian can be thought of as potential energy with a minimum when $\gamma = 0$. Assuming small deviations around this minimum, I can expand $\cos\hat{\gamma} = 1 - \frac{\hat{\gamma}^2}{2!} + \frac{\hat{\gamma}^4}{4!} - \ldots$, and the Hamiltonian can be written as

$$\hat{\mathcal{H}} \;=\; 4E_C\hat{n}^2 \;+\; \frac{E_J}{2}\hat{\gamma}^2 \;-\; E_J \;-\; \frac{E_J}{24}\hat{\gamma}^4 \;+\; \ldots \tag{6.6}$$

The first and second term on the right hand side are simply the Hamiltonian of a harmonic oscillator. The third term is a constant offset and can be ignored. The fourth term is fourth order in $\hat{\gamma}$ and since γ is small by assumption, this term can be thought of as a perturbation to the harmonic oscillator. Analogous to the position and momentum of a harmonic oscillator, $\hat{\gamma}$ and $\hat{n}$ can be written in terms of creation and annihilation operators $\hat{b}^\dagger$ and $\hat{b}$ as

$$\hat{\gamma} \;= \frac{1}{\sqrt{2}}\left(\frac{8E_C}{E_J}\right)^{1/4}(\hat{b}^\dagger + \hat{b}) \tag{6.7}$$

$$\hat{n} \;= \frac{i}{\sqrt{2}}\left(\frac{E_J}{8E_C}\right)^{1/4}(\hat{b}^\dagger - \hat{b}) \tag{6.8}$$

To fourth order, the Hamiltonian can then be rewritten as

$$\hat{\mathcal{H}} \;=\; \sqrt{8E_JE_C}\left(\hat{b}^\dagger\hat{b} + \frac{1}{2}\right) \;-\; E_J \;-\; \frac{E_C}{12}\left(\hat{b}^\dagger + \hat{b}\right)^4. \tag{6.9}$$

The first term is the harmonic oscillator Hamiltonian, with spacing between levels $\sqrt{8E_JE_C}$. Using the definition of E_J and E_C, as well as the Josephson inductance $L_J = \Phi_0/2\pi I_0$ (see Eq. 1.6 with $\gamma = 0$), the level spacing can be written as $\hbar/\sqrt{L_JC_\Sigma}$, which is exactly what would be expected for an LC resonator with inductance L_J and capacitance C_Σ.

I can find the leading order correction to the energy eigenvalues by using first-order perturbation theory. For the $\hat{\gamma}^4$ perturbative term, I find

$$\begin{aligned} E_m^{(1)} &= -\frac{E_C}{12}\langle m^{(0)}|\left(\hat{b}^\dagger + \hat{b}\right)^4 |m^{(0)}\rangle \\ &= -\frac{E_C}{12}(6m^2 + 6m + 3), \end{aligned} \tag{6.10}$$

where $|m^{(0)}\rangle$ is the m-th eigenstate of the unperturbed harmonic oscillator, with $m = 0, 1, 2, \ldots$. Hence the energy of the m-th level E_m is

$$E_m = \sqrt{8E_J E_C}\left(j + \frac{1}{2}\right) - E_J - \frac{E_C}{12}(6m^2 + 6m + 3). \tag{6.11}$$

Thus the transmon transition energy E_{01} is

$$E_{01} = E_1 - E_0 = \sqrt{8E_J E_C} - E_C. \tag{6.12}$$

To be useful as a qubit, the transmon needs to be sufficiently anharmonic. That is, the next highest transition energy $E_{12} = E_2 - E_1$ needs to be far enough away from E_{01} so that the lowest two energy levels can be isolated as a qubit. The anharmonicity α is defined by

$$\alpha = E_{12} - E_{01}. \tag{6.13}$$

Form Eq. 6.11, one finds

$$\alpha = -E_C. \tag{6.14}$$

This negative sign means E_{12} is lower than E_{01}. Typically we would like the anharmonicity to be of order 100 or 200 MHz to allow fast high-power pumping of the $0 \to 1$ transition without causing occupation of $|2\rangle$ state. For $E_{01}/h \sim 5$ to 10 GHz this gives $20 \lesssim E_J/E_C \lesssim 200$ as an acceptable range for the transmon.

6.2 Circuit QED System

A transmon is typically coupled to a microwave resonator which in turn is coupled to a microwave drive line and an output line for state readout. The resonator can be a planar resonator (for 2d transmons) [198] or a 3d cavity (for 3d transmons) [49]. This arrangement is called circuit quantum electrodynamics (QED) [36, 172], analogous to cavity QED systems in quantum optics where atomic states are coupled to an optical cavity [199].

6.2.1 Jaynes-Cummings Hamiltonian

For a two-level system with transition frequency ω_q coupled to a cavity with frequency ω_r with coupling strength g_{ge}, the Hamiltonian in the rotating wave approximation is given by the Jaynes-Cummings Hamiltonian [129]

$$\hat{\mathcal{H}} \;=\; \hbar\omega_r \hat{a}^\dagger \hat{a} \;+\; \frac{\hbar\omega_q}{2}\hat{\sigma}_z \;+\; \hbar g_{ge}(\hat{a}\hat{\sigma}^+ + \hat{a}^\dagger\hat{\sigma}^-). \tag{6.15}$$

Here $\hat{a}^\dagger$ is the creation operator for photons in the harmonic cavity and $\hat{a}$ is the annihilation operator. $\hat{\sigma}_x$, $\hat{\sigma}_y$, and $\hat{\sigma}_z$ are the x-, y- and z-Pauli matrices, respectively (see Eq. 2.36), and $\sigma^\pm$ are defined as

$$\sigma^\pm \;=\; \frac{\sigma_x \pm i\sigma_y}{2}. \tag{6.16}$$

I define $|g\rangle$ as the qubit ground state, $|e\rangle$ as the qubit excited state, and $|m\rangle$ as the cavity state with m photons inside the cavity. Then the qubit-cavity product states can be written as $|g, m\rangle$ and $|e, m\rangle$. Figure 6.4 shows the energy ladder of these states, with the levels shown when $g_{ge} = 0$.

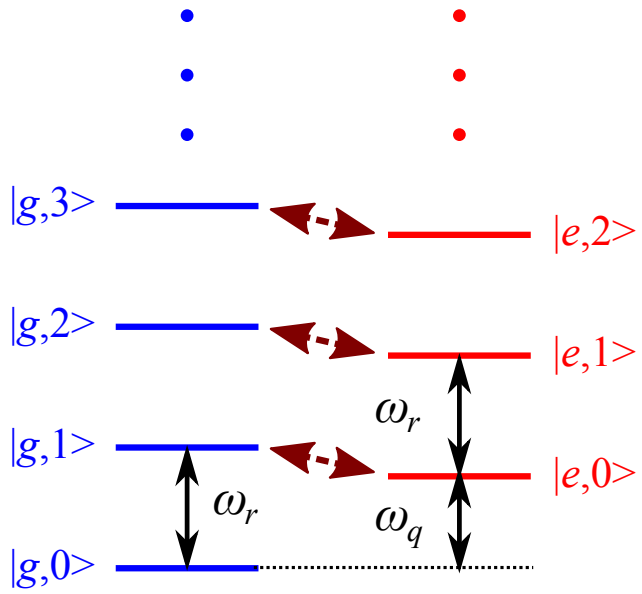

Figure 6.4: Energy diagram of a qubit-cavity system showing the levels for an uncoupled system. The brown arrows represent the states that are coupled.

The coupling term $\hbar g_{ge}(\hat{a}\hat{\sigma}^{+}+\hat{a}^{\dagger}\hat{\sigma}^{-})$ in the Hamiltonian of Eq. 6.15 only couples $|g,m\rangle$ states with $|e,m-1\rangle$ states (shown by the brown arrows in Fig. 6.4). That is, the coupling term only couples states with the same total cavity and qubit excitation numbers. If I write the Hamiltonian in the product state basis, the Hamiltonian then has a block-diagonal form with 2×2 blocks containing states with the same total excitation. For total excitation number $n>0$, the block for $|e,n-1\rangle$ and $|g,n\rangle$ can be written as

$$\mathcal{H}_n = \hbar\begin{pmatrix}(n-1)\omega_r+\omega_q/2 & g_{ge}\sqrt{n}\\ g_{ge}\sqrt{n} & n\omega_r-\omega_q/2\end{pmatrix}. \tag{6.17}$$

Note also the uncoupled ground state $|g,0\rangle$ has energy $E_{|g,0\rangle}=-\hbar\omega_r/2$. The eigen-

values of the $n-$th block of Eq. 6.17 are

$$E_{n,\pm} \;=\; \left(n-\frac{1}{2}\right)\hbar\omega_r \;\pm\; \hbar\sqrt{\left(\frac{\Delta}{2}\right)^2 + g_{ge}^2 n}. \tag{6.18}$$

Here I have defined $\Delta \equiv \omega_r - \omega_q$ as the detuning between the cavity and qubit frequencies, and I have implicitly assumed $\omega_r > \omega_q$ so $\Delta > 0$, even though that need not be the case. The eigenstates are given by

$$|n,-\rangle \;=\; \cos\theta_n|e,n-1\rangle \;-\; \sin\theta_n|g,n\rangle \tag{6.19}$$

$$|n,+\rangle \;=\; \sin\theta_n|e,n-1\rangle \;+\; \cos\theta_n|g,n\rangle, \tag{6.20}$$

where $\tan(2\theta_n) = 2g_{ge}\sqrt{n}/\Delta$.

From Eq. 6.18 one sees that the energies of the coupled states are shifted due to the coupling. These states are called the 'dressed' states because they are 'dressed' by the presence of the photon field. As an example, when the cavity and the qubit are resonant ($\omega_q = \omega_r$), the resulting dressed states for n excitations are separated by $2\hbar g_{ge}\sqrt{n}$ and the states are an equal superposition of $|e,n-1\rangle$ and $|g,n\rangle$.

6.2.2 Dispersive Regime

The energy of the dressed states of Eq. 6.18 can be rearranged such that

$$E_{n,\pm} \;=\; \left(n-\frac{1}{2}\right)\hbar\omega_r \;\pm\; \frac{\hbar\Delta}{2}\sqrt{1+\frac{n}{n_c}}, \tag{6.21}$$

where the critical excitation number n_c is defined by

$$n_c \;\equiv\; \frac{\Delta^2}{4g_{ge}^2}. \tag{6.22}$$

For $n \ll n_c$, I can take the approximation

$$\begin{aligned} E_{n,-} &\approx \left(n - \frac{1}{2}\right)\hbar\omega_r - \frac{\hbar\Delta}{2}\left(1 + \frac{n}{2n_c}\right) \\ &= (n-1)\hbar\omega_r + \frac{\hbar\omega_q}{2} - \frac{n\hbar g_{ge}^2}{\Delta} \qquad (6.23) \\ E_{n,+} &\approx \left(n - \frac{1}{2}\right)\hbar\omega_r + \frac{\hbar\Delta}{2}\left(1 + \frac{n}{2n_c}\right) \\ &= n\hbar\omega_r - \frac{\hbar\omega_q}{2} + \frac{n\hbar g_{ge}^2}{\Delta}. \qquad (6.24) \end{aligned}$$

Equations 6.23 and 6.24 show that for the regime $n \ll n_c$, the coupled energies are shifted by $n\hbar g_{ge}^2/\Delta$. Notice that in order to reach the limit where $n \ll n_c$ requires $g \ll \Delta$, and this is called the dispersive limit. Typically circuit QED systems are operated within this regime, although $n \gg n_c$ may be used during the readout (see Section 6.3.2)

In the dispersive limit, the dressed states of Eqs. 6.19 and 6.20 can be approximated as

$$|n,-\rangle \approx |e,n-1\rangle - \frac{g_{ge}\sqrt{n}}{\Delta}|g,n\rangle \qquad (6.25)$$

$$|n,+\rangle \approx \frac{g_{ge}\sqrt{n}}{\Delta}|e,n-1\rangle + |g,n\rangle. \qquad (6.26)$$

Thus the dressed states in the dispersive limit are nearly the same as the uncoupled qubit-cavity product states, with a small $g\sqrt{n}/\Delta$ contribution from the state it's coupled to.

To diagonalize the Hamiltonian consider the unitary transformation

$$\mathcal{U} = \exp\left[-\frac{g_{ge}}{\Delta}\left(\hat{a}\hat{\sigma}^+ - \hat{a}^\dagger\hat{\sigma}^-\right)\right] \qquad (6.27)$$

Using $\mathcal{U}$ and taking the dispersive approximation $g \ll \Delta$, the Hamiltonian given by

Eq. 6.15 can be rewritten as [172]

$$\mathcal{U}\,\mathcal{H}\,\mathcal{U}^{\dagger} \;=\; \hbar\left(\omega_r - \frac{g_{ge}^2}{\Delta}\hat{\sigma}_z\right)\hat{a}^{\dagger}\hat{a} \;+\; \frac{\hbar}{2}\left(\omega_q - \frac{g_{ge}^2}{\Delta}\right)\hat{\sigma}_z. \tag{6.28}$$

The first term on the right hand side of Eq. 6.28 shows that the cavity frequency is shifted depending on the state of the qubit. When the qubit is in the ground state, the cavity frequency is shifted by g_{ge}^2/Δ, and when the qubit is in the excited state, the cavity frequency is shifted by the same amount in the opposite direction. I define the dispersive shift as $\chi \equiv g_{ge}^2/\Delta$, and the two dressed cavity frequencies are separated by 2χ. The second term on the right hand side of Eq. 6.28 shows that the qubit frequency is also shifted by χ.

Eq. 6.28 can also be rearranged to get

$$\mathcal{U}\,\mathcal{H}\,\mathcal{U}^{\dagger} \;=\; \hbar\omega_r\hat{a}^{\dagger}\hat{a} \;+\; \frac{\hbar}{2}\left[\omega_q - 2\chi\left(\hat{a}^{\dagger}\hat{a} + \frac{1}{2}\right)\right]\hat{\sigma}_z. \tag{6.29}$$

The second term on the right hand side of Eq. 6.29 shows that in addition to the χ shift, the qubit frequency is further shifted depending on the number of photons inside the cavity, with each photon contribute a further shift of 2χ. I can define $\tilde{\omega}_{q,0} = \omega_q - \chi$ as the dressed qubit frequency when there are zero photons in the cavity. Then the qubit frequency when there are m photons in the cavity is given by

$$\tilde{\omega}_{q,m} \;=\; \tilde{\omega}_{q,0} \;-\; 2m\chi. \tag{6.30}$$

The energy level of the circuit QED system in the dispersive regime is summarized in Fig. 6.5. In the figure, the dashed lines represent the energy of the bare (uncoupled) states, while the solid lines represent the energy of the dressed (coupled) states. The black arrows represent the dressed cavity frequencies, with the

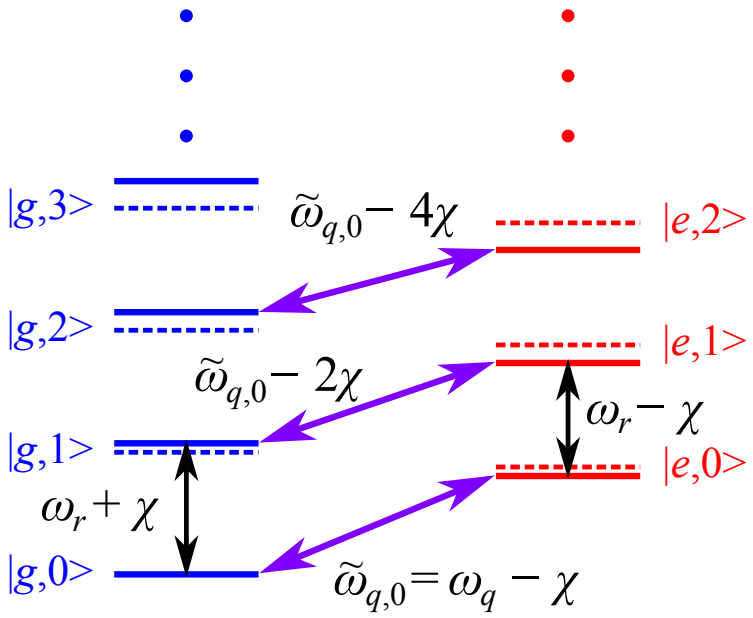

Figure 6.5: Energy diagram of dressed states (solid) and uncoupled bare (dashed) states in a qubit-cavity system in the dispersive regime.

left arrow showing the cavity transition when the qubit is in the ground state, and the right arrow showing the cavity transition when the qubit is in the excited state. The purple arrows represent the dressed qubit frequencies, with the lowermost arrow when there are no photons in the cavity, and the arrows above representing an increasing number of cavity photons.

In practice, the number of photons inside the cavity can fluctuate, with a probability $P(m)$ to have m photons inside the cavity. When one performs qubit spectroscopy, the observed spectrum will include all the allowed qubit transitions that can occur given the initial state of the system. When the linewidth of each peak Γ is larger than χ, the resulting spectrum when the photon number is fluctuating can appear as a non-Lorentzian or distorted peak, as Ben Cooper and I observed in a LC

filtered dc SQUID phase qubit [31, 170]. This regime when $\Gamma > \chi$ is called the weak dispersive regime. The opposite regime, when $\Gamma < \chi$ is called the strong dispersive regime. In the strong dispersive regime, the spectrum shows well-separated peaks, with the relative height of the m-th peak proportional to the probablity $P(m)$. When there is no cavity drive, the probability should follow a thermal distribution approximately $P(m) \propto e^{-m\hbar\tilde{\omega}_{c,g}/k_BT}$ where T is the effective temperature of the cavity. When there is a weak coherent drive at the cavity resonance with power such that the average photon number inside the cavity is $\langle m \rangle$, one expects the probability to follow Poisson distribution $P(m) = e^{-\langle m \rangle}\langle m \rangle^m / m!$ [200, 201], although significant deviations have also been observed [202].

6.2.3 Generalized Jaynes-Cummings Hamiltonian

In the preceding discussions of a circuit QED system the qubit only has two levels. As I discussed in Section 6.1, transmons have more than two energy levels. The Jaynes-Cumming Hamiltonian can be generalized to include multiple levels and the Hamiltonian can be put in the form [32]

$$\hat{\mathcal{H}} = \hbar\omega_r \hat{a}^\dagger \hat{a} + \hbar \sum_m \omega_m |m\rangle\langle m| + \hbar \sum_m \left(g_{m,m+1} |m\rangle\langle m+1| \hat{a}^\dagger + \text{h.c} \right). \quad (6.31)$$

Here $\hbar\omega_m = E_m$ are the transmon energies as discussed in Section 6.1, $|m\rangle$ are the transmon eigenstates, and $g_{m,m+1}$ is the coupling strength between the cavity and the $|m\rangle \leftrightarrow |m+1\rangle$ transition of the transmon. The $|m\rangle \leftrightarrow |n\rangle$ transition frequency of the transmon for $n > m$ is given by $\omega_{m,n} = \omega_n - \omega_m$. To reduce the possibility of confusion with the number states of the cavity, I will write the transmon states

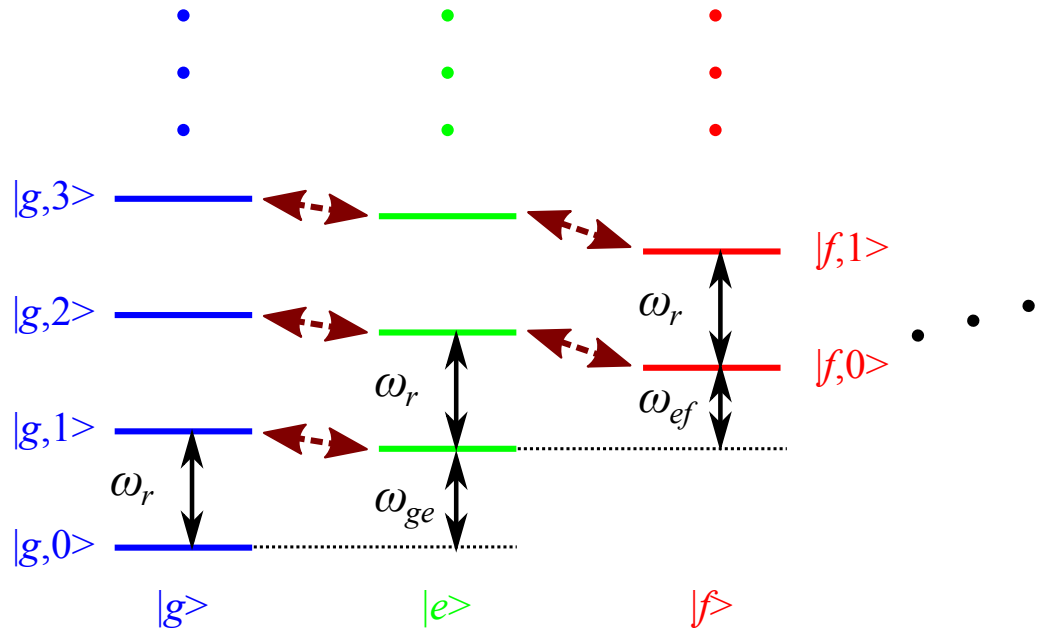

Figure 6.6: Energy diagram of a transmon-cavity system showing the levels for an uncoupled system. The brown arrows represent the states that are coupled.

$|m\rangle$ with indices $g, e, f, \ldots$ similar to the qubit in the previous subsections instead of numbers $0, 1, 2, \ldots$ as in Section 6.1. The Hamiltonian of Eq. 6.31 can also be derived using a circuit model of a transmon (see Fig. 6.3) coupled capacitively to an LC resonator [32, 201]. The energy ladder of the (uncoupled) transmon-cavity system is shown in Fig. 6.6.

Similar to the two-level qubit system, the dispersive limit is achieved when $g_{m,m+1} \ll \Delta_{m,m+1}$, where $\Delta_{m,m+1} = \omega_r - \omega_{m,m+1}$ is the detuning between the cavity and the $|m\rangle \leftrightarrow |m+1\rangle$ qubit transition. Similar to the χ in the two-level case, I can define

$$\chi_{m,m+1} = \frac{g_{m,m+1}^2}{\Delta_{m,m+1}}. \tag{6.32}$$

In the dispersive regime, Koch *et al.* have shown that in the reduced transmon

Hilbert space containing only $|g\rangle$ and $|e\rangle$, the Hamiltonian of Eq. 6.31 becomes the effective Hamiltonian $\mathcal{H}_{\text{eff}}$ given by [32]

$$\mathcal{H}_{\text{eff}} \approx \hbar\tilde{\omega}_r\hat{a}^\dagger\hat{a} + \frac{\hbar\tilde{\omega}_{ge}}{2}\hat{\sigma}_z - \hbar\chi\hat{a}^\dagger\hat{a}\hat{\sigma}_z. \tag{6.33}$$

Here $\tilde{\omega}_r$ is the shifted cavity frequency given by

$$\tilde{\omega}_r \approx \omega_r + \frac{\chi_{ef}}{2}, \tag{6.34}$$

$\tilde{\omega}_{ge}$ is the dressed qubit frequency given by

$$\tilde{\omega}_{ge} \approx \omega_{ge} - \chi_{ge}, \tag{6.35}$$

χ is the effective dispersive shift given by

$$\chi = \chi_{ge} - \frac{\chi_{ef}}{2}, \tag{6.36}$$

Grouping the second and the third term in the right hand side of Eq. 6.33 shows that each photon in the cavity contributes an additional 2χ shift in the qubit frequency. On the other hand, grouping the first and third term in the right hand side of Eq. 6.33 shows that the cavity frequency is further shifted depending on the state of the transmon. When the transmon is at $|g\rangle$, then the cavity frequency is

$$\tilde{\omega}_{r,g} = \tilde{\omega}_r + \chi = \omega_r + \chi_{ge}. \tag{6.37}$$

When the transmon is at $|e\rangle$, then the cavity frequency is

$$\tilde{\omega}_{r,e} = \tilde{\omega}_r - \chi = \omega_r + (\chi_{ef} - \chi_{ge}). \tag{6.38}$$

6.3 State Readout

Below I describe two methods to read out the state of the transmon. For my measurements of the transmon that I describe in Chapter 8, I used a low-power dispersive readout (Section 6.3.1) for the initial search for the qubit transitions. For the rest of the measurements, I used the high-power Jaynes-Cummings readout (Section 6.3.2).

6.3.1 Dispersive (Low Power) Readout

The low-power dispersive readout uses the fact that the cavity resonance frequency depends on the state of the qubit, as discussed in the previous section. In practice, the readout is typically accomplished by applying a continuous tone at the dressed frequency for the ground state ($\omega_r + \chi_{ge}$ for transmon, see Eq. 6.37) and then monitoring the change in amplitude or phase of the output signal. Additional microwave signals can then be used to perform qubit operation while the readout is on

Equation 6.21 implies that the dispersive regime only works for small photon numbers in the cavity. This means the measurement tone needs to be sufficiently weak such that the average photon number $\langle n \rangle$ inside the cavity is $\langle n \rangle \ll n_c = \Delta^2/4g_{ge}^2$. Additionally, as discussed in the previous section, the presence of photons in the cavity will cause additional shift in the qubit frequency as well, and this results in the emergence of multiple photon peaks. To suppress the photon peaks and isolate a single qubit transition peak (corresponding to 0 photons in the cavity),

then the measurement power needs to be very weak, *i.e.* $\langle n \rangle \ll 1$.

As this readout method probes a state that is mainly a cavity state with very small ($\approx g_{ge}/\Delta$) amplitude of the qubit state, the effect of the measurement on the qubit state is weak. Hence the dispersive readout is considered a nearly quantum non-demolition (QND) measurement [172], which does not completely project, collapse, or destroy the quantum state being measured. However, because this readout requires a very small measurement power, typically a large amount of averaging is needed to achieve a good signal to noise ratio. This is the reason why I did not use this readout that much. However, this is a potentially a very powerful technique because of its QND nature. Thus, for example, with the addition of a good low-noise parametric amplifier, Murch *et al.* used this measurement technique to track the trajectory of the state of a qubit in real time [203].

6.3.2 Jaynes-Cummings (High Power) Readout

When the cavity is driven very strongly, the dispersive limit breaks down and the cavity frequency recovers to the bare (uncoupled) cavity frequency ω_r. For a two-level qubit, this can be shown relatively easily from the exact energy eigenvalues given in Eq. 6.18. The cavity frequency $\omega_{r,n,\pm}$ at photon occupation n can be defined as the frequency needed to add additional photon into the cavity, that is, from n to $n+1$. From the definitions of $E_{n,\pm}$ in Eq. 6.18, I can write $\omega_{r,n,\pm}$ as

$$\begin{aligned}\omega_{r,n,\pm} &= (E_{n+1,\pm} - E_{n,\pm})/\hbar \\ &= \omega_r \pm \left[\sqrt{\left(\frac{\Delta}{2}\right)^2 + g_{ge}^2(n+1)} - \sqrt{\left(\frac{\Delta}{2}\right)^2 + g_{ge}^2 n} \right]. \end{aligned} \tag{6.39}$$

For small n, Eq. 6.39 yields the dressed cavity frequencies in the dispersive regime, with $\omega_{r,n,+}$ corresponding to the cavity frequency when the qubit is in $|g\rangle$, and $\omega_{r,n,-}$ corresponding to the cavity frequency when the qubit is in $|e\rangle$. For large n, one finds

$$\omega_{r,n,\pm} \approx \omega_r \pm g_{ge}\left(\sqrt{n+1}-\sqrt{n}\right) \approx \omega_r \pm \frac{g_{ge}}{2n}. \tag{6.40}$$

Thus for very large n, the cavity frequency approaches ω_r for both states.

In Eq. 6.40, the cavity frequency approaches ω_r equally for both $|g\rangle$ and $|e\rangle$ states. For a transmon with higher level states, Boissonneault *et al.* found that the behavior of the cavity frequency as a function of n also depended on the state of the qubit [204]. The dressed cavity frequency approaches the bare cavity frequency faster when the qubit is in the excited state than when it is in the ground state. One implication of this behavior is that if one applies a microwave signal with frequency ω_r, there will be a range of power where the amplitude of the output signal is high when the qubit is in the excited state and low when it is in the ground state. Below this range of power, the cavity resonance is near the low-power dressed frequency (for both ground and excited states) and the output signal would be low at ω_r, while above well this range of power, the cavity resonance is at the bare frequency for both states and the output signal is high independent of the qubit state.

Applying the bare cavity tone changes the states significantly, and thus this readout is not a QND measurement. This means in practice, the cavity tone is applied as a short (a few μs) pulse at the end of the qubit operations. Reed *et al.* were the first to perform this readout on 2d transmon qubits [205] and many other groups have used it since. The fact that the relatively high power is used allows for

good signal-to-noise ratio.

6.4 Relaxation Time in Transmon

As I discussed in Section 1.3, one of the characteristic times for a qubit is the relaxation time T_1. The relaxation time is the mean time for a qubit to decay from the excited state to the ground state. If a qubit is prepared in its excited state and then nothing is done, the probability $P_e(t)$ of the qubit to still be in the excited state a time interval t latershould follow

$$P_e(t) \;=\; e^{-t/T_1}. \tag{6.41}$$

Relaxation is caused by the loss of energy from the qubit to various dissipation channels, either internal or external to the qubit. As an alternative to T_1, relaxation can also be characterized by the relaxation rate $\Gamma \equiv 1/T_1$ or the quality factor $Q = \omega_{ge} T_1$.

6.4.1 Circuit Model for Relaxation

A dissipation channel can be modeled as an arbitrary admittance $Y(\omega)$ connected in parallel to the transmon, as shown in Fig. 6.7. For this circuit model, the relaxation time is just the RC time constant, which is given by [160, 206]

$$T_1 \;=\; \frac{C_\Sigma}{\mathrm{Re}[Y(\omega_{ge})]}. \tag{6.42}$$

Figure 6.8 shows two of the simplest possible dissipation models. The first one, Fig. 6.8(a) shows the junction coupled directly to an impedance Z_0, for example the

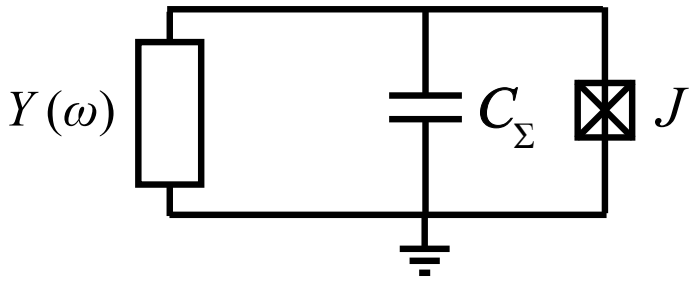

Figure 6.7: Circuit model for relaxation in a transmon. The dissipation channel is modeled as an admittance $Y(\omega)$.

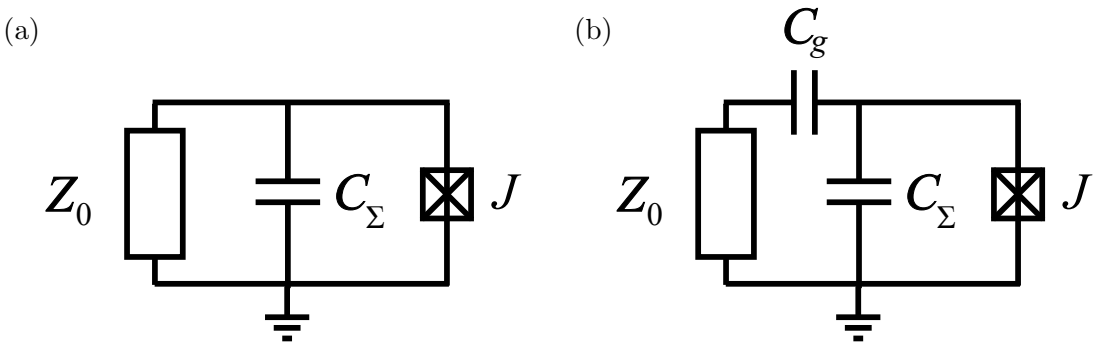

Figure 6.8: Simple dissipation models showing (a) transmon directly coupled to impedance Z_0 and (b) transmon capacitively coupled to impedance Z_0 by capacitance C_g.

50 Ω line. In this case $T_1 = Z_0 C_\Sigma$. However, transmons are not directly coupled to 50 Ω lines because the resulting T_1 would be so short that the device would be useless. Figure 6.8(b) shows an impedance Z_0 that is capacitively coupled to a transmon by a capacitance C_g. The admittance $Y(\omega)$ of this circuit is given by

$$Y(\omega) \;=\; \frac{1}{Z_0 + (i/\omega C_g)} \;=\; \frac{Z_0 - (i/\omega C_g)}{Z_0^2 + (1/\omega C_g)^2}. \tag{6.43}$$

For weak coupling $C_g \ll C_\Sigma$ and $C_g \ll 1/\omega Z_0$, the relaxation time can be approximated as

$$T_1 \;\approx\; \frac{C_\Sigma}{\omega_{ge}^2 C_g^2 Z_0}. \tag{6.44}$$

which will be much longer greater than the value $Z_0 C_\Sigma$ found for the direct coupled case.

There are several known and possible sources of energy relaxation in a transmon. The overall relaxation rate is the sum of all the relaxation rate from all sources, and the overall T_1 is then given by

$$\frac{1}{T_1} \;=\; \sum_i \frac{1}{T_{i,1}}, \tag{6.45}$$

where $1/T_{i,1}$ is the relaxation rate contribution from each source. I describe some of the main known sources of dissipation below.

6.4.2 Purcell Effect

As I showed in Section 6.2.2, in the dispersive regime the dressed states of a circuit QED system are the uncoupled qubit-cavity product states with a small contribution (of order $\sim g/\Delta$) from the states they are coupled to. The qubit-cavity

coupling also means that loss in the cavity will contribute to loss in the qubit. This effect is called the Purcell effect [159] (see also Section 2.4.2). If the relaxation rate of the cavity is $\kappa \equiv 1/T_{1,\mathrm{c}}$, then the Purcell contribution of the relaxation rate is given by

$$\Gamma_{\mathrm{Purcell}} = \left(\frac{\Delta}{g_{ge}}\right)^2 \kappa \tag{6.46}$$

$$\frac{1}{T_{1,\mathrm{Purcell}}} = \left(\frac{\Delta}{g_{ge}}\right)^2 \frac{1}{T_{1,c}}. \tag{6.47}$$

In reality, the cavity or resonator will also have higher order modes, in addition to the fundamental mode typically used for circuit QED. The qubit can couple to these modes as well, and this will give additional Purcell contributions to the qubit relaxation. The Purcell contribution to relaxation, including from higher order modes, can also be found from the admittance $Y(\omega)$ seen by a transmon [160, 201], *i.e.* if one can find $Y(\omega)$ seen by the transmon, the Purcell contribution will be included

6.4.3 Two-Level Systems

In a transmon, two-level systems (TLSs) may be located in the Al oxide in the Josephson junction and in the metal surface, as well as in the substrate-metal and substrate-air boundaries. In Section 2.2 I detailed how a single TLS and an ensemble of TLSs affects the loss and resonance frequency of a superconducting resonator. Since a transmon can be approximated to first order as an LC resonator, we expect TLSs to affect the loss in a transmon similar to how TLSs affect the loss in a resonator. For the standard TLS distribution, loss in a resonator due to an

ensemble of TLS is given by (see Eq. 6.48)

$$\frac{1}{Q_{\mathrm{TLS,e}}}(\langle n\rangle) \;=\; \frac{F\,\tan(\delta)\,\tanh(\hbar\omega/2k_BT)}{\sqrt{1+(\langle n\rangle/n_c)^{\beta}}}, \tag{6.48}$$

where $\langle n\rangle$ is the average photon occupation number (not to be confused with the critical photon number), F is the dielectric fill factor, $\tan(\delta)$ is the dielectric loss tangent, T is the temperature of the resonator, n_c is the characteristic photon occupation number, and $\beta \approx 2$ is the exponent. In a standard qubit operation, typically only the qubit ground and excited states will be occupied, and population in higher states should be negligible. This suggests taking the limit for low $\langle n\rangle$, and the relaxation contribution from TLSs reduces to

$$\frac{1}{T_{1,\mathrm{TLS}}} \;=\; \omega F \tan(\delta)\tanh(\hbar\omega/2k_BT). \tag{6.49}$$

6.4.4 Quasiparticle Tunneling

Quasiparticles within the superconducting film will also contribute to relaxation in a superconducting qubit. In addition to the quasiparticle processes that I described in Section 2.3, quasiparticle can also tunnel through the junction. When a quasiparticle tunnels through the junction, it can gain or lose some of its energy E. Quasiparticle tunneling could cause a qubit that is in the excited state to decay by transferring energy $\hbar\omega_{ge}$ from the qubit to the quasiparticle. Quasiparticle tunneling could also cause a qubit that is in the ground state to get excited by transferring energy $\hbar\omega_{ge}$ from the quasiparticle to the qubit.

Figure 6.9 shows a simple picture for quasiparticles in a Josephson junction. On the left side of the junction the superconductor has a superconducting gap

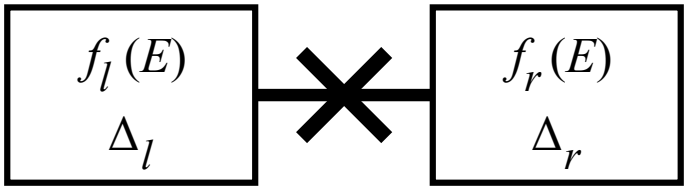

Figure 6.9: Simplified picture of quasiparticles in a Josephson junction: The superconductor on the left of the junction has a gap Δ_l and quasiparticle distribution $f_l(E)$ and the superconductor on the right of the junction has a gap Δ_r and quasiparticle distribution $f_r(E)$

Δ_l and quasiparticle distribution $f_l(E)$, and on the right side of the junction the superconductor has a gap Δ_r and quasiparticle distribution $f_r(E)$. The normalized density of states of the superconductor on the left $\rho_l(E)$ and on the right $\rho_r(E)$ are given by (see Eq. 2.63)

$$\rho_i(E) = \begin{cases} 0, & \text{for } E < \Delta_i \\ \dfrac{E}{\sqrt{E^2 - \Delta_i^2}}, & \text{for } E > \Delta_i. \end{cases} \tag{6.50}$$

where the subscript i is l for left superconductor and r for right superconductor.

There have been many theoretical and experimental studies on quasiparticle induced relaxation in various types of qubits, *e.g.* by Lutchyn *et al.* [207, 208], Martinis *et al.* [20], and Catelani *et al.* [21, 209]. All of them use the assumption that $\Delta_l = \Delta_r \equiv \Delta$, which actually may not be a reasonable assumption for double-angle evaporated Al/AlO_x/Al junctions as it is known from work in CPBs that the gap can be different for the first and second evaporation [210, 211]. Nevertheless, if $\Delta_1 = \Delta_2$, then this means $\rho_l(E) = \rho_r(E) = \rho(E)$ as well. For clarity, however I will continue to distinguish ρ_l and ρ_r from each other.

The qubit relaxation rate due to quasiparticles tunneling from the left to the

right and gaining energy ϵ is given by [20]

$$\Gamma_{\rightarrow}(\epsilon) \;=\; \frac{1}{R_N C_\Sigma}\int_\Delta^\infty \frac{dE}{|\epsilon|}\,\rho_l(E)\,f_l(E)\,\rho_r(E+\epsilon)\;[1-f_r(E+\epsilon)]\left(1+\frac{\Delta^2}{E(E+\epsilon)}\right), \tag{6.51}$$

where R_N is the normal state junction resistance. Similarly, the relaxation due to quasiparticles tunneling from the right superconductor to the left superconductor is given by

$$\Gamma_{\leftarrow}(\epsilon) \;=\; \frac{1}{R_N C_\Sigma}\int_\Delta^\infty \frac{dE}{|\epsilon|}\,\rho_l(E+\epsilon)\;[1-f_l(E+\epsilon)]\;\rho_r(E)\,f_r(E)\left(1+\frac{\Delta^2}{E(E+\epsilon)}\right). \tag{6.52}$$

The total dissipation rate from quasiparticle gaining energy ϵ is

$$\Gamma_{\leftrightarrow}(\epsilon) \;=\; \Gamma_{\rightarrow}(\epsilon) \;+\; \Gamma_{\leftarrow}(\epsilon). \tag{6.53}$$

To proceed, I now explicitly make the assumption $\rho_l(E) = \rho_r(E) = \rho(E)$. If there are no additional nonequilibrium quasiparticle effects on the superconductor, I also have $f_l(E) = f_r(E) = f(E)$, which will simplify the discussion significantly. $\Gamma_{\leftrightarrow}(\epsilon)$ can now be written as

$$\Gamma_{\leftrightarrow}(\epsilon) \;=\; \frac{2}{R_N C_\Sigma}\int_\Delta^\infty \frac{dE}{|\epsilon|}\,\rho(E)\,\rho(E+\epsilon)\,f(E)\;[1-f(E+\epsilon)]\left(1+\frac{\Delta^2}{E(E+\epsilon)}\right). \tag{6.54}$$

Note that using a change of variables, $\Gamma_{\leftrightarrow}(-\epsilon)$ can be written as

$$\Gamma_{\leftrightarrow}(-\epsilon) \;=\; \frac{2}{R_N C_\Sigma}\int_\Delta^\infty \frac{dE}{|\epsilon|}\,\rho(E)\,\rho(E+\epsilon)\,f(E+\epsilon)\;[1-f(E)]\left(1+\frac{\Delta^2}{E(E+\epsilon)}\right). \tag{6.55}$$

The qubit relaxation rate from quasiparticle tunneling includes contributions from

both qubit excitation and decay, and thus

$$\frac{1}{T_{1,\mathrm{qp}}} = \Gamma_{\mathrm{qp}} = \Gamma_{\leftrightarrow}(\hbar\omega_{ge}) + \Gamma_{\leftrightarrow}(-\hbar\omega_{ge}) \tag{6.56}$$

$$= \frac{2}{R_N C_\Sigma} \int_\Delta^\infty \frac{dE}{\hbar\omega_{ge}} \rho(E)\,\rho(E+\hbar\omega_{ge}) \left(1 + \frac{\Delta^2}{E(E+\hbar\omega_{ge})}\right) \times \left\{f(E)\,[1-f(E+\hbar\omega_{ge})] + f(E+\hbar\omega_{ge})\,[1-f(E)]\right\}. \tag{6.57}$$

I also note here that quasiparticle tunneling will cause qubit excitations and leave a background excited state population P_e that is given by [212]

$$P_e = \frac{\Gamma_{\leftrightarrow}(-\hbar\omega_{ge})}{\Gamma_{\leftrightarrow}(\hbar\omega_{ge}) + \Gamma_{\leftrightarrow}(-\hbar\omega_{ge})}. \tag{6.58}$$

Catelani *et al.* used an approach that is similar to the one I described above to take into account the effects due to nonequilibrium quasiparticles. They assumed the density of quasiparticles n_{qp} is given by [209]

$$n_{\mathrm{qp}} = n_{\mathrm{ne}} + n_{\mathrm{th}}, \tag{6.59}$$

where n_{ne} is the nonequilibrium quasiparticle density, $n_{\mathrm{th}} = 2N_0\sqrt{2\pi k_B T\Delta}\, e^{-\frac{\Delta}{k_b T}}$ is the thermal quasiparticle density (see Eq. 2.73), and N_0 is the single-spin density of state. Additionally, the population of nonequilibrium quasiparticle was assumed to be mainly confined to energies between Δ and $\Delta + \delta E$, with $\delta E \ll \hbar\omega_{ge}$. This is a gross simplification, nevertheless, using this assumption, they derived an expression for the decay time [209]

$$\frac{1}{T_{1,\mathrm{qp}}} \approx \frac{\omega_{ge}}{\pi}\left[\frac{n_{\mathrm{ne}}}{N_0\sqrt{2\Delta\hbar\omega_{ge}}} + 4e^{-\Delta/k_B T}\cosh\left(\frac{\hbar\omega_{ge}}{2k_b T}\right) K_0\left(\frac{\hbar\omega_{ge}}{2k_b T}\right)\right], \tag{6.60}$$

where K_n is the n-th order modified Bessel function of the second kind. I note the similarity of the thermal component of $1/T_{1,\mathrm{qp}}$ (the second term in Eq. 6.60) to the

real component of the Mattis-Bardeen conductivity σ_1 from thermal quasiparticles. In particular, comparing to Eq. 2.74, one sees that the only difference is that except the sinh term in Eq. 2.74 is replaced by a cosh term in Eq. 6.60.

The presence of quasiparticles would also cause a shift in the qubit frequency. This shift comes from two effects, the first is from quasiparticle tunneling, which also adds an imaginary component to the admittance $Y(\omega)$ of Fig. 6.7. The second is from changes in E_J due to changes in the density of quasiparticles. Taking into account both effects, Catelani *et al.* also derived the expression of the fractional frequency shift $\delta\omega_{ge}/\omega_{ge}$ [49, 209]

$$\frac{\delta\omega_{ge}}{\omega_{ge}} \approx -\frac{n_{\mathrm{ne}}}{4N_0\Delta}\left(1+\frac{1}{\pi}\sqrt{\frac{2\Delta}{\hbar\omega_{ge}}}\right) - \sqrt{\frac{\pi k_B T}{2\Delta}}e^{-\frac{\Delta}{k_B T}} - e^{-\frac{\Delta+(\hbar\omega_{ge}/2)}{k_B T}} I_0\left(\frac{\hbar\omega_{ge}}{2k_b T}\right), \tag{6.61}$$

where I_n is the n-th order modified Bessel function of the first kind. I also note the similarity of the thermal component of the frequency shift to the imaginary component of Mattis-Bardeen conductivity σ_2 from thermal quasiparticles as given in Eq. 2.75.

So far I have used the assumptions where the superconducting gap and quasiparticle distribution of the left and right superconductors in Fig. 6.9 are identical. In practice, due to differences in evaporation parameters, it is not uncommon for the two sides of the junction to have somewhat different superconducting gaps even when they are made using double-angle evaporation during the same pumpdown, with nominally the same material. The gap in Al in particular is sensitive to oxygen [211]. Furthermore, the actual structure of the superconducting films in a transmon

is significantly more complicated than shown in Fig. 6.9. Another effect that needs to be taken into account is the possibility of having nonequilibrium distribution of quasiparticles, not only due to rf drive and optical illumination (see Section 2.3), but also due to tunneling through the junction [147]. This results in a significantly more complicated picture, as I discuss below.

6.5 Dephasing Time in Transmon

The following discussion of the effect of dephasing on a qubit state is based on the dissertations of Tony Przybysz [213] and Adam Sears [166]. Here I will use the Bloch sphere representation of the qubit state $|\psi\rangle$ (see Eq. 1.1). I start with initial qubit state $|\psi(0)\rangle$ at time $t = 0$, which is given by

$$|\psi(0)\rangle \;=\; \cos(\theta_0/2)|g\rangle \;+\; e^{i\phi_0}\sin(\theta_0/2)|e\rangle. \tag{6.62}$$

Assuming there is no relaxation, I can find the time evolution of the state by applying the propagator $\hat{t} = e^{-i\hat{\mathcal{H}}t/\hbar}$ on $|\psi\rangle$

$$|\psi(t)\rangle \;=\; e^{-i\hat{\mathcal{H}}t/\hbar}|\psi(0)\rangle \;=\; \cos(\theta_0/2)e^{-iE_gt/\hbar}|g\rangle \;+\; e^{i\phi_0}e^{-iE_et/\hbar}\sin(\theta_0/2)|e\rangle. \tag{6.63}$$

Only the phase difference between the $|g\rangle$ and $|e\rangle$ amplitudes is physically important, hence Eq. 6.63 can be rewritten as

$$|\psi(t)\rangle \;=\; \cos(\theta_0/2)|g\rangle \;+\; \exp[i(\phi_0 - \omega_{ge}t)]\sin(\theta_0/2)|e\rangle. \tag{6.64}$$

From Eq. 6.64 I can then write the phase $\phi(t)$ at time t as

$$\phi(t) \;=\; \phi_0 - \omega_{ge}t. \tag{6.65}$$

This means the phase precesses around the Bloch sphere with angular frequency ω_{ge}.

The previous derivation assumed that the qubit frequency ω_{ge} is a constant. If there are fluctuations in ω_{ge}, the frequency as a function of time can be written as

$$\omega_{ge}(t) \;=\; \langle\omega_{ge}\rangle \;+\; \delta\omega_{ge}(t), \tag{6.66}$$

where $\langle\omega_{ge}\rangle$ is the average frequency and $\delta\omega_{ge}(t)$ is the frequency fluctuations from the average value. In this case, $\phi(t)$ becomes

$$\phi(t) \;=\; \phi_0 - \langle\omega_{ge}\rangle t - \int_0^t \delta\omega_{ge}(t')dt'. \tag{6.67}$$

Equation 6.67 shows the phase evolution for a single trial. For qubit measurements that are averaged over many trials, one must take the ensemble average of the phase fluctuation. I now define $\langle\exp(-i\int_0^t \delta\omega_{ge}(t')dt')\rangle \equiv F(t)$. One finds that for a free induction decay $\langle\exp(i\Delta\varphi)\rangle = \exp(-\frac{1}{2}\langle\Delta\varphi^2\rangle)$ [214], and I can write

$$\begin{aligned} F(t) \;&=\; \left\langle \exp\left(-i\int_0^t \delta\omega_{ge}(t')dt'\right)\right\rangle \\ &=\; \exp\left(-\frac{1}{2}\int_0^t dt_1 \int_0^t dt_2 \langle\delta\omega_{ge}(t_1)\,\delta\omega_{ge}(t_2)\rangle\right). \end{aligned} \tag{6.68}$$

Eq. 6.68 means that fluctuations in the qubit frequency result in decay in phase information. This process is called dephasing. Fluctuations in the qubit frequency can be caused by external noise, and the ensemble average in the right hand side of Eq. 6.68 is related to noise power spectral density $S_{\omega_{ge}}(\omega)$ by

$$S_{\omega_{ge}}(\omega) \;=\; \int_{-\infty}^{\infty} \langle\delta\omega_{ge}(t)\,\delta\omega_{ge}(0)\rangle\, e^{i\omega t}\, dt \tag{6.69}$$

$$\langle \delta\omega_{ge}(t)\, \delta\omega_{ge}(0) \rangle \;= \frac{1}{2\pi} \int_{-\infty}^{\infty} S_{\omega_{ge}}(\omega)\, e^{-i\omega t}\, d\omega. \tag{6.70}$$

Using Eq. 6.70, $F(t)$ can be written as

$$\begin{aligned} F(t) \;&= \exp\left(-\frac{1}{4\pi} \int_{-\infty}^{\infty} d\omega\, S_{\omega_{ge}}(\omega) \int_0^t dt_1 \int_0^t dt_2\, e^{-i\omega(t_1 - t_2)} \right) \\ &= \exp\left(-\frac{|t|}{2\pi} \int_{-\infty}^{\infty} d(\omega t/2)\, S_{\omega_{ge}}(\omega)\, \frac{\sin^2(\omega t/2)}{(\omega t/2)^2} \right). \end{aligned} \tag{6.71}$$

The fraction $\sin^2(\omega t/2)/(\omega t/2)^2 = \mathrm{sinc}^2(\omega t/2)$ acts as a weighting factor for the noise. It is maximum for $\omega = 0$, and hence dephasing tends to be dominated by low frequency noise.

For Gaussian white noise, the noise power spectral density is flat, $S_{\omega_{ge}}(\omega) = S_0$. Hence Eq. 6.71 can be written as

$$F(t) \;=\; e^{-|t| S_0/2}. \tag{6.72}$$

Thus for white noise $F(t)$ decays exponentially, and the characteristic decay time is defined by the dephasing time T_ϕ, given by

$$T_\phi \;=\; \frac{2}{S_0}. \tag{6.73}$$

In addition to white noise, another type of noise that is commonly present in superconducting devices is $1/f$ noise [215], where the noise power spectral density follows $S_{1/f}(\omega) \propto 1/|\omega|^\mu$, with $\mu \approx 1$. For μ exactly 1, the phase coherence decays not with an exponential envelope, but with a Gaussian envelope $\propto e^{-t^2/2\sigma^2}$ [213].

One obvious noise source is charge noise, which was typically the limiting noise source for CPBs. The variance of the qubit frequency fluctuations from charge noise is given by

$$\langle \delta\omega_{ge}^2 \rangle \;=\; \left(\frac{\partial \omega_{ge}}{\partial n_g} \right)^2 \langle n_g^2 \rangle. \tag{6.74}$$

Transmons are designed specifically to be insensitive to charge noise by keeping $(\partial\omega_{ge}/\partial n_g)$ exponentially small compared to what it would be in CPBs. Hence charge noise is not the limiting factor of dephasing in transmons unless E_J/E_C got too small or if higher transmon levels are used.

Flux noise is another noise source in transmons, but only for flux tunable SQUID transmons in which a change in flux causes a change in E_J and hence ω_{ge}. The transmon that I l discuss in Chapter 8 has a single junction, which should be very insensitive by flux noise.

Another type of noise in transmons is the $1/f$ critical current noise. Critical current noise can be caused by reconfigurations of the ions inside the Josephson junction [216]. It could also be caused by fluctuations in the number of pairs if pair breaking processes are present. Similar to flux noise, critical current noise will cause fluctuations in E_J and hence ω_{ge}. The variance of the qubit frequency from critical current noise is given by

$$\langle \delta\omega_{ge}^2 \rangle \;=\; \left(\frac{\partial\omega_{ge}}{\partial I_0}\right)^2 \langle I_0^2 \rangle \;\approx\; \left(\frac{\omega_{ge}}{2I_0}\right)^2 \langle I_0^2 \rangle, \tag{6.75}$$

since $\omega_{ge} \propto \sqrt{I_0}$ (see Eq. 6.12).

Another known source of dephasing is cavity photon induced dephasing, due to the coupling between a qubit and a cavity mode. This source of dephasing may generally be the limiting factor in superconducting qubits. Let κ be the relaxation rate of the cavity and χ be the dispersive shift. In the weak dispersive regime $\chi < \kappa$, Schuster *et al.* found that by applying a coherent cavity tone corresponding to average cavity population $\langle n \rangle$ to a CPB coupled to a coplanar waveguide resonator,

the photon-induced dephasing rate of the CPB follows [217]

$$\frac{1}{T_\phi} \approx 8\langle n\rangle \frac{\chi^2}{\kappa}. \tag{6.76}$$

In the weak dispersive regime as well, Bertet *et al.* found with a thermal cavity population $\langle n\rangle = 1/(e^{\hbar\omega_c/k_BT} - 1)$, the photon-induced dephasing rate for a flux qubit follows [218]

$$\frac{1}{T_\phi} = 4\langle n\rangle \left(\langle n\rangle + 1\right) \frac{\chi^2}{\kappa}. \tag{6.77}$$

More recently, in the strong dispersive regime $\chi > \kappa$ where the photon peaks are distinguishable, for a qubit peak corresponding to N photons in the cavity, Sears *et al.* found the photon-induced dephasing rate is given by [219]

$$\frac{1}{T_\phi} = \left[\left(\langle n\rangle + 1\right) N + \langle n\rangle (N+1)\right] \kappa. \tag{6.78}$$

Eq. 6.78 was experimentally verified in 3d transmons for $N = 0$ and 1 [219].

6.6 Microwave Drive and Rabi Oscillation

A circuit QED system with a coherent drive with frequency ω_d has a driving Hamiltonian given by [172]

$$\hat{\mathcal{H}}_d = \frac{\hbar\Omega_r(t)}{2}(\hat{a}^\dagger e^{-i\omega_d t} + \hat{a}e^{i\omega_d t}) + \frac{\hbar\Omega_q(t)}{2}(\hat{\sigma}^+ e^{-i\omega_d t} + \hat{\sigma}^- e^{i\omega_d t}). \tag{6.79}$$

Here I have assumed a two-level qubit system. The first term on the right hand side corresponds to the effect of the drive Eq. 6.79 on the cavity, and the second term corresponds to the effect of the drive on the qubit. $\Omega_r(t)$ and $\Omega_q(t)$ are measures of the power of the drive, and depend on the coupling between the drive line and the cavity or qubit.

I now consider the effect of the drive on the qubit state. I assume that there is a constant drive power $\Omega_q(t) = \Omega_q$, and no relaxation or decoherence. For a two-level qubit, the Hamiltonian can be written as

$$\hat{\mathcal{H}} = \hat{\mathcal{H}}_0 + \hat{\mathcal{H}}_d = \frac{\hbar\omega_{ge}}{2}\hat{\sigma}_z + \frac{\hbar\Omega_q}{2}(\hat{\sigma}^+ e^{-i\omega_d t} + \hat{\sigma}^- e^{i\omega_d t}), \tag{6.80}$$

where $\hat{\mathcal{H}}_0$ is the undriven Hamiltonian and $\hat{\mathcal{H}}_d$ is the drive term. So far I have used a Schrödinger picture of quantum mechanics, but here I will switch to the interaction (Dirac) picture, with $\hat{\mathcal{H}}_d$ as the perturbation term to the Hamiltonian $\hat{\mathcal{H}}_0$. I define the unitary transformation $\hat{\mathcal{U}}$ given by

$$\hat{\mathcal{U}} = e^{i\hat{\mathcal{H}}_0 t/\hbar} = \begin{pmatrix} e^{i\omega_{ge}t/2} & 0 \\ 0 & e^{-i\omega_{ge}t/2} \end{pmatrix} \tag{6.81}$$

The qubit state in the interaction picture $|\psi_I(t)\rangle$ is given by

$$|\psi_I(t)\rangle = \hat{\mathcal{U}}|\psi_S(t)\rangle, \tag{6.82}$$

where $|\psi_S(t)\rangle$ is the qubit state in the Schrödinger picture. The perturbation Hamiltonian in the interaction picture $\hat{\mathcal{H}}_{d,I}(t)$ is given by

$$\hat{\mathcal{H}}_I(t) = \hat{\mathcal{U}}\,\hat{\mathcal{H}}_d\,\hat{\mathcal{U}}^\dagger \tag{6.83}$$

$$= \frac{\hbar\Omega_q}{2}\begin{pmatrix} e^{i\omega_{ge}t/2} & 0 \\ 0 & e^{-i\omega_{ge}t/2} \end{pmatrix}\begin{pmatrix} 0 & e^{-i\omega_d t} \\ e^{i\omega_d t} & 0 \end{pmatrix}\begin{pmatrix} e^{-i\omega_{ge}t/2} & 0 \\ 0 & e^{i\omega_{ge}t/2} \end{pmatrix}$$

$$= \frac{\hbar\Omega_q}{2}\begin{pmatrix} 0 & e^{i(\omega_{ge}-\omega_d)t} \\ e^{-i(\omega_{ge}-\omega_d)t} & 0 \end{pmatrix}. \tag{6.84}$$

The time-evolution of the qubit state in the interaction picture is given by

$$i\hbar\frac{d}{dt}|\psi_I(t)\rangle = \hat{\mathcal{H}}_I(t)|\psi_I(t)\rangle. \tag{6.85}$$

I now define the qubit state in the interaction picture as $|\psi_I(t)\rangle = \alpha_g(t)|g\rangle + \alpha_e(t)|e\rangle$ and rewrite Eq. 6.85 as two coupled differential equations

$$i\frac{d\alpha_g}{dt} = \frac{\Omega_q}{2}e^{-i\,\delta\omega\,t}\alpha_e \tag{6.86}$$

$$i\frac{d\alpha_e}{dt} = \frac{\Omega_q}{2}e^{i\,\delta\omega\,t}\alpha_g, \tag{6.87}$$

where $\delta\omega = \omega_{ge} - \omega_d$ is the detuning of the drive. I assume the initial condition that the qubit is in the ground state, *i.e.*. $|\psi_S(0)\rangle = |g\rangle$ and thus from Eq. 6.82, $|\psi_I(0)\rangle = |g\rangle$. I can solve Eq. 6.86 and 6.87 to obtain $|\psi_I(t)\rangle$. Then I use Eq. 6.81 to evaluate $|\psi_S(t)\rangle$ and find

$$\begin{aligned}|\psi_S(t)\rangle \;=\; &\left[\cos\left(\frac{t}{2}\sqrt{(\delta\omega)^2+\Omega_q^2}\right) \;+\; i\frac{i\,\delta\omega}{\sqrt{(\delta\omega)^2+\Omega_q^2}}\sin\left(\frac{t}{2}\sqrt{(\delta\omega)^2+\Omega_q^2}\right)\right]|g\rangle \\ &-\;\frac{i\,\Omega_q}{\sqrt{(\delta\omega)^2+\Omega_q^2}}\sin\left(\frac{t}{2}\sqrt{(\delta\omega)^2+\Omega_q^2}\right)|e\rangle.\end{aligned} \tag{6.88}$$

The probability for the qubit to be in excited state is given by

$$P_e(t) \;=\; |\langle e|\psi_S(t)\rangle|^2 \;=\; \frac{\Omega_q^2}{2\left[(\delta\omega)^2+\Omega_q^2\right]}\left[1-\cos\left(t\sqrt{(\delta\omega)^2+\Omega_q^2}\right)\right]. \tag{6.89}$$

The probability $P_e(t)$ oscillates as a function of time with frequency

$$\Omega_R = \sqrt{(\delta\omega)^2+\Omega_q^2}. \tag{6.90}$$

This behavior is called a Rabi oscillation and the Ω_R is called the Rabi frequency. When the qubit is driven at the qubit frequency, $\delta\omega = 0$, the Rabi frequency is $\Omega_R = \Omega_q$, and $P_e(t)$ oscillates between 0 and 1. When there is some detuning $\delta\omega \neq 0$, the Rabi frequency is faster ($\Omega_R > \Omega_q$), and $P_e(t)$ is always less than 1.

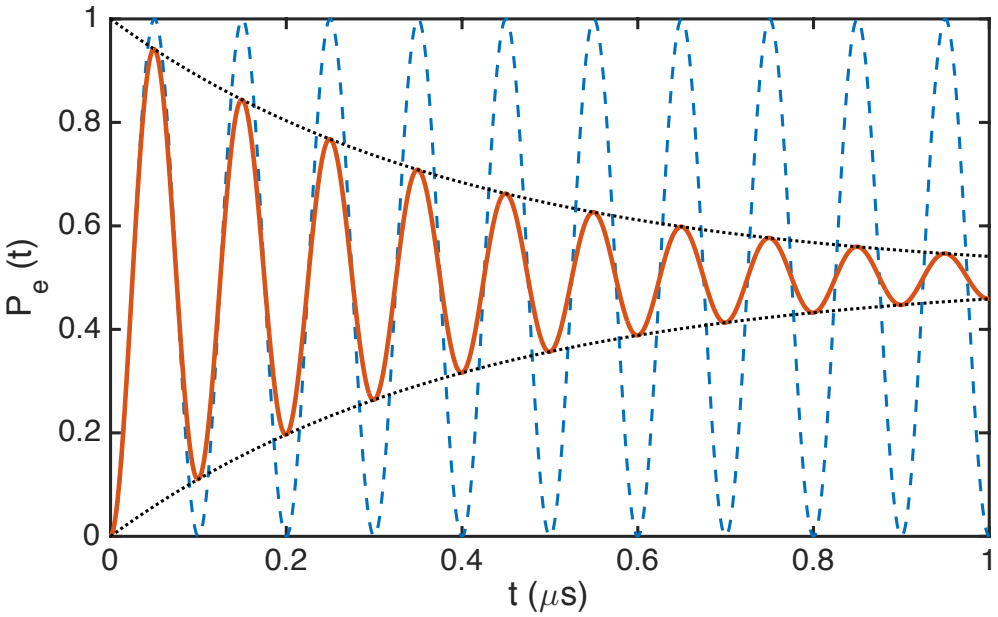

Figure 6.10: Comparison between Rabi oscillations without decoherence (dashed blue curve) and with decoherence (solid red curve). The parameters are $\Omega/2\pi = 10$ MHz and $T' = 400$ ns. The dotted black curves are the envelope of the oscillation with decoherence.

So far I have assumed no decoherence. When there is decoherence but no detuning, the probability $P_e(t)$ instead follows

$$P_e(t) \;=\; \frac{1}{2}\left[1 - e^{-t/T'}\cos(\Omega_q t)\right]. \tag{6.91}$$

Figure 6.10 shows a comparison between Rabi oscillations with and without decoherence. With decoherence, the envelope of the Rabi oscillation exponentially decays with decay time T', which is given by [220]

$$\frac{1}{T'} \;=\; \frac{1}{2}\left(\frac{1}{T_1} + \frac{1}{T_2}\right). \tag{6.92}$$

At long times the probability $P_e(t) \to 1/2$, which can be interpreted as the system is in a mixed state with equal probability to be found in $|g\rangle$ or $|e\rangle$, or the state has spread out over the entire Bloch sphere. I note here that the P_e saturates to $1/2$ only for strong enough drive such that $\Omega \ll T'$. For weak drive, P_e saturates to a lower value [221].

6.7 Nonequilibrium Quasiparticles in Optically Illuminated Transmon

6.7.1 Complete Quasiparticle and Phonon Picture

The picture of quasiparticles in a transmon that was discussed in Section 6.4.4 is a simplified picture of what should occur in an actual transmon. In particular, the cross-section of the superconductor around the Josephson junction in my transmon is depicted in Fig. 6.11. Two separate Al layers are deposited on each side of

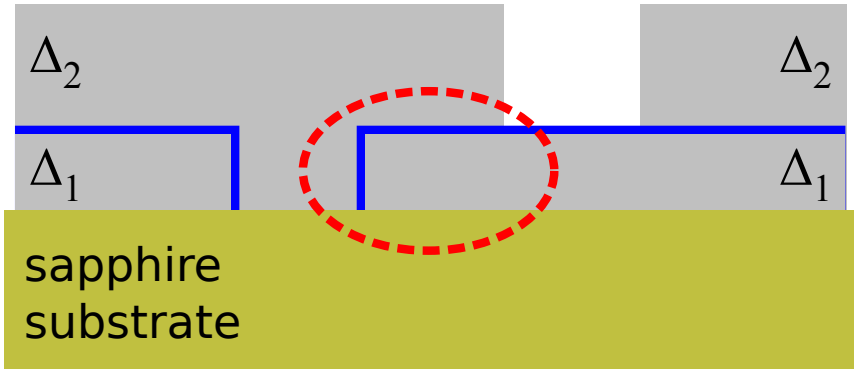

Figure 6.11: Cross-section of the Al layers and junctions in my transmon. Gray squares are the Al layers, with superconducting gaps Δ_1 and Δ_2. Blue lines are the AlO_x junction layers, with the layer inside the red dashed circle acting as the junction for the transmon. The yellow square is the sapphire substrate.

the transmon's junction. As the two layers came from different evaporations, they typically can have somewhat different superconducting gaps. In Fig. 6.11, Δ_1 is the gap for the lower layer and Δ_2 is the gap for the upper layer. The two Al layers are separated by three Josephson junctions (blue lines in Fig. 6.11). The junction used by the transmon is the smallest one (red dashed circle), located in the middle. The other two junctions are much larger, each with a junction area that is equal to the area of a single pad of the transmon. Considering the layout, there are four distinct regions of superconductor, one with gap Δ_1 on the left side, one with Δ_2 on the left side, one with Δ_1 on the right side, and one with Δ_2 on the right side.

Figure 6.12 shows a block diagram for the nonequilibrium quasiparticle and phonon processes for the four superconducting regions. Each region has its own quasiparticle distribution $f(E)$ (blue squares) and phonon distribution $n(\Omega)$ (gray squares), connected through scattering, pair breaking, and recombination processes

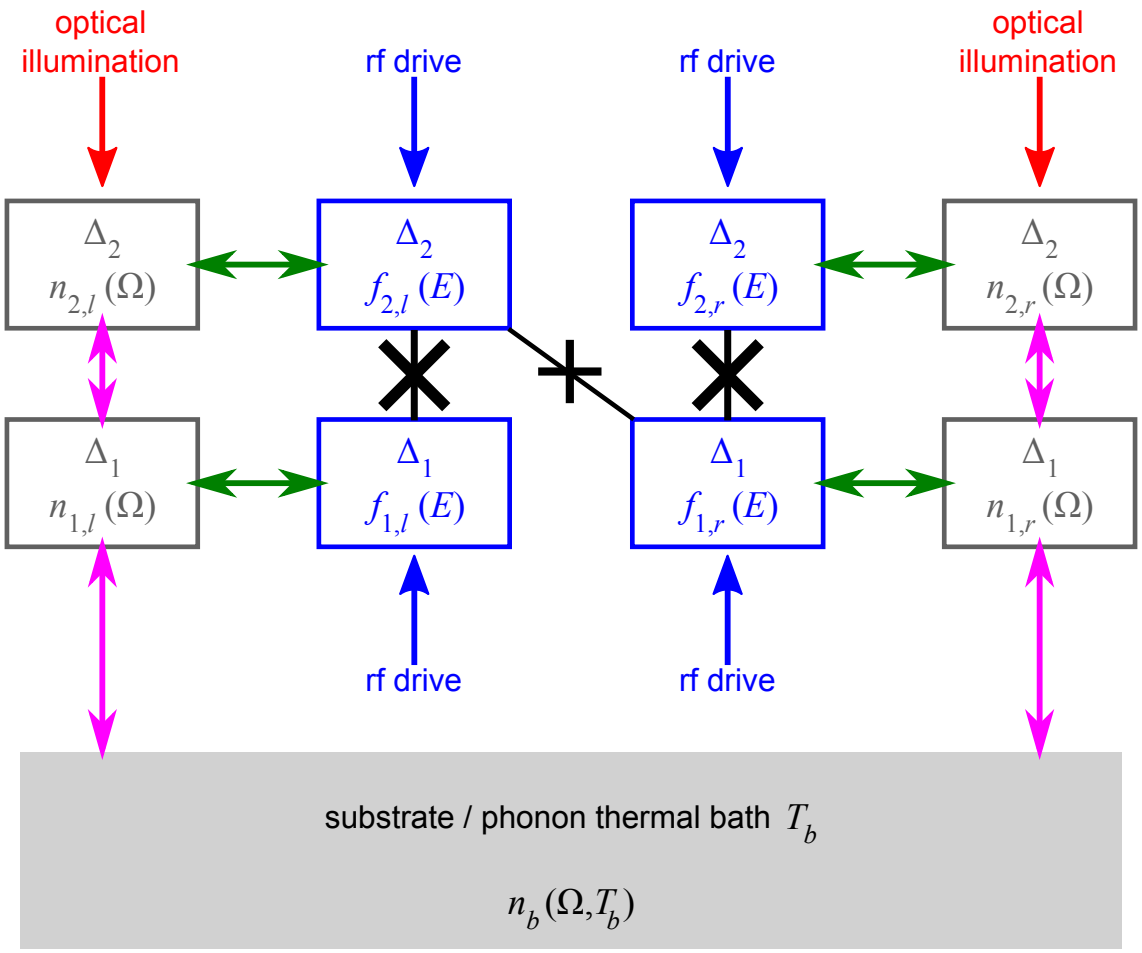

Figure 6.12: Block diagram of all quasiparticle and phonon processes in an optically illuminated transmon (see Fig. 6.11).

(green arrows). A Josephson junction allows quasiparticles to tunnel between two superconducting regions, and the three junctions in Fig. 6.11 connect different quasiparticle regions in Fig. 6.12. The phonon-phonon interactions are represented by the purple arrows. I note that the two phonon regions on each side are directly connected, but there is no direct connection between phonons on opposing sides of the junction. For the most part, the substrate is directly connected only to the lower Al layers. Hence I assume the thermal bath is connected to the phonon distributions for the lower superconductor regions, which have gap Δ_1, but not to the upper superconducting region, which have gap Δ_2. Microwave drive (blue arrows) can directly excite quasiparticles in all four superconducting regions. Also in my experiment the transmon is illuminated from above, so I only allow the illumination (red arrows) to directly create phonons in the upper layers with gap Δ_2.

This picture is fairly comprehensive and significantly more complicated than the simple picture presented in Fig. 6.4.4. Finding the quasiparticle and phonon distributions for all four regions appears to be doable, but will likely take considerable computation time. Instead, I developed a simplified model, as I describe in the next section.

6.7.2 Simplifying the Picture

In the discussion of quasiparticle tunneling in Section 6.4.4, I made an implicit assumption that the tunneling process does not change the distribution of the quasiparticles on either side of the junction, even though there is an exchange of par-

ticles. In fact, Chang and Scalapino discussed quasiparticle tunneling as one of the possible processes that can change the quasiparticle distribution [147]. A normal-superconductor junction biased with voltage V creates an additional quasiparticle generation term $G_{\rm qp}(E)$ (see Eq. 2.76) in the kinetic equations given by [147]

$$G_{\rm qp}(E) \propto [f(E-eV) - f(E+eV)]\,. \tag{6.93}$$

I can generalize this relation to superconductor-superconductor tunneling. I assume two quasiparticle regions with density of states $\rho_1(E)$ and $\rho_2(E)$ and distribution $f_1(E)$ and $f_2(E)$, separated by a junction. If there is a voltage V across the junction, the quasiparticle generation term $G_{\rm qp,1}(E)$ for $f_1(E)$ is given by

$$\begin{aligned} G_{\rm qp,1}(E) &= \frac{M}{\tau_t V_1}\,\rho_2(E+eV)\,\{f_2(E+eV)[1-f_1(E)] - f_1(E)[1-f_2(E+eV)]\} \\ &= \frac{M}{\tau_t V_1}\,\rho_2(E+eV)\,[f_2(E+eV) - f_1(E)]\,. \end{aligned} \tag{6.94}$$

Here M is a proportionality constant, V_1 is the volume of superconducting region 1, and τ_t is the tunneling timescale representing the tunneling strength. In Eq. 6.94 I have assumed tunneling from region 1 to 2 and vice versa. Similarly, the quasiparticle generation term $G_{\rm qp,2}(E)$ for $f_2(E)$ can be written as

$$G_{\rm qp,2}(E) = \frac{M}{\tau_t V_2}\,\rho_1(E-eV)\,[f_1(E-eV) - f_2(E)]\,, \tag{6.95}$$

where V_2 is the volume of superconducting region 2. In Eq. 6.94 and 6.95 the volumes V_1 and V_2 appear in order to maintain power balance from quasiparticle tunneling. I also assumed the same bias voltage, where the voltage is higher on the side of superconductor 1 by V.

As I mentioned above, the timescale τ_t represents the strength of the tunneling in the junction. The tunneling strength should depend on the junction area and the thickness of the oxide layer. When tunneling is weak, τ_t is large, and vice versa. For very weak tunneling $\tau_t \to \infty$, $G_{\mathrm{qp},i}(E)$ of Eqs. 6.94 and 6.95 approach zero, which means that the quasiparticle distributions would not be affected by the tunneling terms. In the other extreme, for very strong tunneling $\tau_t \to 0$, the magnitude of the generation terms $G_{\mathrm{qp},i}(E)$ are very large except when $f_1(E) = f_2(E + eV)$. This implies that the resulting steady-state quasiparticle will obey $f_1(E) = f_2(E + eV)$ above unless they are driven so hard that the quasiparticle generation term from rf drive stand to approach $G_{\mathrm{qp,i}}$

The three junctions in Fig. 6.12 should have the same barrier height as they are oxidized at the same time. As the middle junction is much smaller than the other two, it is reasonable to assume that the effective tunneling strength is much weaker than the other two. I may then assume that the effect of the tunneling in this junction on the distributions are negligible, and $f_{2,l}(E)$ and $f_{1,r}(E)$ regions are not connected. This means the block diagram in Fig. 6.12 can be separated into two disconnected block diagrams, the left half and the right half. As the left and right side of the transmon is symmetric with the same area and film thicknesses, this means the distributions are symmetric as well, and I have $f_{j,l}(E) = f_{j,r}(E)$ and $n_{j,l}(\Omega) = n_{j,r}(\Omega)$ for $j = 1$ and 2. I can then focus just on one half of the block diagram, and in the following I will use the notation for the left side.

Each large junction has area corresponding to half of the transmon area, which in my case is about 2.5×10^4 μm^2. Because of the large area, I assume very strong

strong tunneling effect from this junction. As there is no voltage bias applied across this large junction, I then have $f_{1,l}(E) = f_{2,l}(E)$.

In Section 2.3 I argued that the interaction between a phonon distribution in a superconductor and a phonon distribution in the substrate results in the phonon rate term

$$\left.\frac{dn(\Omega)}{dt}\right|_{\phi-b} = \frac{n_b(\Omega, T_b) - n(\Omega)}{\tau_e}, \tag{6.96}$$

where $n_b(\Omega, T_b)$ is the substrate bath thermal distribution at temperature T_b and τ_e is the phonon escape time from the superconductor to the thermal bath. I can now generalize this term to describe the interaction between the two phonon distributions $n_{1,l}(\Omega)$ and $n_{2,l}(\Omega)$ and write

$$\left.\frac{dn_{1,l}(\Omega)}{dt}\right|_{\phi_1-\phi_2} = \frac{[n_{2,l}(\Omega) - n_{1,l}(\Omega)]}{\tau_p} \frac{\sum_j (N_i/\Omega_D^3)_j V_j}{(N_i/\Omega_D^3)_1 V_1}, \tag{6.97}$$

$$\left.\frac{dn_{2,l}(\Omega)}{dt}\right|_{\phi_1-\phi_2} = \frac{[n_{1,l}(\Omega) - n_{2,l}(\Omega)]}{\tau_p} \frac{\sum_j (N_i/\Omega_D^3)_j V_j}{(N_i/\Omega_D^3)_2 V_2}. \tag{6.98}$$

Here τ_p is the characteristic phonon escape time between the two phonon regions, N_i is the atomic density, and Ω_D^3 is the Debye energy. The ratio on the right hand side appears due to the need to maintain power balance from the phonon-phonon process between the two phonon regions. Here I also use the same assumption that I used in previous nonequilibrium simulations, where I used the theoretical values for the characteristic times τ_0 and τ_ϕ and the single spin density of states N_0. I then use Eq. 2.84 to find N_i/Ω_D^3.

The escape times τ_e and τ_p are governed by the mismatches in the lattice and acoustic modes between the two regions [151]. There should be significantly less lattice mismatch between two Al layers compared to between Al and sapphire.

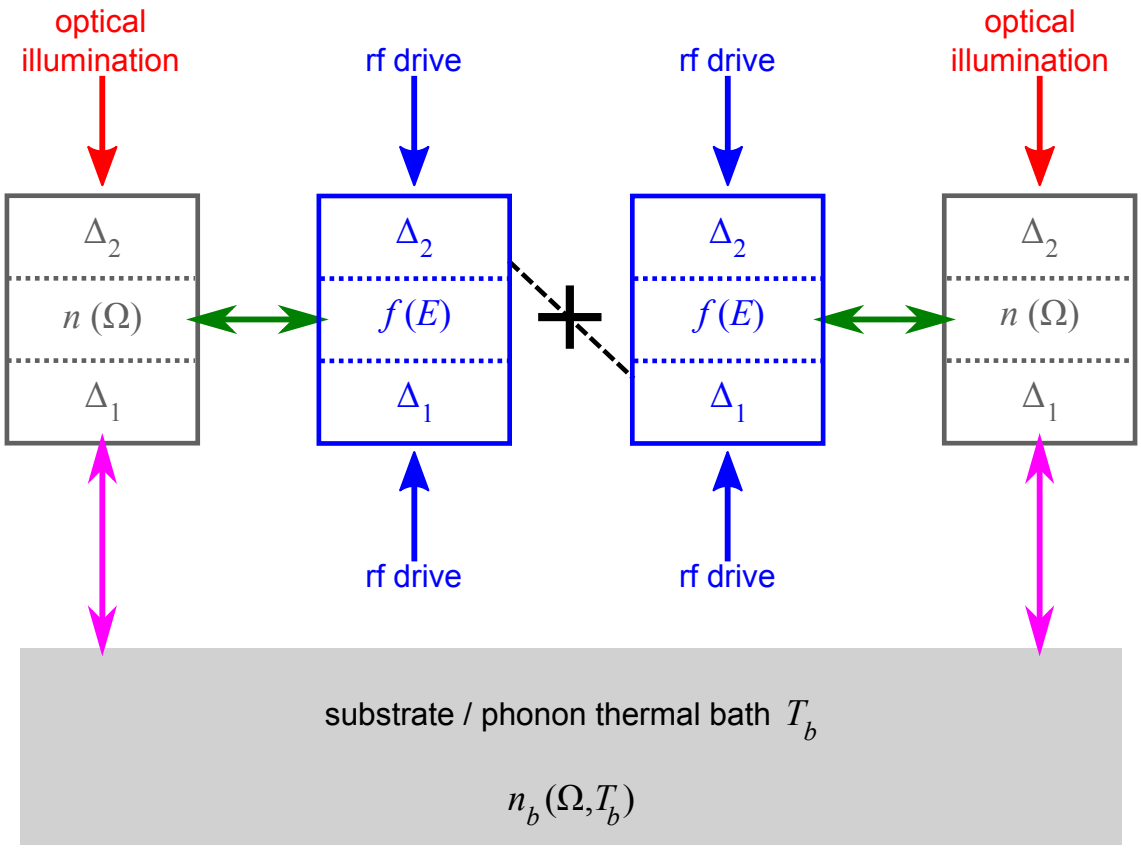

Figure 6.13: Simplified block diagram of the quasiparticle and phonon processes in an optically illuminated transmon (compare with Fig. 6.12).

Hence I expect $\tau_p \ll \tau_e$. If $\tau_p \to 0$, I have a very strong connection between the two phonon baths, similar to the strong junction tunneling connection between the top and bottom quasiparticle regions, as discussed previously. If I use this assumption, I have $n_{1,l}(\Omega) = n_{2,l}(\Omega)$ as well.

Using all these consideration, the block diagram of Fig. 6.12 then reduces to the simplified block diagram shown in Fig. 6.13. There is only one quasiparticle distribution $f(E)$ and one phonon distribution $n(\Omega)$. However, I note that this picture does not require $\Delta_1 = \Delta_2$. The combined kinetic equations $df(E)/dt$ and

$dn(\Omega)/dt$ contain the generation, scattering, pair breaking, recombination, and escape terms from both regions 1 and 2, but no cross quasiparticle-quasiparticle or cross phonon-phonon terms.

The combined kinetic equation $df(E)/dt$ for the quasiparticles is given by

$$[\rho_1(E)V_1 + \rho_2(E)V_2]\,\frac{df(E)}{dt} \;=\; \rho_1(E)V_1\frac{df_1(E)}{dt} \;+\; \rho_2(E)V_2\frac{df_2(E)}{dt}, \tag{6.99}$$

where $df_1(E)/dt$ is the kinetic equation for quasiparticles in region 1 and $df_2(E)/dt$ is the kinetic equation for quasiparticles in region 2. The product $\rho_i(E)V_i$ in Eq. 6.99 acts as a weighting term for the quasiparticles in each superconducting region.

The combined kinetic equation $dn(\Omega)/dt$ for the phonons is given by

$$\left[\left(\frac{N_i}{\Omega_D^3}\right)_1 V_1 + \left(\frac{N_i}{\Omega_D^3}\right)_2 V_2\right]\frac{dn(\Omega)}{dt} \;=\; \left(\frac{N_i}{\Omega_D^3}\right)_1 V_1\frac{dn_1(\Omega)}{dt} \;+\; \left(\frac{N_i}{\Omega_D^3}\right)_2 V_2\frac{dn_2(\Omega)}{dt}, \tag{6.100}$$

where $dn_1(\Omega)/dt$ is the kinetic equation for phonons in region 1 and $dn_2(\Omega)/dt$ is the kinetic equation for phonons in region 2. The product $(N_i/\Omega_D^3)_i V_i$ in Eq. 6.100 acts as a weighting term for the phonons in each superconducting region. The phonon density of states $D(\Omega)$ does not appear in the weighting term as it is independent of Δ and hence cancels out from Eq. 6.100.

When $\Delta_1 = \Delta_2$, I have $\rho_1(E) = \rho_2(E)$ and $(N_i/\Omega_D^3)_1 = (N_i/\Omega_D^3)_2$ and Eq. 6.99 and 6.100 reduce to Eq. 2.76 and 2.77.

6.7.3 Numerical Simulations

To find the quasiparticle distribution $f(E)$ and phonon distribution $n(\Omega)$ of the model of Fig. 6.13, I use the numerical method described in Section 2.3. Here I

also assume $\Delta_1 = \Delta_2$, which is not expected to correspond to the situation in my transmon but simplifies the kinetic equations as discussed in the previous section. In my experiments described in Chapter 8, I mainly measured the qubit relaxation time T_1 as a function of refrigerator temperature and illumination intensity. During the relaxation, there is no applied microwave drive. Of course, there is a microwave pulse during the qubit preparation and this may affect the distribution during relaxation. However, the microwave pulses are typically short (50 to 100 μs). Also, the range of applied rf powers are significantly lower than the powers used in Chapters 4 and 5 where nonequilibrium effects from rf drive are significant. Because of these, I will assume the rf drive can be neglected in the simulation.

Once $f(E)$ and $n(\Omega)$ are obtained from the simulations, I can calculate the expected transmon relaxation rate due to quasiparticles using Eq. 6.57. From the similarities between the expression for the expected frequency shift of the transmon (Eq. 6.61) and of resonators (Eq. 2.75) due to thermal quasiparticles, I assume without proof that

$$\frac{\delta\omega_{ge}}{\omega_{ge}} = -\frac{\delta\sigma_2}{2\sigma_2}. \tag{6.101}$$

This frequency shift is consistent with the picture of the transmon as an anharmonic LC resonator with the Josephson junction as an inductor with an inductance that is mainly proportional to the junction critical current.

Table 6.1 shows the parameters I use in the simulations discussed below. The chosen material parameters are for typical Al films. The R_N and C_Σ values are the typical values for 3d transmons with transition frequency $\omega_{ge}/2\pi \approx 5.1$ GHz ≈ 21

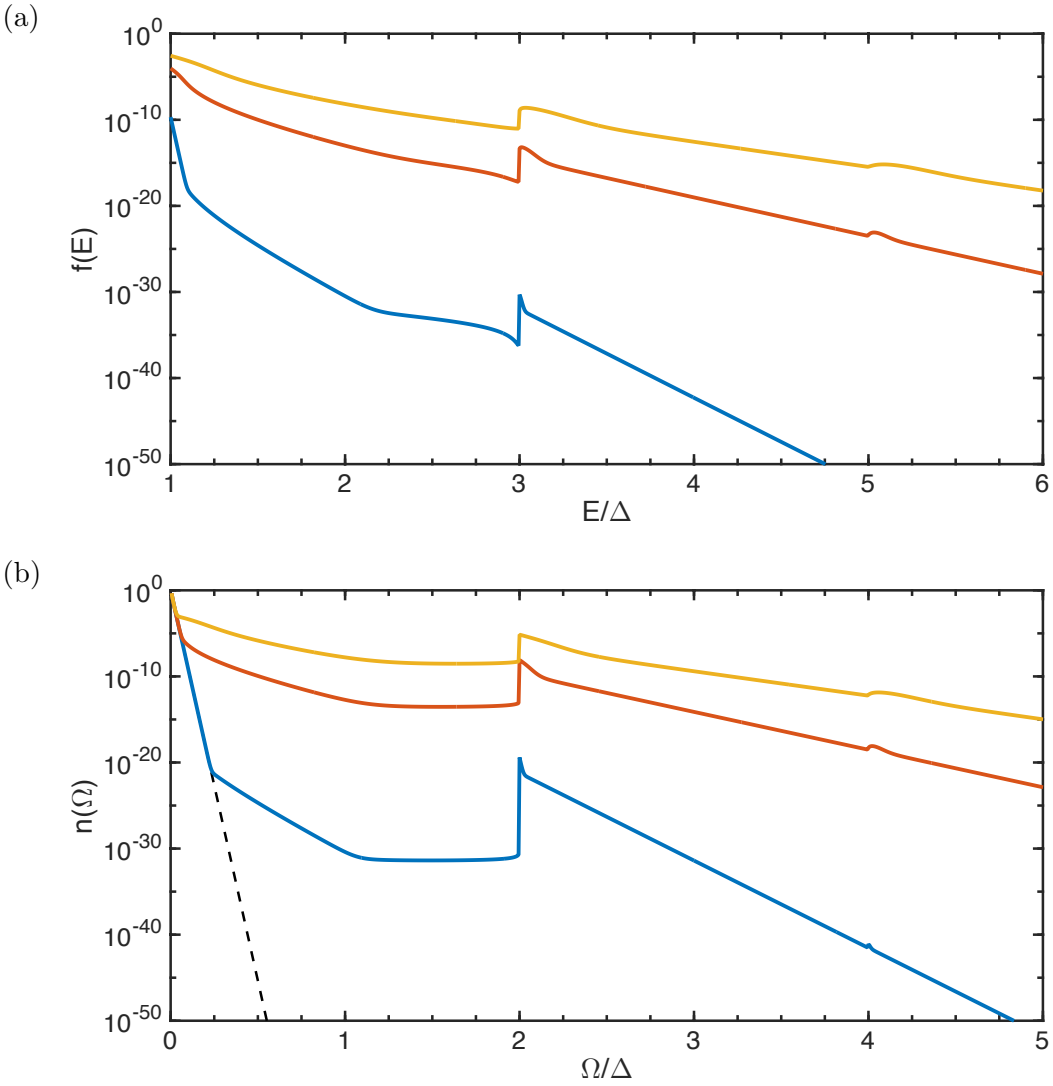

Figure 6.14: (a) Simulated quasiparticle distribution $f(E)$ vs normalized energy E/Δ and (b) simulated phonon distribution $n(\Omega)$ vs normalized energy Ω/Δ for bath temperature $T_b = 10$ mK and effective temperatures T_{eff} of 90 mK (blue curve), 210 mK (red curve), and 330 mK (orange curve). Other parameters are shown in Table 6.1. The black dashed curve in (b) is the thermal distribution for $T_b = 10$ mK.

Table 6.1: Parameters used in nonequilibrium simulations.

Symbol	Parameter	Value
Δ	superconducting gap	180 μeV
$\hbar\omega_{ge}$	rf photon energy in simulation	21 μeV
V	Al volume	1.7×10^4 μm^3
N_0	single spin density of states at Fermi level	1.74×10^{10} /eV μm^3
N_i/Ω_D^3	atomic density/(Debye frequency)^3	1.21×10^{15} (eV μm)$^{-3}$
τ_0	quasiparticle-phonon time	438 ns
τ_ϕ	phonon-quasiparticle time	0.26 ns
τ_e	phonon escape time	3 ns
R_N	normal state junction resistance	7 kΩ
C_Σ	junction total parallel capacitance	100 fF

μeV/h. The volume V is half of the total Al volume in my 3d transmon, as I am effectively simulating only half of the transmon in the simplified model. Figure 6.14 shows the simulated distributions $f(E)$ and $n(\Omega)$ for bath temperature $T_b = 10$ mK and several effective temperature T_{eff} values. As expected, the distributions behave similarly to the distributions for resonators simulated in the earlier chapters, with a large jump in $f(E)$ at $E = 3\Delta$ and in $n(\Omega)$ at $\Omega = 2\Delta$ due to the optical absorption.

Figure 6.15 shows the simulated relaxation time due to quasiparticles $T_{1,\text{qp}}$ and fractional qubit transition frequency shift $-\delta f_{ge}/f_{ge}$ as a function of bath temperatures T_b for three different effective temperature T_{eff} values. The relaxation rate and frequency shift curves show similar behavior. For $T_b \lesssim T_{\text{eff}}$, the curves are relatively flat, while for $T_b \gtrsim T_{\text{eff}}$ the curves follow the no illumination behavior (blue curves) closely, with a kink at $T_b \approx T_{\text{eff}}$.

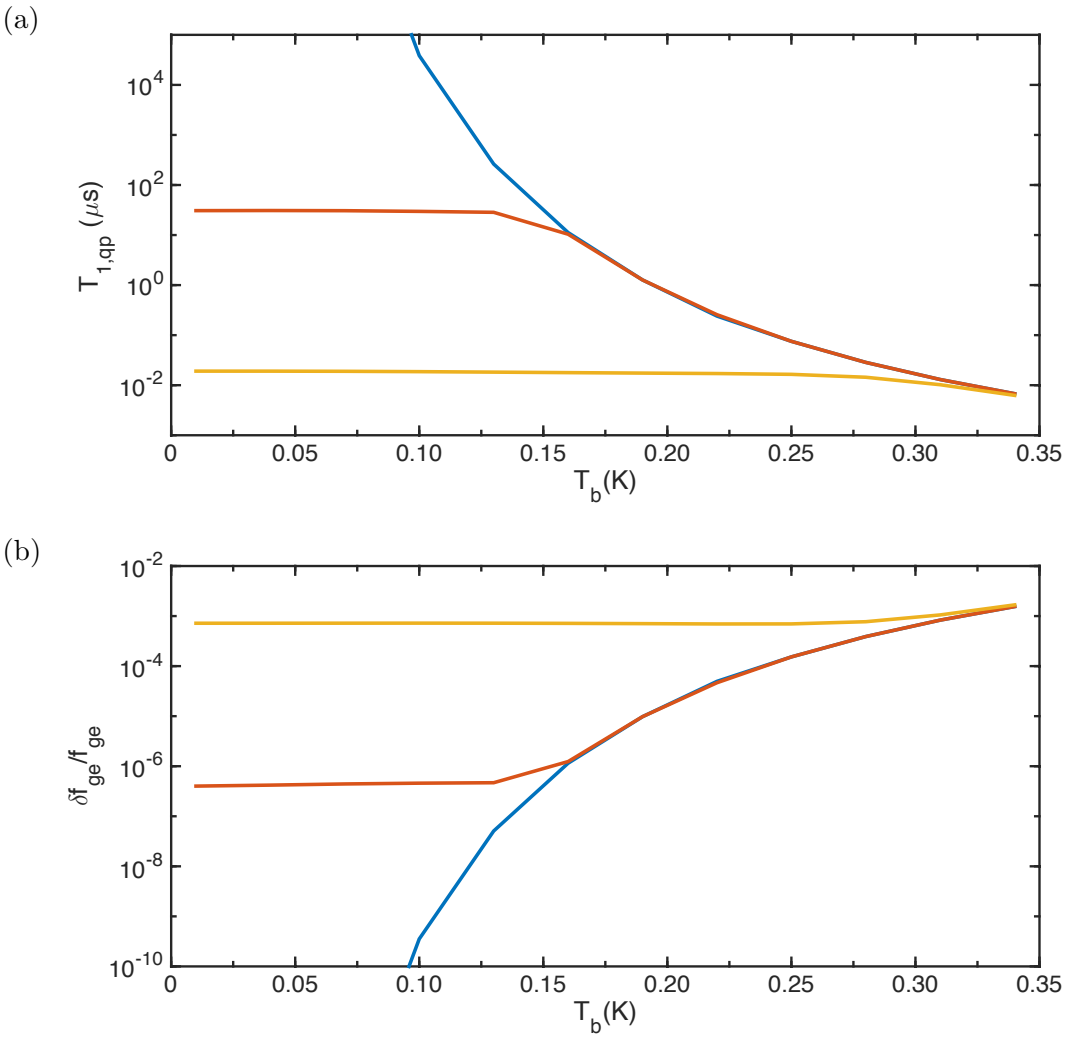

Figure 6.15: (a) Simulated quasiparticle relaxation rate $T_{1,\mathrm{qp}}$ and (b) simulated fractional qubit transition frequency shift $-\delta f_{ge}/f_{ge}$ vs bath temperature T_b and for effective temperatures T_{eff} of 0 mK (no applied optical power, blue curve), 150 mK (red curve), and 300 mK (orange curve). Other parameters are as shown in Table 6.1.

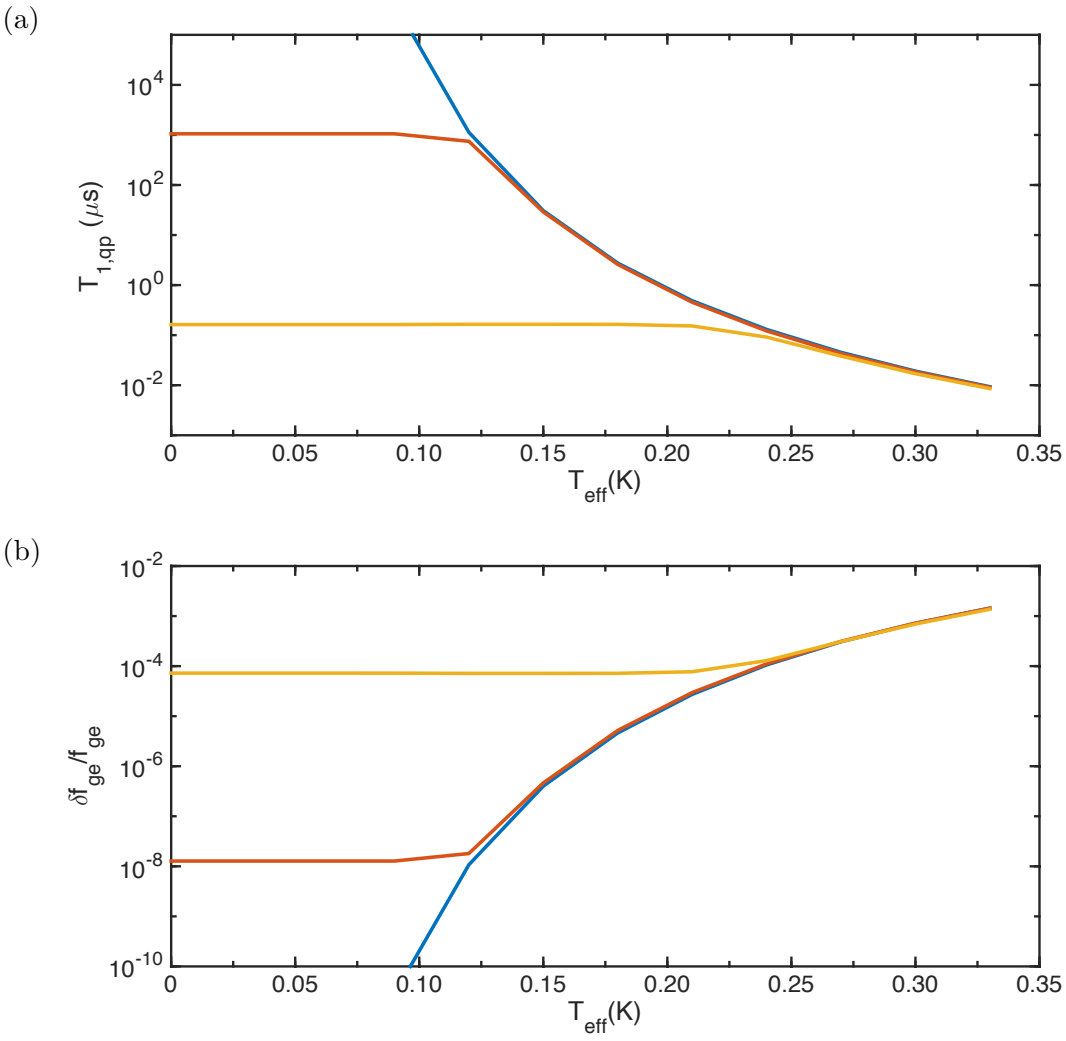

Figure 6.16: (a) Simulated quasiparticle relaxation rate $T_{1,\mathrm{qp}}$ and (b) simulated fractional qubit transition frequency shift $-\delta f_{ge}/f_{ge}$ vs effective temperature T_{eff} and for temperatures T_b: 10 mK (blue curve), 120 mK (red curve), and 230 mK (orange curve). Other parameters are as shown in Table 6.1.

For comparison, Figure 6.16 show the simulated $T_{1,\mathrm{qp}}$ and $-\delta\omega_{ge}/\omega_{ge}$ as a function of effective temperature T_{eff} for three different bath temperatures T_b values. Here the behavior of the curves is similar to when I varied T_b. For $T_{\mathrm{eff}} \lesssim T_b$, the curves are relatively flat, while for $T_{\mathrm{eff}} \gtrsim T_b$ the curves follow the low T_b behavior closely, with a sharp at $T_{\mathrm{eff}} \approx T_b$.

6.7.4 Extensions to the Model

In the numerical simulations that I described in the previous ssection, for simplicity I assumed that the two superconducting layers hde the same superconducting gap Δ. When the gaps are not equal, the kinetic equations become significantly more complicated. The different Δ values affect the distributions $f(E)$ and $n(\Omega)$, as well as the predicted $T_{1,\mathrm{qp}}$ and $-\delta\omega_{ge}/\omega_{ge}$ values. One should expect the effects to be more significant if $|\Delta_1 - \Delta_2| > \hbar\omega_{ge}$.

I also assumed that the rf drive had no effect on the distributions. To include these effects on qubit relaxation, one would need to find the time-dependences of $f(E)$ and $n(\Omega)$, both during the microwave pulse and during the relaxation. I believe a different numerical method, such as a variant of multivariable Runge-Kutta methods [222].

6.8 Summary

In this chapter, I discussed the theory of transmons and circuit QED systems. I started by discussing the circuit representation of a Cooper-pair box and

its Hamiltonian, and how a transmon can be viewed as a modified CPB. I then discussed a coupled cavity and transmon, forming a circuit QED system. I focused on the dispersive regime, where the coupling between the two is weak compared to the detuning, and discussed the energy levels in this regime.

I then discussed relaxation and dephasing in a transmon, and listed possible sources. I then discussed how an applied rf drive at the transition frequency creates Rabi oscillation in the qubit populations, and how decoherence affects Rabi oscillation.

Finally, I examined at length how the presence of nonequilibrium quasiparticles affect the relaxation rate and transition frequency of a transmon. I described the distribution of quasiparticles and phonons in a transmon, and discussed how I modeled the dynamics of this system and possible extensions to the model.

Chapter 7: Experimental Details: Transmon

In this chapter, I describe experimental details for the measurements in Chapter 8 in which I applied optical illumination to a 3d transmon. I discuss the design choices and fabrication steps for building the transmon as well as the 3d cavity in which the transmon is mounted. I also discuss the microwave setup, pulsing sequence for qubit manipulation, and the qubit state readout. Finally, I briefly discuss the optical illumination line, which was nearly identical to the one used in the resonator experiments described in Chapters 4 and 5.

7.1 Transmon Design Considerations

The design of the 3d transmon qubits I used was very similar to the qubit designs used by other groups, including Yale [49], IBM [165], and LPS [189]. Specifically, I designed the qubit based on discussions with Sergey Novikov from Ben Palmer's group at LPS.

Figures 7.1(a) shows the CAD drawing of the transmon I used in the experiment. The largest structures in the design are two 700 μm $\times$ 350 μm pads. These act both as a shunting capacitor and as a dipole antenna to couple to the microwave field in the cavity. Some transmons have had an array of holes patterned into the

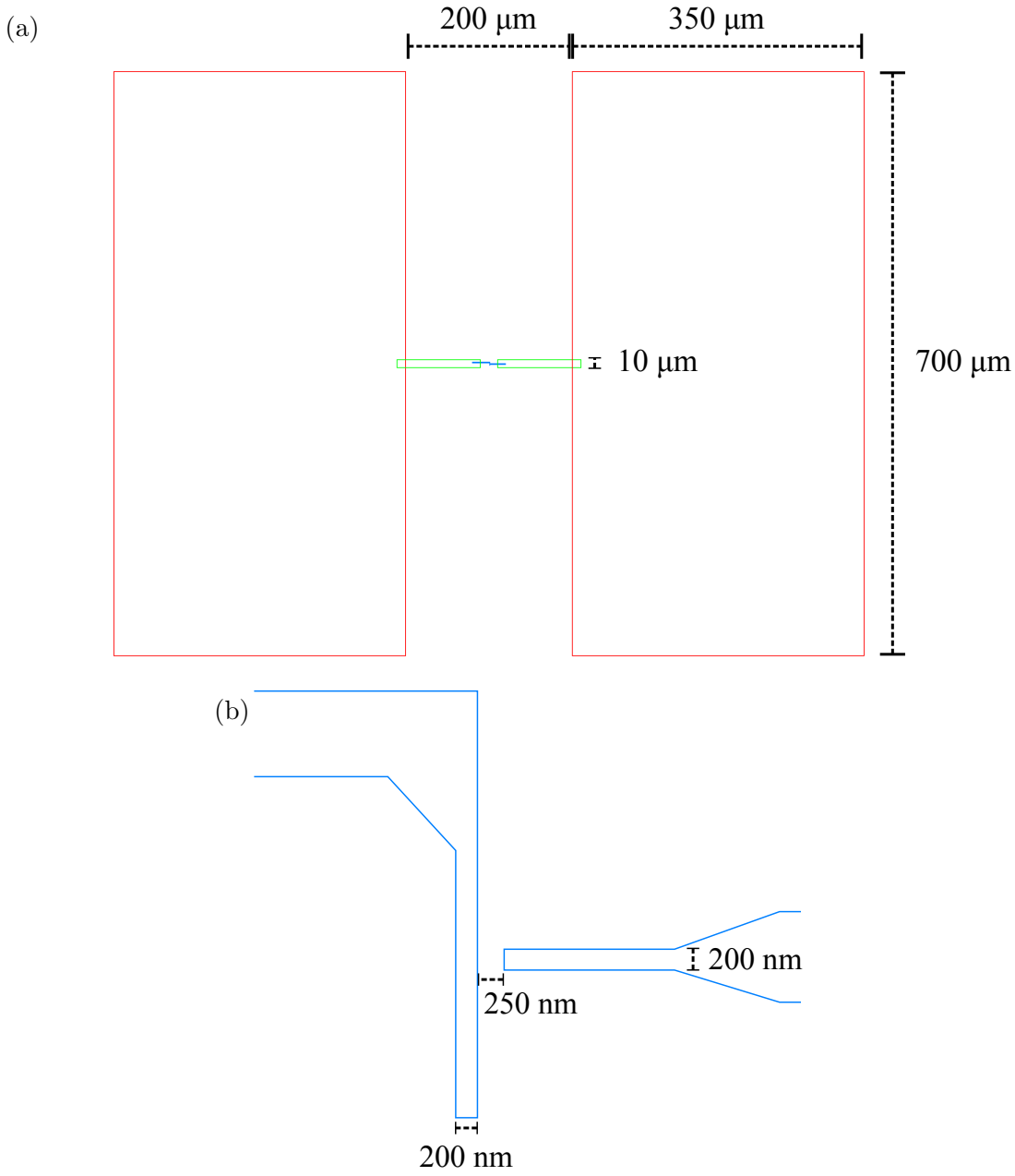

Figure 7.1: CAD drawing of the transmon. (a) Entire transmon device. (b) Detail of the Josephson junction.

pads to trap vortices [165], however I did not include them in my design. The two pads are connected with a 100 μm long line with 5 μm width, with a short break located in the middle where the Josephson junction is located. To reduce effects of dielectric loss from the junction oxide, I wanted the area of the junction to be as small as possible. After testing to fabricate different junction sizes, I decided that a junction with dimensions about 200 nm $\times$ 200 nm was small enough and gave reasonable fabrication yield. In the CAD design, the junction appeared as two 200 nm wide lines, perpendicularly oriented to each other, separated by a 200 nm $\times$ 250 nm bridge (see Fig. 7.1(b)). The lines would overlap and form the junction during the double-angle deposition process.

One of the main parameter choice I made was for the qubit $g \rightarrow e$ transition frequency $f_{ge} = \omega_{ge}/2\pi$ to be between 4 and 5.5 GHz. I chose this range because the frequency needed to be within the working range of all the microwave components (see Section 7.4), and the components with the narrowest range were the isolators at 4-8 GHz. Additionally, I wanted the transmon-cavity system to be in the dispersive regime, with $g_{ge} \ll \Delta_{ge}$, where g_{ge} is the coupling strength and $\Delta_{ge} = \omega_c - \omega_{ge}$ is the detuning between the cavity and the qubit. This limit also reduce the Purcell effect loss in the qubit. For qubits and the cavities similar to the ones I used, reported values of $g_{ge}/2\pi$ ranged between 120 MHz and 150 MHz [49, 189]. Hence I aimed for $\Delta_{ge}/2\pi$ to be 600 MHz or larger. The relevant cavity frequency in the system is the TE_{101} mode frequency f_{101}, which was about 6.1 GHz for the cavity I used (see Section 7.3). That determined the upper limit of f_{ge} to be of 5.5 GHz. In principle, I could have used qubit frequencies above the cavity frequency, *i.e.* between 6.7

GHz and 8 GHz. However, other groups have observed that qubits with frequencies above the cavity frequency typically had lower coherence times than qubits with frequencies below the cavity frequency[160] . This might be due to coupling to the higher order cavity modes which would give additional Purcell loss or to decreased isolation from the input and output lines at higher frequencies.

As I discussed in Section 6.1, the $g \rightarrow e$ transition frequency of the transmon is given by (see Eq. 6.12),

$$f_{ge} \approx \left(\sqrt{8E_J E_C} - E_C\right)/h, \tag{7.1}$$

where E_J is the Josephson energy and the charging energy is given by $E_C = e^2/2C_\Sigma$, where C_Σ is the total capacitance across the junction. In 3d transmons, the capacitances include the junction capacitance C_J, the capacitance between the two pads C_p, and the capacitance between the pads and the cavity C_{p-c}. In my device $C_J \approx 1$ fF is much smaller than the other two capacitances, hence C_Σ largely depends on the geometry and dimensions of the transmon and cavity. For the dimensions of the qubit and cavity similar to the one I used, others have measured the range of E_C/h between 170 and 210 MHz [165, 189]. It is possible to get better bounds on E_C by performing finite-element EM simulations [166, 223], however I did not do so for my design, since it was similar to earlier designs.

For the range of E_C values discussed above, I used Eq. 7.1 to calculate the range of E_J needed to achieve the desired f_{ge} value and found that I needed E_J/h between 11 and 24 GHz. From Eq. 6.2, the Josephson energy is given by $E_J = \Phi_0 I_0/2\pi$, where Φ_0 is the flux quantum and I_C is the junction critical current. The range

of E_J above gives a range of I_0 between 22 and 48 nA. The junction area is fixed, and I did not use a SQUID loop to allow E_J modulation, so the only way I could vary I_C was by varying oxidation parameters (see next Section). Once the junction was fabricated, the I_C value was essentially fixed, and hence f_{ge} was fixed as well (except for a slow oxidation at room temperature which would cause I_0 to decrease with time).

7.2 Transmon Fabrication

I performed the entire transmon fabrication process present below. Part of the fabrication process, especially the e-beam lithography process, was based on a process Ben Cooper and I developed previously for fabricating phase qubits [170]. The main difference was that the transmon process did not require any optical lithography.

7.2.1 Application of E-Beam Layers

The first step in the process was done at FabLab in the Kim Engineering Building. I started with a clean 3 inch c-axis sapphire wafer that was about 430 μm thick and polished on one side. I first cleaned the wafer with acetone, methanol, and IPA, followed by DI water. I then dried the wafer with N_2. To make sure that all the water was completely gone from the surface, I prebaked the wafer on a hot plate at 120°C for 5 minutes.

I then mounted the wafer on a Headway EC101 spinner [224]. With the wafer

spinning at about 1000 rpm, I applied LOR10A resist from a beaker. After the resist was applied, I increased the spin speed to 4000 rpm in about 3 seconds and spun it for another 45 seconds. This resulted in a 1000 nm thick LOR resist layer [225]. If dust particles landed on the surface of the wafer prior to appying the resist, radial streaks would reveal where the dust particles landed and this caused some uneveness in surface thickness, as LOR is much more viscous than typical resists. If the amount of streaking was significant, I removed the resist layer by submerging it in acetone for several minutes. I then recleaned the chip with solvents and applied a new resist layer. For the wafer I ended up using, a few streaks were visible and most of the surface appeared to be clean.

I then baked the wafer inside an oven. In the past, I typically baked the wafer at 180 to 200°C. However, because I was sharing the oven with another FabLab user, I had to bake it at about 230°C for 7 minutes. This higher temperature resulted in a harder resist layer and affected the development time of the LOR resist.

I then mounted the wafer on the spinner again. With the wafer stationary, I applied 950 PMMA C2 resist. I then spun the wafer at 4000 rpm for 45 seconds, leaving a 150 nm thick PMMA layer [226]. I then baked the wafer in the oven for 230°C for about 2 hours and 15 minutes.

7.2.2 Deposition of Al Anti-Charging Layer

I next thermally evaporated an Al layer that was used to prevent charge buildup on the sapphire during the e-beam write. In the past, Ben Cooper and

I found that evaporating this layer using the thermal evaporator at CNAM would create many craters on the surface of the resist after development. We attributed this to dust landing on the surface of the wafer before the wafer was mounted inside the evaporator. We found that by keeping the surface clean by keeping the wafer inside the clean room environment and using the thermal evaporator in FabLab, this problem did not appear [170].

However, the Fablab's evaporator was down when I was planning to do the evaporation. As a result, I used the evaporator in CNAM (see Section 7.2.6 below). During the preparation, I attempted to keep the wafer protected as long as possible. For this deposition, I did not need the pressure to be very low, and I started the Al evaporation when the chamber pressure is at 7×10^{-6} Torr. The deposition speed was approximately 6 Å/s, and the total Al thickness was about 150 Å.

While I observed a few craters on some of the chips after development, the density was significantly less than what we observed in the past. Additionally, the presence of craters was not as catastrophic to transmons as it was to our previous phase qubit designs because the surface area of the transmon was much smaller than the surface area of the phase qubit and its bias leads.

7.2.3 Dicing

Before dicing, I applied 1813 photoresist layer on the wafer. This layer protected the e-beam layers and the anti-charging layer from damage and contamination during dicing. I spun the wafer at 4000 rpm for 45 seconds, then baked it on a hot

plate at 120°C for 5 minutes.

I used the Microautomation Industries Model 1006 dicing saw located in the back room of FabLab, with a 200 μm wide blade for sapphire. Typically when dicing, one attaches the wafer to the vacuum chuck using double-sided tape, then dices the entire thickness of the wafer, in addition to part of the tape. However, I found that the tape did not stick well to sapphire wafers, although it worked fine for silicon wafers and this could result in chips flying away during dicing. In addition to the possibility of losing the chips if they fell into the water drain, this could damage the saw blade as well. Instead, I did not use the tape and attached the wafer directly to the vacuum chuck. I diced the wafer into 5 mm $\times$ 5 mm square chips but did not cut all the way through, leaving about 100 μm thick sapphire intact. This worked well, but meant I would need to break the chips apart later. Due to the dicing process that I used, the size of each individual chip could vary between 4.8 and 5.2 mm.

7.2.4 E-Beam Lithography

Just before doing e-beam lithography, I removed the protective resist layer on the chip that I wanted to use by putting it in an acetone bath for about 5 minutes, and then dried it using N_2.

I performed e-beam lithography using a JEOL 6500 scanning electron microscope (SEM) system [227] with a Nabity Nanometer Pattern Generation System (NPGS) [228] located at the Laboratory for Physical Sciences (LPS). After the chip was mounted inside the SEM chamber, I checked the beam current, found a good fo-

cus, then made sure the design file and run file stored in the NPGS control computer were correct.

For initial focusing, I usually attempted to focus on a scratch mark I made near the edge of the chip or on a dust particle on the surface. Once I managed to get a reasonable focus, I further improved the focus by focusing on contamination spots I made by using the SEM's spot mode for several seconds. Typically I made the spots about 100 μm away from the expected position of the junction. I was usually aiming for a circular spot with 10 to 20 nm diameter. If the spots were elongated, I needed to adjust the stigmation as well.

The SEM CAD files are separated into multiple layers, and each layer can have patterns with different colors. The patterns in the same layer have the same magnification, spacing between points, and emission current. An x- and y- offset between layers may also be defined, as the alignment is not perfect. The patterns in the same layer with different colors may have different dose. All these writing parameters are specified in the run file.

The design file of the transmon I used was called transmon05_200nm.DC2. The file consisted of two layers. The junction was located in the first layer, while the lines and pads were located in the second layer. The writing parameters are shown in Table 7.1, and were saved in a run file called transmon05_200nm_MMDDX.RF6, where MMDD corresponds to the date of writing and X corresponds to the Xth device written that day. The beam current for the first layer was typically around 30 pA, corresponding to spot 2 on the SEM, while the beam current for the second layer was typically around 1500 pA, corresponding to spot 11 on the SEM. Smaller

Table 7.1: Parameters used in SEM writing of transmon

Parameter	Layer 1	Layer 2	
(x,y) offset (μm)	(0,0)	(5,0)	
magnification	900	90	
spacing between points (nm)	24	93	
spot size	2	11	
beam current (pA)	≈ 30	≈ 1500	
dose (μC/cm^2)	600	600	400
color	orange	magenta	cyan
part	junction	line	pads

emission current allows us to draw smaller patterns, while larger emission current allows us to draw larger patterns more quickly. The dose is the total charge per unit surface deposited on the written surface. I found that the junction and the line required higher dose than the pads. For the transmon pattern with the specified parameters, the entire write typically took about 30 minutes.

7.2.5 Development

I performed the development process in FabLab. First, I removed the Al anti-charging layer by putting the chip inside an MF-CD-26 developer [169]. Typically the Al layer was removed after about 3 minutes. I then rinsed the chip in DI water for several seconds, then dried it with N_2.

I then developed the PMMA layer by putting the chip inside an MIBK:IPA 1:3 solution [169] for 60 s. I rinsed the chip in IPA for several seconds, then dried

it with N_2. Finally, I developed the LOR undercut layer by putting the chip in a bath MF-CD-26 developer [169]. The development time for this step depends on the desired undercut width. I found that a development time for 37-40 s was appropriate for the chips I used. I next rinsed the chip in DI water for several seconds and then dried it with N_2. I then examined the chip under a microscope and if the chip looked like it required more LOR development, I repeated the LOR development process for 3-4 seconds, rinsed, and inspected it again.

Figures 7.2 show the transmon05_200nm_0609A chip I used in the experiment after the development process. The undercut was clearly visible as bright edges in Fig. 7.2(a). As Fig. 7.2(b) shows, there were several black spots on the pad surface. I initially thought these were dust particles landing on the surface after development. However, I always found these spots in similar locations for most of my writes and it appears that the locations of these spots corresponded to the locations of the contamination spots. Evidently the resist layer hardened due to the heat from continuous electron beam hitting the surface during the spot making process.

7.2.6 Double-Angle Al Deposition and Oxidation

I performed the double-angle Al deposition and oxidation using the cryo-pumped thermal evaporator in room 0219 in CNAM (see Figure 7.3). During the period when I was performing fabrications, the evaporator used a glass chamber. However, the chamber was recently replaced by an aluminum chamber.

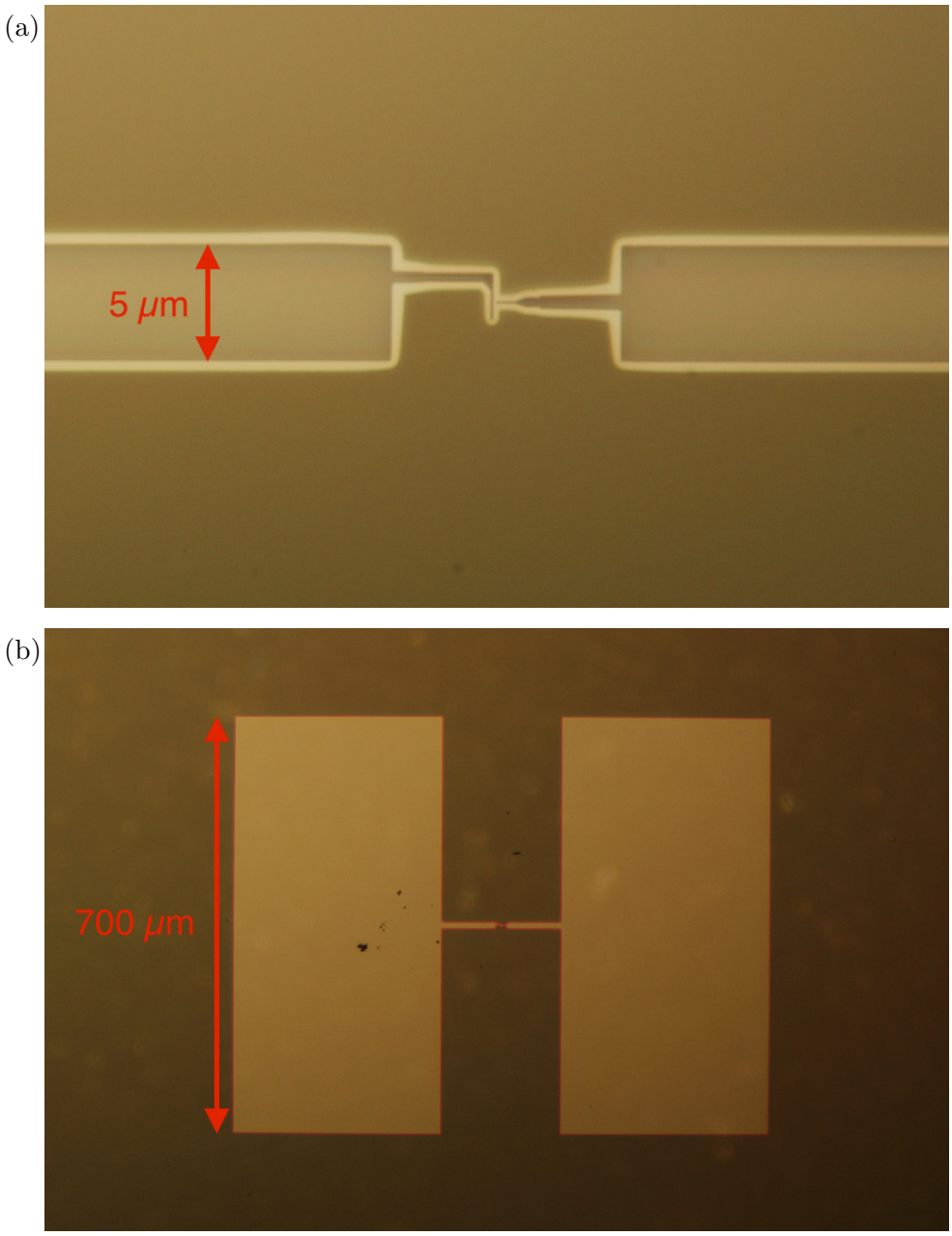

Figure 7.2: Optical pictures of transmon05_200nm_0609A chip after development process.(a) Under 100x magnification, the junction and the undercut are visible. The undercut appears brightest in this image. (b) Under 5x magnification, the pads are visible. The resist layers appear dark while the developed surface appear brighter in this image. The black spots on the pads appears to be related to the contamination spots generated during e-beam writing process

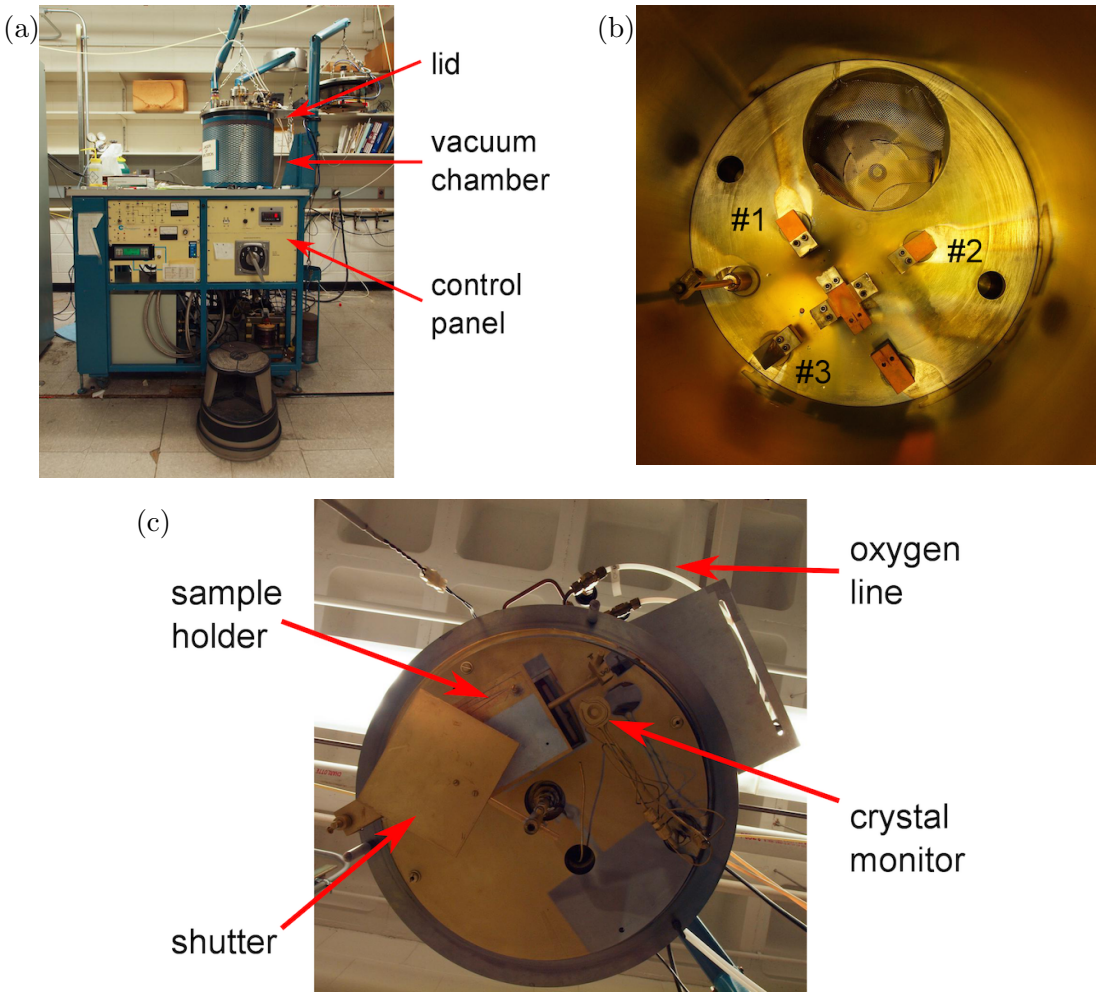

Figure 7.3: Photograph of the thermal evaporator in room 0219 in CNAM. (a) External view. (b) Evaporation electrodes inside the vacuum chamber. (c) The lid viewed from below. The chamber was recently replaced from a glass chamber to an aluminum chamber.

Figure 7.4 shows the step-by-step sequence of the evaporation process. I used Al pellets with 99.999% purity purchased from Alfa Aesar [229], and put 3 to 4 of them in a tungsten boat from R.D. Mathis [230]. The evaporator has three working evaporation electrodes (see Fig. 7.3(b)). I mounted a boat on each of the three electrodes: two for the evaporation, and one as backup in case one of the boats broke.

For transmon junctions, we want the base pressure to be as low as possible during evaporation. The evaporator usually can reach a base pressure of order 10^{-7} Torr after pumping overnight. However, the cryopump performance degraded during the period when I was performing fabrications and was later replaced. This affected the ultimate base pressure of the evaporator and how long the evaporator could hold that pressure. As a result, I evaporated with the base pressure slightly lower than 2×10^{-6} Torr. The incorporation of O_2 in an Al film tends to increase the superconducting gap and critical temperature T_c [211], but probably also leads to more TLSs between the film and substrate.

For the first evaporation (see Fig. 7.4(b)), I used electrode 1 and evaporated at an angle $\theta_1 \approx 10°$. I tried to keep the evaporation speed between 5 and 10 Å/s. I aimed for a total film thickness between 300 to 350 Å according to the crystal monitor. I note that because the electrode was not located directly underneath the chip, the actual deposition angle could have been off by up to 5°. There might also have been a small alignment error. Additionally, as the crystal monitor was oriented horizontally while the chip was tilted, the actual thickness of the film on the chip would be less than what was measured on the monitor, by a factor of $\cos\theta_1$.

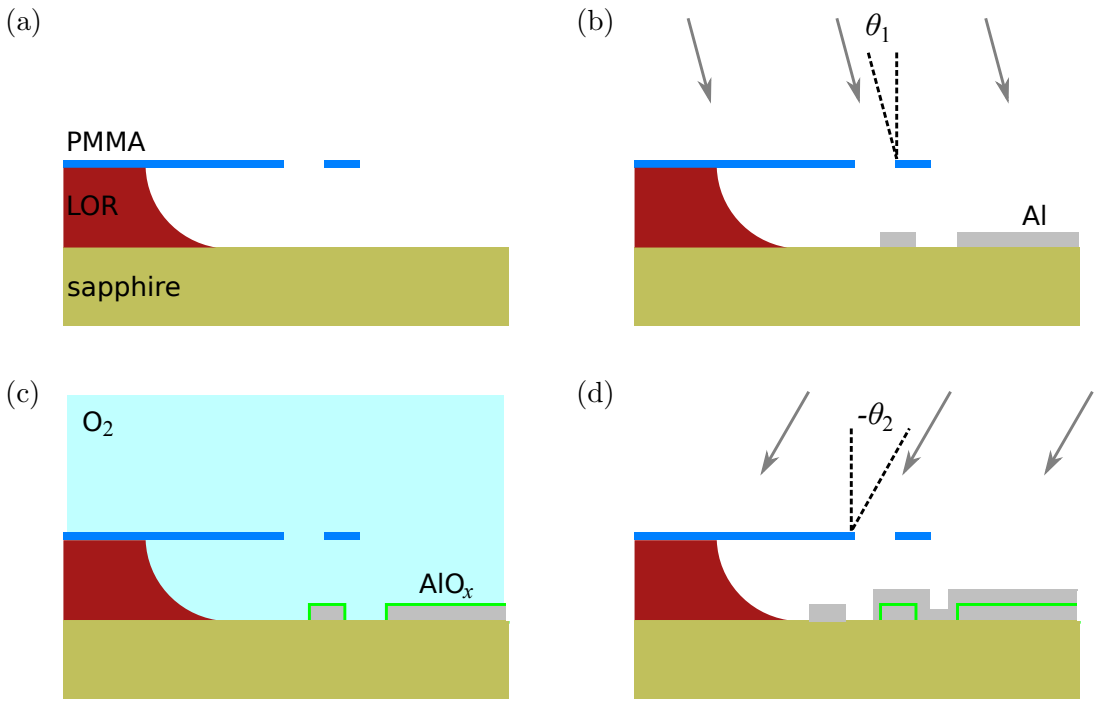

Figure 7.4: The double-angle evaporation and oxidation sequence. (a) The cross-section of the junction bridge before deposition, (b) first Al deposition, (c) oxidation, and (d) Second Al deposition.

After closing the shutter and switching off the power to electrode 1, I oxidized the junction by bleeding a small amount of O_2 gas into the chamber (see Fig. 7.4(c)). For the junction parameters that I was aiming for, I found the optimal O_2 pressure to be between 170 and 200 mTorr, and oxidized for about 3 minutes. With the current setup, it was hard to control the O_2 pressure with great accuracy. If the pressure was too low, I would oxidize longer and vice versa. I typically attempted to keep the pressure $\times$ time product constant. At the end of the time period, I repumped the chamber to base pressure.

For the second evaporation (see Fig. 7.4(d)), I used electrode 3 and evaporated at an angle $\theta_2 \approx -25°$. I kept the same range of evaporation speed, and attempted to extract as much Al as possible. This meant the thickness of the second layer can vary between 400 to 800 Å according to the crystal monitor. Similar errors in alignment and film thickness as I described in the first evaporation also applied here.

For transmon05_200nm_0609A chip which I used in the measurements, I evaporated about 300 Å in the first deposition and about 500 Å in the second deposition. In between the depositions, I oxidized the chip at 165 mTorr for 2 minutes 50 seconds.

7.2.7 Lift-Off

I performed the lift-off process in the FabLab. I started by putting the chip in an acetone bath for 5 minutes. I next put it in a heated bath of Remover PG [169].

After 15 minutes, I took it out of the bath, sprayed it with IPA while it is in an IPA bath. This removed most of the unwanted Al and e-beam resist. To remove any remaining resist residue, I put the chip back inside the heated Remover PG bath for another 15 minutes. I finished by rinsing it with IPA and then dried it using N_2.

I then checked the chip for remaining resist residue by inspecting it under an optical microscope. If needed, I would repeat the lift-off process. Typically at the end, the surface of the sapphire looked clean. However, there could be some nanoscale residue near the junction, which would not be observable under the optical microscope (for example, as reported in Ref. [201]). Figure 7.5 shows photographs of the transmon05_200nm_0609A chip I used in the experiment after lift-off. In Fig. 7.5(b), the junction overlap is clearly visible.

7.2.8 Resistance Measurement

As a final check, I measured the resistance across the junction using the probe station located in the sub-basement lab. To reduce chances of the junction blowing up during measurement, I used as low current as possible, and connected the junction in series to a known resistor. Additionally, I made sure to ground myself (using a grounding strap) and the probe station as well as I could.

In the previous Section, I discussed that the desired range of junction critical current I_C is between 22 and 48 nA. The junction resistance R_N in the normal state and critical current I_C are related by the Ambegaokar-Baratoff formula [231], given

(a)

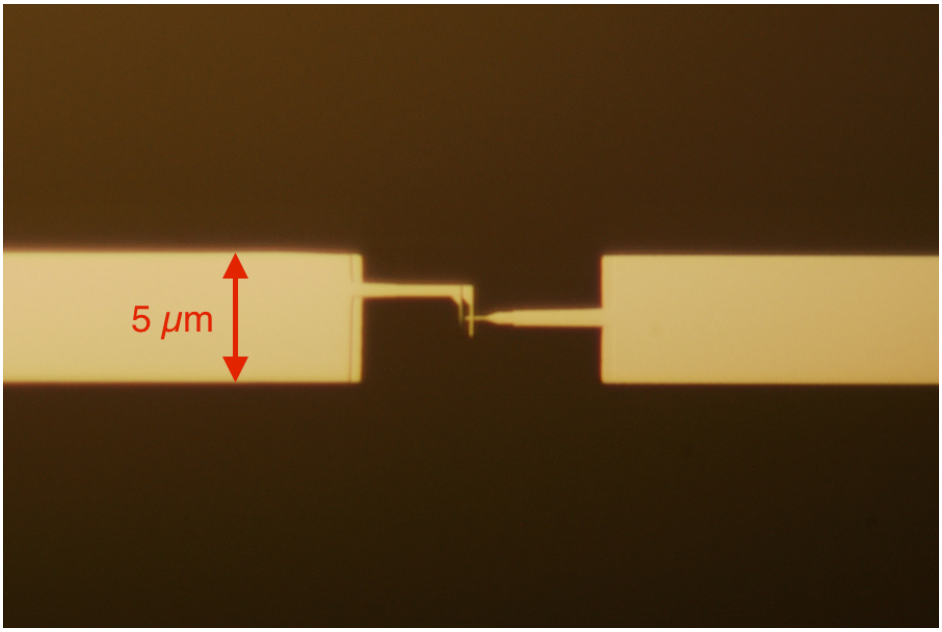

(b)

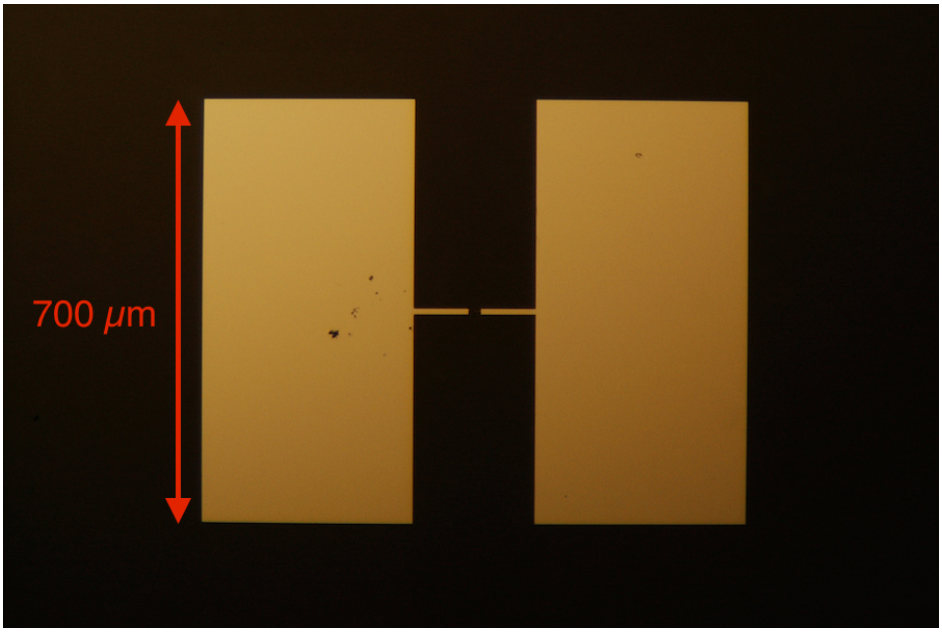

Figure 7.5: Optical pictures of transmon05_200nm_0609A chip after lift-off process: (a) Under 100x magnification, where the junction is visible. (b) Under 5x magnification, where the pads are visible.

by

$$R_N I_C = \frac{\pi\Delta}{2e}, \tag{7.2}$$

where Δ is the superconducting gap. Although Eq. 7.2 describes the relation between R_N and I_C at superconducting temperatures, the junction resistance at room temperature is comparable to R_N and Eq. 7.2 should give a good estimate of critical current I_C. Assuming $\Delta \approx 170$ μeV for Al, the range of R_N I was aiming for was between 6 and 12 kΩ. I measured a resistance of 6 kΩ for the transmon05_200nm_-0609A junction which was acceptable. After this measurement, I mounted the chip was in the cavity.

7.3 3D Cavity

The transmon was mounted inside the 3d cavity SI-2(see Fig. 7.6). This was a modified version of cavity SI-1that was used in the resonator experiments. Figure 7.6 shows the cavity with transmon05_200nm_0609A chip mounted. Cody machined this cavity as well, which had a similar design and machining process as the ones used for cavity SI-1, as detailed in Section 3.3.

There were several differences between the SI-2 and SI-1 cavities. Cavity SI-2 was machined from Al 6063 alloy, which should have fewer magnetic impurities. The dimensions of the cavity were different as well, as shown in Table 7.2. This resulted in different mode frequencies, with the SI-2 TE_{101} mode frequency at about $f_{101} = 6.3$ GHz with no chip inside. Additionally, the smallest dimension $b = 4$ mm allowed us to mount the chip in the standard orientation (see Fig. 7.6(b)).

(a)

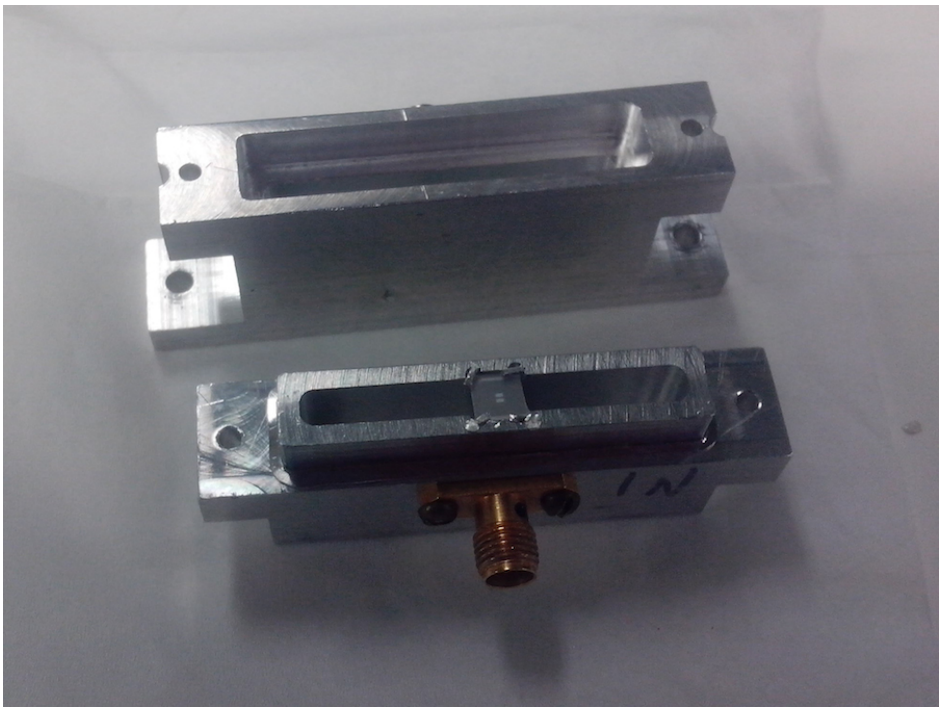

(b)

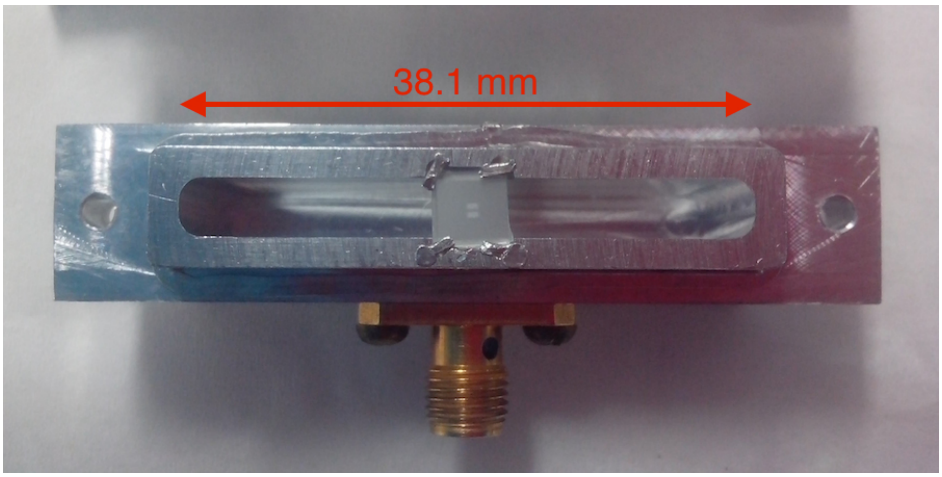

Figure 7.6: Pictures of aluminum cavity SI-2 with transmon05_200nm_-0609A chip mounted. (a) Both halves of the cavity, (b) The lower half of the cavity with the chip mounted. In both photographs, the two transmon pads are visible.

Table 7.2: List of 3d cavity parameters. f_{101} is based on Eq. 3.2 assuming no chip mounted inside the cavity.

Name	Al Alloy	a (mm)	b (mm)	d (mm)	f_{101} (GHz)
SI-1	6061	25.4	5	35.6	7.3
SI-1 (modified)	6061	22.9	5	35.6	7.8
SI-2	6063	30.5	4	38.1	6.3
SI-2b	6063	30.5	4	38.1	6.3

The position of the input and output pins were also changed. In SI-1, the pins were located at the node of the TE_{201} mode, while in SI-2, they were moved to the node of TE_{102} mode. This resulted in extremely weak microwave coupling to the TE_{102} mode and should reduce the coupling between the transmon and the TE_{102} mode, which was the second closest mode to the transmon. In addition to that, the pins used in SI-2 were modified as well. For the input, I used the same pin type as the ones used in SI-1. This gave an input coupling quality factor $Q_{\text{in}} \approx 2 \times 10^5$. For the output, I used a longer and thicker pin (Fairview Microwave SC3778 connector [232]) that gave a smaller output coupling quality factor $Q_{\text{out}} \approx 5 \times 10^4$. The pins were made from berylium-copper, coated with gold. I solder-tinned the larger output pin so that the surface was superconducting at the refrigerator base temperature. The imbalance between the input and output coupling resulted in the microwave signal coming out faster and stronger on the output side, improving the measured signal.

Cody also milled another hole through the cavity walls that allowed illumination from an optical fiber (see Section 7.5). I mounted the chip in the slot on the

cavity and closed the cavity, using the procedure described in Section 3.3. With the chip mounted, the TE_{101} mode frequency went down to about $f_{101} = 6.1$ GHz.

7.4 Electronics Setup

7.4.1 Setup Inside Dilution Refrigerator

Figure 7.7 shows the microwave setup inside the refrigerator for the transmon illumination experiment described in Chapter 8. The wiring inside the refrigerator was largely identical to the wiring used in the resonator experiments (see Section 3.4 and Fig. 3.8). The main difference was the isolator in the input line, right before the cavity, was removed from the refrigerator and mounted in the microwave output line of another dilution refrigerator, located in SB0331.

The microwave lines primarily consisted of semi-rigid UT-85-SS-SS coaxial cable, with stainless steel inner and outer conductors. Some shorter segments used flexible UT-85-Flexi, with silver-plated copper inner and outer conductors. At the input line, Midwest Microwave cryogenic attenuators [179] were anchored to different stages to reduce Johnson-Nyquist noise: 10 dB at the 4 K stage, 10 dB at the 700 mK stage, and 30 dB total at the mixing chamber. At the output line, two Pamtech CTH1409KS isolators [180] were anchored at the mixing chamber to reduce noise and other stray microwaves coming down the output lines, without attenuating the output signal from the cavity. A Caltech CITCRYO4-12A HEMT amplifier was anchored to the 4K stage, with a 3 dB cryogenic attenuator attached to the input of the HEMT to prevent self-oscillation.

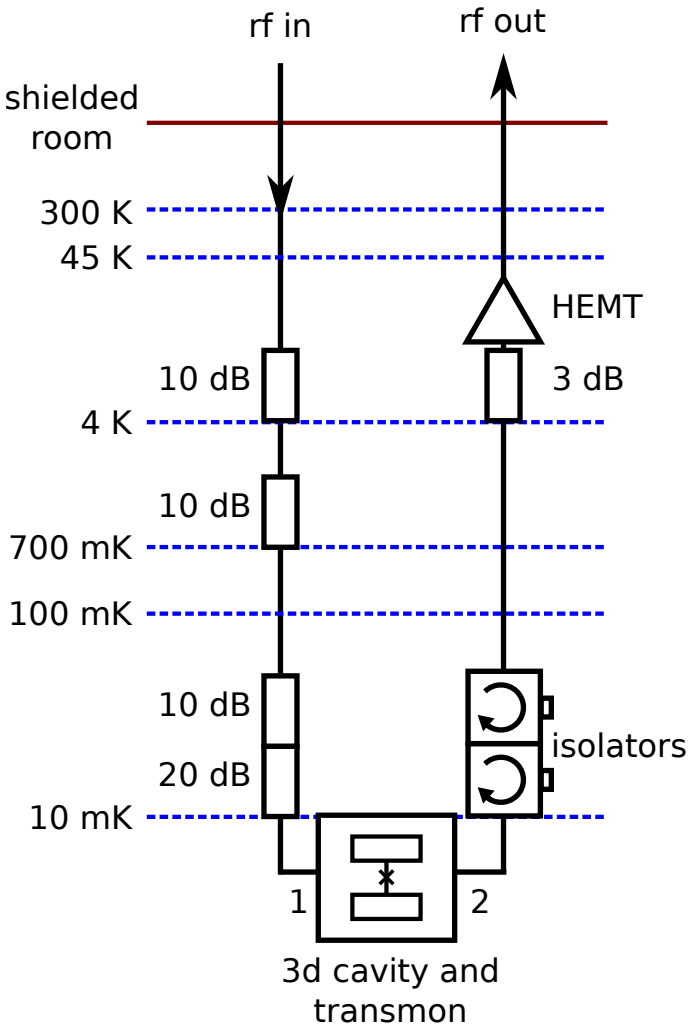

Figure 7.7: Setup for microwave input and output lines in the dilution refrigerator. The lines are either semi-rigid stainless steel UT-85-SS-SS or flexible silver-plated copper UT-85-Flexi coaxial cable.

7.4.2 Room Temperature Setup

Figure 7.8 shows the diagram for electronics setup at room temperature for the transmon experiment described in Chapter 8 and Fig. 7.9 shows the rack that contains most of the measurement instruments. In Fig. 7.8, instruments to the left of the dilution refrigerator set the timing of the pulses and applied various microwave signals, while the instruments to the right were used for readout. The instruments were connected as shown to a 10 MHz reference signal provided by a Stanford FS725 Rb frequency standard [183]. As the frequency standard had a limited number of 10 MHz output ports, I daisy-chained the reference signal by using a 10 MHz output signal from an instrument directly connected to the FS725.

An Agilent 33120A arbitrary waveform generator (AWG) [177] set the repetition rate of the experiment, applying a TTL signal with frequency equal to the repetition rate. Typically, the repetition rate was set at 1 kHz. This signal was then used to trigger multiple Stanford DG535 pulse generators [183] that were used to set the timing of the pulse and readout. I used three microwave sources, one Agilent E8257D, one Agilent 83731B, and one Agilent 83732B [177]. Two sources were used to apply pulses at the cavity and the qubit pulse, respectively, and were gated by pulses from DG535. The last source applied a continuous signal for LO reference signal, with a frequency that was the same or slightly detuned to the cavity frequency, depending on whether I was performing homodyne or heterodyne measurement (see next Ssection). For photon number peak measurements (see Section 8.3.3), I added an additional Agilent 83620B source (not shown in Fig. 7.8), but otherwise I used

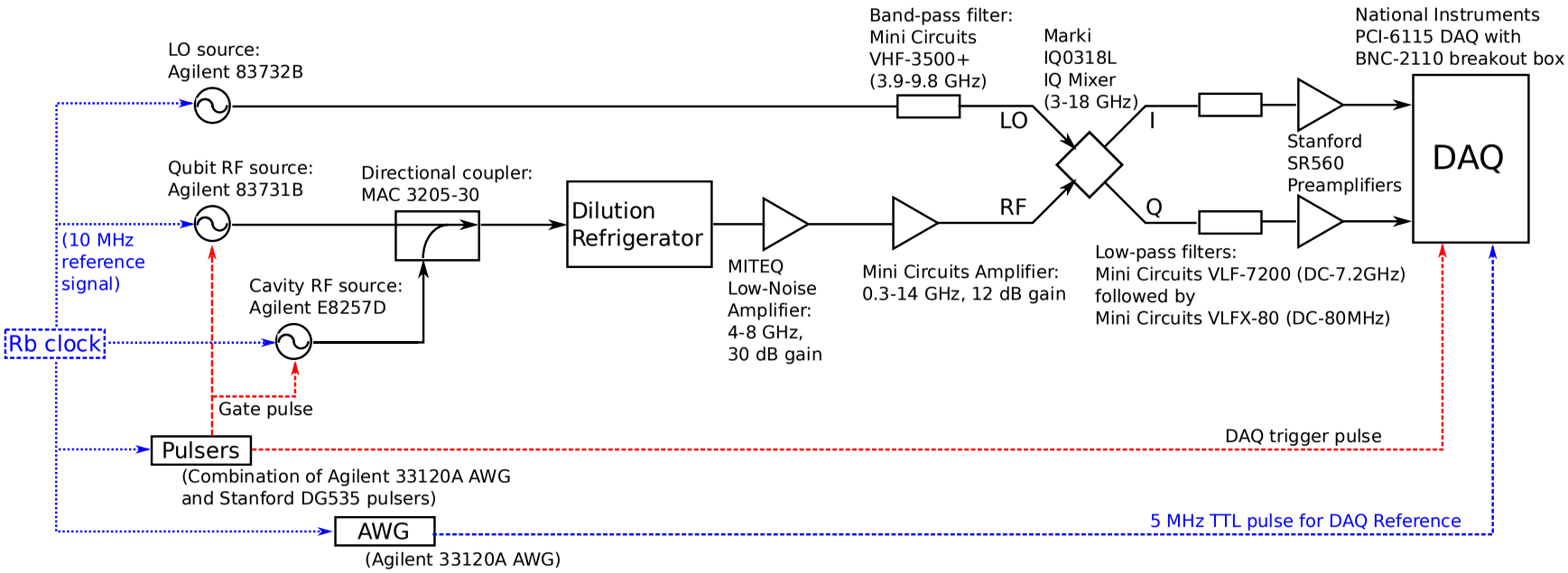

Figure 7.8: Room temperature microwave setup for qubit pulsing and readout.

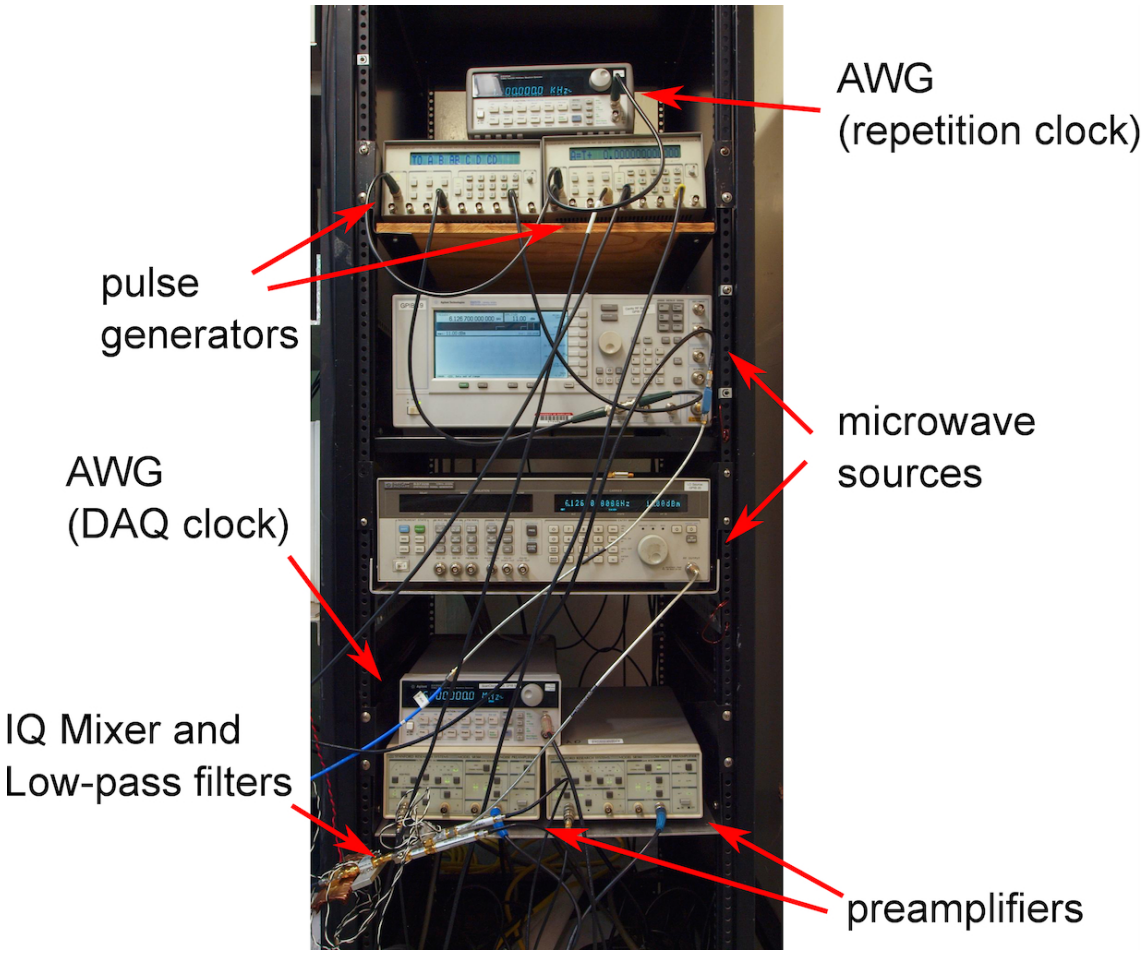

Figure 7.9: Photograph of rack that contains part of qubit pulsing and readout setup.

the aforementioned three sources. All sources, pulsers, and the AWG were connected to a Dell Windows PC with a National Instruments PCI-GPIB card [184]. This allowed us to adjust the measurement parameters from the computer using MATLAB.

The pulses from the cavity and qubit sources were combined using a MAC Technologies C3205-30 directional coupler [233], with a 4 to 8 GHz frequency range and 30 dB coupling. The combined pulse then passed through the screen room wall, to the top plate of the refrigerator, where it was connected to the input line inside the refrigerator.

The signal coming out of the output line of the refrigerator were then amplified further by a Miteq AMF-3F-04000800-07-10P room temperature low-noise amplifier [182] (4-8 GHz range and about 30 dB gain) and a Mini Circuits ZX60-14012L+ amplifier [178] (0.3-14 GHz range and 11 dB gain). The amplified signal was then mixed with the LO signal using a Marki IQ0318L IQ mixer. The mixer had two output ports for the mixed-down signal: the in-phase (I) port and the other for the quadrature (Q) port. The signal from both outputs was passed through two identical sets of low-pass filters, then amplified using two Stanford SR560 preamplifiers [183]. The gain, coupling, and filter settings of the amplifier depended on whether I was performing homodyne or heterodyne measurements, as well as the rf power used. For homodyne measurements, I used DC coupling and low-pass filtering, while for heterodyne measurement, I used AC coupling and band-pass filtering. Finally, the amplified I and Q signals entered a National Instrument BNC-2110 breakout box [184], which was connected to a National Instruments PCI-6115 data acquisition

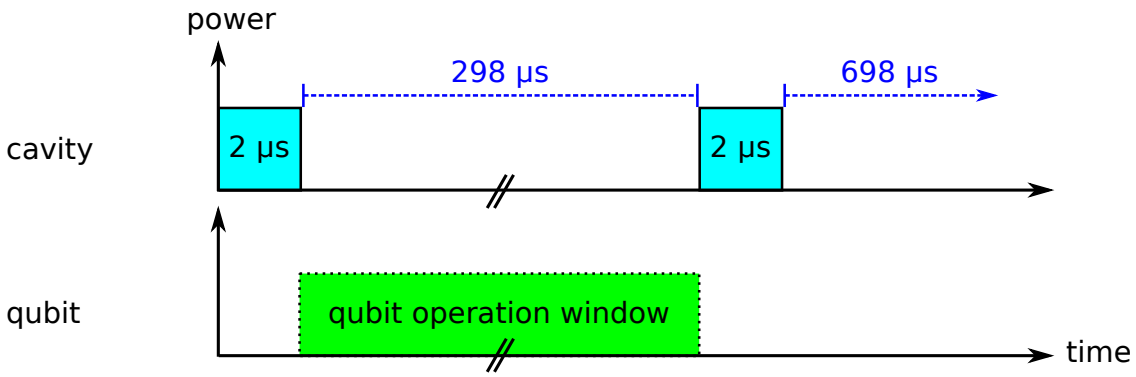

Figure 7.10: Typical timing diagram for the cavity and qubit pulses for each repetition for qubit state readout. Blue denotes measurement pulse applied at the cavity frequency and green denotes qubit manipulation.

card (DAQ) [184] located inside the PC used for instrument control.

The DAQ digitized the I and Q signals, which was then recorded for later processing and analysis. In addition to the two mixed-down signals, two more lines were connected to the breakout panel. The first line supplied a pulse from one of the pulse generators, which acted as a trigger for the DAQ. The other line carried a 5 MHz TTL signal from a second Agilent 33120A AWG. This signal set the acquisition rate for the DAQ to be 5 Msamples/channel/s, as well as made sure that the DAQ was connected to the 10 MHz reference clock. The DAQ should have a maximum acquisition rate of 10 Msamples/channel/s, however I was not able get it to work at this rate with an external reference clock somehow.

7.4.3 Pulsing and Readout Sequence

Figure 7.10 shows the typical pulsing sequence I used for qubit operations and state readout. In each repetition, two microwave pulses were applied for state

measurement. For low power/QND readout (see Section 6.3.1), the frequency of the pulse was at the dressed cavity frequency in the single rf photon regime and the pulse was approximately 80 μs long. For most of the measurements, I used a high power/Jaynes-Cummings readout (see Section 6.3.2), the frequency of the pulse was at the bare cavity frequency and the pulse was between 2 to 6 μs long, with most of the measurements performed with 2 μs long pulses.

The first pulse was at the beginning of each repetition, while the second pulse started 300 μs after the the beginning of the first pulse. I performed qubit operations between the first and second pulses. After the second pulse, I let the system relax thermally for 700 μs before starting another repetition. Hence the first pulse acted as a reference pulse and should always measure a $|g\rangle$ state, with some background $|e\rangle$ state population from thermal effects and other possible background effects. The second pulse measured the excited state population after the qubit operations.

Given the timing of the measurement pulses, I set the overall repetition rate to be 1 kHz. Prior to choosing this rate, I varied the timing between pulses and repetition rates, with rates as low as 500 Hz, allowing for longer relaxation window. However, I found no observable difference between measurement results taken with lower rates. As a result, I chose the higher repetition rate (1 kHz) and this allowed me to perform the measurements faster.

For the transmon illumination experiment, I typically performed three different types of measurements for each refrigerator temperature T and optical intensity $I_{\rm opt}$ value. Figure. 7.11 shows the timing diagrams for the three measurements. Typically the first measurement I performed was qubit spectroscopy (see Fig. 7.11(a)), to find

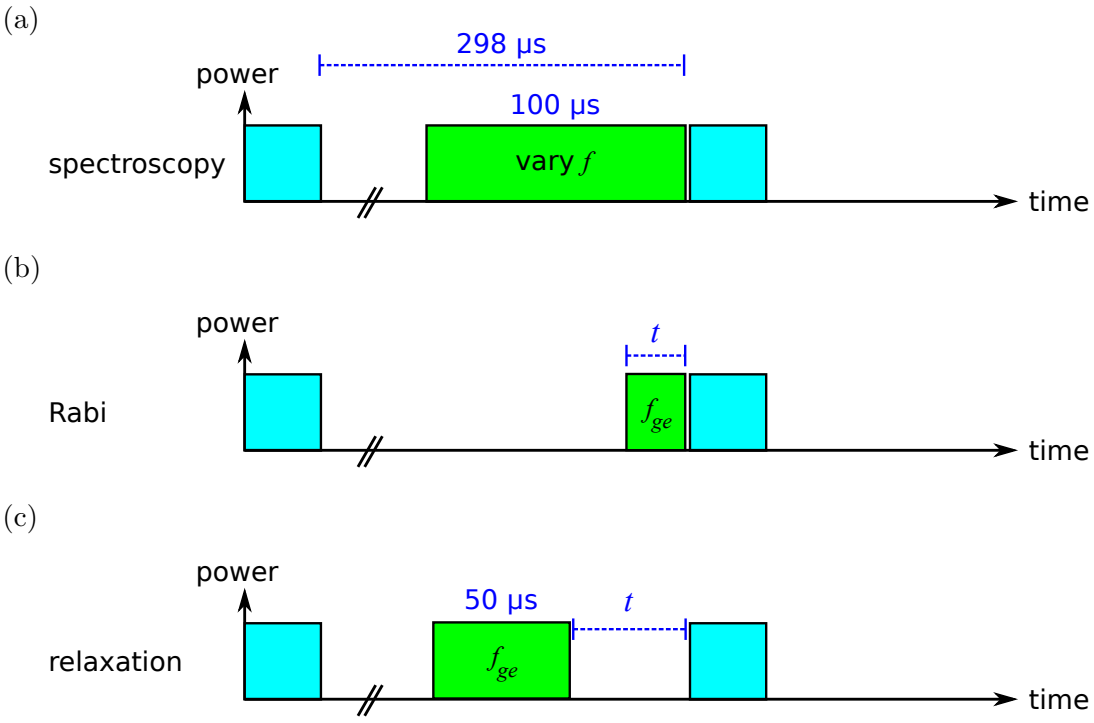

Figure 7.11: Timing diagram for different qubit measurements: (a) spectroscopy, (b) Rabi oscillation, and (c) relaxation (T_1) measurements. Blue denotes measurement pulse applied at the cavity frequency and green denotes qubit drive pulse.

the exact value of the qubit frequency f_{ge} for the given temperature and $I_{\rm opt}$ settings. Here I applied 100 μs long pulse from the qubit source that ended just before the beginning of the second cavity pulse. The frequency of the qubit source was varied to sweep out a range around f_{ge}

Once f_{ge} was found, I set the qubit source frequency to be f_{ge} and measured the Rabi oscillations (see Fig. 7.11(b)). Here I varied the length of the qubit pulse (t in Fig. 7.11(b)), with the qubit pulse ending right at the beginning of the second cavity pulse. As a result, for each different t value, I had to adjust the starting time of the qubit pulse as well.

The final measurement was the qubit relaxation measurement (see Fig. 7.11(c)). Here I typically set the length of the qubit pulse to be 50 μs, with drive power chosen such that the qubit was in the 50-50 saturation state at the end of the pulse. In this measurement, I varied the delay time between the end of the qubit pulse and the beginning of the cavity pulse (t in Fig. 7.11(c)) by adjusting the starting time of the qubit pulse.

I should note that in addition to the three types of measurements that I performed, there are additional types of qubit coherence measurements. These include Ramsey free-induction decay [234] and spin echo [235] measurements. However, these measurements are more complicated and require well shaped qubit pulses. For my measurements, I simply pulsed the microwaves using the internal gating of the sources, which gave me limited pulse shaping capabilities. For pulse shaping, other groups have used a very fast AWG or dedicated pulse shaping boards combined with a set of mixers and filters [166, 189, 201]. Our group plans to acquire

these in the near future.

7.5 Optical Illumination Setup

The setup for optical illumination of the transmon was almost identical to the setup used in optical illumination of resonators described in Section 3.5. The setup on the optical table at room temperature (see Fig. 3.10) and inside the refrigerator were completely identical, and hence I will not repeat them here. I found that the splitting ratio η between the branch going into the refrigerator and the branch going into the power meter was $\eta \approx 0.74$ when I measured it at the end of the cooldown.

I only used one illumination line, oriented perpendicular to the surface of the chip. Since we were concerned with fiber vibrations affecting the resonance frequency of the cavity (see Section 4.3), we decided to reduce the amount of fiber protruding inside the cavity space. Cody machined a new Al mounting bracket, and Jared secured the fiber to the bracket so that the end of the fiber was flush with the wall of the bracket. This meant the end of the fiber was further away from the chip, which resulted in a larger illumination spot diameter of $d_{\text{spot}} \approx 5.2$ mm, comparable to the dimensions of the chip. The combination of the smaller splitting ratio and the larger spot size meant that for the same optical power coupled to the optical fiber, the optical intensity I_{opt} hitting the surface of the chip (see Eq. 3.4) in the transmon measurement was about 25 times smaller than the intensity of perpendicular illumination in the resonator experiments.

7.6 Summary

In this chapter, I discussed the design and fabrication of a transmon which I used for the experiments described in the next chapter. I also briefly discussed the design and fabrication of the 3d cavity, which was similar to the 3d cavity used in the resonator experiments. I then discussed the microwave setup, including wiring inside the dilution refrigerator, the instrument setup for pulsing and readout, as well as the pulsing and readout sequence. Finally, I briefly discussed the optical illumination lines which are largely identical to the illumination line used in the resonator experiments.

Chapter 8: Transmon Results

In this chapter, I discuss the results of my measurements on the device called transmon05_200nm_0609A device. I begin by discussing the initial characterization of the circuit QED system using spectroscopy of the cavity and transmon. I then discuss time dependent measurements of the transmon at 10 mK and no applied optical power. I also discuss spectroscopy and time resolved measurements at increased refrigerator temperature and applied optical power. I next discuss how the transition frequency and characteristic times behave as a function of temperature and optical intensity, and compare it with the prediction from known sources of decoherence. Finally, I discuss the effects of pulsing the illumination on relaxation. I note here that this section is from preliminary analysis of the data. Additional detailed analysis will be needed to fully understand more aspects of the data.

8.1 Measurement Details

Device transmon05_200nm_0609A was measured inside the dilution refrigerator in the Atoms on SQUIDs laboratory in Room 1305B of the Physics Building between June 24 and September 10, 2015. The refrigerator base temperature during the measurements was about 10 mK. The house chilled water failed on July 21,

causing the pulse tube compressor to shut down and the mixing chamber to go up to about 30 K before I could start condensing again. Hence, I divided the measurement is divided into two sessions: before and after the water failure.

During the first measurement session, I initially used one μ-metal shield mounted at room temperature outside of the refrigerator vacuum can, and tried to have the screen room door closed during measurements. However, I observed that the cavity peak frequency and linewidth fluctuated significantly. In particular, the bare and dressed cavity peaks fluctuated by several MHz, which was much larger than the linewidth. Sometimes the peak even appeared to vanish completely. On the other hand, it was unclear whether the qubit peak was affected by these fluctuations. It was possible that some of the jitter I observed in my earlier resonator measurements (see Chapter 4) was related to these fluctuations. One related problem I encountered as that it was hard to perform a long set of measurements, as I would have to adjust the measurement parameters when the frequencies drifted too much.

After further investigations, it appeared that the cavity frequency was affected by curcumstances outside the refrigerator. These include opening and closing the screen room door, or walking around or dancing on the screen room floor. The effect appeared to be random in the sense that sometimes the peak was sharpest when the door was fully open, sometimes it was sharpest when it was half open, and sometimes it was sharpest when the door was closed. Often, I had to adjust the door during measurements to find the optimal position. These observations suggest that the fluctuations might be caused by either mechanical effects, i.e. poor mechanical isolation between the refrigerator and the rest of the screen room, or

magnetic effects, i.e. local fluctuations in magnetic field near the chip. Ben Palmer's group at LPS observed similar fluctuations in high Q cavities before adding more magnetic shielding. This suggested that magnetic fluctuations were the likely cause.

Before starting the second session, while the refrigerator was at about 8 K, with the help of Sudeep Dutta and Roberto Ramos, I added two additional μ-metal shields outside the refrigerator. During the second session, I still observed fluctuations on the cavity peak but the magnitude was much smaller, about 100 kHz maximum, which was less than the cavity linewidth. This was much more manageable, and I did not need to interrupt the measurements very often. This was consistent with magnetic fluctuations being improved by the addition of the shielding. All of the results I present in this chapter came from the second session.

I mainly used the high-power Jaynes-Cummings readout (see Section 6.3.2) for the qubit measurements. As discussed in Section 7.4.3, for each repetition I used two measurement pulses: the first at the beginning acted as a reference, and the second after the qubit operations acted as the actual measurement of the qubit state. I define V_{AB} as the measured voltage from the first pulse, and V_{CD} as the measured voltage from the second pulse, both averaged over many (typically 8000) repetitions. In the Jaynes-Cummings readout, the difference between the two voltages should be proportional to the excited state probability [205]. As the fluctuations were still present, the averaged output signal from the qubit measurements still drifted somewhat. However, I found that the fractional voltage difference $\delta V/V$, defined by

$$\frac{\delta V}{V} \equiv \frac{V_{CD} - V_{AB}}{V_{AB}}, \tag{8.1}$$

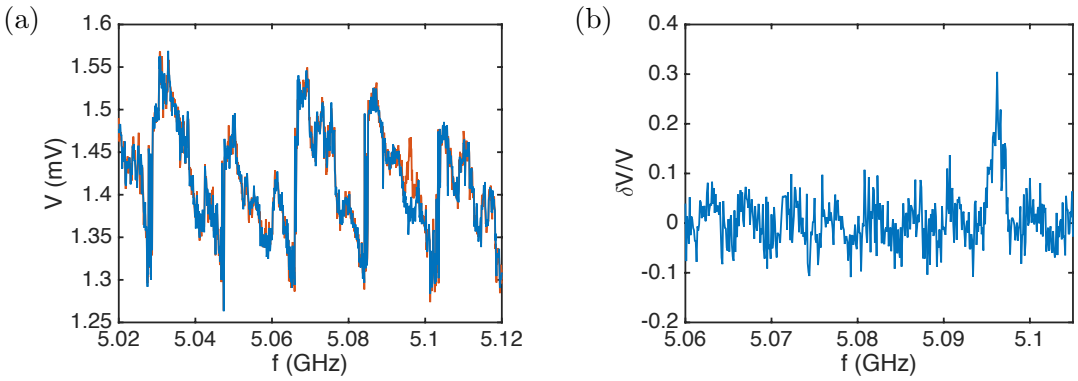

Figure 8.1: Periodic artifacts that could appear in qubit measurements: (a) Periodic sawtooth pattern in average voltage in heterodyne measurements. Blue curve is V_{AB} and red curve is V_{CD}. (b) Periodic pattern that occasionally appear in spectrum in homodyne measureements. For both plots, the feature at 5.096 GHz is the qubit $g \rightarrow e$ transition peak.

appeared to be unaffected by the fluctuations for a set applied cavity power. In this chapter, I use $\delta V/V$ as the measure of excited state probability. I typically chose the cavity power such that $\delta V/V$ was maximized. For homodyne measurements at 10 mK and no optical power, I used a cavity power of -5 dBm at the source for readout.

For the first several weeks of measurements, I used a heterodyne Jaynes-Cummings readout with the LO source frequency set 625 kHz higher than the cavity source frequency. I observed that in addition to the random fluctuations, the measured voltages V_{AB} and V_{CD} consistently followed what looked like a sawtooth pattern [see Fig. 8.1(a)], with a period of the pattern approximately 1 hour of measurement time. As I used a DAQ acquisition rate of 5 Msamples/s, I captured 8 points for each oscillation of the mixed down signal. It was possible that the sawtooth pattern was caused by sampling drift due to frequency errors between the

sources and the DAQ, which would be unexpected because all of them were basically connected to the same 10 MHz Rb clock. The sawtooth pattern appeared to create a similar periodic pattern in $\delta V/V$.

To eliminate this artifact, from about August 5, 2015, until the end of the cooldown I used a homodyne readout with the LO frequency set at the bare cavity resonance frequency. This appeared to remove the sawtooth pattern, although the fluctuations remained. However, some spectroscopy measurements of $\delta V/V$ still appeared to exhibit a small oscillation in the background level [see Fig. 8.1(b)]. This oscillation behavior appeared to have a period of about 1 hour of measurement time as well, suggesting it was caused by the same issue as the original oscillation. However, this behavior did not always appear, and could appear or disappear between spectroscopy measurements taken a few hours apart. While I did not observe this behavior directly in the time dependence measurements, it's possible this behavior caused some sets of measurements to have larger scatter than than would otherwise have been the case.

8.2 Initial Cavity Characterization

For the initial cavity characterization, I did not use the qubit measurement setup described in Section 7.4.2. Instead, I used the VNA to measure the transmission S_{21} and varied the applied rf powers, similar to the resonator measurements described in Section 3.4.

Figure 8.2 show the color map of $|S_{21}|^2$ in dB as a function of frequency and rf

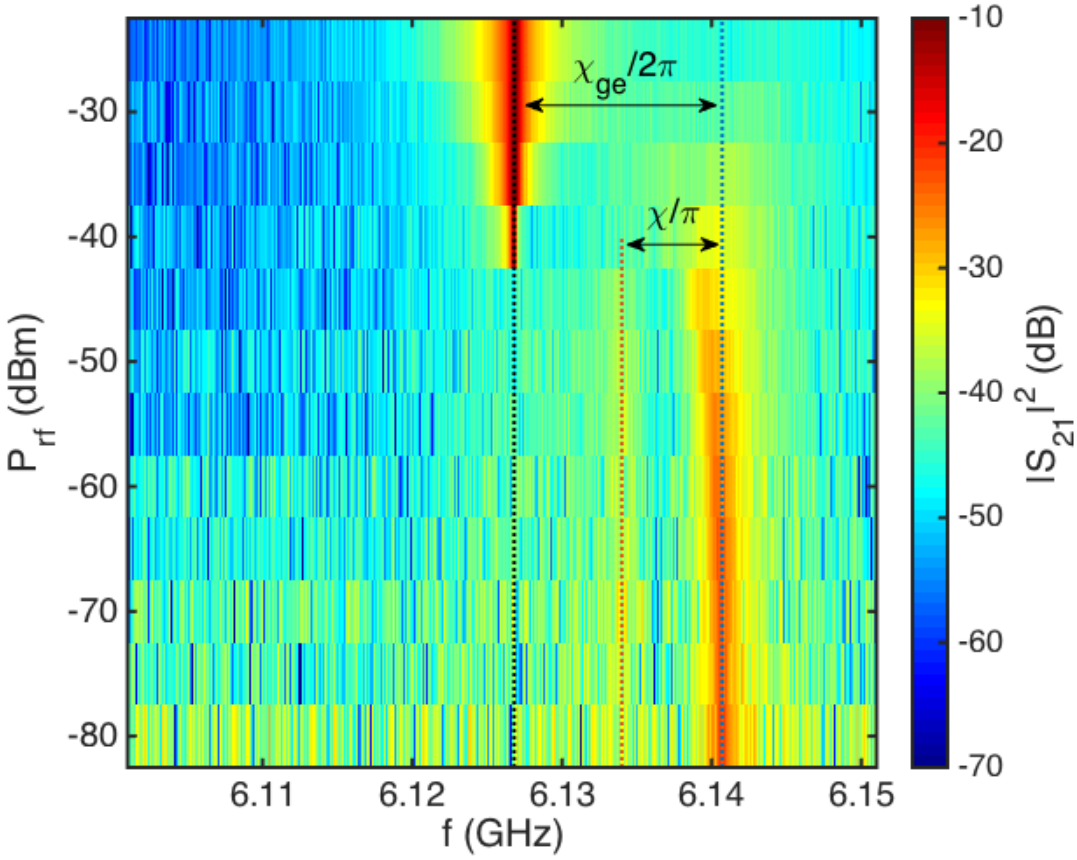

Figure 8.2: Map of the cavity $|S_{21}|^2$ as a function of frequency and rf power applied by the VNA. The main cavity transition peaks are indicated by the dashed lines.

power applied by the VNA. Several features can be clearly seen. At high powers, the peak frequency is located at 6.1268 GHz (black dashed line). This is the bare cavity frequency $\omega_c/2\pi$. In Fig. 8.2, the bare cavity peak vanished below -40 dBm. Note that due to the presence of the 30 dB directional coupler and slightly different lines for the standard qubit readout (see Fig. 7.8), this power was roughly comparable to the -5 dBm cavity power at the source I used for most of the qubit measurements.

At lower powers, the peak frequency is located at 6.1407 GHz (blue dashed line). As there is no applied qubit drive, the qubit is at the ground state, and this dressed frequency is given by $\tilde{\omega}_{r,g}/2\pi = (\omega_r + \chi_{ge})/2\pi$ (see Eq. 6.37). From these frequency values, I extract $\chi_{ge}/2\pi = 13.9$ MHz.

Additionally, at low powers a faint peak at $\approx$ 6.1340 GHz (red dashed line) was present. Most likely this peak is due to the dressed cavity transition when the qubit is in the excited state $\tilde{\omega}_{r,e}$. The fact that it was visible implies the presence of a background qubit excited state population. In this case, from Eqs. 6.36 and 6.38 I can extract $\chi/\pi = 6.7$ MHz. Given χ and χ_{ge}, I also find $\chi_{ef}/2\pi = 21.1$ MHz.

To show the behavior of the cavity transition peak in more detail, in Fig. 8.3 I plot the cavity spectrum as a function of frequency for several different P_{rf} values. For the y-axis, I use P_2, which is the power measured at port 2 of the VNA, instead of $|S_{21}|^2$. At the highest power ($P_{\mathrm{rf}} = -25$ dBm, blue curve), the bare peak appeared to be Lorentzian. By fitting this peak, I found the total quality factor $Q \approx 3.2 \times 10^4$. Since for the cavity $Q_{\mathrm{in}} \approx 2 \times 10^5$ and $Q_{\mathrm{in}} \approx 5 \times 10^4$, this meant the internal quality factor $Q_i \approx 2 \times 10^5$. This value was typical for the Al 3D cavities I used (see Section 4.3), but lower than ones typically reported by other groups [49].

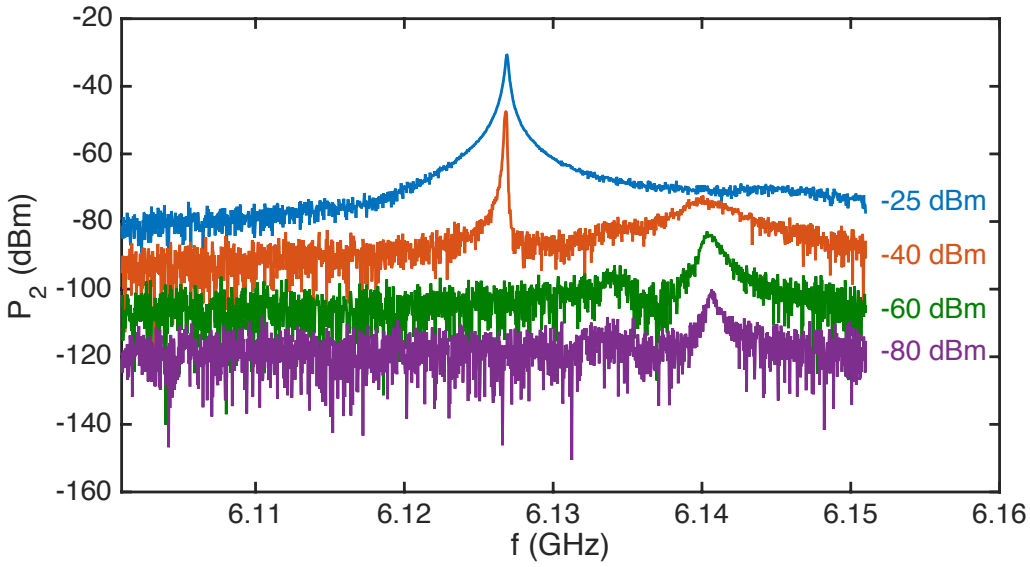

Figure 8.3: Individual line traces showing measured power P_2 at VNA port 2 as a function of frequency f for several applied rf powers P_{rf}.

With decreasing power, the bare peak started to get distorted before vanishing completely. At the same time, the dressed peak started very broad, then slowly got sharper with decreasing power. At the lowest power ($P_{\mathrm{rf}} = -80$ dBm, purple curve), the extracted quality factor was $Q \approx 9.4 \times 10^3$. The fact that the Q was much lower for the dressed peak suggests a significant addition of loss or dephasing due to coupling to the qubit.

8.3 Qubit Spectroscopy

For qubit spectroscopy, I used a low-power dispersive readout initially to find where the qubit transitions were located. For all further measurements I discuss below, I used the high-power Jaynes-Cummings readout with the pulse timings

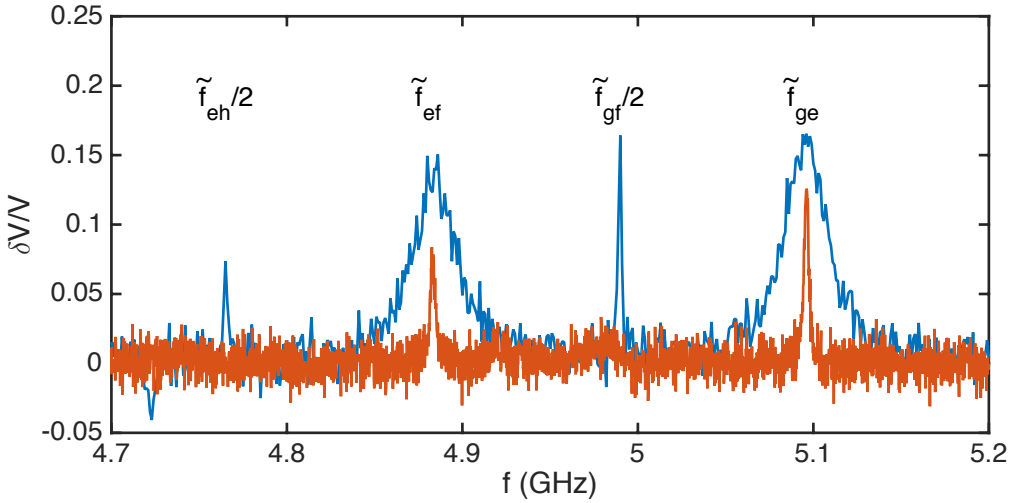

Figure 8.4: Qubit spectroscopy at high ($P_q = -20$ dBm, blue curve) and low ($P_q = -40$ dBm, red curve) qubit drive powers. The qubit transition peaks are labeled.

discussed in Section 7.4.3.

8.3.1 Extraction of Qubit Parameters

Figure 8.4 shows the qubit transition spectrum for two different applied qubit drive powers P_q. The blue curve corresponds $P_q = -20$ dBm and this spectrum has two broad peaks and two sharp peaks, roughly regularly spaced. The red curve corresponds to $P_q = -40$ dBm. In this lower power spectrum the sharp peaks vanished, while the broad peaks have sharper width and shorter height. The broad peaks correspond to the single-photon qubit transitions; the peak at 5.096 GHz is the $|g\rangle \leftrightarrow |e\rangle$ transition and the peak at 4.883 GHz is the $|e\rangle \leftrightarrow |f\rangle$ transition. The sharp peaks correspond to multi-photon qubit transitions, with the right sharp peak corresponding to the two-photon $|g\rangle \leftrightarrow |f\rangle$ and the left peak most likely

corresponding to the two-photon $|e\rangle \leftrightarrow |h\rangle$ transition.

I note here that these peaks are not the bare qubit peaks. As discussed in Chapter 6, the qubit peaks are also shifted due to coupling to the cavity, and the peaks shown in Fig. 8.4 are the dressed cavity peaks. This gives $\tilde{f}_{ge} = \tilde{\omega}_{ge}/2\pi = 5.096$ GHz and $\tilde{f}_{ef} = \tilde{\omega}_{ef}/2\pi = 4.883$ GHz. In Eq. 6.35, the dressed qubit transition frequency is given by $\tilde{\omega}_{ge}/2\pi = (\omega_{ge} - \chi_{ge})/2\pi$, which I can use to extract the bare $|g\rangle \leftrightarrow |e\rangle$ transition frequency $\omega_{ge}/2\pi = 5.110$ GHz. From the bare cavity and qubit transitions, I get the detuning $\Delta_{ge}/2\pi = (\omega_c - \omega_{ge})/2\pi = 1.017$ GHz, and I can then calculate the coupling strength between the cavity and the $|g\rangle \leftrightarrow |e\rangle$ transition to be $g_{ge}/2\pi = \sqrt{\Delta_{ge}\chi_{ge}}/2\pi = 119$ MHz.

Using $\chi_{ef}/2\pi = 21.1$ MHz as extracted from the cavity spectroscopy, and the $|e\rangle \leftrightarrow |f\rangle$ transition, I can similarly find $\Delta_{ef}/2\pi \approx 1.23$ GHz and $g_{ef}/2\pi \approx 160$ MHz. Here I assumed that the dressed $|e\rangle \leftrightarrow |f\rangle$ transition was shifted from the bare transition by the same amount as the $|g\rangle \leftrightarrow |e\rangle$ transition. More accurate estimates would require numerical calculation of the eigenvalues of the generalized Jaynes-Cummings Hamiltonian with additional levels [236].

As discussed in Section 6.1, the anharmonicity $(\omega_{ge} - \omega_{ef})/2\pi$ in a transmon is given by E_C. From the spectroscopy, I find $E_C/h = 213$ MHz. Using $\hbar\omega_{ge} = \sqrt{8E_J E_C} - E_C$, I can then extract $E_J/h = 16.6$ GHz. The values of E_J and E_C, as well as the coupling strength g_{ge} were within or very close to the range of expected values as discussed in Section 7.1.

The fact that I observed the $|e\rangle \leftrightarrow |f\rangle$ peak with standard qubit spectroscopy was initially unexpected. This suggested that there was a significant background

$|e\rangle$ state population at base temperature when no optical illumination was applied. This was evident in both the qubit spectrum and the cavity spectrum. The likely source was stray radiation hitting the cavity, similar to the effects I saw in Chapter 4. I note here that for the transmon measurements, the 4 K hot finger was not present, but there were other possible sources of background radiation, for example the still shield at 700 mK. I did not use any additional shielding schemes to reduce the effects of background radiation [45, 46]. Another possibility was that light in the cladding of the fiber, directly illuminating the transmon. A third possibility was that there was insufficient noise-filtering on the input and output microwave lines.

8.3.2 Peak Linewidths

In Fig. 8.4 the width of the qubit peak increased with increasing drive power. This effect is called power broadening. Additionally, the height of the peak also initially increased with increasing power, before saturating at highest powers. As I discussed in Section 6.6, due to decoherence a strong continuous drive at the qubit frequency will result in saturation at an excited state probability of 1/2.

The full-width half maximum (FWHM) of the qubit peak Δf is given by [130, 221]

$$\Delta f \;=\; \frac{1}{\pi T_2}\sqrt{1+\Omega_R^2 T_1 T_2} \;+\; \frac{1}{\pi T_2^\dagger}, \tag{8.2}$$

where T_1 is the relaxation time, T_2 is the coherence time, $T_2^\dagger$ is the inhomogenous broadening time, and Ω_R is the Rabi oscillation frequency. Ω_R is related to the applied qubit drive power P_q by $\Omega_R \propto \sqrt{P_q}$. The inhomogenous broadening time $T_2^\dagger$

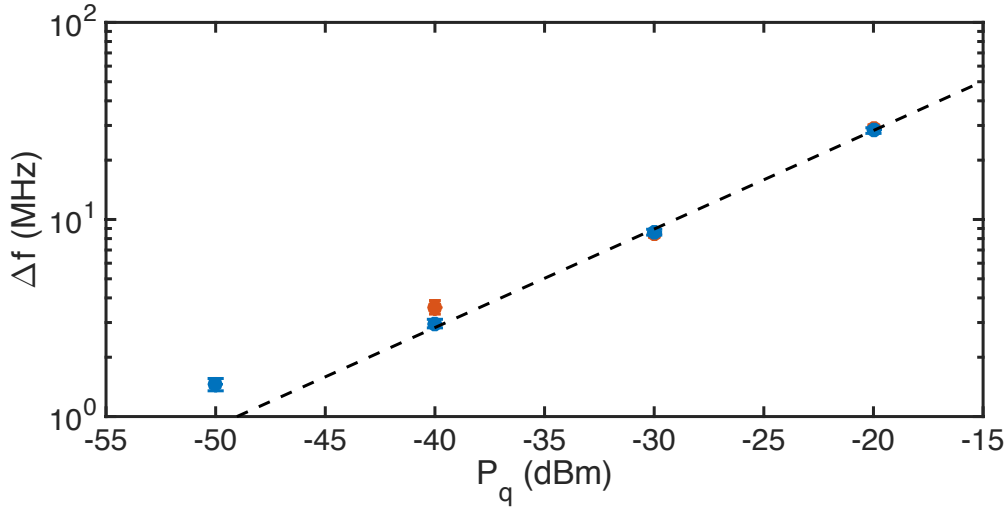

Figure 8.5: Qubit peak linewidth Δf vs qubit drive power P_q for $\tilde{\omega}_{ge}/2\pi$ peak (blue dots) and $\tilde{\omega}_{ef}/2\pi$ (red dots). The black dashed line shows the expected behavior in the limit of high drive power.

is related to low frequency fluctuations. At low powers $\Omega_R^2 \ll 1/T_1T_2$, the FWHM is

$$\Delta f \;=\; \frac{1}{\pi T_2} + \frac{1}{\pi T_2^{\dagger}} \;\equiv\; \frac{1}{\pi T_2^*}. \tag{8.3}$$

T_2^* is defined as the spectroscopic coherence time, and is the lower limit of T_2. At high powers $\Omega_R^2 \gg 1/T_1T_2$, the FWHM becomes $\Delta f \approx \Omega_R\sqrt{T_1/T_2} \propto \sqrt{P_q}$.

I fit the $\tilde{\omega}_{ge}/2\pi$ and $\tilde{\omega}_{ef}/2\pi$ qubit resonances at different P_q values to a Lorentzian. I did not take many measurements of the qubit spectrum at different P_q during the second session, but Figure 8.5 shows the extracted linewidth for the data I acquired. At high powers, Δf for both $\tilde{\omega}_{ge}/2\pi$ and $\tilde{\omega}_{ef}/2\pi$ peaks appeared to have the same width. I also compared the extracted widths to the expected Δf dependence for high powers (black dashed line), and they showed good agreement. At the lowest powers, Δf values were higher than the black dashed lines as would

be expected. The lowest measured linewidth of $|g\rangle \leftrightarrow |e\rangle$ transition was about 1.5 MHz at $P_q = -50$ dBm. This gave a lower limit of T_2 of 210 ns, which turned out to be much shorter than $2T_1$. This is consistent with a large contribution from inhomogenous broadening or dephasing

8.3.3 Photon Number Peaks

As I discussed in Chapter 6, when there are n rf photons inside the cavity, the dressed qubit frequency is shifted from the zero photon peak by $2n\chi/2\pi$ (see Eq. 6.33). For a distribution of rf photons, multiple photon peaks can be observed. For a coherent drive with average photon number $\bar{n}$, the expected probability distribution of the peaks follows a Poisson distribution [200].

To observe the photon number peaks, I applied a continuous tone using an additional microwave source set at the dressed cavity frequency of $\tilde{\omega}_{r,g}/2\pi = 6.1407$ GHz ('cavity pump'), while performing qubit spectroscopy with $P_q = -40$ dBm. Figure 8.6 shows spectra taken at three different cavity pump powers P_c. I compare the data with a Poisson distribution of photon peaks (red curves), using the extracted width of 1.4 MHz and $n = 0$ frequency from the previous section. I then varied $\bar{n}$ and χ to find best agreement. I found $2\chi/2\pi \approx 6.3$ MHz, slightly smaller than the value of 6.7 MHz I extracted from cavity spectroscopy. This value of χ gave slightly higher $\chi_{ef}/w\pi \approx 21.5$ MHz and thus g_{ef} as well. I note here that the periodic artifacts in the homodyne measurements I discussed in Section 8.1 resulted in an apparent 6 to 7 MHz periodic structure in some spectra, comparable to χ/π

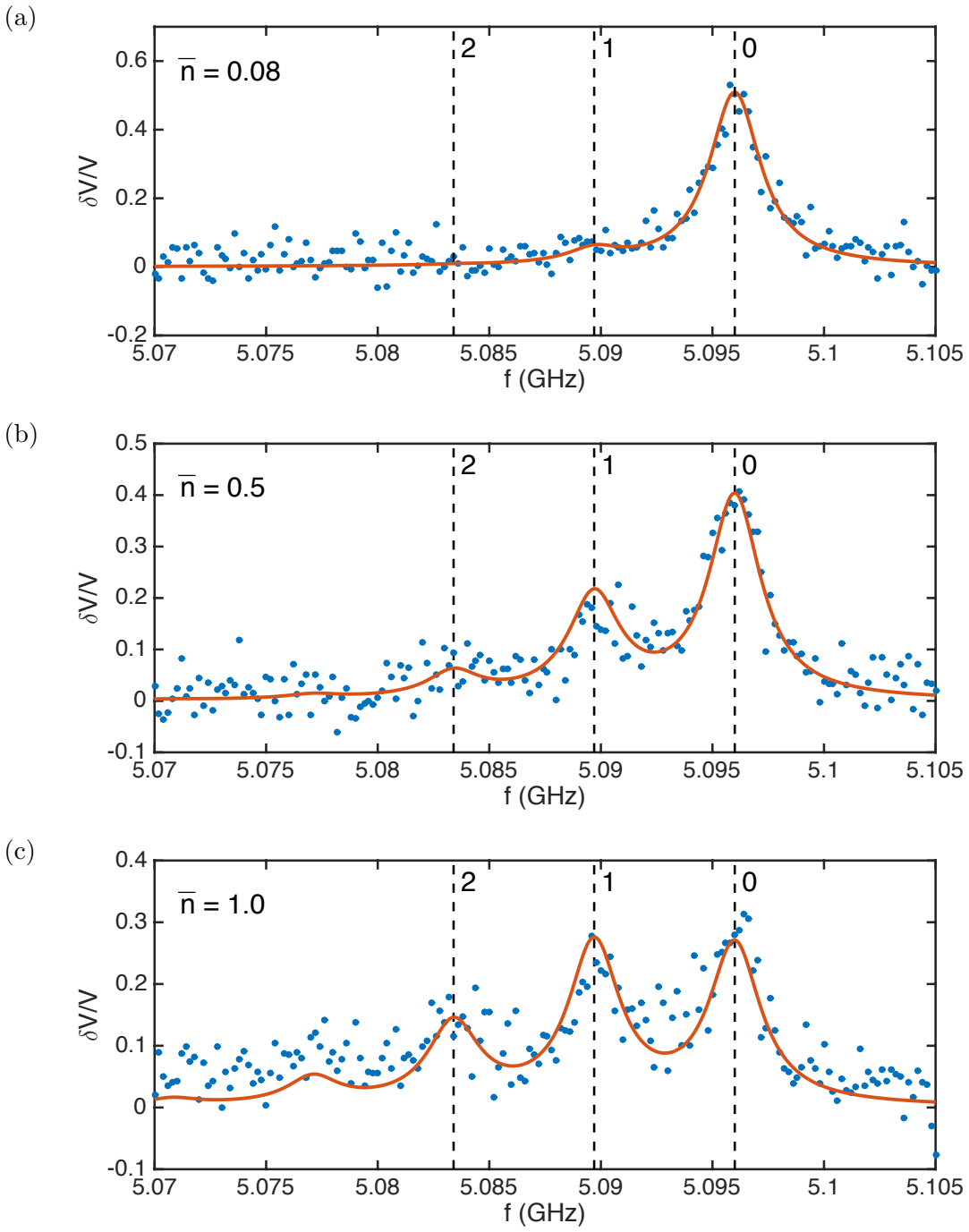

Figure 8.6: Measured (blue dots) and fit (red curves) photon number peaks in qubit spectrum for coherent distributions with average photon number (a) $\bar{n} \approx 0.08$ for no applied drive, (b) $\bar{n} \approx 0.5$ for P_c = -40 dBm, and (c) $\bar{n} \approx 1.0$ for P_c = -35 dBm.

which made it difficult to extract $\bar{n}$.

In Fig. 8.6(a) I plot the qubit spectrum when no cavity pump was applied. I observed a presence of a small 1-photon peak, corresponding to a background photon population of $\bar{n} \approx 0.08$. This suggested an 8% background probability of the cavity in the 1-photon state. Some possible causes of this background probability were a higher cavity temperature than base temperature due to imperfect thermalization, the presence of the background radiation increasing the effective temperature of the cavity (see Section 4.2.3), or insufficient filtering of the noise on the input and output microwave lines. These are the same possible causes of the qubit's background excited state populations. An the two populations are similar. Assuming a Boltzmann distribution, an 8% 1-photon state probability corresponds to temperature of $T \approx 120$ mK for a 6.14 GHz resonance.

For higher cavity pump powers (see Fig. 8.6(c)), the position of the higher number photon peaks, as well as the relative distributions, appeared to deviate somewhat from the simplified low-power Jaynes-Cummings model. More sophisticated models that include higher states of the qubit and higher order nonlinearities [201] may be needed to explain this behavior.

8.4 Characteristic Time Measurements

8.4.1 Rabi Oscillation

Figure 8.7 shows the typical $\delta V/V$ vs pulse length results of Rabi oscillation measurements. While I observed an oscillation with an amplitude that decayed with

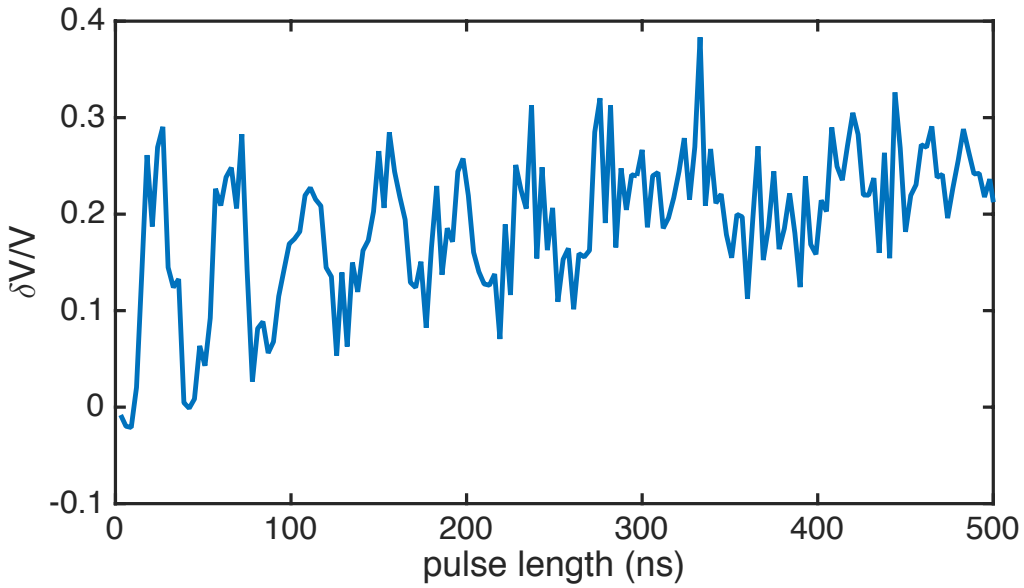

Figure 8.7: $\delta V/V$ vs qubit pulse length for a typical Rabi oscillation driven at frequency $\tilde{\omega}_{ge}$. The Rabi oscillation appears to be very distorted and the saturation level of $\delta V/V \approx 0.25$ appears to be far above the 50% population of $\delta V/V \approx 0.15$.

time, it did not look like one expects. In particular, as the oscillation decayed away, the output appeared to saturate at higher than 50%. Comparing the saturation point in the 0.5 to 1 μs range with the saturated spectrum levels after a 100 μs pulse, the saturation point appeared to also slowly increased from $\delta V/V \approx 0.25$ at 0.5 μs to $\delta V/V \approx 0.5$ at 100 μs.

The reasons for this unusual looking oscillation were unclear. One possibility is that I ended up exciting higher levels in the qubit. It was possible that this may have been caused by imperfect pulse shape, as I used the internal gating from the sources instead of a dedicated board for optimal pulse shaping. Imperfect qubit pulse shape may cause leakage to higher excited states [237]. Sudeep Dutta and I checked the shape of the pulses using a Tektronix TDS8000B fast oscilloscope [238] and found that the pulses from the source had a rise time of about 3 to 5 ns without a noticeable overshot. This was much less than the apparent Rabi period. However, this is so short it may have caused significant spectral broadening of the pulse, which could have led to higher-level qubit transitions. This suggested that the pulse may well have been the cause of the unusual oscillation. Another possible reason was that this qubit appears to have a non-negligible background $|e\rangle$ state population as observed in the spectroscopy, where $e \rightarrow f$ transition peak height is comparable to $g \rightarrow e$ transition peak height (see Fig. 8.4). This would have reduced the fidelity of the Rabi oscillation behavior.

Even though the unusual oscillation made it hard for me to extract the relevant Rabi oscillation parameters, I observed that when I varied the qubit drive power, the apparent Rabi oscillation frequency roughly followed the expected dependence

on power $\Omega_R \propto \sqrt{P}$, as discussed above. Additionally, if I assumed the envelope of the oscillation still follow an $e^{-t/T'}$ dependence, I could extract a rough value for the Rabi decay time of $T' = 300$ to 400 ns.

I observed similarly unusual Rabi oscillations at all temperatures and illumination intensities.

8.4.2 Qubit Relaxation

As the Rabi oscillation was unusual, as described in the previous subsection, it was somewhat hard to set the proper timing for a π or $\pi/2$ pulse. Instead for the qubit relaxation measurements, I measured qubit relaxation from the saturated state after a 50 μs long qubit pulse. This should have left the device in a 50-50 mixed state of $|g\rangle$ and $|e\rangle$. However, it is possible that the system was left with a small population of higher level qubit states such as $|f\rangle$. A typical $\delta V/V$ vs measurement delay time result is shown in Figs. 8.8. Here I used $P_q = -30$ dBm. The data points with negative time meant the measurement pulse started before the qubit drive pulse ended, and below I fit starting from a time when I started observing a rapid decrease in $\delta V/V$, which occurred around -0.2 μs.

As seen in Fig. 8.8(b), a semi-log plot of $\delta V/V$ vs delay time is not a straight line and thus P_e did not follow an exponential dependence of. Instead, it looked like there were two exponential timescales, a short exponential timescales for approximately the first 1 μs, and a longer timescale after that. Thus I tried fitting the

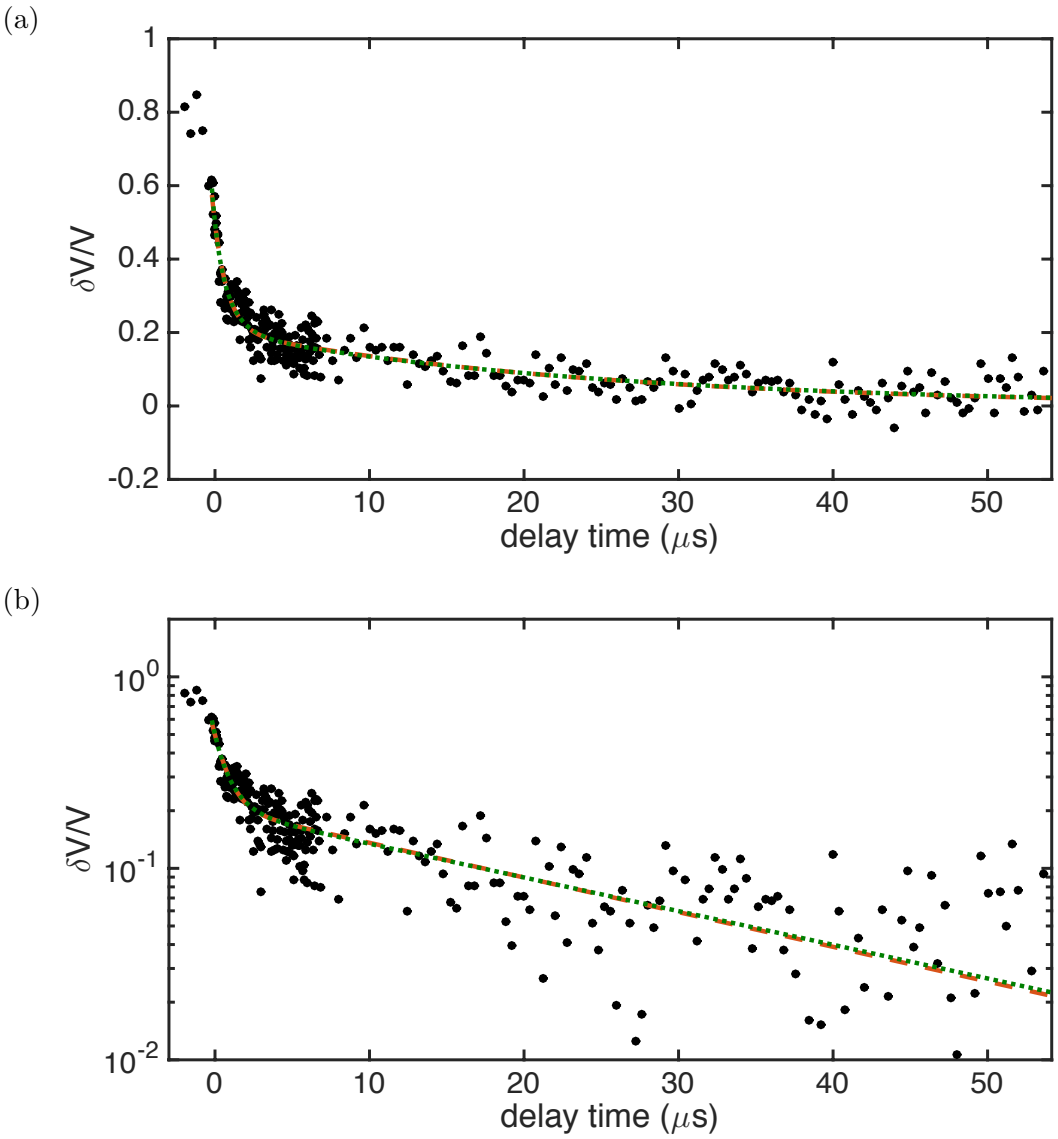

Figure 8.8: (a) Linear plot and (b) semilog plot of $\delta V/V$ vs delay time for typical relaxation measurements. Curves show fit to two models: red dashed curves are sum of two exponentials as in Eq. 8.4 and green dotted curves are quasiparticle fluctuation model as in Eq. 8.5.

decay to a sum of two exponentials

$$\frac{\delta V}{V}(t) \;=\; Ae^{-t/T_1} \;+\; A'e^{-t/T_1'}, \tag{8.4}$$

where A and A' are the exponential decay amplitudes, T_1 the longer decay time, and T_1' the shorter decay time. The red dashed curve in Fig. 8.8 shows this fit, with $T_1' = (0.86 \pm 0.08)$ μs and $T_1 = (24.0 \pm 2.0)$ μs. Eq. 8.4 would be roughly what one expects if there is a small probability to be in a higher level qubit state ($|f\rangle$ and higher) which is detected with high visibility but decays rapidly. With this interpretation, T_1 is the lifetime of the excited state of the qubit and T_1' is the lifetime of the higher levels.

Recently Pop *et al.* reported observation of a similar nonexponential decay in their long-lived 3d fluxonium qubit [23]. They attributed this behavior to fluctuations in the number of quasiparticle within the superconducting islands between the Josephson junctions in their junction array. They fit the decay to the expression

$$P_e(t) \;=\; A \exp\left[\lambda\left(e^{-t/T_{1,q}} - 1\right)\right] e^{-t/T_{1,r}}, \tag{8.5}$$

where A is the decay amplitude, λ is the average number of quasiparticle in the islands, $T_{1,q}$ is the relaxation time from a single quasiparticle, and $T_{1,r}$ is the relaxation time from other sources of dissipation.

Unlike fluxonium, my transmon did not have superconducting islands. Nevertheless, I fit Eq. 8.5 to the nonexponential decay in my device. Although the superconducting volume of the transmon would be too high to have only a few quasiparticles at one time, it could be plausible to have only a few tunnel through the junction at one time. Attempting to fit the data in Fig. 8.8 to Eq. 8.5 (green

dotted curves) gave $\lambda = (0.91 \pm 0.05)$, $T_{1,q} = (1.22 \pm 0.14)$ μs, and $T_{1,r} = (24.7 \pm 2.1)$ μs. Comparing the fits to Eqs. 8.4 and 8.5, the two curves are indistinguishable within the fit region in Fig. 8.8 and the shirt and long time constants from each fit are comparable. For the subsequent relaxation measurements, unless noted, I will fit only to Eq. 8.5.

I note here that I performed relaxation measurements from the saturated state at 10 mK with no applied optical powers multiple times. I always observed the nonexponential behavior and the extracted decay times were quite repeatable, with fluctuations comparable to the error. This was in contrast to the results by Pop *et al.*, who observed a nonexponential behavior and an exponential behavior for identical measurements separated by several days [23].

I also attempted to perform relaxation measurements using 50 μs qubit pulses with weaker drive powers such that the saturation level was lower than the "50-50 saturation". When the level was high enough such that I could observe the relaxation behavior, I also found nonexponential behavior with similar decay times. For example, in Fig. 8.9, I showed two relaxation measurements. The black dots correspond to $P_q = -30$ dBm (the same data as Fig. 8.8) and the blue dots correspond to $P_q = -45$ dBm. For the lower power dataset, I extracted $\lambda = (0.95 \pm 0.07)$, $T_{1,q} = (1.40 \pm 0.21)$ μs, and $T_{1,r} = (27.4 \pm 3.3)$ μs, which are very similar to the higher power numbers.

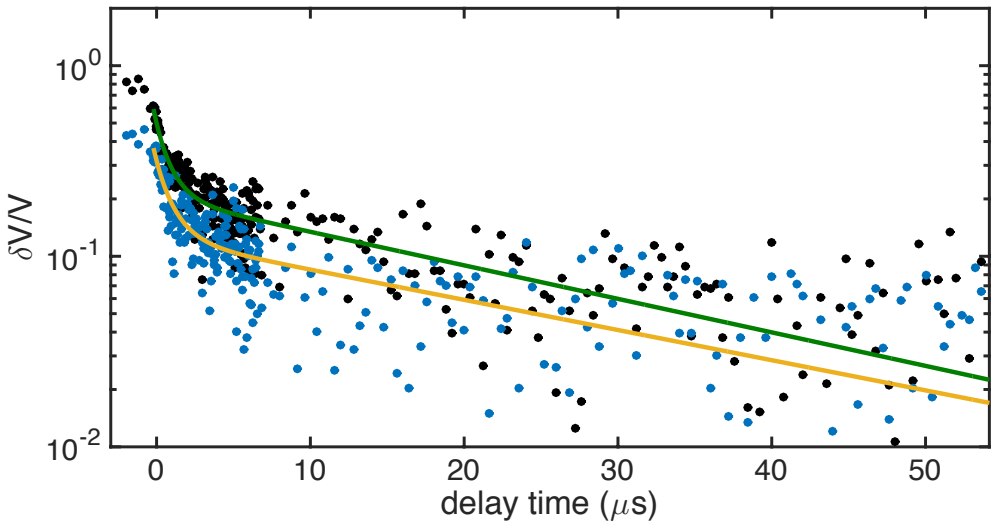

Figure 8.9: Comparison of two relaxation measurements with different qubit drive powers. Black dots are data for $P_q = -30$ dBm with the green curve the fit to data, and blue dots are data for $P_q = -45$ dBm with yellow curve showing the fit to data. For both fit curves, I used Eq. 8.5.

8.5 Illumination Dependence

8.5.1 Measurement Details

For each illumination intensity $I_{\rm opt}$, I performed qubit spectroscopy measurements at several qubit drive powers, as well as Rabi oscillation and relaxation measurements. As mentioned in the previous section, I mainly focused on the relaxation measurements because the Rabi oscillation results looking unusual (see Fig. 8.7). I note that for each $I_{\rm opt}$ value, I typically had to adjust the measurement rf power to find the best $\delta V/V$; I found that I had to increase $P_{\rm rf}$ slightly with increasing $I_{\rm opt}$, from -5 dBm for $I_{\rm opt} = 0$ to -2 dBm at maximum $I_{\rm opt}$.

The range of optical powers I used was between 0.12 nW and 25 nW after the ND filters were taken into account. This corresponded to optical intensities $I_{\rm opt}$ between 4.3 and 860 aW/μm^2 incident on the resonator. The power from the laser could drift, and most of the optical powers I used were smaller than the resolution of the power meter, which was about 1 nW. To check for drifts in the optical power I used the same method I used in the resonator measurements (see Section 5.2.1) which involved measuring the optical power without the ND filters before and after a set of qubit measurements. If the power had drifted by 20% or more, I retook that set. I had to do this several times during the cooldown. For the highest optical powers (above 5 nW) I used, the power were resolvable by the power meter, which meant I could check the power in real time during measurements.

I also observed that the frequency lock on the laser jumped to a different

position two or three times over the approximately 2 weeks I took optical data on the transmon. Although the lock jumped, I did not observe a significant power change after the jumps. The cause of the lock jump was unclear, but probably due to temperature or humidity changes in the lab or laser setup.

8.5.2 Qubit Spectroscopy

For each I_{opt}, I typically performed qubit spectroscopy at two qubit rf drive powers P_q. For lower I_{opt} values, typically these were P_q = -50 dBm and -40 dBm. For higher I_{opt} values, as the peaks became broader it became harder to observe a qubit peak at these values, and I had to use higher P_q values. For the highest intensity I_{opt} = 860 aW/μm^2, I used P_q = -30 dBm and -20 dBm. The peaks observed at these measurements were the dressed qubit peak $\tilde{\omega}_{ge}/2\pi$.

I fit the qubit spectra to a Lorentzian and extracted the frequency and linewidth of the peak. Figure 8.10(a) shows the extracted $\tilde{\omega}_{ge}/2\pi$ frequencies as a function of I_{opt}. The frequency roughly decreased with increasing I_{opt} as expected. At the highest optical intensity the frequency shifted down by about 5 MHz from the $I_{\text{opt}} = 0$ value, corresponding to $\delta\omega_{ge}/\omega_{ge} \approx -10^{-3}$. However, when I zoomed in at low I_{opt} values (see Fig. 8.10(b)), I found that the frequency appeared to increase with increasing I_{opt} at the lowest I_{opt} values. From $I_{\text{opt}} = 0$ to about 10 aW/μm^2, $\tilde{\omega}_{ge}/2\pi$ increased by about 250 kHz ($\delta\omega_{ge}/\omega_{ge} \approx 5 \times 10^{-5}$) before starting to decrease at about 15 aW/μm^2. While the increase was only slightly higher than the error bars, it appeared to be systematic with I_{opt}, suggesting that this increase was real instead

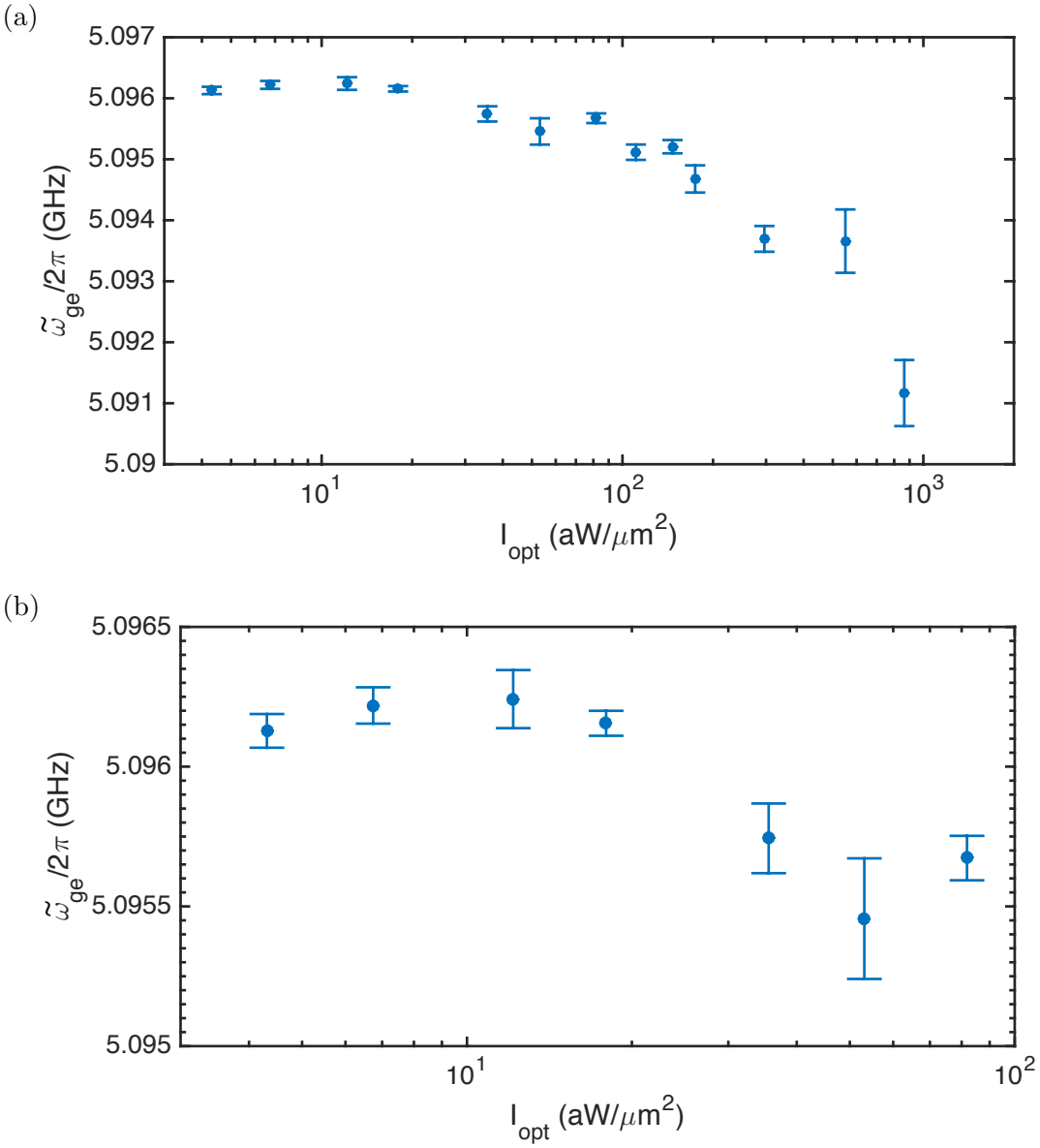

Figure 8.10: (a) Extracted dressed qubit frequency $\tilde{\omega}_{ge}/2\pi$ from fit vs optical intensity I_{opt} at 10 mK. (b) Detailed view of (a) showing $\tilde{\omega}_{ge}/2\pi$ at low I_{opt} values.

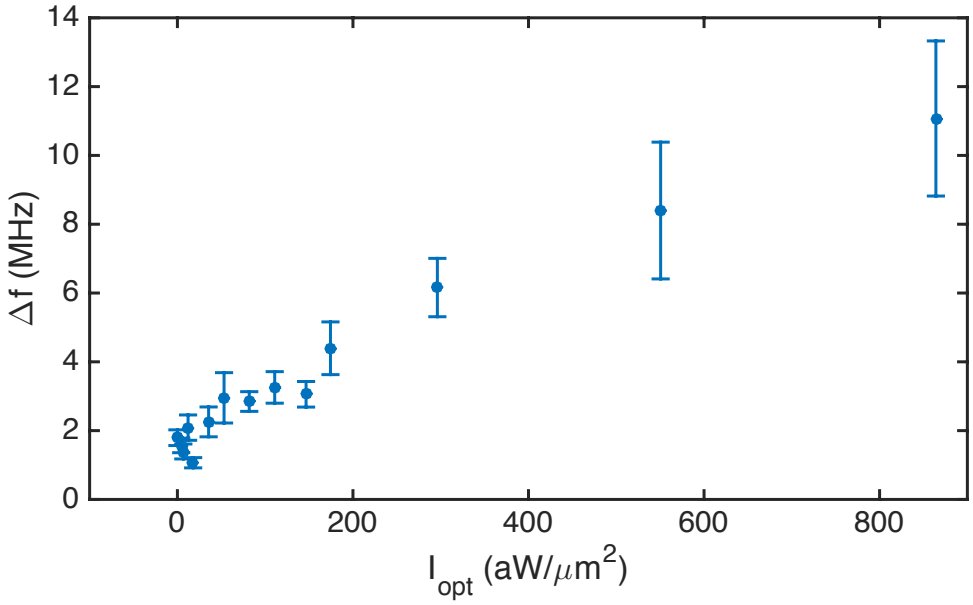

Figure 8.11: Extracted qubit peak linewidth Δf vs $I_{\rm opt}$ at 10 mK.

of from random scatter in the data.

Figure 8.11 shows the extracted peak FWHM vs $I_{\rm opt}$. Similar to the frequency, the linewidth appeared to initially decrease with increasing $I_{\rm opt}$, reaching a minimum of $\Delta f \approx 1.1$ MHz at $I_{\rm opt} \approx 20$ aW/μm^2 and increased with increasing $I_{\rm opt}$ afterwards, with $\Delta f \approx 11$ MHz at the highest $I_{\rm opt}$. I note here that for the qubit drive powers P_q that I used, none of the peaks were saturated at the long-time pulse 50-50 value, there might have been some power broadening in the linewidths.

I note here that I did not observe evidence of photon number peaks in the spectrum when optical illumination was applied to the transmon. For example, in Fig. 8.12 I show a qubit spectrum taken for $P_q = -30$ dBm and $I_{\rm opt} = 300$ aW/μm^2, along with the fit from which I extracted $\tilde{\omega}_{ge} = 5.0937$ GHz and $\Delta f = 6.2$ MHz. Since $\chi/\pi \approx 6.3$ MHz, the first photon peak would be at 5.0874 GHz and would

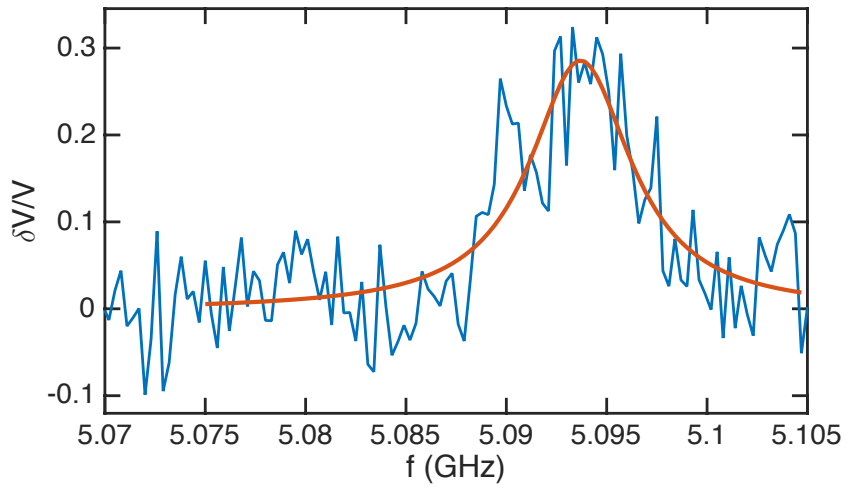

Figure 8.12: Qubit spectrum for $P_q = -30$ dBm and $I_{\text{opt}} = 300$ aW/μm^2. Blue curve is data, red curve is fit of data to a Lorentzian.

result in an asymmetric peak. The peak appeared quite Lorentzian, but of course there was also significant scatter and a small peak could have been present at 5.0874 GHz. I note that the optical illumination mainly illuminated the transmon which had a very small volume and the power levels were so low that one would not expect heating of the cavity with a much larger volume. Hence the fact that I did not see photon peaks made sense, as I did not expect the cavity's microwave photon distribution to be affected by the optical illumination at the power levels I used.

8.5.3 Relaxation Times

I performed qubit relaxation measurements for similar I_{opt} values as the ones used in the spectroscopy measurements in the previous section. For all optical intensities, I observed nonexponential behavior similar to the example discussed in

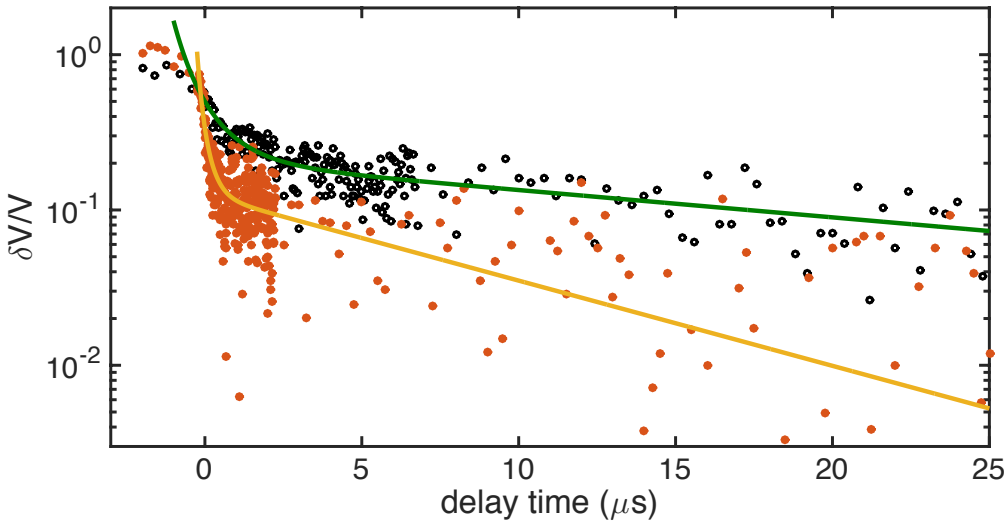

Figure 8.13: Comparison of two relaxation measurements with different optical intensities: Black dots are data for $I_{\rm opt} = 0$ with the green curve the fit to data, and orange dots are data for $I_{\rm opt} = 170$ aW/μm^2 with the yellow curve the fit to data.

Section 8.4.2. For example, in Fig. 8.13 I show $\delta V/V$ vs delay time for no optical illumination (the black points show same data that was discussed in Section 8.4.2) and for $I_{\rm opt} = 170$ aW/μm^2 (orange dots). Here both the long and short decay times for the illuminated case appeared shorter than those for the no illuminated case, as expected (see discussion in Section 6.7).

Figure 8.14 shows the fit parameters I extracted as a function $I_{\rm opt}$. The shorter relaxation time $T_{1,q}$ decreased with increasing $I_{\rm opt}$, from 1.2 μs to 0.2 μs at the highest $I_{\rm opt}$ (see Fig. 8.14(a)). The longer relaxation time $T_{1,r}$ also decreased with increasing $I_{\rm opt}$, from about 30 μs to 5 μs at the highest $I_{\rm opt}$ (see Fig. 8.14(b)). The average quasiparticle number λ was at about 0.9 for $I_{\rm opt} = 0$, initially increased with increasing $I_{\rm opt}$, up to a maximum of about 1.4 at $I_{\rm opt} \approx 30$ to 80 aW/μm^2, then

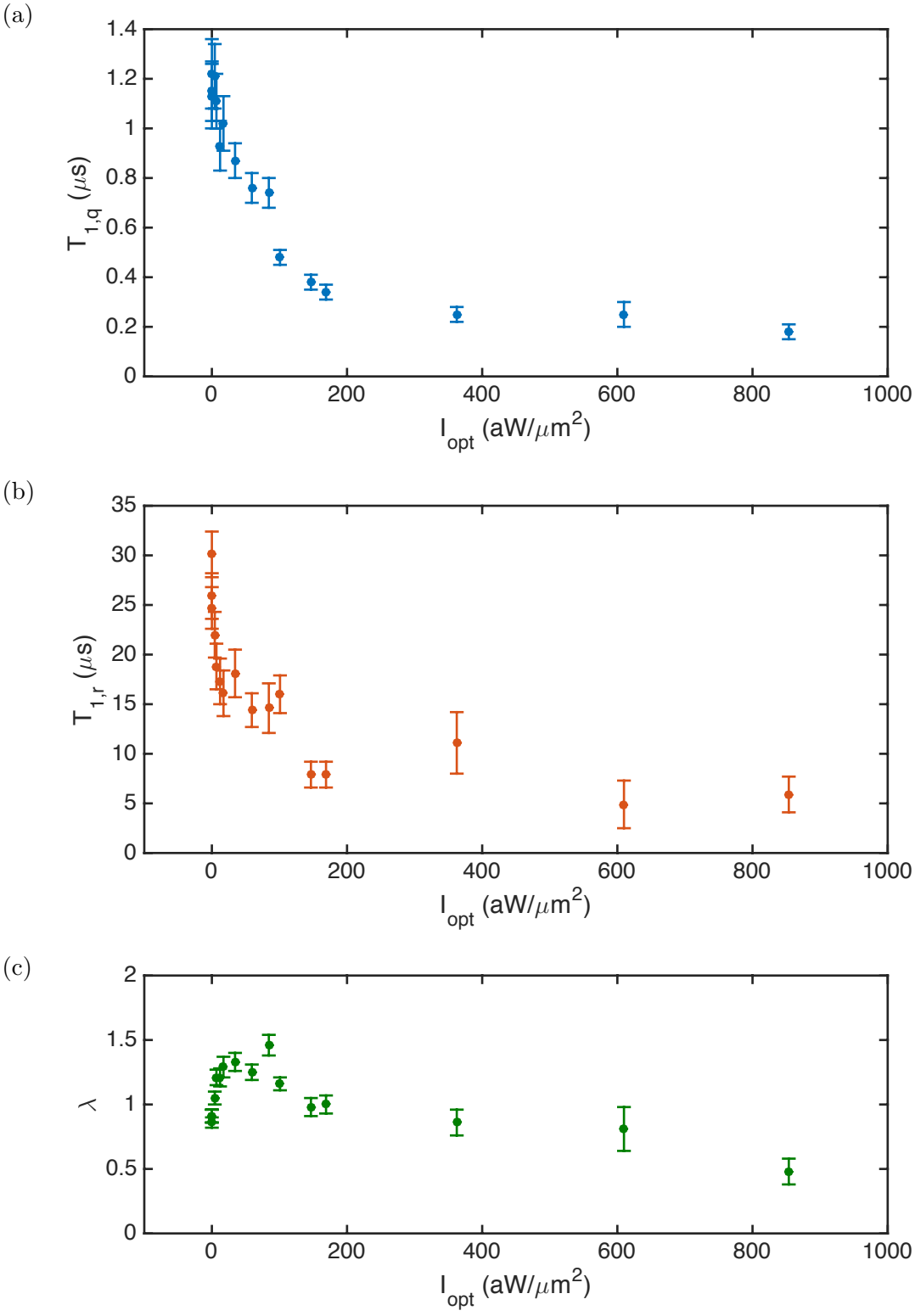

Figure 8.14: Extracted relaxation fit parameters vs I_{opt} showing (a) short relaxation time $T_{1,q}$, (b) long relaxation time $T_{1,r}$, and (c) average quasiparticle number λ parameter from fit to Eq. 8.5.

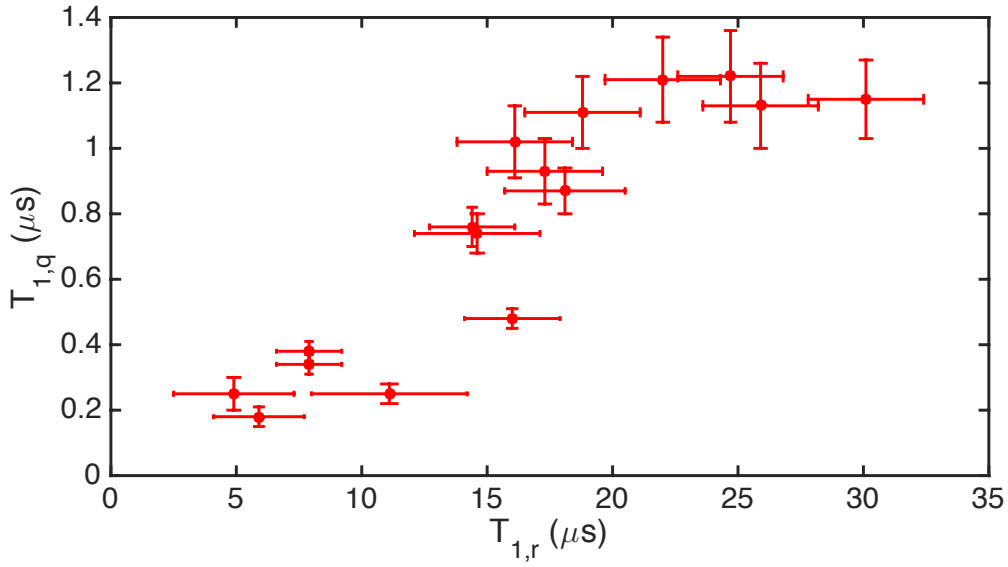

Figure 8.15: Extracted relaxation times $T_{1,q}$ vs $T_{1,r}$ for all optical intensities I_{opt}.

gradually decreased with increasing I_{opt} to 0.5 at maximum I_{opt} (see Fig. 8.14(c)). The intensity where λ was highest was comparable, if not exactly equal to the I_{opt} value where the qubit frequency $\tilde{\omega}_{ge}$ was highest in the spectrum. I note that this variation of λ with I_{opt} does not make good physical sense, suggesting that this may not be an appropriate model for my device.

As Figs. 8.14(a) and (b) show, the short and long the relaxation times have a similar dependence on I_{opt}. In Fig. 8.15 I plot $T_{1,q}$ vs $T_{1,r}$ for all data points in Figs. 8.14. It appears that $T_{1,q}$ increased with increasing $T_{1,r}$, roughly linearly, up to $T_{1,q} \approx 1.2$ μs and $T_{1,r} \approx 20$ μs. For $T_{1,r}$ values above 20 μs, $T_{1,q}$ may have flattened out at 1.2 μs.

8.5.4 Discussion of Illumination Dependence

If optical illumination only affected the loss and frequency of the qubit through quasiparticles, and the quasiparticle tunneling picture followed the simplified picture I described in Section 6.7, I would not expect the frequency to initially increase with increasing illumination. It is possible that extending the model to include different gaps on each side of the junction could reveal the cause of this behavior. As the transmon was operated at low rf photon numbers, dielectric loss from one or more TLSs might also have contributed significantly to the loss. The TLS effective temperature could increase with illumination, and as I discussed in Chapter 2, an increase in TLS temperature would result in an increase in resonance frequency and decrease in TLS loss. The fact that the average quasiparticle number parameter λ appeared to behave similarly to the qubit frequency suggests that it was possible the frequency behavior was due to quasiparticles. However, this model does not appear to be well-founded for my device and λ does not appear to correspond to quasiparticle number.

In the fitting model, $T_{1,q}$ was supposed to be the relaxation time due to quasiparticles and $T_{1,r}$ was supposed to be the relaxation time from other sources, not including quasiparticles. However, for most of the data, the two relaxation times appeared to behave similarly (see Fig. 8.15). This again suggests that this is not a physically reasonable model for my system. In contrast, much of the behavior makes sense if the fast exponential is due to the decay of a small population in higher levels while the slow decay is the decay of the state $|e\rangle$, as both rates would depend on

quasiparticle loss. λ may then be related to the initial relative populations of $|e\rangle$, $|f\rangle$, and higher level states.

8.6 Temperature Dependence

8.6.1 Measurement Details

Similar to the previous section, for each refrigerator temperature I performed qubit spectroscopy, Rabi oscillation, and relaxation measurements. While for the illumination measurements I had to adjust the cavity measurement rf powers to find optimal $\delta V/V$, for elevated temperatures this appeared to be unchanged, and I used -5 dBm for all temperatures.

The range of temperatures I used was between 10 mK and 265 mK. At 235 mK I also performed the same set of measurements with several applied optical powers, and for these I had to adjust the cavity rf powers for each $I_{\rm opt}$. The results from these optical measurements are discussed separately in Section 8.6.4 below.

8.6.2 Qubit Spectroscopy

For each temperature, I typically measured the qubit spectrum at two or three different qubit drive powers. I fit the spectra for the lowest power where the qubit peak was visible. For the highest temperatures, the qubit peaks became asymmetric, wider on the low frequency side (see Fig. 8.16 for example). This was consistent with the presence of cavity photon number peaks, as for a thermal distribution at

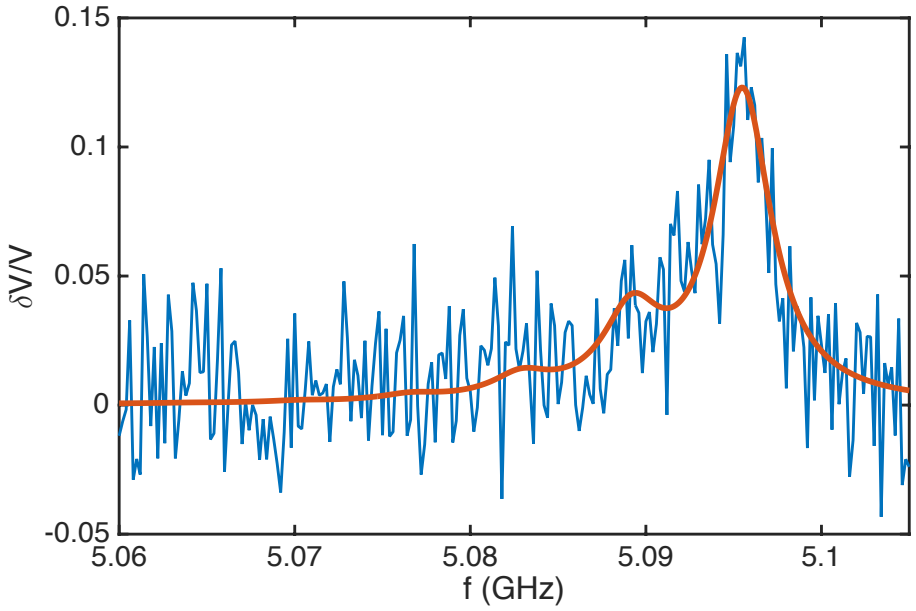

Figure 8.16: Asymmetric qubit spectrum at 220 mK due to thermal cavity photon peaks. Blue curve is the spectrum data, red curve is spectrum fit to thermal distribution of photon number peaks at 220 mK.

temperature T, the probability $P(n)$ to find n photon in the cavity is given by

$$P(n) = \frac{e^{-n\hbar\tilde{\omega}_{c,g}/k_BT}}{1 - e^{-\hbar\tilde{\omega}_{c,g}/k_BT}}, \tag{8.6}$$

where the denominator is the normalization factor, and the cavity is at the dressed frequency $\tilde{\omega}_{c,g}/2\pi$. When the peak appeared asymmetric, I fit the spectra to the sum of the photon peaks with distribution given by Eq. 8.6 and a temperature equal to the refrigerator temperature (solid red line in Fig. 8.16). I assumed $\chi/\pi = 6.3$ MHz as in the photon peak measurements, and varied $\tilde{\omega}_{ge}$ and Δf. For example, in Fig. 8.16 I have $\tilde{\omega}_{ge}/2\pi = 5.0955$ GHz and $\Delta f = 4$ MHz. The resulting fits were typically in good agreement with the data. However, I varied the parameters by hand, the spectra at the highest temperatures were very noisy, the parameters were rough estimates, and I didn't attempt to find the uncertainty values for these parameters.

Figure 8.17(a) shows the dressed qubit frequency $\tilde{\omega}_{ge}/2\pi$ and Fig. 8.17(b) shows the linewidth, both as a function of refrigerator temperature. In both plots, blue dots are fit of the spectrum to a single Lorentzian peak and red circles were from thermal photon peak fit. In both plots, the two dots at 220 mK were from two fits to the same spectrum, hence both fit methods appeared to agree quite well at least at 220 mK.

In Fig. 8.17(a), $\tilde{\omega}_{ge}/2\pi$ appeared to slightly increase with increasing temperature, up to a maximum of about 5.0965 GHz at 100 mK, before decreasing with increasing temperature. At 265 mK, $\tilde{\omega}_{ge}/2\pi$ was at about 5.0945 GHz ($\delta\omega_{ge}/\omega_{ge} \approx 3 \times 10^{-4}$). In Fig. 8.17(b), Δf initially decreased with increasing tem-

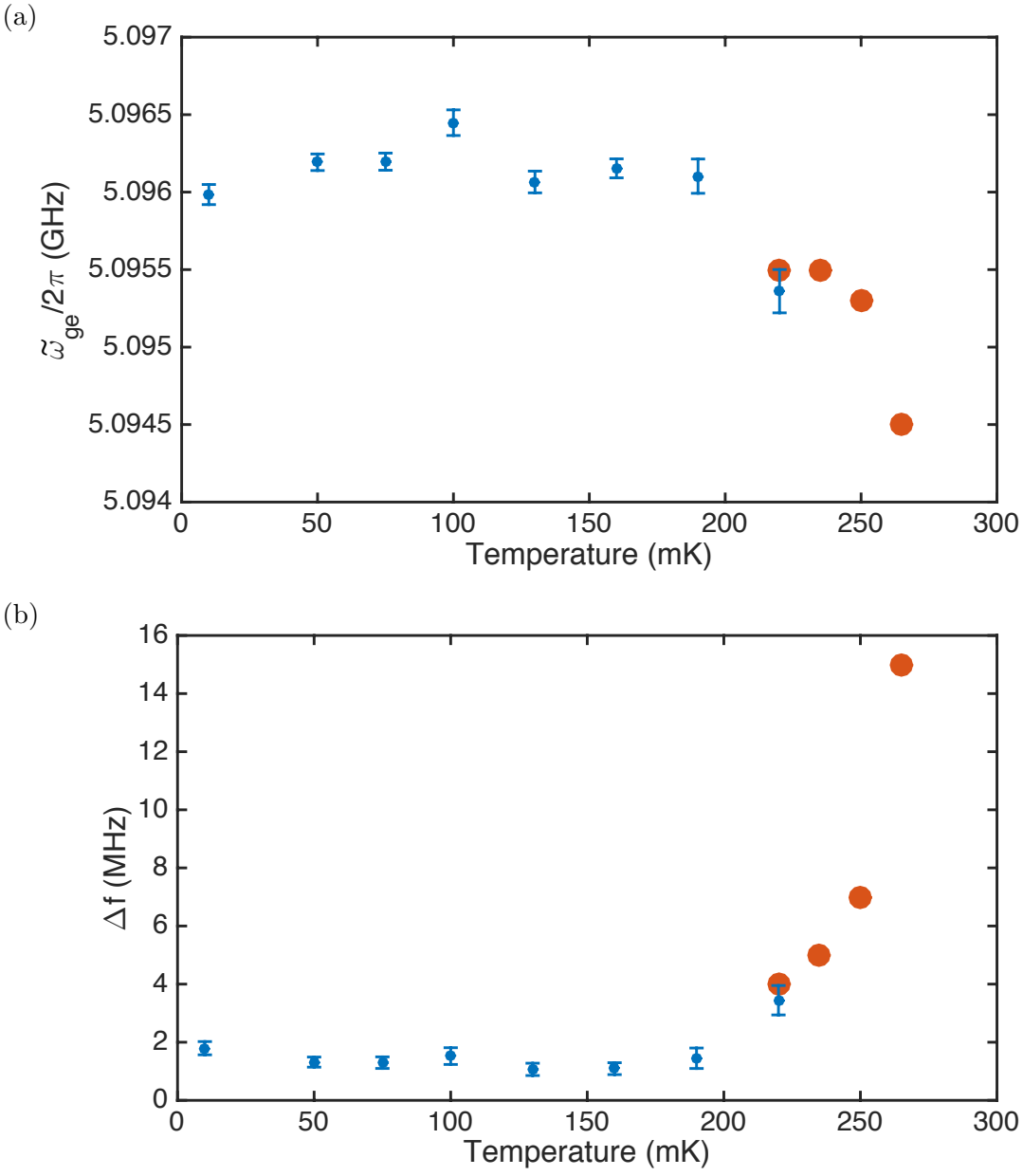

Figure 8.17: (a) Dressed qubit frequency $\tilde{\omega}_{ge}/2\pi$ vs refrigerator temperature.(b) Qubit linewidth Δf vs refrigerator temperature. For both plots, blue dots are fit to single Lorentzian peak and orange circles were from thermal photon peak fit. The orange and blue dots at 220 mK were from the same spectrum.

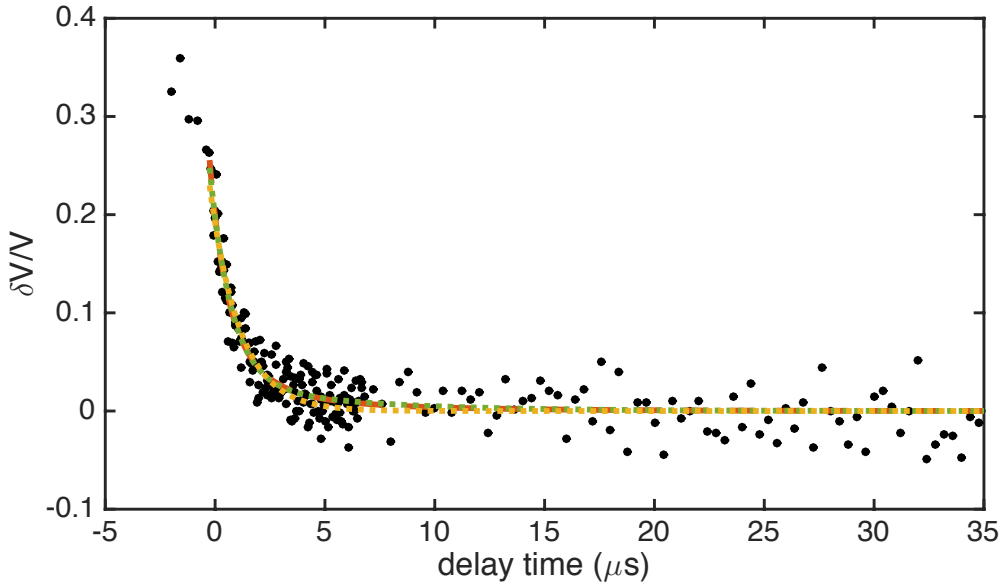

Figure 8.18: $\delta V/V$ vs pulse delay time of a relaxation measurement at 160 mK (black dots) as well as fit to single exponential decay (yellow curve), sum of two exponentials as in Eq. 8.4 (red dashed curve), and quasiparticle fluctuation model as in Eq. 8.5 (green dotted curve).

perature, with the minimum width of around 1.1 MHz reached at about 150 mK. Above 150 mK, Δf increased with increasing temperature, with $\Delta f \approx 15$ MHz at 265 mK. I note here that the maximum Δf in the temperature measurements was comparable or even larger than the maximum Δf in the illumination measurements, but the maximum frequency shift $\delta\omega_{ge}/\omega_{ge}$ in the temperature measurements was only about 1/3 of the maximum shift in the illumination measurements.

8.6.3 Relaxation Times

For refrigerator temperatures of 130 mK and lower, I observed a nonexponential relaxation behavior similar to the base temperature meaurements, and the

relaxation could be fit well to Eq. 8.5. However, the uncertainties in the fit parameters grew with increasing temperatures as well (see Figs. 8.19 below).

For 160 mK and above, the relaxation curves fit well to Eq. 8.4 and 8.5 but the parameters had significant uncertainties. For example, Fig. 8.18 shows a plot of $\delta V/V$ vs pulse delay time for a relaxation measurement at 160 mK. I fit the data to Eqs. 8.4 (red curve) and 8.5 (green curve). The fit curves appeared to agree well with the data and with each other, but the extracted parameters had significant uncertainties, with $T_1' = (0.99 \pm 0.49)$ μs and $T_1 = (5.8 \pm 4.5)$ μs for Eq. 8.4 and $T_{1,q} = (3.0 \pm 2.1)$ μs, $T_{1,r} = (6.6 \pm 11.5)$ μs, and $\lambda = 2.5 \pm 2.3$ for Eq. 8.5. I also fit the data in Fig. 8.18 to a single exponential decay. This also appeared to fit quite well with $T_1 = (1.37 \pm 0.07)$ μs and the uncertainty in T_1 is reasonable. For even higher temperatures, the single exponential fit the data well. This difficulty is what one would expect if one tries to fit a double-exponential decay to a curve with a single exponential decay.

Figure 8.19 shows the extracted fit parameters from relaxation measurements at different temperatures. For 130 mK and below, I fit the results to Eq. 8.5, while for above 130 mK, I fit to a single exponential decay with decay time T_1. As discussed above, the uncertainties in the extracted fit values, grew with increasing temperature. Nevertheless, although the scatter is large, $T_{1,q}$ appeared to increase with increasing temperatures up to 130 mK where I switched to a single exponential fit (see Fig. 8.19(a)). Above 130 mK, T_1 appeared to initially follow $T_{1,q}$ with $T_1 \approx 1.5$ μs but decreased with increasing temperature to $T_1 \approx 300$ ns at 265 mK (see Fig. 8.19(a)).

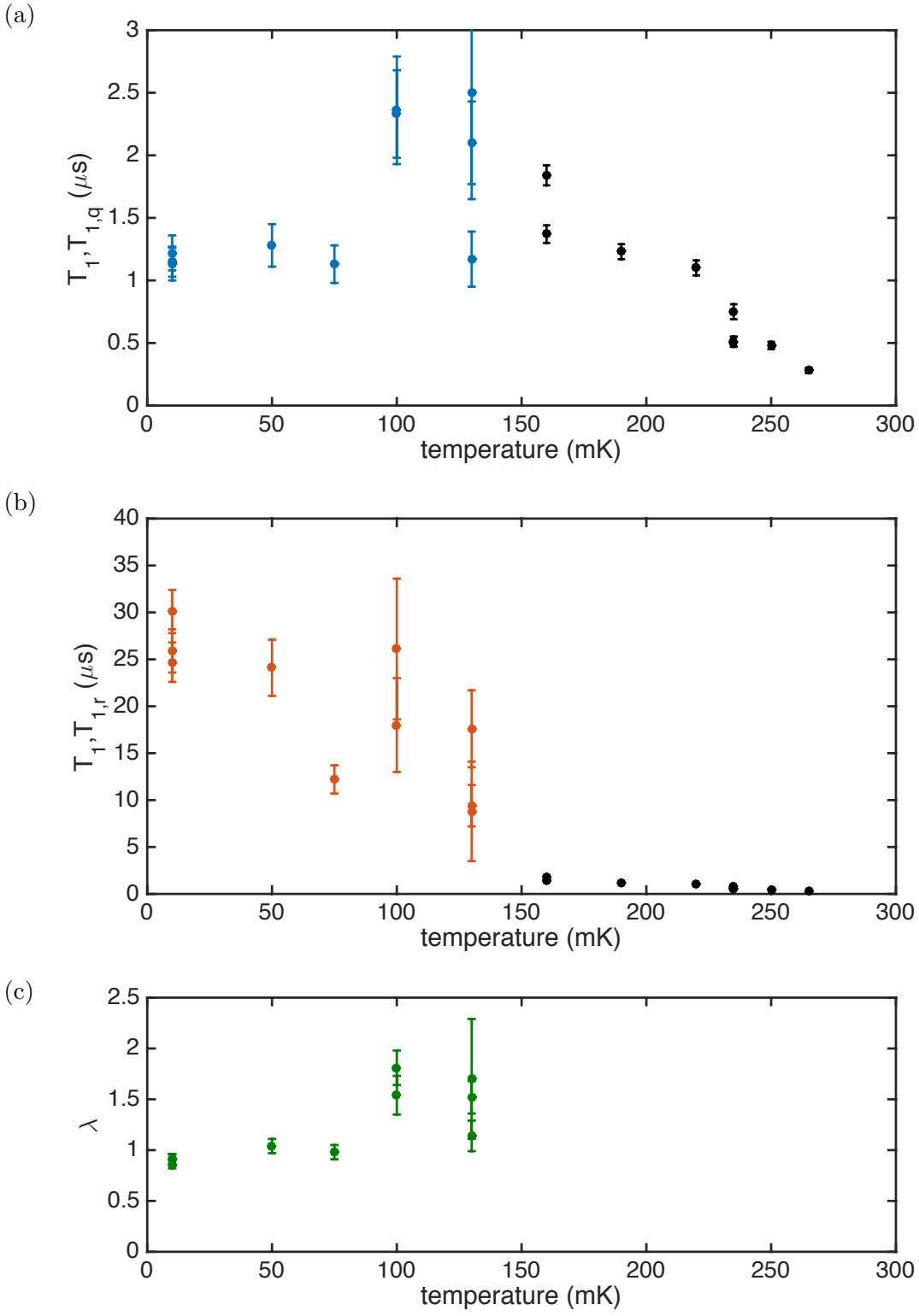

Figure 8.19: Extracted relaxation fit parameters vs temperature. (a) $T_{1,q}$ (blue dots) for temperatures 130 mK and lower and T_1 (black dots) for temperatures above 130 mK. (b) $T_{1,r}$ (red dots) for temperatures 130 mK and lower and T_1 (black dots) for temperatures above 130 mK. (c) parameter λ.

$T_{1,r}$ appeared to decrease with increasing temperature from an average of 27 μs at 10 mK to about 10 μs at 130 mK (see Fig. 8.19(b)). λ increased with increasing temperature from 0.9 at 10 mK to about 1.5 at 100 mK (see Fig. 8.19(c)). Thus $T_{1,q}$ vs $T_{1,r}$ appeared to have an inverse dependence in the high temperature measurements compared to the optical illumination measurements. Furthermore, it is possible that Eq. 8.5 failed to fit at higher temperatures because $T_{1,r}$ became low enough at higher temperatures, that the decay was dominated by $T_{1,r}$.

8.6.4 Illumination Dependence at 235 mK

With the refrigerator temperature set at 235 mK, I applied optical illumination on the qubit and performed qubit measurements for a few values of I_{opt}. Similar to the higher temperature results when no optical illumination was applied (Section 8.6.2), the qubit transmon peak appeared asymmetric due to cavity thermal photon number peaks. However, due to the a large scatter in the data, it was hard to fit to the same model I used and extract a good set of spectrum parameters, especially at the highest I_{opt} values.

For the relaxation measurements, the $\delta V/V$ vs pulse delay time results could be fit well to a single exponential decay with the decay time defined as T_1. Figure 8.20 shows the fit T_1 values as a function of I_{opt} (red dots), compared to the $T_{1,q}$ values for relaxation measurements at 10 mK (blue dots, the same as Fig. 8.14(a)). As shown previously in Fig. 8.19(a), $T_1 \approx 0.5$ to 0.7 μs when no optical power was applied at 235 mK. For low optical intensities below $I_{\text{opt}} \approx 100$ aW/μm^2 where $T_{1,q} \gtrsim 0.5$ μs,

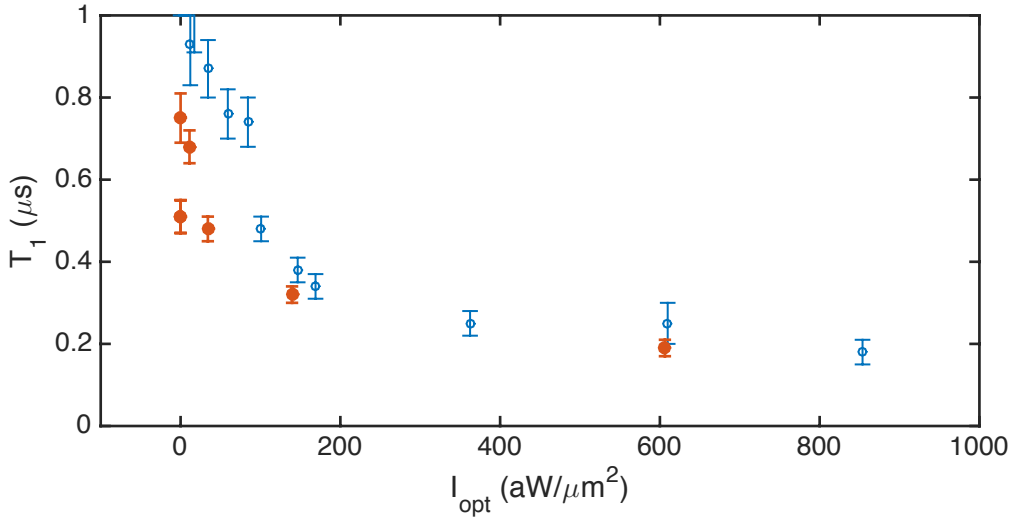

Figure 8.20: T_1 vs I_{opt} for relaxation measurements taken at 235 mK (red dots) overlaid over the $T_{1,q}$ vs I_{opt} from 10 mK measurements (blue dots).

T_1 appeared to be minimally changed by I_{opt}. For higher intensities, T_1 appeared to follow the $T_{1,q}$ vs I_{opt} dependence at 10 mK, with slightly lower values. Assuming the quasiparticle picture of Section 6.7, one might then estimate that $I_{\text{opt}} \approx 100$ aW/μm^2 corresponds to phonon effective temperature $T_{\text{eff}} \approx 235$ mK.

8.6.5 Discussion of Temperature Dependence

In the simple quasiparticle tunneling picture of Section 6.7, for a constant illumination intensity I_{opt} (and hence phonon effective temperature T_{eff}), T_1 and ω_{ge} should consistently decrease with increasing bath temperature T_b. The fact that the short time $T_{1,q}$ increased and the long time $T_{1,r}$ decreased with increasing temperature suggested that $T_{1,q}$ might be due to TLSs and $T_{1,r}$ which disagrees with the discussion in Section 8.4.2 and 8.5.4. Similarly, the illumination measurements sug-

gested (see Section 8.5.4) that both timescales were likely affected by quasiparticle loss. These discrepancies again suggests that Eq. 8.5 model may not be appropriate.

8.7 Modeling Relaxation Time and Frequency Shift Behavior

8.7.1 Sources of Loss

Some of the parameters I extracted my from spectroscopy and relaxation measurements had significant uncertainty, especially for the temperature dependent results (see Fig. 8.19). This makes it more challenging to distinguish different sources of loss as it allows a much wider range of parameters to be used in the models. Furthermore, the relaxation showed a decay with two characteristic decay times for most of the measurements. It was not obvious whether one or the other relaxation times, or both were of interest.

The sources of relaxation I initially considered included Purcell loss, coupling toTLSs, and dissipation from quasiparticle tunneling quasiparticle tunneling. Some of these were easy to pin down. For example, from the extracted parameters, I could calculate the Purcell decay time using Eq. 6.47. Around the cavity single photon occupation, the quality factor of the dressed cavity peak was $Q \approx 9400$. This gave a Purcell contribution from the TE101 mode of $T_{1,\mathrm{Purcell}} = (\Delta_{ge}/g_{ge})^2(Q/\omega_c) \approx 18$ μs. I note that this value was actually shorter than the $T_{1,r}$ values at 10 mK under no illumination and thus not consistent. However, the bare cavity peak had a significantly higher quality factor at $Q \approx 3.2 \times 10^4$, which gave $T_{1,\mathrm{Purcell}} \approx 61$ μs, which was consistent with $T_{1,r}$. Since the dressed states are superpositions of qubit

and cavity states, the lower Q of the dressed cavity peak was likely due to coupling to the qubit, or possibly other microwave modes with a short coherence time. A self consistent analysis would need to be done and I suspect this will reveal that either $T_{1,q}$ or $T_{1,r}$ is the true lifetime of the qubit. I note that both possible Purcell times were much longer than the measured decay time of $T_{1,q} \approx 1.2$ μs.

I next consider if the relaxation time $T_{1,q} \approx 1.2$ μs at 10 mK and no optical illumination was due to TLS. With this assumption I could use Eq. 6.49 to find $F\tan(\delta) = 1/\omega_{ge}T_{1,q} \approx 2.6 \times 10^{-5}$. Using this value and Eq. 2.60 to calculate the frequency shift as a function of temperature I found a shift of only about 15 kHz between 10 mK and 300 mK, much smaller than the observed shifts in the resonance. Thus one conclusion was that the effect of TLS on frequency shift should be negligible. Another conclusion was that $T_{1,q}$ was not consistent with TLS loss. I note that there could still be a nonequilibrium quasiparticle and constant loss components in the relaxation time, and thus these were upper limits on $F\tan(\delta)$ and frequency shift. In fact, since I observed a significant $|e\rangle$ state population in qubit spectroscopy, it was likely that the quasiparticles in the qubit were hot, either due to a background radiation or poor thermalization.

8.7.2 Nonequilibrium Quasiparticles

I simulated the loss and frequency shift due to quasiparticle tunneling using the simplified tunneling model and the nonequilibrium quasiparticle simulation described in Section 6.7.3. Unlike the resonator simulations, because I did not take rf

Table 8.1: Parameters used in nonequilibrium simulations of the transmon.

Symbol	Parameter	Value	Source
Δ	superconducting gap	190 μeV	simulation parameter
$\hbar\omega_{ge}$	qubit energy in simulation	21 μeV	closest 1 μeV multiple
		($h \times 5.07$ GHz)	to measured energy
A	half of transmon Al surface area	2.45×10^5 μm^2	design parameter
V	half of transmon Al volume	1.75×10^4 μm^3	design parameter
N_0	single spin density of states	1.74×10^{10} eV$^{-1}\mu$m^{-3}	Ref. [149]
	at Fermi level		
N_i/Ω_D^3	atomic density/(Debye frequency)^3	1.09×10^{15} (eV μm)$^{-3}$	Eq. 2.84
τ_0	quasiparticle-phonon time	438 ns	Ref. [150]
τ_ϕ	characteristic phonon time	0.26 ns	Ref. [149]
τ_e	phonon escape time	0.2 ns	simulation parameter
ϵ	Al absorption coefficient	$\approx 10\%$	nominal
$\tilde{\omega}_{ge,0}/2\pi$	baseline transmon frequency	5.096 GHz	simulation parameter
$T_{\text{eff},0}$	effective temperature	163 mK	simulation parameter
	of background radiation		(compare with $T_{1,r}$)
$T'_{\text{eff},0}$	effective temperature	200 mK	simulation parameter
	of background radiation		(compare with $T_{1,q}$)
E_J/h	Josephson energy	16.6 GHz	fit to spectrum
E_C/h	charging energy	213 MHz	fit to spectrum
R_N	junction normal resistance	8.93 kΩ	Eqs. 1.8 and 7.2
C_Σ	total parallel capacitance	91 fF	Eq. 1.9

absorption into account in Eq. 2.76, I did not need the measured quality factors as inputs in the simulation. Table 8.1 shows the parameters I used in the simulation. I note here that most of these parameters were from a preliminary analysis, and further analysis is needed to see if better agreement with the data can be obtained.

In the simulation, the superconducting gap Δ was an adjustable parameter but single-valued *i.e.* the same on both junction electrodes, even though the difference in Δ between the two sides was likely greater than the grid size 1 μeV [211]. In the simulations I used $\hbar\omega_{ge} = 21$ μeV $= h \times 5.07$ GHz, which was the closest integer multiple of 1 μeV from the qubit transition frequency ≈ 5.1 GHz. As I discussed in Section 6.7, for the simplified model I effectively simulated only one half of the transmon, thus the Al surface area A and volume V were half of the transmon surface area and volume. However, as I discussed in Section 4.2.3, the effect of illumination was largely independent of the Al dimensions. Similar to the resonator simulations (see Chapter 2), I used standard values for aluminum quasiparticle-phonon characteristic scattering time $\tau_0 = 438$ ns [150] and phonon-quasiparticle characteristic scattering time $\tau_\phi = 0.26$ ns [149]. The phonon escape time τ_e was an adjustable parameter in the model, obtained from the optical power absorption. I used an approximate Al emissivity of $\varepsilon \approx 10\%$. For the temperature of the phonon bath T_b, I used the refrigerator temperature. In Chapter 6, I used the parallel capacitance C_Σ and the junction normal state resistance R_N in the simulations. Here C_Σ was calculated from E_C using Eq. 1.9. R_N was calculated from E_J using Eq. 1.8 and the Ambegaokar-Baratoff formula of Eq. 7.2. I used E_J and E_C values from the spectroscopy results. All of these parameters are summarized in Table 8.1.

8.7.3 Temperature Dependence

Figure 8.21(a) shows the measured $T_{1,r}$ (red dots) and T_1 (black dots) as a function of refrigerator temperature along with T_1 from the nonequilibrium simulation (green curve). For the chosen parameters, the simulated values appeared to be flat and consistent with data up to about 130 mK. Above 130 mK, both the simulated and measured values of T_1 rapidly decreased with increasing temperature, although the simulated values decreased faster. Figure 8.21(b) shows a comparison between the measured $\omega_{ge}/2\pi$ (dots) and the expected $\omega_{ge}/2\pi$ (green curve) from the nonequilibrium simulations as a function of refrigerator temperature. The simulated curve roughly followed the measured values, although with slightly less shift than measured. It did not capture the apparent slight increase in frequency between 0 and 100 mK, but it was possible the increase was just due to fluctuations.

The typical value for the superconducting gap for aluminum is $\Delta = 170$ μeV. In the simulations, I used $\Delta = 190$ μeV, which was about 10% higher. This value was chosen to balance the discrepancy in the measured and simulated values of T_1 and $\delta\omega_{ge}/\omega_{ge}$. T_1 appeared to agree to the data best for $\Delta \approx 200$ to 210 μeV, while $\delta\omega_{ge}/\omega_{ge}$ agreed best for $\Delta \approx 170$ to 180 μeV. Superconducting gaps of $\Delta \approx 200$ μeV and higher have been measured in Al-AlO_x-Al Josephson junctions many times before [211, 219, 239]. A higher superconducting gap in a junction is very typical if the Al film is deposited under some ambient oxygen [211], which is likely for double angle junction depositions.

In the simulations, I also needed to take into account the effects of background

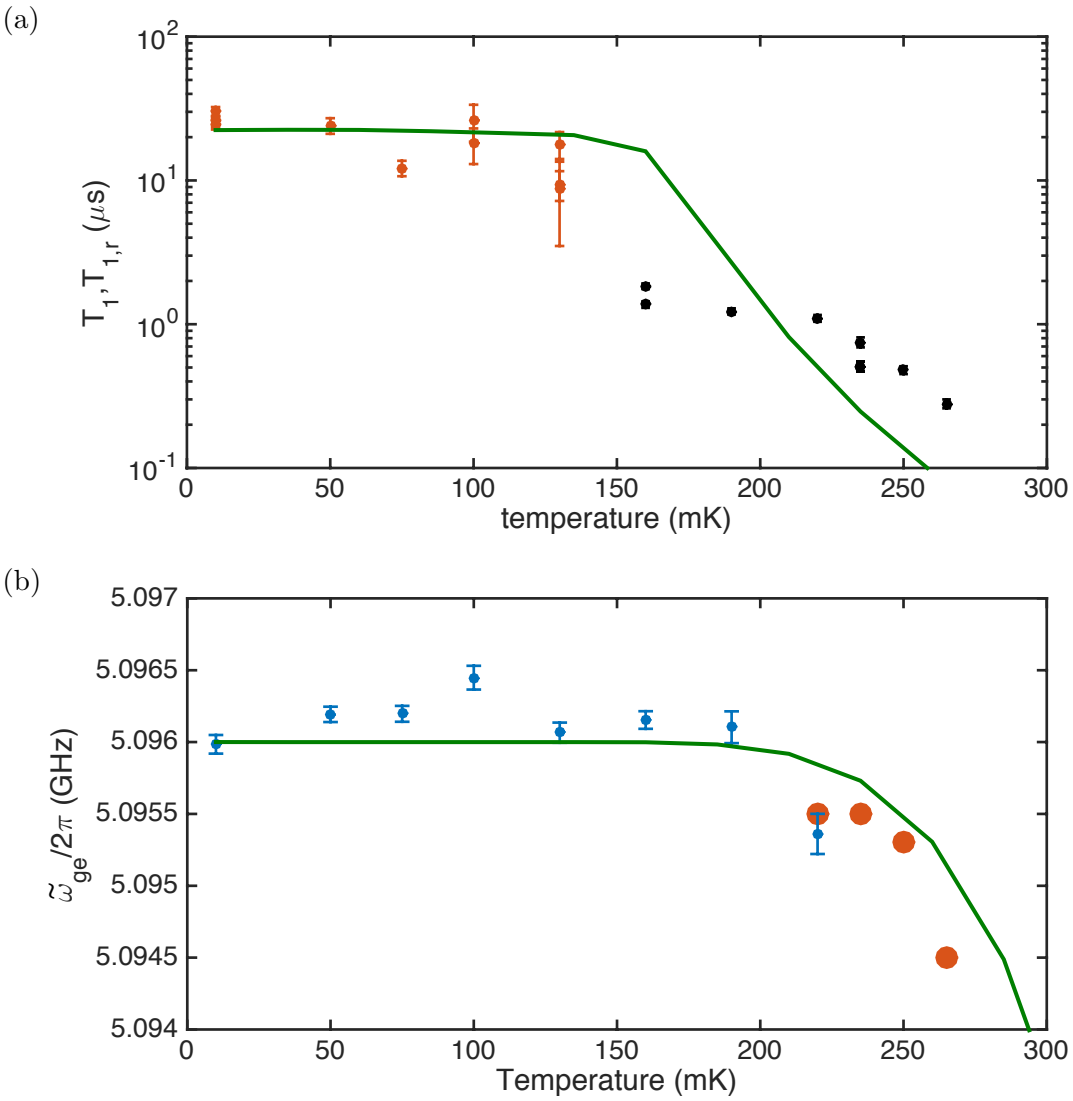

Figure 8.21: (a) Relaxation times $T_{1,r}$ (red dots) and T_1 (black dots) as a function of refrigerator temperature and (b) qubit transition frequency $\omega_{ge}/2\pi$ as a function of refrigerator temperature. I compare data in both plots to expected results (green curve) using nonequilibrium quasiparticle simulation using $T_{\text{eff},0} \approx 163$ mK and other parameters in Table 8.1.

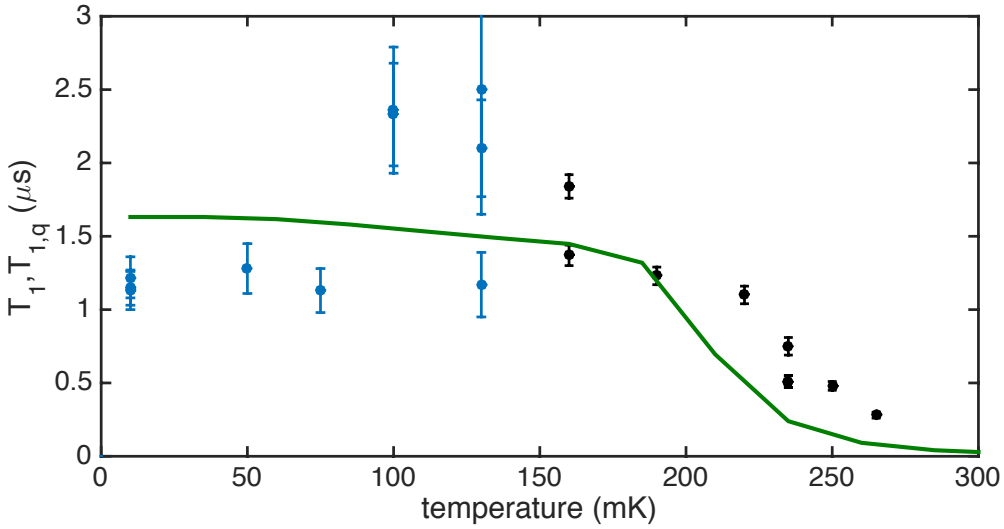

Figure 8.22: Relaxation times $T_{1,q}$ (blue dots) and T_1 (black dots) as a function of refrigerator temperature. I compare data to expected results (green curve) using nonequilibrium quasiparticle simulation using $T'_{\text{eff},0} \approx$ 200 mK and other parameters in Table 8.1.

radiation represented by the effective temperature $T_{\text{eff},0} \approx 163$ mK. This value was lower than the effective temperature $T_{\text{eff},0} \approx 236$ mK I found during resonator measurements (see Chapters 4 and 5). This was expected because I removed 4 K hot finger for the transmon measurements and this reduced the background radiation level on the cavity. However, 163 mK was still relatively high and this suggests further steps would be needed to shield the cavity and reduce the effective temperature further. Of course, many other parameters were also different between the resonator measurements and transmon measurements, hence this was not a perfect comparison. I note that if I compare the measured $T_{1,q}$ with the calculated T_1 from nonequilibrium simulations I needed to use higher background effective temperature $T'_{\text{eff},0} \approx 200$ mK (see Fig. 8.22) while other parameters shown in Table 8.1 are

unchanged.

8.7.4 Illumination Dependence

To connect the applied optical intensity $I_{\rm opt}$ with the effective temperature $T_{\rm eff}$, similar to the resonator analysis, I used Eq. 5.5 where

$$P_{\rm opt}(T_{\rm eff}) \;=\; P_{\rm opt}(T_{\rm eff,0}) \;+\; \varepsilon A I_{\rm opt}. \tag{8.7}$$

Here I used $T_{\rm eff,0} = 163$ mK and assumed the emissivity $\varepsilon \approx 10\%$. In the nonequilibrium simulations, I used the $T_{\rm eff}$ values shown in the plot $T_{\rm eff}$ vs $I_{\rm opt}$ of Fig. 8.23(a) and calculated using Eq. 8.7. In Chapters 4 and 5 I used $\tau_e \approx 9$ ns for a 215 nm film, which gives $\tau_e \approx 3$ ns for a 70 nm film. To achieve power balance, I had to use $\tau_e = 0.2$ ns, which was an order of magnitude lower. However, this value was similar to the τ_e values used by de Visser *et al.* [48] and within the possible τ_e values for aluminum [151].

I used the nonequilibrium simulation to calculate T_1 and $\omega_{ge}/2\pi$ for several values of $I_{\rm opt}$, and these simulations are compared to the measured values in Figs. 8.23(b) and 8.23(c). While the measured values captured the general behavior, the agreement was poor. The T_1 from simulations were much lower than the measured $T_{1,r}$, while the simulated shifts in $\omega_{ge}/2\pi$ were much less than the data. For a given $I_{\rm opt}$, increasing $T_{\rm eff}$ would result in better agreement in $\omega_{ge}/2\pi$ but worse agreement in T_1, and vice versa. Thus the values of $T_{\rm eff}$ were chosen above to balance the two.

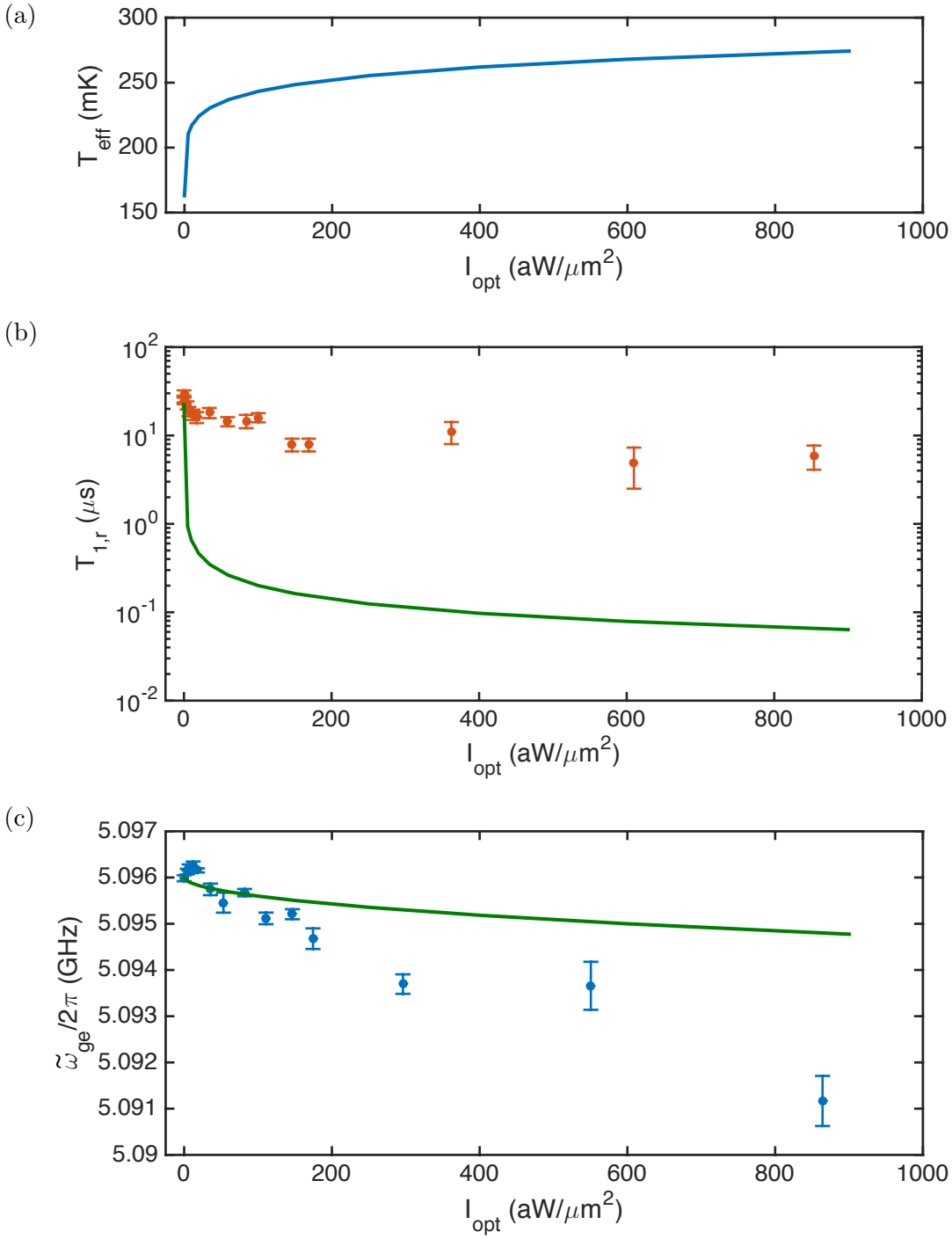

Figure 8.23: (a) Effective temperature T_{eff} vs optical intensity I_{opt} calculated using Eq. 8.7. (b) Relaxation time $T_{1,r}$ vs I_{opt} and (c) transition frequency $\omega_{ge}/2\pi$ vs I_{opt}. I compare data in both plots to expected results (green curve) using nonequilibrium quasiparticle simulation using T_{eff} value from (a) and parameters in Table 8.1.

8.7.5 Further Extensions to Model

The relatively poor agreement between the data and the simulation suggests that something essential has been left out in the model. In Section 6.7.4 I briefly discussed several possible extensions to the quasiparticle model in the transmon. These include considering that the two Al layers may have different Δ, as well as attempting to find the time dependence of the distributions $f(E)$ and $n(\Omega)$ to take microwave drive into account. So far, for simplicity, I have assumed that the superconducting gap Δ the same on both sides of the junction, but this is unlikely to be the case. Furthermore, a difference in Δ on the two sides would cause dramatic changes in the tunneling resistance. This is the most likely shortcoming of the simple model.

8.8 Pulsed Light Measurements

When optical illumination or rf drive is turned on or off, the quasiparticle distribution $f(E)$ will reach a new steady state distribution after a time on the order of the recombination time τ_R. In the resonator measurements, I measured the recombination time in the resonator's Al film by measuring the change in the phase of S_{21} as a function of time as the illumination is pulsed (see Section 5.3.3). A direct analog for this measurement on a qubit would be performing a measurement of the qubit spectrum as a function of time under pulsed illumination. This would require a QND readout, which was prohibitively slow in the current measurement setup.

Instead, I performed relaxation measurements under a pulsed illumination.

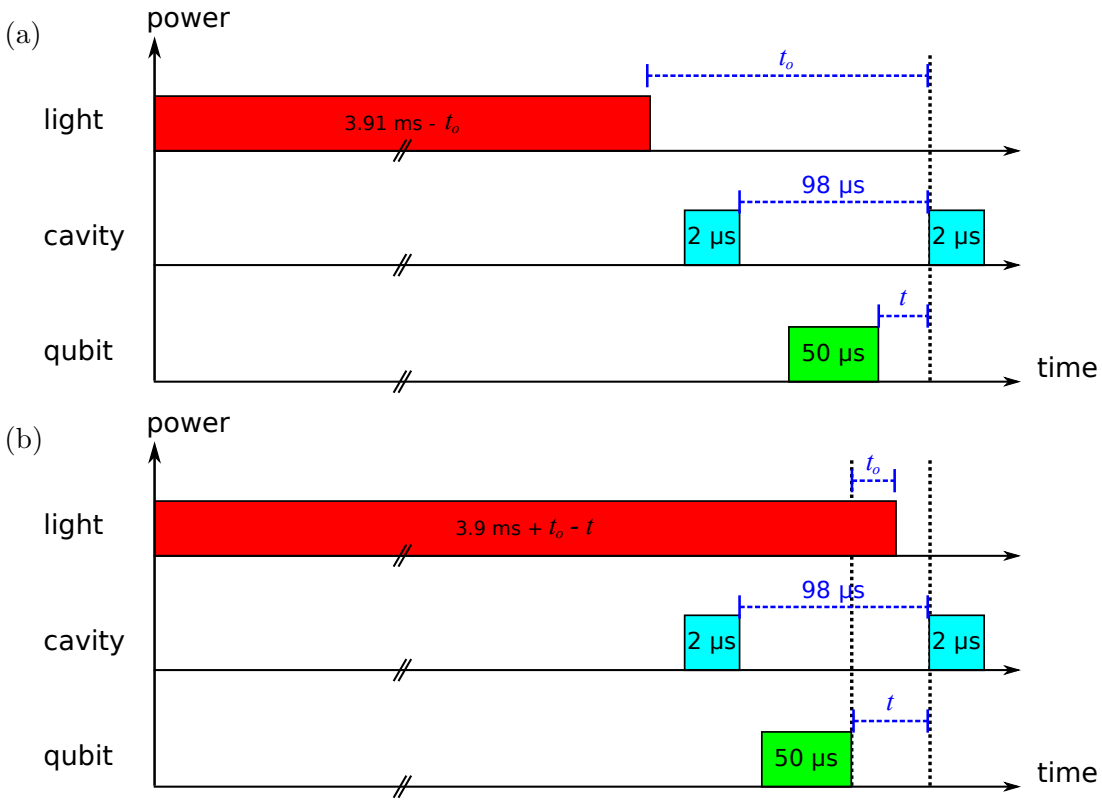

Figure 8.24: Pulse timing diagram for optical pulse experiments: (a) Relaxation measurements where the optical pulse turn-off time is fixed relative to cavity pulses. (b) Relaxation measurements where the optical pulse turn-off time is fixed relative to qubit pulse.

As before, the timing of the optical pulse was controlled by sending pulses to the acousto-optic modulator. I used two different timing schemes, shown in Fig. 8.24. Since the recombination time can be as high as 2 ms (see Section 5.3.3), I wanted the optical pulses to be at least 1 ms to make sure the quasiparticle reached a steady state distribution before turning off. This required a slower repetition rate, which I set to 250 Hz, or one repetition for 4 ms for these measurements.

For the first set of measurements, I kept the optical pulse fixed relative to the cavity rf measurement pulses with delay time t_o (the time difference between the end of the optical pulse and the beginning of the second measurement pulse) (see Fig. 8.24(a)). Here the optical pulse timing changed relative to the qubit drive pulse over the course of the measurement. The length of the optical pulse was 3.91 ms$-t_o$, fixed over the course of a single relaxation measurement but varied for different values of t_o.

In the second set of pulsed optical measurements, I changed the optical pulse timing such that it turned off at fixed time relative to the qubit pulse instead (see Fig. 8.24(b)). For these measurements, the optical pulse was set to end roughly a duration t_o after the end of the qubit pulse. I kept the start time of the optical pulse fixed. Since the qubit pulse changed over the course of the measurement, the length of the optical pulse changed as well. If t is the delay time between the end of the qubit pulse and the second measurement pulse, then the length of the optical pulse is given by 3.9 ms$+t_o - t$.

The optical intensity was set at $I_{\text{opt}} \approx 35$ aW/μm^2. This intensity was measured for a continuous illumination, and may be different or drift when pulsed using

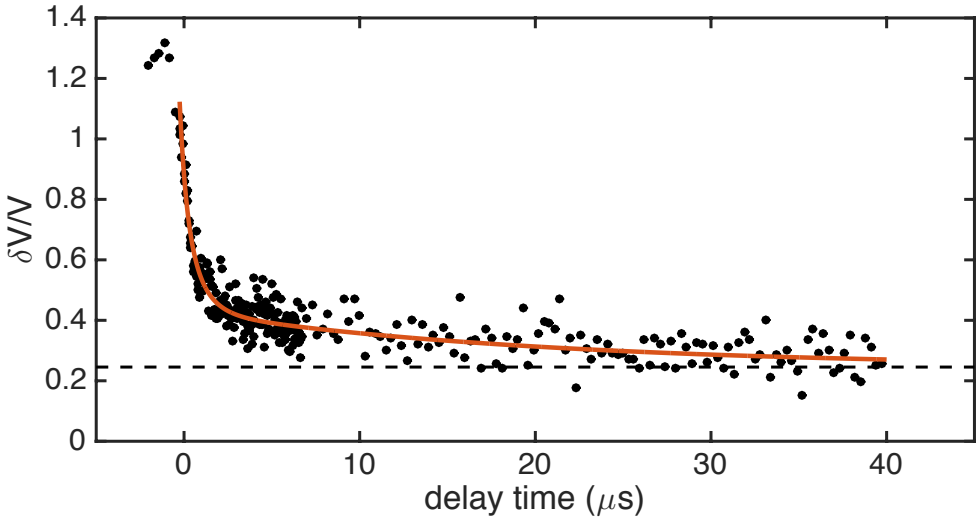

Figure 8.25: $\delta V/V$ vs pulse delay time for a relaxation measurement under pulsed illumination using timing scheme shown in Fig. 8.24(a). Red curve is fit of data to Eq. 8.8. Black dashed line is the offset value obtained from fit.

the AOM. For continuous illumination, the measured relaxation times for this intensity is $T_{1,q} \approx 0.9$ μs and $T_{1,r} \approx 15$ μs.

Figure 8.25 show a plot of $\delta V/V$ as a function of the delay time t_0 between the qubit pulse and cavity pulse for the pulse timing given by Fig. 8.24(a) with $t_0 = 200$ μs. Unlike previous relaxation measurements, here $\delta V/V$ does not appear to reach zero for long times, but a constant nonzero value. This could be explained by the fact that in continuous illumination measurements, I had to vary the cavity drive power to find optimal $\delta V/V$. It could be that as the light was turned off, the optimal point for the cavity power also changed over time. If the optimal power for reading out the cavity changed, then it would mean the two cavity pulses had different effective powers within the repetition, and this would give $\delta V/V \neq 0$ at

long delay times. To take this effect into account, I fit the relaxation $\delta V/V$ to the same form as Eq. 8.5, with an additional constant C such that

$$(\delta V/V)(t) \;=\; A\,\exp\left[\lambda\left(e^{-t/T_{1,q}}-1\right)\right]\,e^{-t/T_{1,r}}+C. \tag{8.8}$$

In Fig. 8.25, the fit to Eq. 8.8 gave $T_{1,q} = (1.12 \pm 0.11)$ μs, $T_{1,r} = (20 \pm 9)$ μs, and $\lambda = 1.24 \pm 0.10$.

Figures 8.26 show the extracted fit parameters as a function of t_o for the timing using Fig. 8.24(a). I expected for $t_o \to \infty$ the fit parameters would approach the values for $I_{\rm opt} = 0$ (red dotted line) while for $t_o \to 0$ they would approach the values for continuous $I_{\rm opt} = 35$ aW/μm^2. Although I only had a few data points, $T_{1,q}$ (Fig. 8.26(a)) and λ (Fig. 8.26(c)) appeared to roughly follow this behavior with some spread. On the other hand, $T_{1,r}$ did not appear to follow any obvious behavior with most of the values at 20 μs or lower. It is possible the addition of a constant C in the fit, with a relatively large scatter in the $\delta V/V$ vs t data, caused the extracted $T_{1,r}$ to go down. More data and further analysis would be needed to come to a definite conclusion.

I also performed a few relaxation measurements with the pulse timing given by Fig. 8.24(b) where the light turned off some time t_o after the end of the cavity pulse. If the change in quasiparticle distributions were instantaneous, one would observe a sharp change in the behavior of $\delta V/V$ vs t at $t \approx t_o$. However, due to an expected long recombination time I would expect a slower change. For $t_o \gtrsim T_{1,q}$ the signal $\delta V/V$ was already very low at $t \approx t_o$, and it was hard to observe any changes. I also performed one measurement where $t_o = 1$ μs $\approx T_{1,q}$ (see Fig. 8.27),

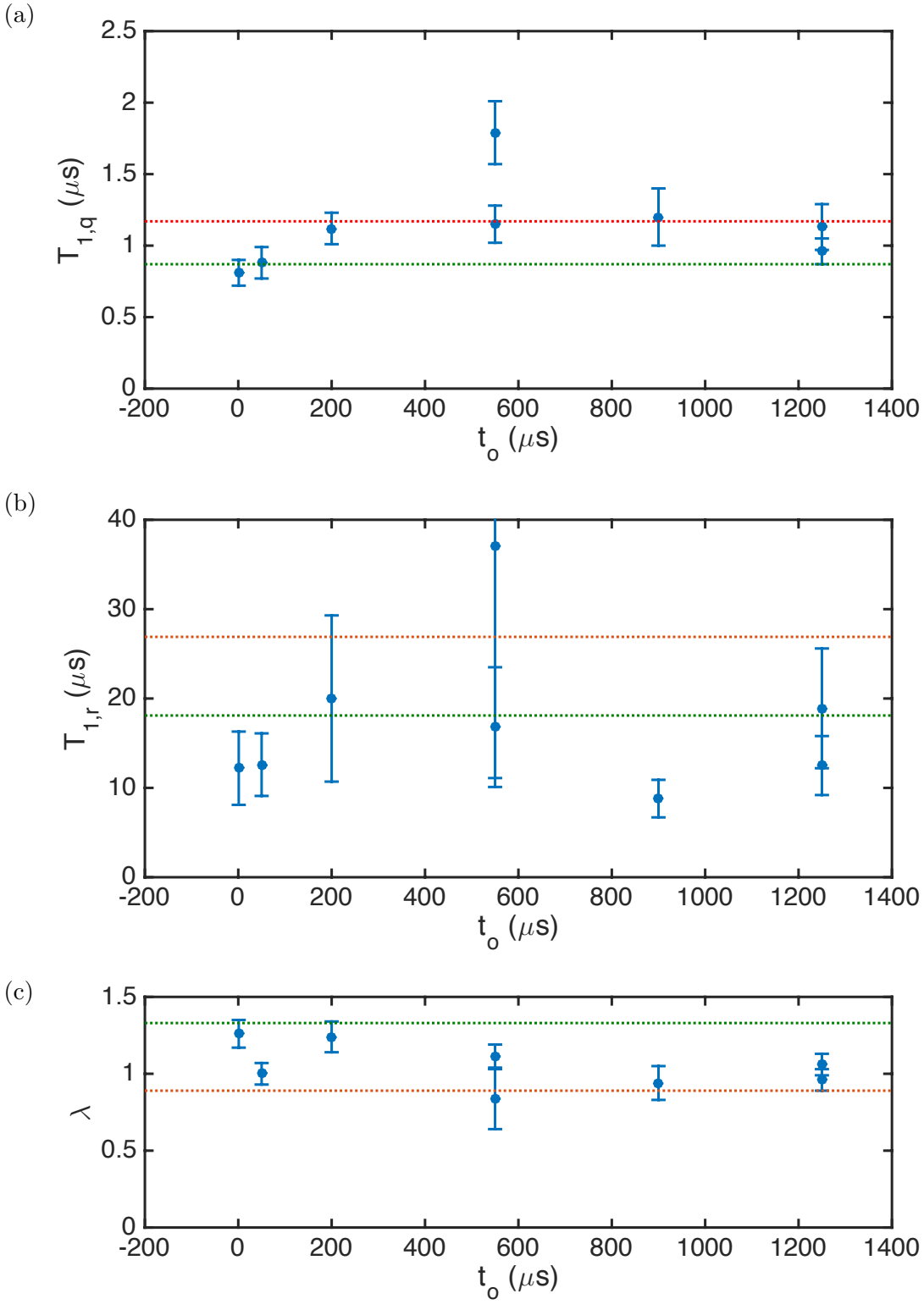

Figure 8.26: Extracted relaxation fit parameters vs t_o in pulsed illumination measurements: (a) $T_{1,q}$, (b) $T_{1,r}$, and (c) λ. Red dotted line are from the parameters for $I_{\text{opt}} = 0$ and green dotted line are from the parameters for continuous $I_{\text{opt}} = 35$ aW/μm^2.

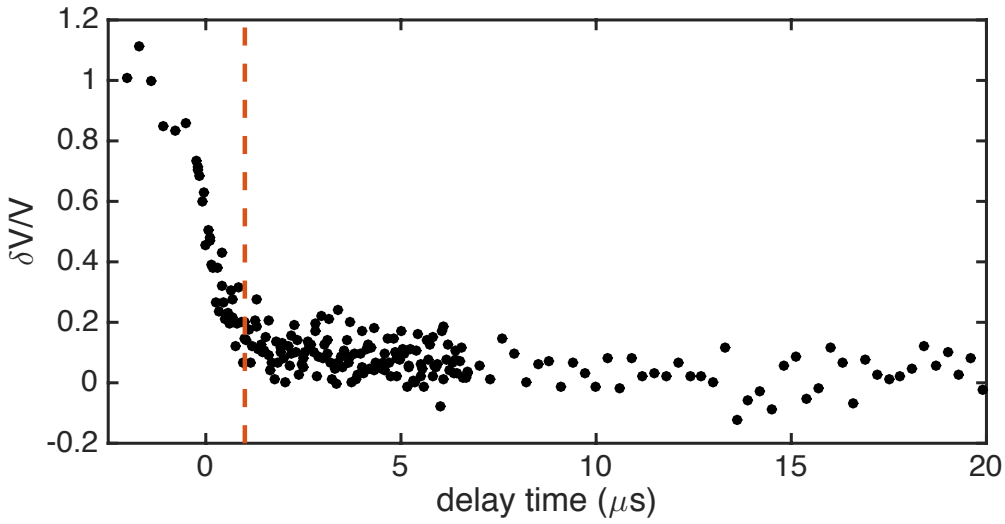

Figure 8.27: $\delta V/V$ vs pulse delay time for a relaxation measurement under pulsed illumination using timing scheme shown in Fig. 8.24(b). Red vertical dashed line at $t_0 = 1$ μs shows the approximate position of the turn-off of the optical pulse.

and I did not observe any major changes there either. This might be because the recombination time were much larger than $T_{1,q}$ (which should be the case), or the data was too noisy to observe changes in $T_{1,q}$.

8.9 Summary

In this chapter I presented my results from measurements on an optically illuminated transmon. Qubit and cavity spectroscopies revealed that the device had energy and coupling parameters very close to the design values. However, in the qubit spectroscopy I also observed a significant $|e\rangle \leftrightarrow |f\rangle$ transition peak. This suggests that I had a high background $|e\rangle$ state population. The cavity may also showed background qubit excited state population of about 8%.

The time dependent measurements showed some deviation from the expected behavior. The measurement fidelity was low and the Rabi oscillation measurements showed unusual behavior including a 50-50 saturation level that appeared to slowly increase over a time scale of tens of μs. In addiation, the qubit relaxation showed non-exponential behavior. It could be fit to a quasiparticle fluctuation model based on Ref [23] with two characteristic times $T_{1,q} \approx 1.2$ μs and $T_{1,r} \approx 25$ μs although this picture does not appear to be appropriate for my device. It also fits well to the sum of two exponentials, which suggests that there was a small population of higher levels being excited.

When I applied optical illumination, the qubit frequency appeared to initially slightly increase with increasing intensity $I_{\rm opt}$ before decreasing with increasing $I_{\rm opt}$ as expected from the simple quasiparticle picture. Both relaxation times $T_{1,q}$ and $T_{1,r}$ decreased with increasing $I_{\rm opt}$ as expected.

When I increased the temperature, the qubit frequency also appeared to initially slightly increase with increasing temperature before decreasing with increasing temperature. Above about 220 mK, the qubit peak became asymmetric, consistent with the cavity photon peaks picture with a thermal distribution. $T_{1,q}$ slightly increased while $T_{1,r}$ decreased with increasing temperature. Above about 160 mK, the relaxation measurements became a simple exponential with a single decay time T_1.

I simulated the effect of illumination and temperature on the quasiparticles using the simple junction picture described in Chapter 6 and calculated the expected qubit frequencies and relaxation times. While the simulation captured the rough behavior, the agreement was relatively poor. This suggests the model may need to

be extended to include different superconducting gaps on each side of the junction.

Finally, I performed a few relaxation measurements with a pulsed illumination, varying the delay time t_o between the turn off time of the light and the cavity measurement time. $T_{1,q}$ appeared to depend on t_o, from the continuous illumination value at low t_o to the no illumination value at high t_o.

Chapter 9: Conclusions and Outlook

In this dissertation, I reported measurements on the effect of 780 nm optical illumination on two different superconducting devices. Below I will summarize the results and discuss possible extensions to the work, as well as briefly describe progress in building a superconductor-atom hybrid system.

9.1 Conclusions of Resonator Measurements

9.1.1 Summary of Results

In Chapters 4 and 5 I described measurements of the resonance frequency f_r and quality factor Q of an Al thin film lumped-element microwave resonator inside a 3d aluminum cavity at temperatures down to 25 mK. I studied the dependence of f_r and Q on microwave drive power $P_{\rm rf}$, optical illumination intensity $I_{\rm opt}$, and refrigerator temperature T between 20 and 300 mK. At the base temperature of 25 mK with no illumination and for low microwave powers, both f_r and Q showed multiple branches. f_r in particular appeared to jump randomly between branches every several days. In the low rf power limit, Q rapidly increased with increasing $P_{\rm rf}$. This behavior suggested that in the low rf power regime, the loss was dominated

by coupling to a single or a few two-level systems (TLSs).

At higher rf powers, Q continued to increase with increasing $P_{\rm rf}$ up to a maximum of about 2×10^6 at $P_{\rm rf} = -45$ dBm (corresponding to $\langle n\rangle \approx 2\times10^8$ rf photons in the cavity). At higher powers the peak was distortion. Under optical illumination, the optically-induced loss caused Q to decrease with increasing $I_{\rm opt}$ and increase with increasing $P_{\rm rf}$. The variation in Q due to $P_{\rm rf}$ was very similar to the behavior expected for loss from a distribution of two-level systems. This behavior suggested the presence of optically activated TLSs, however I found that the loss was better explained by the presence of nonequilibrium distribution of quasiparticles generated by the illumination and excited by the microwave drive.

I developed a model for the nonequilibrium quasiparticle distribution following the approach developed by Goldie and Withington [149], based on the kinetic equations by Chang and Scalapino [147]. I extended their technique to include effects due to optical illumination. Using Parker's heating model [107] I assumed the optical illumination creates an effective source of phonons with energy higher than twice the superconducting gap. I solved the the coupled quasiparticle-phonon rate equations numerically and fit the simulation results to the measurements. The best fit curves were in good agreement with the observed dependence of the resonator quality factor Q and frequency shift δf_r on temperature, microwave power, and optical illumination. In the simulations, I had to include the presence of background illumination with $T_{\rm eff} \approx 236$ mK, which I attributed to blackbody radiation from a 4K hot finger located a few inches from the cavity. This result confirmed the importance of shielding a superconducting device from radiation and also revealed

the importance of shielding the resonator from high-energy phonons produced by such illumination.

9.1.2 Possible Improvements and Extensions

Measurements of the rf-dependence of the photo-induced loss in superconducting thin-films can be used to discriminate quasiparticle loss from TLS induced loss, confirm optical absorption in a resonator, detect nonequilibrium quasiparticles, and study quasiparticle dynamics at high rf-drive.

Examination of the kinetic equations suggest several methods for reducing quasiparticle loss. Protecting the device from stray light [45, 46] and reducing the emissivity of the device should obviously reduce loss. To be effective, the shielding needs to protect the device not only from stray light and background blackbody radiation, but also from phonons of energy $> 2\Delta$ created by the absorbed light that cause pair breaking. Minimizing the kinetic inductance ratio will reduce the sensitivity of loss and frequency shift to temperature changes and optical illumination. For kinetic-inductance detectors it is instead desirable to increase the optical frequency shift sensitivity while keeping the loss low.

By performing quasiparticle simulations using different material parameters [156], one may be able to identify optimal materials for different purposes. For example, de Visser *et al.* has suggested that the rf-dependence of quasiparticle loss is stronger for superconductors with a smaller superconducting gap [48]. Results from such simulations could be compared to measurements of optically-induced and rf-

dependent loss on resonators made from Nb, Ta, and TiN_x. Also, my results suggest that the use of quasiparticle traps or the use of materials with short quasiparticle recombination times should reduce the quasiparticle density and its associated loss. Finally, despite its complexities, I note that the model was still relatively simple in its treatment of optical effects. I believe this approach can be extended to simulate time-dependent behavior and can be improved by using a more complete model of the optical absorption process [157, 158].

9.2 Conclusions of Transmon Measurements

9.2.1 Summary of Results

I fabricated an Al transmon qubit with a $g \rightarrow e$ transition frequency of about 5.1 GHz, mounted it in a 3d cavity with a TE101 mode frequency of 6.13 GHz. I illuminated the transmon with 780 nm light from an optical fiber and measured the qubit transition frequency and relaxation time as a function of illumination intensity and temperature between 10 and 265 mK. Cavity spectroscopy measurements 10 mK revealed the presence of a background $|e\rangle$ state population of about 8% and qubit spectroscopy revealed a cavity photon excited state population of about 8% as well. This suggests a qubit temperature higher than the refrigerator temperature or the presence of background radiation. This may have been due to radiation from the 700 mK shield, optical photons in the fiber cladding, insufficient attenuation on the input and output microwave lines, or insufficient cooling of the cold attenuators on the input and output microwave lines.

The Rabi oscillations showed unusual behavior where the 50-50 saturation level appeared to slowly increase over time suggesting excitations to higher level qubit states. The qubit relaxation showed non-exponential behavior which I fit to a quasiparticle fluctuation model based on Ref [23] with characteristic times $T_{1,q} \approx 1.2$ μs and $T_{1,r} \approx 25$ μs for no illumination at 10 mK.

With increasing $I_{\rm opt}$, the qubit frequency appeared to initially slightly increase before decreasing. The decrease was expected from a simple quasiparticle tunneling picture. Both relaxation times $T_{1,q}$ and $T_{1,r}$ decreased with increasing $I_{\rm opt}$ as expected.

With increasing temperature, the qubit frequency also appeared to slightly increase from 10 mK to 100 mK before decreasing at higher temperatures. Above about 220 mK, the qubit peak became asymmetric, consistent with a thermal distribution of cavity photon number peaks. Initially $T_{1,q}$ slightly increased while $T_{1,r}$ decreased with increasing temperature. Above about 130 mK, the relaxation measurements revealed a simple exponential with a single decay time T_1.

I simulated the effect of illumination and temperature on the distribution of quasiparticles using a simple junction picture and calculated the expected qubit frequencies and relaxation times. While the simulation captured the rough behavior, the agreement was relatively poor. This suggests the model had some incorrect parameters or needed to be extended to include different superconducting gaps on each side of the junctions.

9.2.2 Possible Improvements and Extensions

As discussed above, the quasiparticle tunneling model only gave rough qualitative agreement but poor quantitative agreement with the transmon data. Further analysis is needed to understand this discrepancy. Of course there might be other sources of decoherence that need to be taken into account, for example TLSs or coupling to other modes, but these are not expected to vary with optical intensity.

Two serious experimental complications were the presence of magnetic fluctuations and a relatively high background excited state population. These suggest that the refrigerator needs better magnetic and optical shielding. The group is currently in the process of obtaining room-temperature and cryogenic magnetic shields and copper thermal shields at the mixing chamber. This should improve both magnetic and optical shielding at the same time. To reduce magnetic fluctuations further, it is desirable to reduce the amount of magnetic materials near the device, for example in the cavity connectors. To reduce background radiation further, we can add additional layers of absorptive coating on the shields [45, 46].

The relaxation appeared to be limited by the background radiation, but it is also important to have a clean substrate surface and metal film to reduce dielectric loss [115]. SEM imaging of the junctions I fabricated revealed what appeared to be resist residue around the junction, which can contribute significant loss. Developing a better and cleaner fabrication process should reduce the effect of dielectric loss on qubit decoherence.

The pulsing scheme I used provided very limited control of the shape of the

pulses, which in turn limited the type of measurements that I could do. These can be improved by using a dedicated pulse shaping board instead of just using the internal gating of the source. It is also possible some of the unusual behavior in the time-dependent measurements were caused by measurement issues, including the sawtooth patterns observed in heterodyne measurements, the distorted Rabi oscillation, and the nonexponential qubit relaxation. One way to improve the measurement would be to use a faster data acquisition card. This would allow us to perform heterodyne and homodyne measurements at higher sampling rate than what I used (5 Msamples/s).

Finally, the models suggest that quasiparticle induced loss in superconducting qubits may be reduced by using materials with two different gaps to form the tunnel junction. Further analysis and experiments are needed to confirm this possibility.

9.3 Progress Towards Building a Hybrid System

Understanding the effects of illumination on resonators and transmons, and designing possible schemes to mitigate photo-induced loss on the resonator are just some of the steps towards building a hybrid quantum system that couples atoms to superconducting devices. Based on the resonator measurements, Jared Hertzberg and Kristen Voigt have redesigned the resonator setup such that the light absorption has been greatly reduced. Compared to the setup I used, the new setup was also closer to the design of the proposed hybrid system (see Fig. 1.3).

Jared also redesigned the resonator. To increase the coupling of the resonator

to the microwave cavity, he added a 3d transmon-like dipole antenna structure. To increase the effective coupling between the trapped atoms and the resonator, he also redesigned the inductor into a single line inductor which reduced the inductance. To keep the resonance frequency of the resonator the same, he increased the capacitance of the interdigitated capacitor.

As the system is being cooled down from room temperature to base temperature, thermal contraction will cause the relative position between the fiber and the resonator to change. To control the relative position of the fiber at cryogenic temperatures, the cavity and resonator is mounted on Attocube piezostages [103] to allow movement on two axes, while the fiber is fixed.

In fact, Jared and Kristen have found that they can infer the relative position between the fiber and the resonator by observing the response of the LC resonator peak to illumination [240]. The illumination cross-section changes depending on the position of the fiber, and is minimized when the fiber is aligned parallel to and in the same plane as the surface of the chip and the inductor. As the illumination intensity, and thus quasiparticle generation rate, are not uniform over the surface of the resonator, quasiparticle diffusion needs to be taken into account to understand the response. To understand their data, I helped Kristen and Jared develop a quasiparticle diffusion model in the resonator using finite-element solver COMSOL [188]. The relative position obtained from the resonator response can then be compared with the absolute position of the cavity measured by PCB resonator sensors positioned outside the cavity. Initial measurements by Kristen and Jared showed that the resonance response as a function of position was roughly consistent with

the quasiparticle model [240].

9.4 Final Remarks

In addition to the hybrid quantum system, I believe my results are of interest to the field of microwave kinetic-inductance detectors (MKIDs) [105, 106]. MKIDs use superconducting resonators as detectors for x-ray photons. In fact, many of the analytical tools I used came from the MKID field, and I hope this work can be useful for them as well.

The fact that quasiparticles were the source of optically-induced loss in a superconducting film was not unexpected. What was unexpected, at least for me initially, was that the quasiparticle loss in the thin-film resonator showed a complicated dependence on rf power, temperature, and incident optical intensity, and the rf power dependence appeared to be very similar to that from loss due to a distribution of TLSs. It took us a while to finish the analysis of the resonator results and there were a few detours and false starts. I believe we now have a reasonable starting point for a detailed analysis of the transmon results and for other devices that the group may study in the future, including a hybrid quantum system that couples trapped atoms to a superconducting qubit.

Appendix A: Building the Jacobian in the Nonequilibrium Quasiparticle Simulations

As described in Section 2.3.4, the simulation to find the nonequilibrium quasiparticle distribution requires the $(2N+1)\times(2N+1)$ Jacobian matrix given by

$$J(\alpha_l) = \begin{pmatrix} \frac{\partial(df_1/dt)}{\partial f_1} & \cdots & \frac{\partial(df_1/dt)}{\partial f_N} & \frac{\partial(df_1/dt)}{\partial B} & \frac{\partial(df_1/dt)}{\partial n_1} & \cdots & \frac{\partial(df_1/dt)}{\partial n_N} \\ \vdots & \ddots & \vdots & \vdots & \vdots & \ddots & \vdots \\ \frac{\partial(df_N/dt)}{\partial f_1} & \cdots & \frac{\partial(df_N/dt)}{\partial f_N} & \frac{\partial(df_N/dt)}{\partial B} & \frac{\partial(df_N/dt)}{\partial n_1} & \cdots & \frac{\partial(df_N/dt)}{\partial n_N} \\ \frac{\partial\delta P_{\rm rf,ab}}{\partial f_1} & \cdots & \frac{\partial\delta P_{\rm rf,ab}}{\partial f_N} & \frac{\partial\delta P_{\rm rf,ab}}{\partial B} & \frac{\partial\delta P_{\rm rf,ab}}{\partial n_1} & \cdots & \frac{\partial\delta P_{\rm rf,ab}}{\partial n_N} \\ \frac{\partial(dn_1/dt)}{\partial f_1} & \cdots & \frac{\partial(dn_1/dt)}{\partial f_N} & \frac{\partial(dn_1/dt)}{\partial B} & \frac{\partial(dn_1/dt)}{\partial n_1} & \cdots & \frac{\partial(dn_1/dt)}{\partial n_N} \\ \vdots & \ddots & \vdots & \vdots & \vdots & \ddots & \vdots \\ \frac{\partial(dn_N/dt)}{\partial f_1} & \cdots & \frac{\partial(dn_N/dt)}{\partial f_N} & \frac{\partial(dn_N/dt)}{\partial B} & \frac{\partial(dn_N/dt)}{\partial n_1} & \cdots & \frac{\partial(dn_N/dt)}{\partial n_N} \end{pmatrix}. \quad \text{(A.1)}$$

Here I previously defined $f_j = f(E_j)$ and $n_j = n(\Omega_j)$, with $E_j = j + \Delta - 1$ μeV and $\Omega_j = j$ μeV.

In the simulations, I build the Jacobian matrix element-by-element, by taking the partial derivatives of Eq. 2.90 and discretized versions of Eqs. 2.76 and 2.77. Here I will briefly summarize the elements of the Jacobian. I note that Eqs. 2.76 and 2.77 contain multiple terms and I will describe each term separately.

In all of the equations, the energies E and Ω are written in units of step size 1 μeV and hence they are integers. This is also the case for superconducting gap Δ and rf photon energy $\hbar\omega_r$. The dE and $d\Omega$ are artifacts from discretization of

the integrals, and their values are the step size of 1 μeV. Also note that the allowed values of the subscript j in f_j and n_j are integers between 1 and N. f_j and n_j are assumed to be zero for values outside the evaluated range of E and Ω.

Partial Derivatives of df_j/dt

The right hand side of the rate equation of df_j/dt of Eq. 2.76 contains four terms: the quasiparticle excitation from rf drive $G_{\rm qp}(E, \omega_r)$ and three sums. The first two sums represent quasiparticle-phonon scattering and the last sum represents recombination and pair breaking processes. Here I define the three sum terms as $f_{j,1}$, $f_{j,2}$, and $f_{j,3}$ respectively.

$\partial(df_j/dt)/\partial f_k$

f_k appears in the first (rf drive) term when E_k equals either E_j, $E_j + \hbar\omega_r$, or $E_j - \hbar\omega_r$. Hence I have

$$\frac{\partial G_{qp,j}}{\partial f_k} = \begin{cases} -2B\,\left[h_+(E_k, E_k + \hbar\omega_r) + h_+(E_k, E_k - \hbar\omega_r)\right], & \text{for } E_j = E_k \\ 2B\,h_+(E_j, E_j + \hbar\omega_r) \;=\; 2B\,h_+(E_k - \hbar\omega_r, E_k), & \text{for } E_j = E_k - \hbar\omega_r \\ 2B\,h_+(E_j, E_j - \hbar\omega_r) \;=\; 2B\,h_+(E_k + \hbar\omega_r, E_k), & \text{for } E_j = E_k - \hbar\omega_r \\ 0, & \text{otherwise} \end{cases} \tag{A.2}$$

For the scattering terms, if $k \neq j$, f_k only appears in at most one term within the sum, and as a result the partial derivative of the remaining terms within the sum is zero. If $k = j$, f_k appears in all terms, and the sum is preserved.

Second term ($f_{j,1}$):

$$\frac{\partial(df_{j,1}/dt)}{\partial f_k} = \begin{cases} 0, & \text{for } k < j \\ -\dfrac{1}{\tau_0(k_B T_c)^3} \displaystyle\sum_{\Omega=0}^{\infty} d\Omega\, \Omega^2\, h_-(E_j, E_j+\Omega)\,(n_\Omega + f_{j+\Omega})\,, & \text{for } k = j \\ \dfrac{1}{\tau_0(k_B T_c)^3}\, d\Omega\, (E_k - E_j)^2\, h_-(E_j, E_k)\,(1 - f_j + n_{k-j})\,, & \text{for } k > j \end{cases} \tag{A.3}$$

I note that in practice the sum for $j = k$ does not go to $\Omega = \infty$ but to $N - j$.

Third term ($f_{j,2}$):

$$\frac{\partial(df_{j,2}/dt)}{\partial f_k} = \begin{cases} \dfrac{1}{\tau_0(k_B T_c)^3}\, d\Omega\, (E_j - E_k)^2\, h_-(E_j, E_k)\,(f_j + n_{j-k})\,, & \text{for } k < j \\ -\dfrac{1}{\tau_0(k_B T_c)^3} \displaystyle\sum_{\Omega=0}^{j-1} d\Omega\, \Omega^2\, h_-(E_j, E_j-\Omega)\,(1 + n_\Omega - f_{j-\Omega})\,, & \text{for } k = j \\ 0, & \text{for } k > j \end{cases} \tag{A.4}$$

For the fourth term ($f_{j,3}$), if $k = j$, $f_k = f_j$ appears once in each of the terms within the sum, except when $\Omega = 2E_j$ where it appears twice within that term. In the end, I have

$$\begin{aligned} \frac{\partial(df_{j,3}/dt)}{\partial f_j} = &-\frac{1}{\tau_0(k_B T_c)^3} \Big[d\Omega\, (2E_j)^2\, h_+(E_j, E_j)\,(f_j + n_{2j}) \\ &+ \sum_{\Omega=j-1}^{\infty} d\Omega\, \Omega^2\, h_+(E_j, \Omega - E_j)\left(f_{\Omega-j-2(\Delta+1)} + n_\Omega\right) \Big] \end{aligned} \tag{A.5}$$

I note the long subscript on one of the f's is because f_0 corresponds to $f(\Delta)$, and hence $f_{\Omega-j-2(\Delta+1)}$ corresponds to $f(\Omega - E_j)$. Also note that the sum, in practice does not go to $\Omega = \infty$.

Otherwise if $k \neq j$, f_k only appears once in the sum when $\Omega = E_j + E_k$

$$\frac{\partial(df_{j,3}/dt)}{\partial f_k} = -\frac{1}{\tau_0(k_B T_c)^3}\, d\Omega\, (E_j + E_k)^2\, h_+(E_j, E_k)\, (f_j + n_{j+k}) \tag{A.6}$$

$\partial(df_j/dt)/\partial B$

In Eq. 2.76 of the paper, only G_{qp} depends on B, and the dependence is linear, and hence it is straightforward to write

$$\frac{\partial(df_j/dt)}{\partial B} = \frac{G_{qp,j}}{B}. \tag{A.7}$$

$\partial(df_j/dt)/\partial n_k$

G_{qp} is independent of n_k, but the other three terms depend on it. In all three, n_k only appears in at most one of the terms within the sum.

Second term ($f_{j,1}$):

$$\frac{\partial(df_{j,1}/dt)}{\partial n_k} = -\frac{1}{\tau_0(k_B T_c)^3}\, d\Omega\, \Omega_k^2\, h_-(E_j, E_j + \Omega_k)\, (f_j - f_{j+k}) \tag{A.8}$$

Third term ($f_{j,2}$):

$$\frac{\partial(df_{j,2}/dt)}{\partial n_k} = \begin{cases} -\dfrac{1}{\tau_0(k_B T_c)^3}\, d\Omega\, \Omega_k^2\, h_-(E_j, E_j - \Omega_k)\, (f_j - f_{j-k}), & \text{for } \Omega_k < E_n - \Delta \\ 0, & \text{otherwise} \end{cases} \tag{A.9}$$

Fourth term ($f_{j,3}$):

$$\frac{\partial(df_{j,3}/dt)}{\partial n_k} = \begin{cases} \dfrac{1}{\tau_0(k_B T_c)^3}\, d\Omega\, \Omega_k^2\, h_-(E_j, \Omega_k - E_j) & \\ \quad \times \left(1 - f_j - f_{k-j-2(\Delta-1)}\right), & \text{for } \Omega_k > E_n + \Delta \\ 0, & \text{otherwise} \end{cases} \tag{A.10}$$

I note the long subscript at the second f on the right hand side where $f_{k-j-2(\Delta-1)}$ corresponds to $f(\Omega_k - E_j)$.

Partial Derivatives of δP

The right hand side of Eq. 2.90 only contains a single sum term and $-P_{\mathrm{rf,ab}}$, which is a number.

$\partial\delta P/\partial f_k$

f_k appears four times in the sum over E, twice when $E = E_k$ and once each for $E = E_k - \hbar\omega_r$ and for $E = E_k + \hbar\omega_r$. However, some of the terms cancel out and this results in

$$\begin{aligned}\frac{\partial\delta P}{\partial f_k} &= 8N_0\, dE\, B\, \hbar\omega_r[h_+(E_k + \hbar\omega_r, E_k)\,\rho(E_k + \hbar\omega_r) \\ &\quad - h_+(E_k - \hbar\omega_r, E_k)\,\rho(E_k - \hbar\omega_r)].\end{aligned} \tag{A.11}$$

$\partial\delta P/\partial B$

The sum term in δP is proportional to B, and hence it is straightforward to write

$$\frac{\partial\delta P}{\partial B} = \frac{4N_0\sum_{E=\Delta}^{\infty} dE\, I_{qp}(E)E\rho(E)}{B} = \frac{\delta P + P_{rf,ab}}{B} \tag{A.12}$$

$\partial\delta P/\partial n_k$

Expression of δP is independent of n_k, so this is straightforward and $\partial\delta P/\partial n_k = 0$ for all n_k.

Partial Derivatives of dn_j/dt

The right hand side of the rate equation of dn_j/dt of Eq. 2.77 contains four terms: the phonon generation term from optical illumination, two sums, and the escape term to thermal bath. The first sum represents the quasiparticle-phonon scattering and the second sum represents recombination and pair breaking processes. Here I define the two sum terms as $n_{j,1}$ and $n_{j,2}$ respectively, and the escape term as $n_{j,3}$. I note that the optical generation term is independent of f_k, B, and n_k and hence will not contribute to the Jacobian.

$\partial(dn_j/dt)/\partial f_k$

For the first sum term ($n_{j,1}$), f_k appears twice within the sum, when $E = E_k - \Omega_n$ and $E = E_k$. In the end I have

$$\begin{aligned}\frac{\partial(dn_{j,1}/dt)}{\partial f_k} \;=\; -\,\frac{2}{\pi\tau_0^{\phi}\Delta}\,dE\,\Big[&h_-(E_k-\Omega_j,E_k)\,\rho(E_k-\Omega_j)\,(f_{k-j}-n_j-1)\\ &+\;h_-(E_k,E_k+\Omega_j)\,\rho(E_k)(n_j+f_{k+j})\Big]\end{aligned} \tag{A.13}$$

For the second sum term ($n_{j,2}$), if $\Omega_j < 2\Delta$ there is nothing to sum, and the term $\partial(dn_{j,2}/dt)/\partial f_k = 0$.

If $E_k > \Omega_j - \Delta$, f_k does not appear in the sum, and hence $\partial(dn_{j,2}/dt)/\partial f_k = 0$ as well.

Otherwise, f_k appears twice in the sum, when $E = E_k$ and $E = \Omega_j - E_k$, and I can write

$$\frac{\partial(dn_{j,2}/dt)}{\partial f_k} = \frac{2}{\pi\tau_0^\phi\Delta}\, dE\, h_+(E_k, \Omega_j - E_k)\, \rho(E_k)\, \left(n_j + f_{j-k-2(\Delta-1)}\right) \tag{A.14}$$

Again, I note the subscript of f where here $f_{j-k-2(\Delta-1)}$ corresponds to $f(\Omega_j - E_k)$.

The escape term is independent of f_k and hence $\partial(dn_{j,3}/dt)/\partial f_k = 0$.

$\partial(dn_m/dt)/\partial B$

The expression for (dn_j/dt) is independent of B for all n_j, so this is straightforward and $\partial(dn_j/dt)/\partial B = 0$.

$\partial(dn_j/dt)/\partial n_k$

The expression for (dn_j/dt) only depends on n_j, and so for $k \neq j$ I have $\partial(dn_j/dt)/\partial n_k = 0$.

For $k = j$, the terms are nonzero.

First term $(n_{j,1})$:

$$\frac{\partial(dn_{j,1}/dt)}{\partial n_j} = -\frac{2}{\pi\tau_0^\phi\Delta}\sum_{E=\Delta}^{\infty} dE\, h_-(E, E+\Omega_j)\, \rho(E)\, \left(f_{E-\Delta+1} - f_{E+\Omega_j-\Delta+1}\right) \tag{A.15}$$

Again, I note the long subscript on both f's. Also, in practice, the sum only goes to $E = N$ instead of ∞.

Second term ($n_{j,2}$):

$$\frac{\partial(dn_{j,2}/dt)}{\partial n_j} = -\frac{1}{\pi\tau_0^{\phi}\Delta}\sum_{E=\Delta}^{\Omega_j-\Delta} dE\, h_+(E, E-\Omega_j)\,\rho(E)\left(1 - f_{E-\Delta+1} - f_{\Omega_j-E-2(\Delta-1)}\right) \tag{A.16}$$

As before, I note long the subscript on both f's. I also note that for $\Omega_j < 2\Delta$ the sum contains zero terms, and the term $\partial(dn_{j,2}/dt)/\partial n_j = 0$.

The third term ($n_{j,3}$) is straightforward:

$$\frac{\partial(dn_{j,3}/dt)}{\partial n_j} = -\frac{1}{\tau_e} \tag{A.17}$$

Bibliography

[1] R. P. Feynman, "Simulating physics with computers", Intl. J. Theor. Phys. **21**, 467 (1982).

[2] D. Deutsch, "Quantum theory, the Church-Turing principle and the universal quantum computer", Proc. Royal Soc. London A: Math. Phys. Eng. Sci. **400**, 97 (1985).

[3] D. Deutsch and R. Jozsa, "Rapid solution of problems by quantum computation", Proc. Royal Soc. London A: Math. Phys. Eng. Sci. **439**, 553 (1992).

[4] L. K. Grover, "Quantum mechanics helps in searching for a needle in a haystack", Phys. Rev. Lett. **79**, 325 (1997).

[5] P. W. Shor, "Polynomial-time algorithms for prime factorization and discrete logarithms on a quantum computer", SIAM Review **41**, 303 (1999).

[6] A. K. Lenstra and H. W. Lenstra, eds., *The development of the number field sieve*, Lecture Notes in Mathematics 1554 (Springer-Verlag, Berlin, 1990).

[7] E. Knill, R. Laflamme, and G. J. Milburn, "A scheme for efficient quantum computation with linear optics", Nature **409**, 46 (2001).

[8] J. I. Cirac and P. Zoller, "A scalable quantum computer with ions in an array of microtraps", Nature **404**, 579 (2000).

[9] R. Blatt and D. Wineland, "Entangled states of trapped atomic ions", Nature **453**, 1008 (2008).

[10] M. D. Lukin, "*Colloquium*: trapping and manipulating photon states in atomic ensembles", Rev. Mod. Phys. **75**, 457 (2003).

[11] D. Loss and D. P. DiVincenzo, "Quantum computation with quantum dots", Phys. Rev. A **57**, 120 (1998).

[12] N. A. Gershenfeld and I. L. Chuang, "Bulk spin-resonance quantum computation", Science **275**, 350 (1997).

[13] R. Hanson and D. D. Awschalom, "Coherent manipulation of single spins in semiconductors", Nature **453**, 1043 (2008).

[14] M. H. Devoret and R. J. Schoelkopf, "Superconducting circuits for quantum information: an outlook", Science **339**, 1169 (2013).

[15] K. K. Likharev, "Superconducting weak links", Rev. Mod. Phys. **51**, 101 (1979).

[16] B. Josephson, "Possible new effects in superconductive tunnelling", Phys. Lett. **1**, 251 (1962).

[17] Y. Nakamura, Y. A. Pashkin, and J. S. Tsai, "Coherent control of macroscopic quantum states in a single-Cooper-pair box", Nature **398**, 786 (1999).

[18] A. Abragam, *Principles of nuclear magnetism*, International Series of Monographs of Physics 32 (Oxford University Press, Oxford, UK, 1961).

[19] J. M. Martinis, K. B. Cooper, R. McDermott, M. Steffen, M. Ansmann, K. D. Osborn, K. Cicak, S. Oh, D. P. Pappas, R. W. Simmonds, and C. C. Yu, "Decoherence in Josephson qubits from dielectric loss", Phys. Rev. Lett. **95**, 210503 (2005).

[20] J. M. Martinis, M. Ansmann, and J. Aumentado, "Energy decay in superconducting Josephson-junction qubits from nonequilibrium quasiparticle excitations", Phys. Rev. Lett. **103**, 097002 (2009).

[21] G. Catelani, J. Koch, L. Frunzio, R. J. Schoelkopf, M. H. Devoret, and L. I. Glazman, "Quasiparticle relaxation of superconducting qubits in the presence of flux", Phys. Rev. Lett. **106**, 077002 (2011).

[22] X. Y. Jin, A. Kamal, A. P. Sears, T. Gudmundsen, D. Hover, J. Miloshi, R. Slattery, F. Yan, J. Yoder, T. P. Orlando, S. Gustavsson, and W. D. Oliver, "Thermal and residual excited-state population in a 3d transmon qubit", Phys. Rev. Lett. **114**, 240501 (2015).

[23] I. M. Pop, K. Geerlings, G. Catelani, R. J. Schoelkopf, L. I. Glazman, and M. H. Devoret, "Coherent suppression of electromagnetic dissipation due to superconducting quasiparticles", Nature **508**, 369 (2014).

[24] V. Bouchiat, D. Vion, P. Joyez, D. Esteve, and M. H. Devoret, "Quantum coherence with a single Cooper pair", Phys. Scripta **1998**, 165 (1998).

[25] J. E. Mooij, T. P. Orlando, L. Levitov, L. Tian, C. H. van der Wal, and S. Lloyd, "Josephson persistent-current qubit", Science **285**, 1036 (1999).

[26] I. Chiorescu, Y. Nakamura, C. J. P. M. Harmans, and J. E. Mooij, "Coherent quantum dynamics of a superconducting flux qubit", Science **299**, 1869 (2003).

[27] R. Ramos, M. Gubrud, A. Berkley, J. Anderson, C. Lobb, and F. Wellstood, "Design for effective thermalization of junctions for quantum coherence", IEEE Trans. Appl. Supercond. **11**, 998 (2001).

[28] Y. Yu, S. Han, X. Chu, S.-I. Chu, and Z. Wang, "Coherent temporal oscillations of macroscopic quantum states in a Josephson junction", Science **296**, 889 (2002).

[29] J. M. Martinis, S. Nam, J. Aumentado, and C. Urbina, "Rabi oscillations in a large Josephson-junction qubit", Phys. Rev. Lett. **89**, 117901 (2002).

[30] A. J. Przybysz, H. Kwon, R. Budoyo, B. K. Cooper, E. Crowe, A. J. Dragt, J. R. Anderson, C. J. Lobb, and F. C. Wellstood, "Identifying sources of decoherence in a dc SQUID phase qubit with a sub-μm junction and interdigitated capacitor", IEEE Trans. Appl. Supercond. **21**, 867 (2011).

[31] R. Budoyo, B. Cooper, V. Zaretskey, C. Ballard, J. Anderson, C. Lobb, and F. Wellstood, "Dc SQUID phase qubit coupled to an on-chip LC resonator", IEEE Trans. Appl. Supercond. **23**, 1701504 (2013).

[32] J. Koch, T. M. Yu, J. Gambetta, A. A. Houck, D. I. Schuster, J. Majer, A. Blais, M. H. Devoret, S. M. Girvin, and R. J. Schoelkopf, "Charge-insensitive qubit design derived from the Cooper pair box", Phys. Rev. A **76**, 042319 (2007).

[33] J. Q. You, X. Hu, S. Ashhab, and F. Nori, "Low-decoherence flux qubit", Phys. Rev. B **75**, 140515 (2007).

[34] V. E. Manucharyan, J. Koch, L. I. Glazman, and M. H. Devoret, "Fluxonium: single Cooper-pair circuit free of charge offsets", Science **326**, 113 (2009).

[35] R. Barends, J. Kelly, A. Megrant, D. Sank, E. Jeffrey, Y. Chen, Y. Yin, B. Chiaro, J. Mutus, C. Neill, P. O'Malley, P. Roushan, J. Wenner, T. C. White, A. N. Cleland, and J. M. Martinis, "Coherent Josephson qubit suitable for scalable quantum integrated circuits", Phys. Rev. Lett. **111**, 080502 (2013).

[36] A. Wallraff, D. I. Schuster, A. Blais, L. Frunzio, R. S. Huang, J. Majer, S. Kumar, S. M. Girvin, and R. J. Schoelkopf, "Strong coupling of a single photon to a superconducting qubit using circuit quantum electrodynamics", Nature **431**, 162 (2004).

[37] M. A. Sillanpaa, J. I. Park, and R. W. Simmonds, "Coherent quantum state storage and transfer between two phase qubits via a resonant cavity", Nature **449**, 438 (2007).

[38] H. Paik and K. D. Osborn, "Reducing quantum-regime dielectric loss of silicon nitride for superconducting quantum circuits", Appl. Phys. Lett. **96**, 072505 (2010).

[39] A. Megrant, C. Neill, R. Barends, B. Chiaro, Y. Chen, L. Feigl, J. Kelly, E. Lucero, M. Mariantoni, P. J. J. O'Malley, D. Sank, A. Vainsencher, J. Wenner, T. C. White, Y. Yin, J. Zhao, C. J. Palmstrøm, J. M. Martinis, and A. N. Cleland, "Planar superconducting resonators with internal quality factors above one million", Appl. Phys. Lett. **100**, 113510 (2012).

[40] A. D. O'Connell, M. Ansmann, R. C. Bialczak, M. Hofheinz, N. Katz, E. Lucero, C. McKenney, M. Neeley, H. Wang, E. M. Weig, A. N. Cleland, and J. M. Martinis, "Microwave dielectric loss at single photon energies and millikelvin temperatures", Appl. Phys. Lett. **92**, 112903 (2008).

[41] J. Gao, M. Daal, A. Vayonakis, S. Kumar, J. Zmuidzinas, B. Sadoulet, B. A. Mazin, P. K. Day, and H. G. Leduc, "Experimental evidence for a surface distribution of two-level systems in superconducting lithographed microwave resonators", Appl. Phys. Lett. **92**, 152505 (2008).

[42] J. Gao, J. Zmuidzinas, A. Vayonakis, P. Day, B. Mazin, and H. Leduc, "Equivalence of the effects on the complex conductivity of superconductor due to temperature change and external pair breaking", J. Low Temp. Phys. **151**, 557 (2008).

[43] R. Barends, J. J. A. Baselmans, S. J. C. Yates, J. R. Gao, J. N. Hovenier, and T. M. Klapwijk, "Quasiparticle relaxation in optically excited high-Q superconducting resonators", Phys. Rev. Lett. **100**, 257002 (2008).

[44] M. Lenander, H. Wang, R. C. Bialczak, E. Lucero, M. Mariantoni, M. Neeley, A. D. O'Connell, D. Sank, M. Weides, J. Wenner, T. Yamamoto, Y. Yin, J. Zhao, A. N. Cleland, and J. M. Martinis, "Measurement of energy decay in superconducting qubits from nonequilibrium quasiparticles", Phys. Rev. B **84**, 024501 (2011).

[45] R. Barends, J. Wenner, M. Lenander, Y. Chen, R. C. Bialczak, J. Kelly, E. Lucero, P. O'Malley, M. Mariantoni, D. Sank, H. Wang, T. C. White, Y. Yin, J. Zhao, A. N. Cleland, J. M. Martinis, and J. J. A. Baselmans, "Minimizing quasiparticle generation from stray infrared light in superconducting quantum circuits", Appl. Phys. Lett. **99**, 113507 (2011).

[46] A. D. Córcoles, J. M. Chow, J. M. Gambetta, C. Rigetti, J. R. Rozen, G. A. Keefe, M. Beth Rothwell, M. B. Ketchen, and M. Steffen, "Protecting superconducting qubits from radiation", Appl. Phys. Lett. **99**, 181906 (2011).

[47] P. J. de Visser, J. J. A. Baselmans, J. Bueno, N. Llombart, and T. M. Klapwijk, "Fluctuations in the electron system of a superconductor exposed to a photon flux", Nature Commun. **5**, 4130 (2014).

[48] P. J. de Visser, D. J. Goldie, P. Diener, S. Withington, J. J. A. Baselmans, and T. M. Klapwijk, "Evidence of a nonequilibrium distribution of quasiparticles in the microwave response of a superconducting aluminum resonator", Phys. Rev. Lett. **112**, 047004 (2014).

[49] H. Paik, D. I. Schuster, L. S. Bishop, G. Kirchmair, G. Catelani, A. P. Sears, B. R. Johnson, M. J. Reagor, L. Frunzio, L. I. Glazman, S. M. Girvin, M. H. Devoret, and R. J. Schoelkopf, "Observation of high coherence in Josephson junction qubits measured in a three-dimensional circuit QED architecture", Phys. Rev. Lett. **107**, 240501 (2011).

[50] P. C. Maurer, G. Kucsko, C. Latta, L. Jiang, N. Y. Yao, S. D. Bennett, F. Pastawski, D. Hunger, N. Chisholm, M. Markham, D. J. Twitchen, J. I. Cirac, and M. D. Lukin, "Room-temperature quantum bit memory exceeding one second", Science **336**, 1283 (2012).

[51] M. Steger, K. Saeedi, M. L. W. Thewalt, J. J. L. Morton, H. Riemann, N. V. Abrosimov, P. Becker, and H.-J. Pohl, "Quantum information storage for over 180 s using donor spins in a ^{28}Si "semiconductor vacuum"", Science **336**, 1280 (2012).

[52] P. Treutlein, P. Hommelhoff, T. Steinmetz, T. W. Hänsch, and J. Reichel, "Coherence in microchip traps", Phys. Rev. Lett. **92**, 203005 (2004).

[53] I. Bloch, "Quantum coherence and entanglement with ultracold atoms in optical lattices", Nature **453**, 1016 (2008).

[54] L. Tian, P. Rabl, R. Blatt, and P. Zoller, "Interfacing quantum-optical and solid-state qubits", Phys. Rev. Lett. **92**, 247902 (2004).

[55] D. I. Schuster, L. S. Bishop, I. L. Chuang, D. DeMille, and R. J. Schoelkopf, "Cavity QED in a molecular ion trap", Phys. Rev. A **83**, 012311 (2011).

[56] A. S. Sørensen, C. H. van der Wal, L. I. Childress, and M. D. Lukin, "Capacitive coupling of atomic systems to mesoscopic conductors", Phys. Rev. Lett. **92**, 063601 (2004).

[57] J. Verdú, H. Zoubi, C. Koller, J. Majer, H. Ritsch, and J. Schmiedmayer, "Strong magnetic coupling of an ultracold gas to a superconducting waveguide cavity", Phys. Rev. Lett. **103**, 043603 (2009).

[58] D. Petrosyan, G. Bensky, G. Kurizki, I. Mazets, J. Majer, and J. Schmiedmayer, "Reversible state transfer between superconducting qubits and atomic ensembles", Phys. Rev. A **79**, 040304 (2009).

[59] J. D. Pritchard, J. A. Isaacs, M. A. Beck, R. McDermott, and M. Saffman, "Hybrid atom-photon quantum gate in a superconducting microwave resonator", Phys. Rev. A **89**, 010301 (2014).

[60] P. Rabl, D. DeMille, J. M. Doyle, M. D. Lukin, R. J. Schoelkopf, and P. Zoller, "Hybrid quantum processors: molecular ensembles as quantum memory for solid state circuits", Phys. Rev. Lett. **97**, 033003 (2006).

[61] A. Andre, D. DeMille, J. M. Doyle, M. D. Lukin, S. E. Maxwell, P. Rabl, R. J. Schoelkopf, and P. Zoller, "A coherent all-electrical interface between polar molecules and mesoscopic superconducting resonators", Nature Phys. **2**, 636 (2006).

[62] L. Childress, A. S. Sørensen, and M. D. Lukin, "Mesoscopic cavity quantum electrodynamics with quantum dots", Phys. Rev. A **69**, 042302 (2004).

[63] Z.-L. Xiang, S. Ashhab, J. Q. You, and F. Nori, "Hybrid quantum circuits: superconducting circuits interacting with other quantum systems", Rev. Mod. Phys. **85**, 623 (2013).

[64] J. Wrachtrup and F. Jelezko, "Processing quantum information in diamond", J. Phys: Cond. Mat **18**, S807 (2006).

[65] D. Marcos, M. Wubs, J. M. Taylor, R. Aguado, M. D. Lukin, and A. S. Sørensen, "Coupling nitrogen-vacancy centers in diamond to superconducting flux qubits", Phys. Rev. Lett. **105**, 210501 (2010).

[66] X. Zhu, S. Saito, A. Kemp, K. Kakuyanagi, S.-i. Karimoto, H. Nakano, W. J. Munro, Y. Tokura, M. S. Everitt, K. Nemoto, M. Kasu, N. Mizuochi, and K. Semba, "Coherent coupling of a superconducting flux qubit to an electron spin ensemble in diamond", Nature **478**, 221 (2011).

[67] Y. Kubo, F. R. Ong, P. Bertet, D. Vion, V. Jacques, D. Zheng, A. Dréau, J.-F. Roch, A. Auffeves, F. Jelezko, J. Wrachtrup, M. F. Barthe, P. Bergonzo, and D. Esteve, "Strong coupling of a spin ensemble to a superconducting resonator", Phys. Rev. Lett. **105**, 140502 (2010).

[68] Y. Kubo, C. Grezes, A. Dewes, T. Umeda, J. Isoya, H. Sumiya, N. Morishita, H. Abe, S. Onoda, T. Ohshima, V. Jacques, A. Dréau, J.-F. Roch, I. Diniz, A. Auffeves, D. Vion, D. Esteve, and P. Bertet, "Hybrid quantum circuit with a superconducting qubit coupled to a spin ensemble", Phys. Rev. Lett. **107**, 220501 (2011).

[69] Y. Kubo, I. Diniz, A. Dewes, V. Jacques, A. Dréau, J.-F. Roch, A. Auffeves, D. Vion, D. Esteve, and P. Bertet, "Storage and retrieval of a microwave field in a spin ensemble", Phys. Rev. A **85**, 012333 (2012).

[70] C. Grezes, B. Julsgaard, Y. Kubo, M. Stern, T. Umeda, J. Isoya, H. Sumiya, H. Abe, S. Onoda, T. Ohshima, V. Jacques, J. Esteve, D. Vion, D. Esteve, K. Mølmer, and P. Bertet, "Multimode storage and retrieval of microwave fields in a spin ensemble", Phys. Rev. X **4**, 021049 (2014).

[71] D. I. Schuster, A. P. Sears, E. Ginossar, L. DiCarlo, L. Frunzio, J. J. L. Morton, H. Wu, G. A. D. Briggs, B. B. Buckley, D. D. Awschalom, and R. J. Schoelkopf, "High-cooperativity coupling of electron-spin ensembles to superconducting cavities", Phys. Rev. Lett. **105**, 140501 (2010).

[72] P. Bushev, A. K. Feofanov, H. Rotzinger, I. Protopopov, J. H. Cole, C. M. Wilson, G. Fischer, A. Lukashenko, and A. V. Ustinov, "Ultralow-power spectroscopy of a rare-earth spin ensemble using a superconducting resonator", Phys. Rev. B **84**, 060501 (2011).

[73] S. Probst, H. Rotzinger, S. Wünsch, P. Jung, M. Jerger, M. Siegel, A. V. Ustinov, and P. A. Bushev, "Anisotropic rare-earth spin ensemble strongly coupled to a superconducting resonator", Phys. Rev. Lett. **110**, 157001 (2013).

[74] O. O. Soykal and M. E. Flatté, "Strong field interactions between a nanomagnet and a photonic cavity", Phys. Rev. Lett. **104**, 077202 (2010).

[75] O. O. Soykal and M. E. Flatté, "Size dependence of strong coupling between nanomagnets and photonic cavities", Phys. Rev. B **82**, 104413 (2010).

[76] H. Huebl, C. W. Zollitsch, J. Lotze, F. Hocke, M. Greifenstein, A. Marx, R. Gross, and S. T. B. Goennenwein, "High cooperativity in coupled microwave resonator ferrimagnetic insulator hybrids", Phys. Rev. Lett. **111**, 127003 (2013).

[77] Y. Tabuchi, S. Ishino, T. Ishikawa, R. Yamazaki, K. Usami, and Y. Nakamura, "Hybridizing ferromagnetic magnons and microwave photons in the quantum limit", Phys. Rev. Lett. **113**, 083603 (2014).

[78] X. Zhang, C.-L. Zou, L. Jiang, and H. X. Tang, "Strongly coupled magnons and cavity microwave photons", Phys. Rev. Lett. **113**, 156401 (2014).

[79] M. Goryachev, W. G. Farr, D. L. Creedon, Y. Fan, M. Kostylev, and M. E. Tobar, "High-cooperativity cavity QED with magnons at microwave frequencies", Phys. Rev. Applied **2**, 054002 (2014).

[80] Y. Tabuchi, S. Ishino, A. Noguchi, T. Ishikawa, R. Yamazaki, K. Usami, and Y. Nakamura, "Coherent coupling between a ferromagnetic magnon and a superconducting qubit", Science **349**, 405 (2015).

[81] J. Hoffman, J. Grover, Z. Kim, A. Wood, J. Anderson, A. Dragt, M. Hafezi, C. Lobb, L. Orozco, S. Rolston, J. Taylor, C. Vlahacos, and F. Wellstood, "Atoms talking to SQUIDs", Rev. Mex. Fis. S **57**, 1 (2011).

[82] J. E. Hoffman, "Optical nanofiber fabrication and analysis: towards coupling atoms to superconducting qubits", PhD thesis (University of Maryland, College Park, MD, 2014).

[83] M. Hafezi, Z. Kim, S. L. Rolston, L. A. Orozco, B. L. Lev, and J. M. Taylor, "Atomic interface between microwave and optical photons", Phys. Rev. A **85**, 020302 (2012).

[84] S. Bernon, H. Hattermann, D. Bothner, M. Knufinke, P. Weiss, F. Jessen, D. Cano, M. Kemmler, R. Kleiner, D. Koelle, and J. Fortágh, "Manipulation and coherence of ultra-cold atoms on a superconducting atom chip", Nature Commun. **4** (2013).

[85] C. Song, T. W. Heitmann, M. P. DeFeo, K. Yu, R. McDermott, M. Neeley, J. M. Martinis, and B. L. T. Plourde, "Microwave response of vortices in superconducting thin films of Re and Al", Phys. Rev. B **79**, 174512 (2009).

[86] *Triton 200/400 Cryofree dilution refrigerator operating manual*, ver 3.0 (Oxford Instruments, Abingdon, Oxfordshire, UK).

[87] V. I. Balykin, K. Hakuta, F. Le Kien, J. Q. Liang, and M. Morinaga, "Atom trapping and guiding with a subwavelength-diameter optical fiber", Phys. Rev. A **70**, 011401 (2004).

[88] F. Le Kien, V. I. Balykin, and K. Hakuta, "Atom trap and waveguide using a two-color evanescent light field around a subwavelength-diameter optical fiber", Phys. Rev. A **70**, 063403 (2004).

[89] E. Vetsch, D. Reitz, G. Sagué, R. Schmidt, S. T. Dawkins, and A. Rauschenbeutel, "Optical interface created by laser-cooled atoms trapped in the evanescent field surrounding an optical nanofiber", Phys. Rev. Lett. **104**, 203603 (2010).

[90] A. Goban, K. S. Choi, D. J. Alton, D. Ding, C. Lacroûte, M. Pototschnig, T. Thiele, N. P. Stern, and H. J. Kimble, "Demonstration of a state-insensitive, compensated nanofiber trap", Phys. Rev. Lett. **109**, 033603 (2012).

[91] M. Vangeleyn, P. F. Griffin, E. Riis, and A. S. Arnold, "Laser cooling with a single laser beam and a planar diffractor", Opt. Lett. **35**, 3453 (2010).

[92] J. Lee, J. A. Grover, L. A. Orozco, and S. L. Rolston, "Sub-doppler cooling of neutral atoms in a grating magneto-optical trap", J. Opt. Soc. Am. B **30**, 2869 (2013).

[93] S. Kuhr, W. Alt, D. Schrader, M. Müller, V. Gomer, and D. Meschede, "Deterministic delivery of a single atom", Science **293**, 278 (2001).

[94] J. Schoser, A. Batär, R. Löw, V. Schweikhard, A. Grabowski, Y. B. Ovchinnikov, and T. Pfau, "Intense source of cold rb atoms from a pure two-dimensional magneto-optical trap", Phys. Rev. A **66**, 023410 (2002).

[95] J. E. Hoffman, S. Ravets, J. A. Grover, P. Solano, P. R. Kordell, J. D. Wong-Campos, L. A. Orozco, and S. L. Rolston, "Ultrahigh transmission optical nanofibers", AIP Advances **4**, 067124 (2014).

[96] S. Ravets, J. E. Hoffman, L. A. Orozco, S. L. Rolston, G. Beadie, and F. K. Fatemi, "A low-loss photonic silica nanofiber for higher-order modes", Opt. Express **21**, 18325 (2013).

[97] S. Ravets, J. E. Hoffman, P. R. Kordell, J. D. Wong-Campos, S. L. Rolston, and L. A. Orozco, "Intermodal energy transfer in a tapered optical fiber: optimizing transmission", J. Opt. Soc. Am. A **30**, 2361 (2013).

[98] J. A. Grover, "Atom-trapping and photon-counting experiments with optical nanofibers", PhD thesis (University of Maryland, College Park, MD, 2015).

[99] J. A. Grover, P. Solano, L. A. Orozco, and S. L. Rolston, "Photon-correlation measurements of atomic-cloud temperature using an optical nanofiber", Phys. Rev. A **92**, 013850 (2015).

[100] B. Sarabi, A. N. Ramanayaka, A. L. Burin, F. C. Wellstood, and K. D. Osborn, "Cavity quantum electrodynamics using a near-resonance two-level system: Emergence of the Glauber state", Appl. Phys. Lett. **106**, 172601 (2015).

[101] B. Sarabi, "Cavity quantum electrodynamics of nanoscale two-level systems", PhD thesis (University of Maryland, College Park, MD, 2014).

[102] M. J. A. Stoutimore, M. S. Khalil, C. J. Lobb, and K. D. Osborn, "A Josephson junction defect spectrometer for measuring two-level systems", Appl. Phys. Lett. **101**, 062602 (2012).

[103] Attocube, `http://www.attocube.com/`.

[104] Z. Kim, C. P. Vlahacos, J. E. Hoffman, J. A. Grover, K. D. Voigt, B. K. Cooper, C. J. Ballard, B. S. Palmer, M. Hafezi, J. M. Taylor, J. R. Anderson, A. J. Dragt, C. J. Lobb, L. A. Orozco, S. L. Rolston, and F. C. Wellstood, "Thin-film superconducting resonator tunable to the ground-state hyperfine splitting of ^{87}Rb", AIP Advances **1**, 042107 (2011).

[105] P. K. Day, H. G. LeDuc, B. A. Mazin, A. Vayonakis, and J. Zmuidzinas, "A broadband superconducting detector suitable for use in large arrays", Nature **425**, 817 (2003).

[106] J. Zmuidzinas, "Superconducting microresonators: physics and applications", Annu. Rev. Cond. Mat. Phys. **3**, 169 (2012).

[107] W. H. Parker, "Modified heating theory of nonequilibrium superconductors", Phys. Rev. B **12**, 3667 (1975).

[108] M. S. Khalil, "A study of two-level system defects in dielectric films using superconducting resonators", PhD thesis (University of Maryland, College Park, MD, 2013).

[109] D. I. Schuster, "Circuit quantum electrodynamics", PhD thesis (Yale University, New Haven, CT, 2007).

[110] L. Thévenin, "Extension de la loi d'Ohm aux circuits électromoteurs complexes (extension of Ohm's law to complex electromotive circuits)", Annales Télégraphiques **10**, 222 (1883).

[111] R. C. Zeller and R. O. Pohl, "Thermal conductivity and specific heat of noncrystalline solids", Phys. Rev. B **4**, 2029 (1971).

[112] M. V. Schickfus and S. Hunklinger, "The dielectric coupling of low-energy excitations in vitreous silica to electromagnetic waves", J. Phys. C: Sol. St. Phys. **9**, L439 (1976).

[113] M. V. Schickfus and S. Hunklinger, "Saturation of the dielectric absorption of vitreous silica at low temperatures", Phys. Lett. A **64**, 144 (1977).

[114] R. Barends, N. Vercruyssen, A. Endo, P. J. de Visser, T. Zijlstra, T. M. Klapwijk, P. Diener, S. J. C. Yates, and J. J. A. Baselmans, "Minimal resonator loss for circuit quantum electrodynamics", Appl. Phys. Lett. **97**, 023508 (2010).

[115] M. R. Vissers, J. S. Kline, J. Gao, D. S. Wisbey, and D. P. Pappas, "Reduced microwave loss in trenched superconducting coplanar waveguides", Appl. Phys. Lett. **100**, 082602 (2012).

[116] M. Sandberg, M. R. Vissers, J. S. Kline, M. Weides, J. Gao, D. S. Wisbey, and D. P. Pappas, "Etch induced microwave losses in titanium nitride superconducting resonators", Appl. Phys. Lett. **100**, 262605 (2012).

[117] D. L. Creedon, Y. Reshitnyk, W. Farr, J. M. Martinis, T. L. Duty, and M. E. Tobar, "High Q-factor sapphire whispering gallery mode microwave resonator at single photon energies and millikelvin temperatures", Appl. Phys. Lett. **98**, 222903 (2011).

[118] Z. K. Minev, I. M. Pop, and M. H. Devoret, "Planar superconducting whispering gallery mode resonators", Appl. Phys. Lett. **103**, 142604 (2013).

[119] W. A. Phillips, "Tunneling states in amorphous solids", J. Low Temp. Phys. **7**, 351 (1972).

[120] W. A. Phillips, "Tunneling states and the low-temperature thermal expansion of glasses", J. Low Temp. Phys. **11**, 757 (1973).

[121] W. A. Phillips, "Two-level states in glasses", Rep. Prog. Phys. **50**, 1657 (1987).

[122] P. W. Anderson, B. I. Halperin, and C. M. Varma, "Anomalous low-temperature thermal properties of glasses and spin glasses", Philos. Mag. **25**, 1 (1972).

[123] M. S. Khalil, S. Gladchenko, M. J. A. Stoutimore, F. C. Wellstood, A. L. Burin, and K. D. Osborn, "Landau-Zener population control and dipole measurement of a two-level-system bath", Phys. Rev. B **90**, 100201 (2014).

[124] J. C. Phillips, "Structural model of two-level glass states", Phys. Rev. B **24**, 1744 (1981).

[125] A. C. Anderson, "Low-temperature thermal expansion of glassy solids", Phys. Rev. B **34**, 1317 (1986).

[126] J. Gao, "The physics of superconducting microwave resonators", PhD thesis (California Institute of Technology, Pasadena, CA, 2008).

[127] F. Bloch, "Nuclear induction", Phys. Rev. **70**, 460 (1946).

[128] M. Bhattacharya, K. D. Osborn, and A. Mizel, "Jaynes-Cummings treatment of superconducting resonators with dielectric loss due to two-level systems", Phys. Rev. B **84**, 104517 (2011).

[129] E. T. Jaynes and F. W. Cummings, "Comparison of the quantum and semiclassical radiation theories with application to the beam maser", Proc. of the IEEE **51**, 89 (1963).

[130] Z. Kim, "Dissipative and dispersive measurements of a Cooper pair box", PhD thesis (University of Maryland, College Park, MD, 2010).

[131] J. M. Sage, V. Bolkhovsky, W. D. Oliver, B. Turek, and P. B. Welander, "Study of loss in superconducting coplanar waveguide resonators", J. Appl. Phys. **109**, 063915 (2011).

[132] M. R. Vissers, M. P. Weides, J. S. Kline, M. Sandberg, and D. P. Pappas, "Identifying capacitive and inductive loss in lumped element superconducting hybrid titanium nitride/aluminum resonators", Appl. Phys. Lett. **101**, 022601 (2012).

[133] C. M. Quintana, A. Megrant, Z. Chen, A. Dunsworth, B. Chiaro, R. Barends, B. Campbell, Y. Chen, I.-C. Hoi, E. Jeffrey, J. Kelly, J. Y. Mutus, P. J. J. O'Malley, C. Neill, P. Roushan, D. Sank, A. Vainsencher, J. Wenner, T. C. White, A. N. Cleland, and J. M. Martinis, "Characterization and reduction of microfabrication-induced decoherence in superconducting quantum circuits", Appl. Phys. Lett. **105**, 062601 (2014).

[134] M. Abramowitz and I. A. Stegun, "Handbook of mathematical functions with formulas, graphs, and mathematical tables", in (Dover Publications, Mineola, NY, 1972) Chap. 6.3, pp. 258–259.

[135] J. Wenner, R. Barends, R. C. Bialczak, Y. Chen, J. Kelly, E. Lucero, M. Mariantoni, A. Megrant, P. J. J. O'Malley, D. Sank, A. Vainsencher, H. Wang, T. C. White, Y. Yin, J. Zhao, A. N. Cleland, and J. M. Martinis, "Surface loss simulations of superconducting coplanar waveguide resonators", Appl. Phys. Lett. **99**, 113513 (2011).

[136] H. Wang, M. Hofheinz, J. Wenner, M. Ansmann, R. C. Bialczak, M. Lenander, E. Lucero, M. Neeley, A. D. O'Connell, D. Sank, M. Weides, A. N. Cleland, and J. M. Martinis, "Improving the coherence time of superconducting coplanar resonators", Appl. Phys. Lett. **95**, 233508 (2009).

[137] P. Macha, S. H. W. van der Ploeg, G. Oelsner, E. Il'ichev, H.-G. Meyer, S. Wünsch, and M. Siegel, "Losses in coplanar waveguide resonators at millikelvin temperatures", Appl. Phys. Lett. **96**, 062503 (2010).

[138] M. Khalil, F. Wellstood, and K. Osborn, "Loss dependence on geometry and applied power in superconducting coplanar resonators", IEEE Trans. Appl. Supercond. **21**, 879 (2011).

[139] L. Faoro and L. B. Ioffe, "Internal loss of superconducting resonators induced by interacting two-level systems", Phys. Rev. Lett. **109**, 157005 (2012).

[140] L. Faoro and L. B. Ioffe, "Interacting tunneling model for two-level systems in amorphous materials and its predictions for their dephasing and noise in superconducting microresonators", Phys. Rev. B **91**, 014201 (2015).

[141] J. Bardeen, L. N. Cooper, and J. R. Schrieffer, "Microscopic theory of superconductivity", Phys. Rev. **106**, 162 (1957).

[142] J. Bardeen, L. N. Cooper, and J. R. Schrieffer, "Theory of superconductivity", Phys. Rev. **108**, 1175 (1957).

[143] L. N. Cooper, "Bound electron pairs in a degenerate fermi gas", Phys. Rev. **104**, 1189 (1956).

[144] M. Tinkham, *Introduction to superconductivity*, 2nd Ed. (Dover Publications, Mineola, NY, 1996).

[145] D. C. Mattis and J. Bardeen, "Theory of the anomalous skin effect in normal and superconducting metals", Phys. Rev. **111**, 412 (1958).

[146] A. Rothwarf and B. N. Taylor, "Measurement of recombination lifetimes in superconductors", Phys. Rev. Lett. **19**, 27 (1967).

[147] J.-J. Chang and D. Scalapino, "Kinetic-equation approach to nonequilibrium superconductivity", Phys. Rev. B **15**, 2651 (1977).

[148] J.-J. Chang and D. Scalapino, "Nonequilibrium superconductivity", J. Low Temp. Phys. **31**, 1 (1978).

[149] D. J. Goldie and S. Withington, "Non-equilibrium superconductivity in quantum-sensing superconducting resonators", Supercond. Sci. Technol. **26**, 015004 (2013).

[150] S. Kaplan, C. Chi, D. Langenberg, J. Chang, S. Jafarey, and D. Scalapino, "Quasiparticle and phonon lifetimes in superconductors", Phys. Rev. B **14**, 4854 (1976).

[151] S. B. Kaplan, "Acoustic matching of superconducting films to substrates", English, J. Low Temp. Phys. **37**, 343 (1979).

[152] J. R. Schrieffer, D. J. Scalapino, and J. W. Wilkins, "Effective tunneling density of states in superconductors", Phys. Rev. Lett. **10**, 336 (1963).

[153] I. Giaever, H. R. Hart, and K. Megerle, "Tunneling into superconductors at temperatures below 1° K", Phys. Rev. **126**, 941 (1962).

[154] *Newton's Method - Wikipedia, the free encyclopedia*, `http://en.wikipedia.org/wiki/Newton's_method`, Accessed: 10/27/2015.

[155] T. Guruswamy, D. J. Goldie, and S. Withington, "Quasiparticle generation efficiency in superconducting thin films", Supercond. Sci. Technol. **27**, 055012 (2014).

[156] T. Guruswamy, D. J. Goldie, and S. Withington, "Nonequilibrium superconducting thin films with sub-gap and pair-breaking photon illumination", Supercond. Sci. Technol. **28**, 054002 (2015).

[157] A. Zehnder, "Response of superconductive films to localized energy deposition", Phys. Rev. B **52**, 12858 (1995).

[158] A. G. Kozorezov, A. F. Volkov, J. K. Wigmore, A. Peacock, A. Poelaert, and R. den Hartog, "Quasiparticle-phonon downconversion in nonequilibrium superconductors", Phys. Rev. B **61**, 11807 (2000).

[159] E. M. Purcell, "Spontaneous emission probabilities at radio frequencies", Phys. Rev. **69**, 681 (1946).

[160] A. A. Houck, J. A. Schreier, B. R. Johnson, J. M. Chow, J. Koch, J. M. Gambetta, D. I. Schuster, L. Frunzio, M. H. Devoret, S. M. Girvin, and R. J. Schoelkopf, "Controlling the spontaneous emission of a superconducting transmon qubit", Phys. Rev. Lett. **101**, 080502 (2008).

[161] C. Song, M. P. DeFeo, K. Yu, and B. L. T. Plourde, "Reducing microwave loss in superconducting resonators due to trapped vortices", Appl. Phys. Lett. **95**, 232501 (2009).

[162] D. Bothner, T. Gaber, M. Kemmler, D. Koelle, and R. Kleiner, "Improving the performance of superconducting microwave resonators in magnetic fields", Appl. Phys. Lett. **98**, 102504 (2011).

[163] D. Bothner, C. Clauss, E. Koroknay, M. Kemmler, T. Gaber, M. Jetter, M. Scheffler, P. Michler, M. Dressel, D. Koelle, and R. Kleiner, "Reducing vortex losses in superconducting microwave resonators with microsphere patterned antidot arrays", Appl. Phys. Lett. **100**, 012601 (2012).

[164] I. Nsanzineza and B. L. T. Plourde, "Trapping a single vortex and reducing quasiparticles in a superconducting resonator", Phys. Rev. Lett. **113**, 117002 (2014).

[165] C. Rigetti, J. M. Gambetta, S. Poletto, B. L. T. Plourde, J. M. Chow, A. D. Córcoles, J. A. Smolin, S. T. Merkel, J. R. Rozen, G. A. Keefe, M. B. Rothwell, M. B. Ketchen, and M. Steffen, "Superconducting qubit in a waveguide cavity with a coherence time approaching 0.1 ms", Phys. Rev. B **86**, 100506 (2012).

[166] A. P. Sears, "Extending coherence in superconducting qubits: from microseconds to milliseconds", PhD thesis (Yale University, New Haven, CT, 2013).

[167] Z. Kim, B. Suri, V. Zaretskey, S. Novikov, K. D. Osborn, A. Mizel, F. C. Wellstood, and B. S. Palmer, "Decoupling a Cooper-pair box to enhance the lifetime to 0.2 ms", Phys. Rev. Lett. **106**, 120501 (2011).

[168] *Microwave Office*, AWR Corporation/National Instruments, `www.awrcorp.com`.

[169] MicroChem, `www.microchem.com`.

[170] B. K. Cooper, "Multi-junction effects in dc SQUID phase qubits", PhD thesis (University of Maryland, College Park, MD, 2013).

[171] Transene Company, Inc. `www.transene.com`.

[172] A. Blais, R. S. Huang, A. Wallraff, S. M. Girvin, and R. J. Schoelkopf, "Cavity quantum electrodynamics for superconducting electrical circuits: an architecture for quantum computation", Phys. Rev. A **69**, 062320 (2004).

[173] D. M. Pozar, *Microwave Engineering*, 3rd Edition (John Wiley & Sons Inc., Hoboken, NJ, 2005).

[174] T. Nishikado, *Space Invaders*, Taito, Japan, 1978.

[175] Pasternack, `www.pasternack.com`.

[176] Oxford Instruments, Abingdon, Oxfordshire, UK, `www.oxford-instruments.com`.

[177] Keysight Technologies (formerly Agilent), `www.keysight.com`.

[178] Mini Circuits, `www.minicircuits.com`.

[179] Midwest Microwave (Cinch Connectivity), `cinchconnectivity.com`.

[180] Pamtech Inc. `pamtechinc.com`.

[181] Microwave Research Group (Weinreb Group), California Institute of Technology, www.caltechmicrowave.org.

[182] Miteq, www.miteq.com.

[183] Stanford Research Systems, www.thinksrs.com.

[184] National Instruments, www.ni.com.

[185] Thorlabs Inc. www.thorlabs.com.

[186] P. J. de Visser, S. Withington, and D. J. Goldie, "Readout-power heating and hysteretic switching between thermal quasiparticle states in kinetic inductance detectors", J. Appl. Phys. **108**, 114504 (2010).

[187] L. J. Swenson, P. K. Day, B. H. Eom, H. G. Leduc, N. Llombart, C. M. McKenney, O. Noroozian, and J. Zmuidzinas, "Operation of a titanium nitride superconducting microresonator detector in the nonlinear regime", J. Appl. Phys. **113**, 104501 (2013).

[188] COMSOL Multiphysics, COMSOL, Inc., www.comsol.com.

[189] S. Novikov, J. E. Robinson, Z. K. Keane, B. Suri, F. C. Wellstood, and B. S. Palmer, "Autler-Townes splitting in a three-dimensional transmon superconducting qubit", Phys. Rev. B **88**, 060503 (2013).

[190] *Euler–Bernoulli beam theory - Wikipedia, the free encyclopedia*, http://en.wikipedia.org/wiki/Euler-Bernoulli_beam_theory, Accessed: 10/27/2015.

[191] Y. Wang, P. Zhou, L. Wei, H. Li, B. Zhang, M. Zhang, Q. Wei, Y. Fang, and C. Cao, "Photon-induced thermal effects in superconducting coplanar waveguide resonators", J. Appl. Phys. **114**, 153109 (2013).

[192] V. Anant, A. J. Kerman, E. A. Dauler, J. K. W. Yang, K. M. Rosfjord, and K. K. Berggren, "Optical properties of superconducting nanowire single-photon detectors", Opt. Express **16**, 10750 (2008).

[193] S. N. Dorenbos, E. M. Reiger, N. Akopian, U. Perinetti, V. Zwiller, T. Zijlstra, and T. M. Klapwijk, "Superconducting single photon detectors with minimized polarization dependence", Appl. Phys. Lett. **93**, 161102 (2008).

[194] P. Solano, Personal communication.

[195] J. Hertzberg, *Development of a hybrid quantum system between a high-Q superconducting microwave resonator and trapped laser-cooled atoms*, Applied Superconductivity Conference poster, 2014.

[196] M. H. Devoret and J. M. Martinis, "Superconducting qubits", in *Quantum Entanglement and Information Processing (Les Houches Session LXXIX)*, edited by J.-M. Raimond, J. Dalibard, and D. Esteve (Elsevier, New York, NY, 2003), pp. 443–485.

[197] D. Vion, A. Aassime, A. Cottet, P. Joyez, H. Pothier, C. Urbina, D. Esteve, and M. H. Devoret, "Manipulating the quantum state of an electrical circuit", Science **296**, 886 (2002).

[198] J. A. Schreier, A. A. Houck, J. Koch, D. I. Schuster, B. R. Johnson, J. M. Chow, J. M. Gambetta, J. Majer, L. Frunzio, M. H. Devoret, S. M. Girvin, and R. J. Schoelkopf, "Suppressing charge noise decoherence in superconducting charge qubits", Phys. Rev. B **77**, 180502 (2008).

[199] H. Walther, B. T. H. Varcoe, B.-G. Englert, and T. Becker, "Cavity quantum electrodynamics", Rep. Prog. Phys. **69**, 1325 (2006).

[200] D. I. Schuster, A. A. Houck, J. A. Schreier, A. Wallraff, J. M. Gambetta, A. Blais, L. Frunzio, J. Majer, B. Johnson, M. H. Devoret, S. M. Girvin, and R. J. Schoelkopf, "Resolving photon number states in a superconducting circuit", Nature **445**, 515 (2007).

[201] B. Suri, "Transmon qubits coupled to superconducting lumped-element resonators", PhD thesis (University of Maryland, College Park, MD, 2015).

[202] S. Premaratne, Personal communication.

[203] K. W. Murch, S. J. Weber, C. Macklin, and I. Siddiqi, "Observing single quantum trajectories of a superconducting quantum bit", Nature **502**, 211 (2013).

[204] M. Boissonneault, J. M. Gambetta, and A. Blais, "Improved superconducting qubit readout by qubit-induced nonlinearities", Phys. Rev. Lett. **105**, 100504 (2010).

[205] M. D. Reed, L. DiCarlo, B. R. Johnson, L. Sun, D. I. Schuster, L. Frunzio, and R. J. Schoelkopf, "High-fidelity readout in circuit quantum electrodynamics using the Jaynes-Cummings nonlinearity", Phys. Rev. Lett. **105**, 173601 (2010).

[206] D. Esteve, M. H. Devoret, and J. M. Martinis, "Effect of an arbitrary dissipative circuit on the quantum energy levels and tunneling of a Josephson junction", Phys. Rev. B **34**, 158 (1986).

[207] R. Lutchyn, L. Glazman, and A. Larkin, "Quasiparticle decay rate of Josephson charge qubit oscillations", Phys. Rev. B **72**, 014517 (2005).

[208] R. M. Lutchyn, L. I. Glazman, and A. I. Larkin, "Kinetics of the superconducting charge qubit in the presence of a quasiparticle", Phys. Rev. B **74**, 064515 (2006).

[209] G. Catelani, R. J. Schoelkopf, M. H. Devoret, and L. I. Glazman, "Relaxation and frequency shifts induced by quasiparticles in superconducting qubits", Phys. Rev. B **84**, 064517 (2011).

[210] C. A. Sanchez, "Towards single shot measurement of a Cooper pair box using an RF-SET", PhD thesis (University of Maryland, College Park, MD, 2005).

[211] J. Aumentado, M. W. Keller, J. M. Martinis, and M. H. Devoret, "Nonequilibrium quasiparticles and $2e$ periodicity in single-cooper-pair transistors", Phys. Rev. Lett. **92**, 066802 (2004).

[212] J. Wenner, Y. Yin, E. Lucero, R. Barends, Y. Chen, B. Chiaro, J. Kelly, M. Lenander, M. Mariantoni, A. Megrant, C. Neill, P. J. J. O'Malley, D. Sank, A. Vainsencher, H. Wang, T. C. White, A. N. Cleland, and J. M. Martinis, "Excitation of superconducting qubits from hot nonequilibrium quasiparticles", Phys. Rev. Lett. **110**, 150502 (2013).

[213] A. J. Przybysz, "Reducing decoherence in dc SQUID phase qubits", PhD thesis (University of Maryland, College Park, MD, 2010).

[214] G. Ithier, E. Collin, P. Joyez, P. J. Meeson, D. Vion, D. Esteve, F. Chiarello, A. Shnirman, Y. Makhlin, J. Schriefl, and G. Schön, "Decoherence in a superconducting quantum bit circuit", Phys. Rev. B **72**, 134519 (2005).

[215] F. C. Wellstood, C. Urbina, and J. Clarke, "Flicker noise in the critical current of Josephson junctions at 0.09–4.2K", Appl. Phys. Lett. **85**, 5296 (2004).

[216] D. J. Van Harlingen, T. L. Robertson, B. L. T. Plourde, P. A. Reichardt, T. A. Crane, and J. Clarke, "Decoherence in Josephson-junction qubits due to critical-current fluctuations", Phys. Rev. B **70**, 064517 (2004).

[217] D. I. Schuster, A. Wallraff, A. Blais, L. Frunzio, R.-S. Huang, J. Majer, S. M. Girvin, and R. J. Schoelkopf, "ac Stark shift and dephasing of a superconducting qubit strongly coupled to a cavity field", Phys. Rev. Lett. **94**, 123602 (2005).

[218] P. Bertet, I. Chiorescu, G. Burkard, K. Semba, C. J. P. M. Harmans, D. P. DiVincenzo, and J. E. Mooij, "Dephasing of a superconducting qubit induced by photon noise", Phys. Rev. Lett. **95**, 257002 (2005).

[219] A. P. Sears, A. Petrenko, G. Catelani, L. Sun, H. Paik, G. Kirchmair, L. Frunzio, L. I. Glazman, S. M. Girvin, and R. J. Schoelkopf, "Photon shot noise dephasing in the strong-dispersive limit of circuit QED", Phys. Rev. B **86**, 180504 (2012).

[220] H. C. Torrey, "Transient nutations in nuclear magnetic resonance", Phys. Rev. **76**, 1059 (1949).

[221] R. A. Smith, "Excitation of transitions between atomic or molecular energy levels by monochromatic laser radiation", Proc. Royal Soc. London A: Math. Phys. Eng. Sci. **362**, 13 (1978).

[222] *Runge-Kutta Methods - Wikipedia, the free encyclopedia*, `http://en.wikipedia.org/wiki/Runge-Kutta_methods`, Accessed: 10/27/2015.

[223] S. Novikov, "Raman coherence effects in a superconducting Jaynes-Cummings system", PhD thesis (University of Maryland, College Park, MD, 2015).

[224] Headway Research, Inc. `www.headwayresearch.com`.

[225] *LOR and PMGI resists data sheet*, Micro Chem.

[226] *Nano PMMA and copolymer data sheet*, Micro Chem.

[227] JEOL Ltd. `www.jeolusa.com`.

[228] Nanometer Pattern Generation System, www.jcnabity.com.

[229] Alfa Aesar, www.alfa.com.

[230] The R. D. Mathis Company, www.rdmathis.com.

[231] V. Ambegaokar and A. Baratoff, "Tunneling between superconductors", Phys. Rev. Lett. **10**, 486 (1963).

[232] Fairview Microwave, www.fairviewmicrowave.com.

[233] MAC Technologies, www.mactechnology.com.

[234] F. A. Hopf, R. F. Shea, and M. O. Scully, "Theory of optical free-induction decay and two-photon superradiance", Phys. Rev. A **7**, 2105 (1973).

[235] E. L. Hahn, "Spin echoes", Phys. Rev. **80**, 580 (1950).

[236] L. S. Bishop, "Circuit quantum electrodynamics: volume II", PhD thesis (Yale University, New Haven, CT, 2010).

[237] S. K. Dutta, F. W. Strauch, R. M. Lewis, K. Mitra, H. Paik, T. A. Palomaki, E. Tiesinga, J. R. Anderson, A. J. Dragt, C. J. Lobb, and F. C. Wellstood, "Multilevel effects in the Rabi oscillations of a Josephson phase qubit", Phys. Rev. B **78**, 104510 (2008).

[238] Tektronix, www.tek.com.

[239] N. A. Court, A. J. Ferguson, and R. G. Clark, "Energy gap measurement of nanostructured aluminium thin films for single Cooper-pair devices", Supercond. Sci. Technol. **21**, 015013 (2008).

[240] K. Voigt, J. Hertzberg, J. Hoffman, J. Grover, P. Solano, R. Budoyo, C. Ballard, J. Lee, J. Anderson, C. Lobb, L. Orozco, S. Rolston, and F. Wellstood, "Movable thin-film superconducting resonator coupled to a tapered optical microfiber at 15 mK", IEEE Trans. Appl. Supercond. **25**, 1 (2015).